NASA-CR-192940

DEVELOPMENT AND APPLICATION OF COMPUTATIONAL AEROTHERMODYNAMICS FLOWFIELD COMPUTER CODES

AMES
GRANT
IN-02-CR

Technical Progress Report (Substitution)

for
Cooperative Agreement No. NCC2-420

158844

for the period
April 1, 1992 - January 31, 1993

P-157

Submitted to

National Aeronautics and Space Administration
Ames Research Center
Moffett Field, California 94035

Aerothermodynamics Branch
Dr. George S. Deiwert, Technical Officer

Thermosciences Division
Dr. Jim Arnold, Chief

Prepared by

ELORET INSTITUTE
1178 Maraschino Drive
Sunnyvale, CA 94087
Phone: 408 730-8422 and 415 493-4710
Telefax: 408 730-1441
K. Heinemann, President and Grant Administrator
Ethiraj Venkatapathy, Principal Investigator

23 April, 1993

(NASA-CR-192940) DEVELOPMENT AND
APPLICATION OF COMPUTATIONAL
AEROTHERMODYNAMICS FLOWFIELD
COMPUTER CODES Progress Report, 1
Apr. 1992 - 31 Jan. 1993 (Eloret
Corp.) 157 p

N93-24736

Unclas

G3/02 0158844

The following publications and papers resulted from the research performed during this performance period:

(1) I.D. Boyd and T. Gkcen, "*Evaluation of Thermochemical Models for Particle and Continuum Simulations of Hypersonic Flow,*" AIAA 27th Thermophysics Conf., Nashville, TN, 1992, AIAA-paper 92-2971.

(2) J.-L. Cambier, S. Tokarcik, and D.K. Prabhu, "*Numerical Simulations of Unsteady Flow in a Hypersonic Shock Tunnel Facility,*" AIAA 27th Thermophysics Conference, Nashville, TN, 1992, AIAA-Paper 92-4029.

(3) I.D. Boyd and E.E. Whiting, "*Decoupled Predictions of Radiative Heating in Air Using a Particle Simulation Method,*" AIAA 23rd Plasmadynamics & Lasers Conf., Nashville, TN, 1992, AIAA-Paper 92-2954.

(4) G. Wilson, "*Time-Dependent Quasi-One-Dimensional Simulations of High-Enthalpy Pulse Facilities,*", AIAA 4th Int. Aerospace Planes Conf., Orlando, FL, 1992, AIAA-Paper 92-5096.

(5) S.-H. Lee and Chul Park, *"Validation of Three-Temperature Nozzle Flow Code NOZ3T,"* submitted for publication.

(6) S. Tokarcik, E. Venkatapathy, and M. Tauber, *"Computational Study of a Lunar Return Aerobrake Concept,"* Abstract for 31st Aerospace Sciences Meeting, Reno, NV. 1993.

(7) S. (Tokarcik) Polsky, E. Venkatapathy, and M. Tauber, *"Computational Study of a Lunar Return Aerobrake Concept,"* 31st Aerospace Sciences Meeting, Reno, NV. 1993 AIAA-Paper 93-0037.

(8) G. Wilson, S.P. Sharma, and W.D. Gillespie, *"Time-Dependent Simulations of Reflected-Shock/Boundary Layer Interaction,"* 31st Aerospace Sciences Meeting, Reno, NV. 1993 AIAA-Paper 93-0480.

(9) S. Tokarcik and J.-L. Cambier, *"Numerical Study of the Transient Flow in the Driven Tube and the Nozzle Section of a Shock Tunnel,"* Submitted for Publication.

(10) G.J. Wilson and M.A. Sussman, *"Computation of Unsteady*

Shock-Induced Combustion Using Logarithmic Species Conservation Equations," AIAA Journal Vol.31, 1993, 294.

(11) S. Tokarcik and E. Venkatapathy, *"Hypersonic Aerodynamic Decelerators Design Using CFD: Part II - Turbulent Computations,"* Submitted for publication.

(12) D.A. Levin, G.V. Candler, R.J. Collins, C.L. Howlett, E.E. Whiting and Ch. Park, *"Comparison of Theory with Atomic Oxygen 1304 A Radiation Data from the Bow Shock Ultraviolet 2 Rocket Flight,"* Abstract for 28th AIAA Thermophysics Conf., 1993.

(13) N.K.J.M. Gopaul, D. Babikian, and Ch. Park, *"Measurement and Analysis of NO Radiation in an Arc-Jet Flow,"* Abstract for 28th AIAA Thermophysics Conf., 1993.

AIAA-92-2954

Evaluation of Thermochemical Models for Particle and Continuum Simulations of Hypersonic Flow

I. D. Boyd and T. Gökçen
Eloret Institute
Palo Alto, CA 94303.

ORIGINAL PAGE IS
OF POOR QUALITY

AIAA 27th Thermophysics Conference
July 6-8, 1992 / Nashville, TN

AIAA-92-2954

EVALUATION OF THERMOCHEMICAL MODELS FOR PARTICLE AND CONTINUUM SIMULATIONS OF HYPERSONIC FLOW

Iain D. Boyd † and Tahir Gökçen †
Eloret Institute, 3788 Fabian Way
Palo Alto, California.

Abstract

Computations are presented for one-dimensional, strong shock waves that are typical of those that form in front of a reentering spacecraft. The fluid mechanics and thermochemistry are modeled using two different approaches. The first employs traditional continuum techniques in solving the Navier-Stokes equations. The second approach employs a particle simulation technique (the direct simulation Monte Carlo method, DSMC). The thermochemical models employed in these two techniques are quite different. The present investigation presents an evaluation of thermochemical models for nitrogen under hypersonic flow conditions. Four separate cases are considered that are dominated in turn by vibrational relaxation, weak dissociation, strong dissociation and weak ionisation. In near-continuum, hypersonic flow, the nonequilibrium thermochemical models employed in continuum and particle simulations produce nearly identical solutions. Further, the two approaches are evaluated successfully against available experimental data for weakly and strongly dissociating flows.

Introduction

A space-vehicle passing through the earth's atmosphere will traverse a number of different flow regimes. At lower altitudes, the fluid density is sufficiently large for the flow to be considered in thermochemical equilibrium. However, as the vehicle ascends higher into the atmosphere, the molecular collision rate will fall, and low-density effects will become increasingly important.

Continuum methods are successfully applied to flows in which the collision rate of the gas is sufficient to maintain Boltsmann energy distributions for the various thermal modes of the gas. It is not necessary that the temperatures associated with each of the different modes be equal, or that chemical equilibrium prevails. Particle methods, such as the direct simulation Monte Carlo method (DSMC), are successfully applied to flows in which a reduced collision rate no longer supports equilibrium energy distributions. As the numerical cost of this technique is proportional to the fluid density, application has been limited to rarefied flows.

The computation of flow properties for the flight trajectories of many space vehicles will require the use of both continuum and particle methods mentioned above. The interface between the different flow regimes is therefore of great importance. Clearly, it is desirable to obtain consistent results with these numerical methods in an overlapping near-continuum flow regime. Although the thermochemical models employed in continuum and particle methods are quite different, under conditions of thermochemical equilibrium they are expected to provide identical solutions. The relationship between the continuum and particle simulation under conditions of thermochemical nonequilibrium, however, has not been investigated previously. It is therefore the purpose of the present paper to study this relationship by computing typical hypersonic flows with both the continuum and particle simulation methods.

Evaluation of the thermochemical models is made through the computation of four different cases. The flow conditions in the studies are given in Table 1 and are chosen to examine the effects of vibrational relaxation, dissociation, and ionisation. These processes are considered in an accumulative sense through a gradual increase in the initial enthalpy of the flow. The continuum and particle approaches employed in

---

† Research Scientist. Mailing address:
NASA Ames Research Center, MS 230-2, CA 94035.

this work are briefly described below.

Table 1. Flow conditions.

Case	U_1 (m/s)	ρ_1 (kg/m^3)	p_1 (torr)	U_2 (m/s)
1	4000	$1.75\text{x}10^{-3}$	1.17	541
2	4800	$4.67\text{x}10^{-2}$	31.2	480
3	7310	$7.48\text{x}10^{-3}$	5.00	496
4	10000	$5.00\text{x}10^{-4}$	0.33	640

Continuum Approach

In the continuum formulation, the nonequilibrium gas model for air consists of eleven chemical species, (N_2, O_2, NO, N, O, N_2^+, O_2^+, NO^+, N^+, O^+, e^-), and the thermal state of the gas is described by three temperatures: translational, rotational and vibrational (vibrational-electronic). The governing Navier-Stokes equations are supplemented by the equations accounting for thermochemical nonequilibrium processes. The equation set consists of fifteen partial differential equations: eleven mass conservation equations for species, one momentum equation for quasi one-dimensional flow, and three energy equations. For this work, only nitrogen reactions are considered. The thermochemistry model is basically that proposed by Park.[1-2] The relaxation time for vibrational-translational energy exchange is taken from Millikan and White[3] with Park's modification which accounts for the limiting cross-section at high temperatures. Another of Park's modifications concerning the diffusive nature of vibrational relaxation is not included to be consistent with the current particle model. For Vibration-Dissociation coupling, the average removal of vibrational energy due to dissociation is taken as 30 percent of the dissociation energy.[1] The chemical reaction rates are prescribed by Park's model where the basic dissociation rate is assumed to be governed by the geometric average of translational and vibrational temperatures.

The numerical approach to solve the governing equations is fully implicit for fluid dynamics and chemistry. It uses flux vector splitting for convective fluxes, and shock capturing. An adaptive grid strategy is also implemented. For the computations in this paper, a quasi one-dimensional code is used and a freestream of pure nitrogen is prescribed. The details of the numerical method can be found in Refs. 4-6.

Particle Approach

The particle simulation code employed in this investigation provides modeling of the translational, rotational, vibrational, and electron kinetic energy distributions. These are complemented through simulation of dissociative, recombinative, ionizing, and exchange reactions. The code is vectorized for efficient execution on a Cray-YMP. Description of the vectorized implementation may be found in Refs. 7 and 8. The boundary conditions employed in the one-dimensional flow are reflecting pistons set to the upstream and downstream velocities. The downstream velocity is obtained either from the continuum calculations, or from available experimental data. Previous DSMC simulations of the relaxation zone behind strong shocks[8] were commenced at the point of translational-rotational equilibrium (where the ratio of local to freestream density is equal to 6). The present simulations represent an improvement in that the computation of the entire shock structure is included from upstream to downstream conditions. Once the shock reaches a specified location, small adjustments are made to the coordinate system of the computational grid to maintain a steady shock position.

The rate of energy exchange between the translational and rotational energy modes is simulated using the model of Boyd.[9] The mechanics of rotational energy exchange is performed by the Borgnakke-Larsen[10] approach. The rate of energy exchange involving the vibrational energy mode is simulated using a high-temperature model also proposed by Boyd.[11] The mechanics of vibrational energy exchange are computed using two different schemes. The first again uses the Borgnakke-Larsen approach in with a continuous vibrational energy distribution described by a number of vibrational degrees of freedom, ζ_v, which is fixed. The second approach, due to McDonald,[12] allows sampling of post-collision vibrational energy levels from the discrete form of the Simple Harmonic Oscillator (SHO). This approach does not require the value of ζ_v to be estimated for the whole flowfield. Instead, it effectively varies ζ_v according to the local energy content of the flow, and is the preferred approach from a physical standpoint. The manner in which the mechanics of energy exchange is performed in the particle simulation is shown by Lumpkin *et al.*[13]

Table 2. Leading constants in chemical rate data (m^3/molecule/s).

Number	Reaction	Continuum[2]	Particle[19]	Particle (present)
1.	$N_2 + N_2 \rightarrow N + N + N_2$	$1.16\text{x}10^{-8}\ T^{-1.6}$	$6.17\text{x}10^{-9}\ T^{-1.6}$	$7.97\text{x}10^{-13}\ T^{-0.5}$
2.	$N_2 + N \rightarrow N + N + N$	$4.98\text{x}10^{-8}\ T^{-1.6}$	$1.85\text{x}10^{-8}\ T^{-1.6}$	$7.14\text{x}10^{-8}\ T^{-1.5}$
3a.	$N^+ + N_2 \rightarrow N + N_2{}^+$	$1.66\text{x}10^{-18}\ T^{0.5}$	$1.67\text{x}10^{-17}\ T^{-0.18}$	$1.66\text{x}10^{-18}\ T^{0.5}$
3b.	$N + N_2{}^+ \rightarrow N^+ + N_2$	See Ref. 1	$2.37\text{x}10^{-18}\ T^{-0.52}$	$2.34\text{x}10^{-14}\ T^{-0.61}$
4a.	$N + N \rightarrow N_2{}^+ + e^-$	$7.31\text{x}10^{-23}\ T^{1.5}$	$2.98\text{x}10^{-20}\ T^{0.77}$	$7.31\text{x}10^{-23}\ T^{1.5}$
4b.	$N_2{}^+ + e^- \rightarrow N + N$	See Ref. 1	$8.88\text{x}10^{-10}\ T^{-1.23}$	$1.57\text{x}10^{-11}\ T^{0.85}$
5.	$N + e^- \rightarrow N^+ + e^- + e^-$	$4.15\text{x}10^{4}\ T^{-3.82}$	$1.00\text{x}10^{-14}$	$5.81\text{x}10^{-8}\ T^{-1.0}$

to affect the rate of relaxation. Therefore, all the rotational and vibrational relaxation models employed in the particle simulations are adjusted to match the continuum values by the correction developed in Ref. 13.

Dissociation reactions are modeled with the Vibrationally Favored Dissociation model (VFD) proposed by Haas and Boyd.[14] As its name suggests, this model includes the important physical phenomenon of vibration-dissociation coupling. The model contains a free parameter ϕ which controls the degree of coupling between vibrational and dissociative relaxation effects. It was demonstrated in Ref. 14 that, by increasing the value of ϕ, it is possible to increase the dissociation incubation time in the simulation. Also in Ref. 14, through comparison with experimental data, the value of ϕ for nitrogen was determined assuming Borgnakke-Larsen mechanics for vibrational energy exchange with a fixed value for ζ_v. In the DSMC code, the model employed for the reverse recombination reaction appropriate to VFD is that developed by Boyd.[8] All other chemical reactions (ionisation and exchange reactions) are simulated using the steric factor developed by Bird.[15] The inclusion of electrons in the simulation is discussed in detail in Ref. 16.

Chemical Rate Coefficients

The rate coefficients employed in the reactions of interest in the present study are given in Table 2. These are described in the usual Arrhenius form:

$$k(T) = aT^b exp(-E_a/kT)$$

where a and b are empirically determined constants, E_a is the activation energy, and T is the controlling temperature. Three different sets of coefficients are given corresponding to those used in the continuum code, in previous DSMC investigations, and in the present DSMC code. The values of the activation energy used in the three sets of rate data are unchanged for each separate reaction. Therefore, the exponential term in the Arrhenius form has been omitted from Table 2.

The rate expressions employed in the continuum code are those recommended in the review by Park *et al.*[2] Generally, only the forward rate constants are specified. In the dissociation reactions, numbers 1 and 2, the controlling temperature in the continuum two-temperature approach is given by $T_a=(TT_v)^{\frac{1}{2}}$. For nitrogen dissociation, the particle code employs the rates of Byron[17] in the Vibrationally Favored Dissociation model (VFD). It was shown previously by Boyd[8] that these rates, when used with the VFD model, are capable of reproducing vibration-dissociation coupling observed at high temperatures.

The reverse rates for each reaction are obtained by evaluating the following temperature-dependent form for the equilibrium constants proposed by Park[1]:

$$ln(K_e(T)) = A_1z + A_2 + A_3ln(z) + A_4/z + A_5/z^2$$

where the A_i are constants and z=10000/T. In the continuum code, the values of A_i for reaction 3 are obtained from Ref. 18 while those for reaction 4 are taken from Ref. 1. Unfortunately, this form for the equilibrium constant is not mathematically convenient for implementation in the DSMC chemistry models. However, a set of reverse reaction rates for use in DSMC has been proposed by Bird,[19] and these have been used in a number of studies. It is possible to determine the equilibrium constants employed in Bird's reaction set by considering the ratio of the forward and reverse ratesfor each reaction. This is performed for reactions 3 and 4 of Table 2. The equilibrium constants employed by Bird and those used in the continuum code

are shown as a function of temperature for these reactions in Figs. 1 and 2, respectively. It should be noted that the exponential term has again been omitted for the sake of simplicity. For the charge exchange reaction, it is found that the equilibrium constant employed by Bird is about 2 orders of magnitude higher than the continuum expression. In the associative ionisation reaction, the equilibrium constant of Bird gives values which are again generally higher than the continuum model.

The goal of the present study is to evaluate differences in the chemical models employed in the continuum and particle methods. To limit the number of factors involved in our comparisons, it is the aim to maintain consistency between the relaxation rates employed in the solution techniques. Therefore, a form for the equilibrium constant which takes the traditional Arrhenius form is fit as a function of temperature to Park's expression. The limitation on the type of Arrhenius form which may be used conveniently in Bird's expression for the probability of chemical reaction[15] is discussed by Boyd and Stark.[20] The curve fits for reactions 3 and 4 are also shown in Figs. 1 and 2. The resulting rate constants for the reverse reactions are listed in Table 2. Generally, good agreement is obtained between the new DSMC expressions and Park's results, particularly over the temperature range of interest, i.e. from 10,000 to 20,000 K.

For reaction 5, the temperature dependent form proposed in Ref. 2 is not convenient for use in the DSMC chemistry models. In Fig. 3, the forward rate constants employed by Park and Bird for this reaction are shown as a function of temperature. It is noted that Bird's reaction rates are several orders of magnitude lower. Once again, a fit is made to Park's expression in an Arrhenius form which may be employed in the particle chemistry models. The new form, which is given in Table 2 and included in Fig. 3, gives closer correspondence to Park's results over the temperature range of interest.

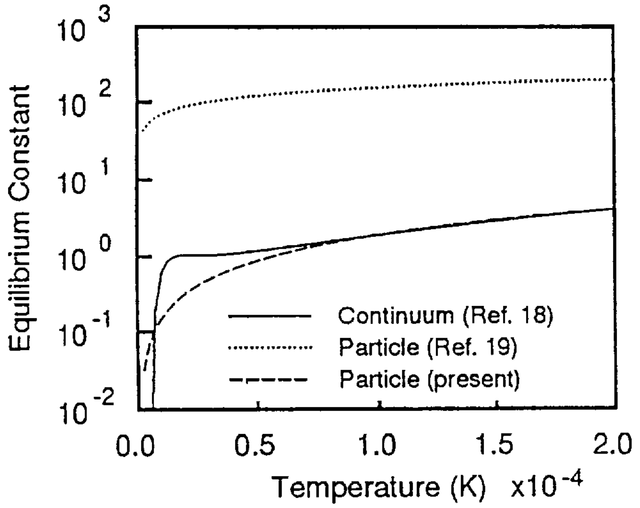

Fig. 1. Variation of the equilibrium constant with temperature for reaction 3.

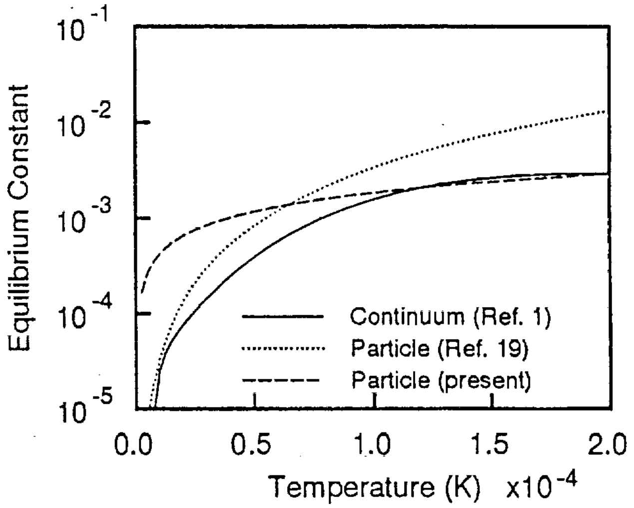

Fig. 2. Variation of the equilibrium constant with temperature for reaction 4.

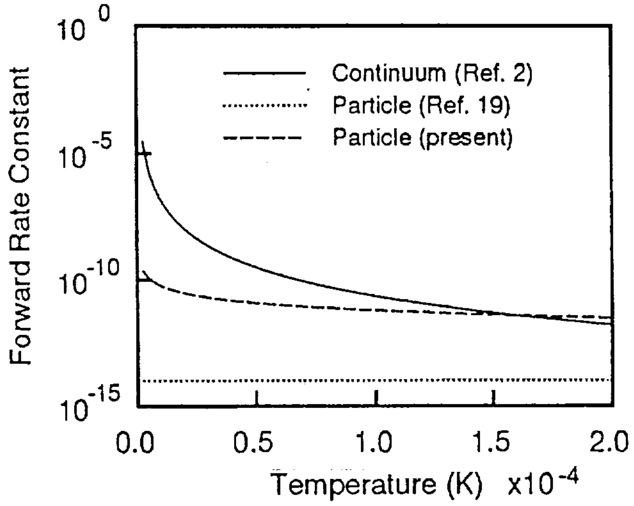

Fig. 3. Variation of the forward rate constant with temperature for reaction 5.

Further analyses have been performed which improve the correspondence between the chemical rates employed in continuum and particle simulation for all reactions in air involving charged species and are reported in Ref. 16.

Presentation of Results

Computations are performed for four different sets of flow conditions for pure nitrogen and these are listed in Table 1 in which subscripts 1 and 2 indicate upstream and downstream conditions, respectively. The upstream temperature is prescribed to be 300 K for all cases. The upstream density together with the length of the computational domain simulated are chosen such that the flows are in the near-continuum regime. The different upstream flow conditions also provide increasing enthalpy: thus, the flow behind the shock is characterised in Case 1 by vibrational relaxation processes; in Case 2 by weak dissociation; in Case 3 by strong dissociation; and in Case 4 by weak ionisation. The conditions in Cases 2 and 3 correspond to those investigated experimentally by Kewley and Hornung.[21] The results for each of these investigations are described in the following sub-sections.

Case 1: Vibrationally Relaxing Flow

Density profiles for the first case investigated are shown in Fig. 4. Very good agreement is found between the continuum and particle siumulation results. Two different DSMC computations are shown: the first corresponds to the use of the Borgnakke-Larsen approach (BL) for performing the mechanics of vibrational energy exchange with a constant number of vibrational degrees of freedom, ζ_v=1.6. This value corresponds closely to that evaluated at the downstream equilibrium temperature. The second solution employed the discrete vibrational energy sampling approach for the Simple Harmonic Oscillator (SHO) of McDonald[7] which automatically varies ζ_v. This is the first time that comparison is made between continuum and particle simulations for vibrational relaxation behind a strong shock. It is very encouraging to observe, under near-continuum conditions, that the two methods give such close agreement.

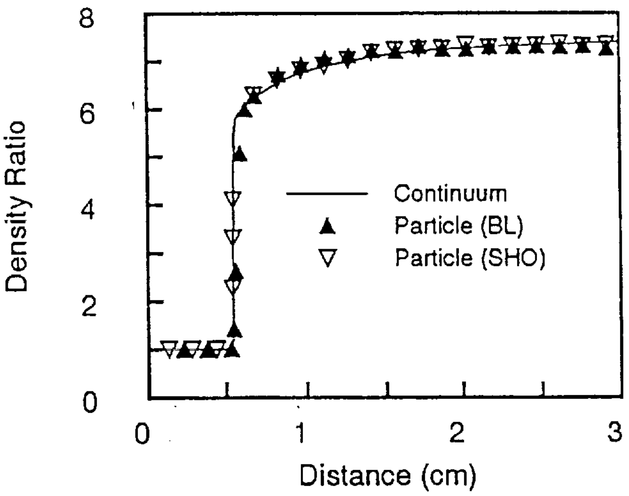

Fig. 4. Comparison of continuum and particle solutions of the local to upstream density ratio for Case 1.

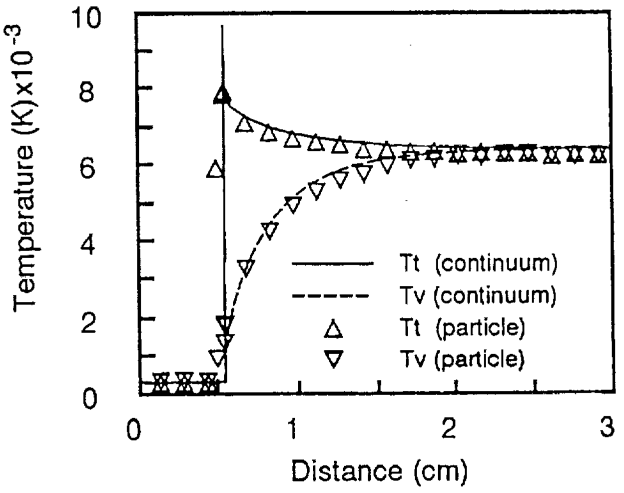

Fig. 5. Comparison of continuum and particle solutions of the translational and vibrational temperatures for Case 1.

The variation in translational and vibrational temperatures for this case are shown in Fig. 5. The particle solutions are obtained with McDonald's variable ζ_v model. Once again, very good agreement is obtained between the two solution techniques. Temperature is generally a much more sensitive quantity to simulate than density. The close correspondence between the continuum and particle results indicates that the vibrational relaxation models employed in each are very nearly equivalent. This comparison therefore lends

strong support to the use in the particle simulation of the vibrational energy exchange probabilities developed for the DSMC method,[11] the correction term required to equate the continuum and particle relaxation rates,[13] and the mechanics of vibrational energy exchange.[12] It should be noted that the degree of dissociation under these flow conditions is less than 1%.

Case 2: Weakly Dissociating Flow

The second set of conditions considered has an increased enthalpy which gives rise to weak dissociation behind the shock. This case is of additional interest as it was studied experimentally by Kewley and Hornung[21] who employed interferograms to measure the variation in density behind strong shocks of nitrogen. The increase in enthalpy is revealed in the density profiles shown in Fig. 6 in which the normalised density rise reaches a value of about 10 at the downstream boundary. While both solutions give good agreement with the experimental data, it is clear that the particle solution provides the better correspondence. The DSMC profile is obtained with the variable ζ_v model. Comparison of the translational and vibrational temperatures computed through the shock are shown in Fig. 7. Again, a very good agreement is observed for the two sets of results. Considering the excellent agreement obtained in Fig. 7 between the continuum and particle methods, and also for the case of vibrational relaxation, it is concluded that the differences observed in Fig. 6 must be due to the dissociation models employed in each simulation technique. This indicates that the continuum two-temperature model gives a dissociation rate which is slightly slower than that of experiment and DSMC. In other words, for a weakly dissociating gas, while the effect of dissociation on vibrational relaxation is small, the effect of vibrational relaxation on dissociation is overestimated in Park's two-temperature model.

The results for the mole fractions of molecular and atomic nitrogen are shown in Fig. 8. As expected from the previous comparisons, there is close agreement between the two numerical approaches with DSMC predicting slightly more dissociation than is obtained in the continuum solution.

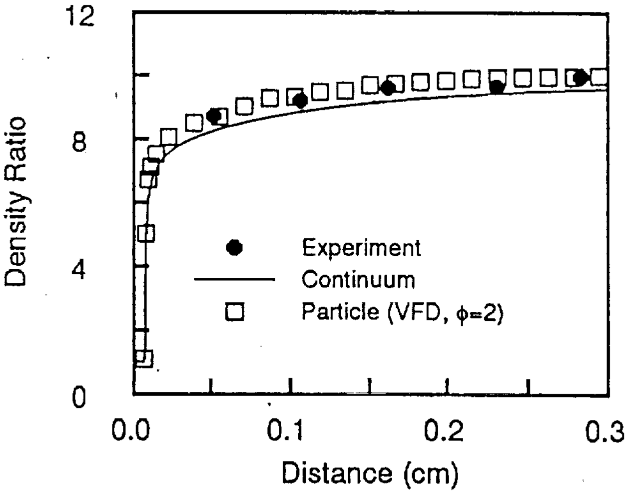

Fig. 6. Comparison of continuum and particle solutions of the local to upstream density ratio for Case 2.

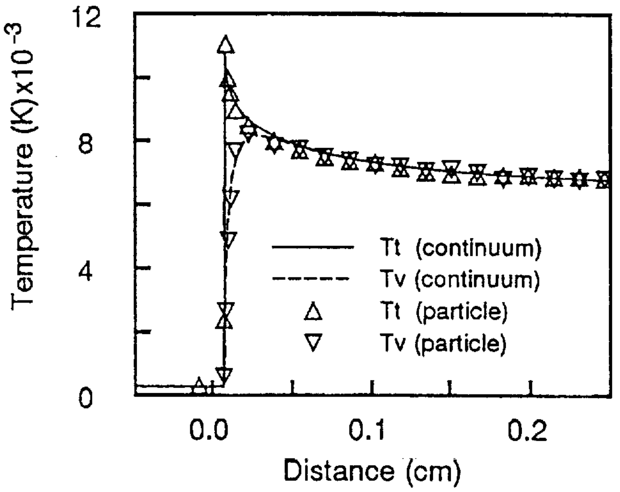

Fig. 7. Comparison of continuum and particle solutions of the translational and vibrational temperatures for Case 2.

Case 3: Strongly Dissociating Flow

The further increase in enthalpy for Case 3 gives rise to stronger dissociation effects. Once again, the flow conditions modeled match those considered experimentally by Kewley and Hornung.[21] The experimental profile of density behind the shock is compared with several different computational results in Fig. 9. The comparison between the continuum solution and the experimental data is excellent. Two different DSMC profiles are also shown in Fig. 9: the first employed

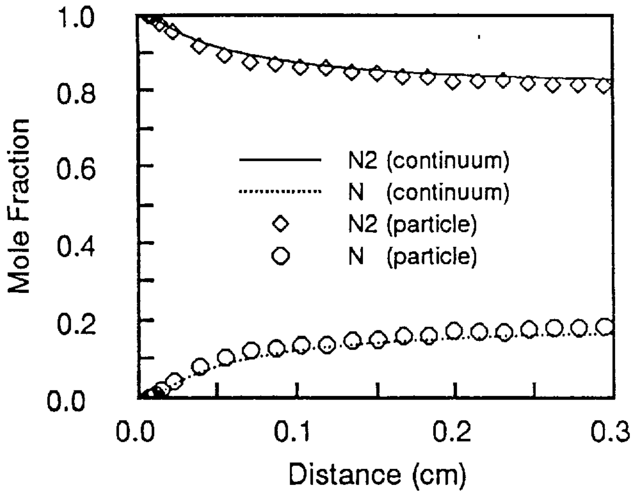

Fig. 8. Comparison of continuum and particle solutions of the species mole fractions for Case 2.

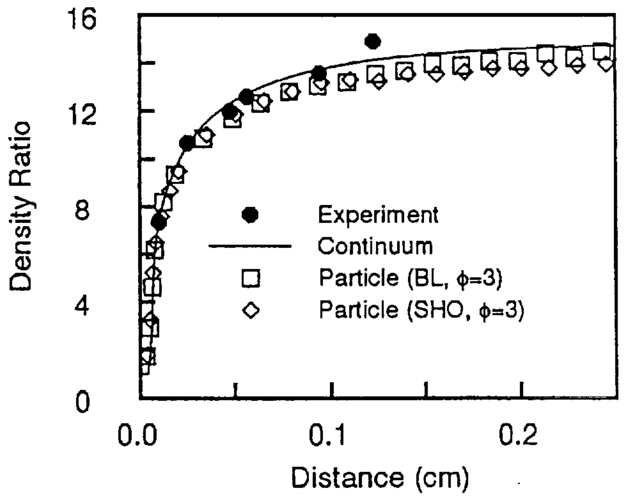

Fig. 9. Local to upstream density ratio for Case 3: particle simulation employed old VFD and exchange mechanics models.

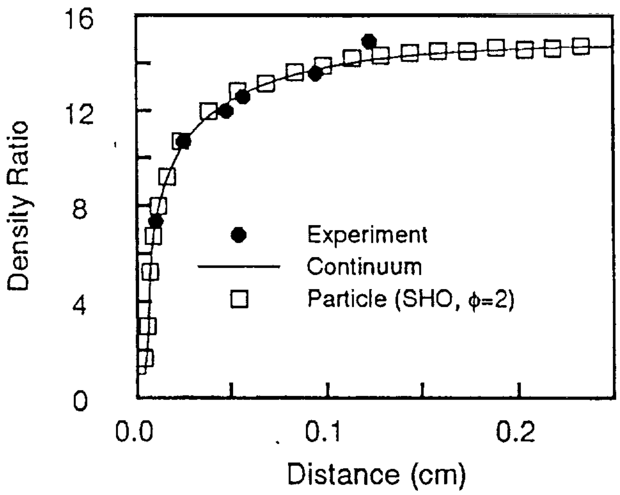

Fig. 10. Local to upstream density ratio for Case 3: particle simulation employed new VFD and exchange mechanics models.

ζ_v=2 and ϕ=3. This represents the model proposed previously in Ref. 8. The second particle simulation employed the variable ζ_v model and again used ϕ=3. For both of these DSMC modeling configurations, the computed density profile lies a little below both the experimental data and the continuum solution. A further DSMC solution is generated in which the VFD parameter ϕ is reduced to 2 for use with variable ζ_v. The results of this simulation are compared with both the experimental and continuum profiles in Fig. 10. As expected, a reduction in the value of ϕ reduces the degree of vibration-dissociation coupling which leads to a slightly increased dissociation rate immediately behind the shock. With this model configuration, the particle method provides excellent agreement with both the experiment and the continuum solution. It should be noted that this is the DSMC model configuration employed in the computations for Case 2.

The translational and vibrational temperature profiles computed with the continuum and DSMC techniques are shown in Fig. 11. Generally, very good agreement is observed between the two. There is a noticeable difference in the peak vibrational temperatures computed by the two methods. This has quite significant implications for the estimation of radiative emission in such flows. The difference is attributable to dissociation-vibration coupling, i.e. how the vibrational energy distribution is affected by dissociation. This process is modeled quite differently in the continuum and particle approaches. These results indicate the need for experimental measurement of vibrational temperature profiles behind shock waves under conditions similar to those considered here. For completeness, the profiles of mole fractions of the neutral species are shown in Fig. 12. The stronger degree of dissociation for these flow conditions is very evident and, as expected, very good agreement is found between the two solutions.

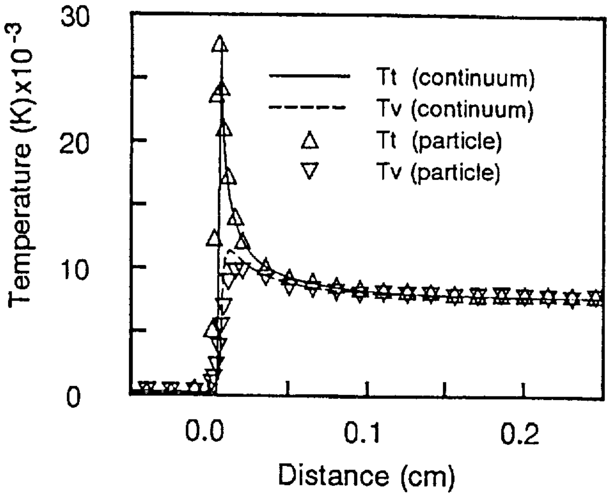

Fig. 11. Comparison of continuum and particle solutions of the translational and vibrational temperatures for Case 3.

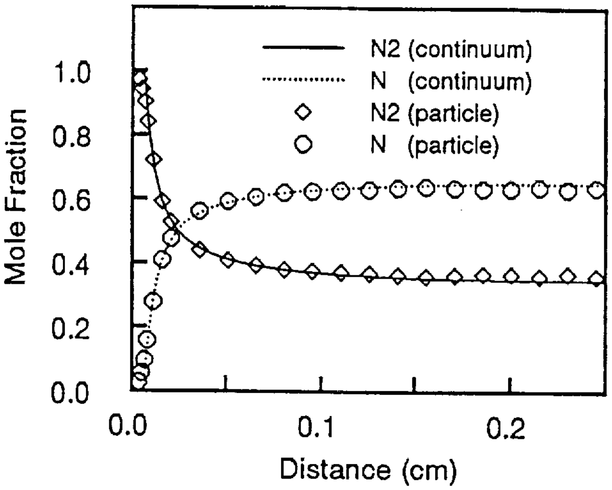

Fig. 12. Comparison of continuum and particle solutions of the species mole fractions for Case 3.

For this strongly dissociating case, it is found that Park's two temperature model reproduces the experimental data very well. It is very encouraging that the two temperature model gives such a favorable comparison with the experimental data in strongly dissociating flow as this is the regime for which the model has been developed. Indeed, the present comparison arguably provides the strongest evidence to date that, despite its weak theoretical basis, the two-temperature model does produce adequate simulation of strongly coupled vibration-dissociation processes. The present investigation is unique in that evaluation of the model is performed through direct comparison with experimental measurements of a fundamental flow quantity. The model was previously calibrated against experimental data by Park[1] through comparison with radiation emission spectra, and by Candler[22] through comparison with shock stand-off distance. Due to the excellent comparisons between DSMC and experiment in Figs. 6 and 10, it is recommended that McDonald's collision mechanics and the VFD model with $\phi=2$ be used for simulating nitrogen dissociation with the particle method.

Case 4: Weakly Ionising Flow

The increase in enthalpy for Case 4 is sufficient to give rise to significant ionisation effects behind the shock. In performing the DSMC computations of the ionised flowfield, a steady shock solution is first obtained with the ionising reactions omitted. After reaching this point, the ionised species are included and a further short transient phase in the simulation then allowed before sampling of flow properties is commenced. These procedures are adopted because the inclusion of electrons in the flowfield requires a reduction in computational time-step by two orders of magnitude. To compute the entire flowfield with such a small time-step would expend much larger computational resources. The comparison for density profiles computed with the numerical techniques is shown in Fig. 13. As with the previous cases, good agreement is obtained between the two solutions. The temperature profiles computed with the continuum and particle methods for the translational and vibrational modes are compared in Fig. 14. The peak values for each energy mode are in good agreement. It is observed that the translational temperature shock computed with DSMC is thicker than the continuum result. This is due to the relatively low upstream density employed in this investigation. A more thorough analysis of such behavior will form the basis of future study. The computed mole fractions for the neutral species obtained with the numerical techniques are compared in Fig. 15 and those for the charges species are compared in Fig. 16. The agreement which is generally obtained is very satisfactory. This comparison verifies that the new forms of the reverse reaction rates employed in the particle simulation are nearly equivalent to the expressions used

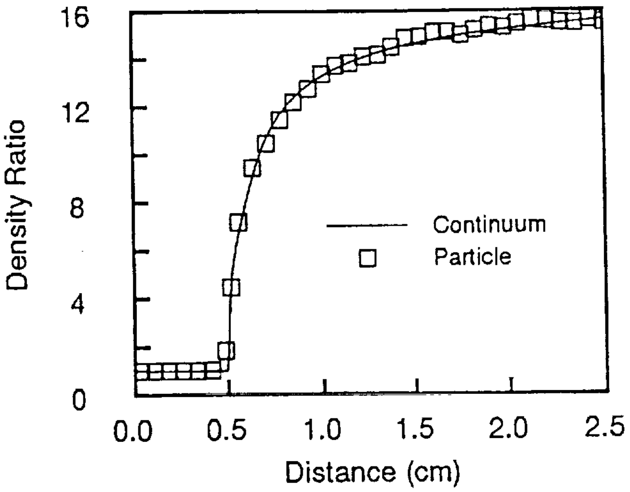

Fig. 13. Comparison of continuum and particle solutions of the local to upstream density ratio for Case 4.

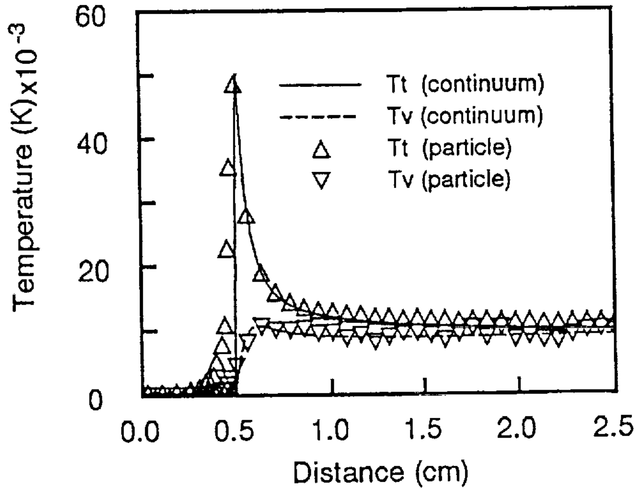

Fig. 14. Comparison of continuum and particle solutions of the translational and vibrational temperatures for Case 4.

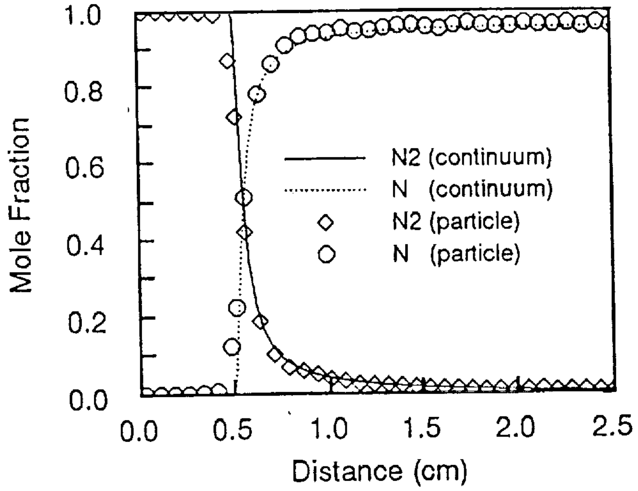

Fig. 15. Comparison of continuum and particle solutions of the neutral species mole fractions for Case 4.

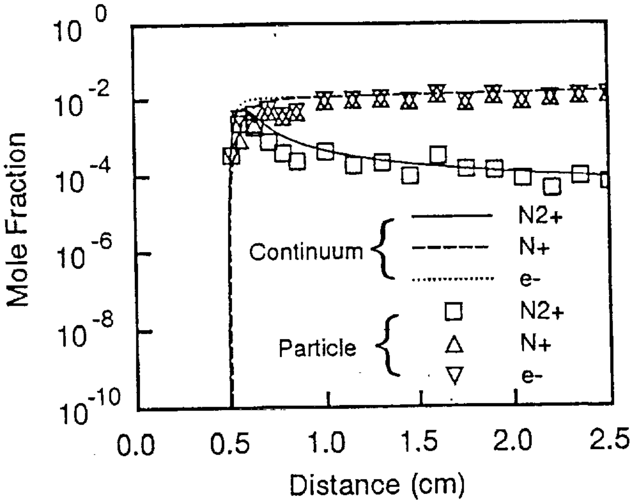

Fig. 16. Charged species mole fractions for Case 4: particle simulation employed new chemical rate data.

in the continuum analysis. It should be noted that a degree of statistical scatter is exhibited by the DSMC results for the less abundant species. To assess the effect of using the new reaction rates, a particle simulation is also performed with Bird's rate data[19]. The variation in the mole fractions of the charged species computed in this way are compared with the continuum results in Fig. 17. None of the species profiles are found to be in good agreement. With Bird's rates, the most populous ion is N_2^+, whereas the new particle rate data agrees with the continuum solution in giving N^+ as the most abundant ion. With Bird's rate data, the mole fraction of electrons at the downstream boundary is about 2.5×10^{-3} whereas the continuum simulation gives a value of about 1.8×10^{-2}. If it is accepted that the rate coefficients provided in Refs. 1 and 2 are the more physically realistic, these large differences observed with Bird's older data set must call into question previous DSMC investigations which employed those reaction rates.

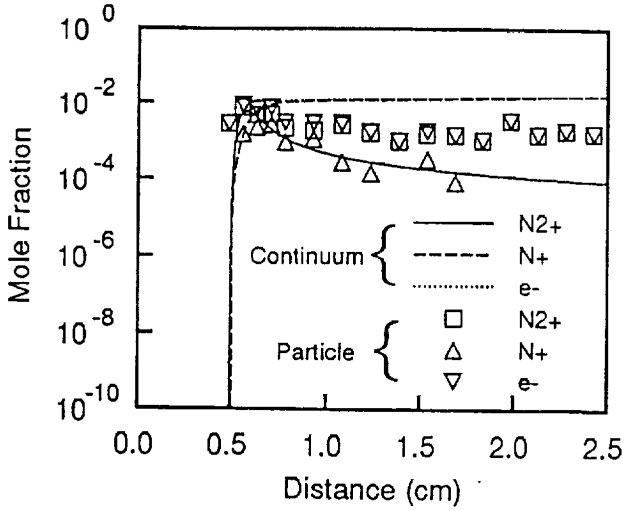

Fig. 17. Charged species mole fractions for Case 4: particle simulation employed old chemical rate data.

Concluding Remarks

This study was motivated by the requirement to evaluate the relationship between continuum and particle simulations of hypersonic flows in the near-continuum regime. The results obtained in the investigation have established that a close correspondence exists between the thermochemical nonequilibrium models employed in these solution techniques. In the case of vibrational nonequilibrium, the agreement between the two sets of numerical results validated a number of recent modeling developments for computing the rate and mechanics of vibrational energy exchange in the particle simulation. In the cases of weak and strong dissociation, both the continuum and particle models for vibration-dissociation coupling were successfully evaluated against experimental data. This is a most interesting result considering the large differences in the dissociation models employed in the two techniques. In the case of weakly ionised flow, it was necessary to develop new forms for some of the chemical rate constants for use in the particle simulation. These were developed so as to be nearly consistent with the continuum expressions, and also to be mathematically convenient for use in the particle chemistry models. The next stage in this continuing investigation will be evaluation of these methods for flow conditions in the transition regime, i.e. at higher Knudsen numbers. In such flows, rarefaction effects may invalidate use of the Navier-Stokes equations, and give rise to large differences between the continuum and particle simulation results.

Acknowledgements

Support by NASA for I.D.B. (Grant NCC2-582) and for T.G. (Grant NCC2-420) is gratefully acknowledged.

References

[1] Park, C., *Nonequilibrium Hypersonic Aerothermodynamics*, John Wiley and Sons, Inc., New York, 1989.

[2] Park,C., Howe, J.T., Jaffe, R.L., and Candler, G.V., "Chemical-Kinetic Problems of Future NASA Missions," AIAA Paper 91-0464, AIAA 29th Aerospace Sciences Meeting, Reno, NV, January 1991.

[3] Millikan, R. C., and White, D. R., "Systematics of Vibrational Relaxation," *Journal of Chemical Physics*, Vol. 39, No. 12, 1963, pp. 3209-3213.

[4] MacCormack, R. W., "Current Status of the Numerical Solutions of the Navier-Stokes Equations," AIAA paper 85-0032, AIAA 23rd Aerospace Sciences Meeting, Reno, NV, January 1985.

[5] Candler, G.V., "The Computation of Weakly Ionised Hypersonic Flowsin Thermo-Chemical Nonequilibrium," *Ph. D.Thesis*, Stanford University, 1988.

[6] Gökçen, T., "Computation of Hypersonic Low Density Flows with Thermochemical Nonequilibrium," *Ph. D Thesis*, Stanford University, 1989.

[7] Boyd, I.D., "Vectorisation of a Monte Carlo Method For Nonequilibrium Gas Dynamics," *Journal of Computational Physics*, Vol. 96, 1991, pp. 411-427.

[8] Boyd, I.D., "Analysis of Vibration-Dissociation-Recombination Processes Behind Strong Shock Waves of Nitrogen," *Physics of Fluids A*, Vol. 4, No. 1, 1992, pp. 178-185.

[9] Boyd, I.D., "Analysis of Rotational Nonequilibrium in Standing Shock Waves of Nitrogen," *AIAA Journal*, Vol. 28, No. 11, 1990, pp. 1997-1999.

[10] Borgnakke, C. and Larsen, P.S., "Statistical Collision Model for Monte Carlo Simulation of Polyatomic Gas Mixtures," *Journal of Computational Physics*, Vol. 18, 1975, pp. 405-420.

[11] Boyd, I.D., "Rotational and Vibrational Nonequilibrium Effects in Rarefied Hypersonic Flow," *Journal*

of Thermophysics and Heat Transfer, Vol. 4, No. 4, 1990, pp. 478-484.

[12] McDonald, J.D., "A Computationally Efficient Particle Simulation Method Suited to Vector Computer Architectures," *Ph. D. Thesis*, Stanford University, 1990.

[13] Lumpkin, F.E., Haas, B.L., and Boyd, I.D., "Resolution of Differences Between Collision Number Definitions in Particle and Continuum Simulations," *Physics of Fluids A*, Vol. 3, No. 9, 1991, pp. 2282-2284.

[14] Haas, B.L. and Boyd, I.D., "Models for Vibrationally-Favored Dissociation Applicable to a Particle Simulation," AIAA Paper 91-0774, AIAA 29th Aerospace Sciences Meeting, Reno, NV, January 1991.

[15] Bird, G.A., "Simulation of Multi-dimensional and Chemically Reacting Flows," in *Rarefied Gas Dynamics*, edited by R. Campargue, CEA, Paris, 1979, pp. 365-388.

[16] Boyd, I.D. and Whiting, E.E., "Comparison of Radiative Heating Estimates Using Particle Simulation and Continuum Methods," AIAA Paper 92-2971, AIAA 23rd Plasmadynamics and Lasers Conference, Nashville, Tennessee, July 1992.

[17] Byron, S., "Shock-Tube Measurement of the Rate of Dissociation of Nitrogen," *Journal of Chemical Physics*, Vol. 44, Feb. 1966, pp. 1378-1388.

[18] Mitcheltree, R.A., "A Parametric Study of Dissociation and Ionization at 12 km/sec," AIAA Paper 91-1368, AIAA 26th Thermophysics Conference, Honolulu, HA, June 1991.

[19] Bird, G.A., "Nonequilibrium Radiation During Reentry at 10 km/s," AIAA Paper 87-1543, 22nd AIAA Thermophysics Conference, Honolulu, HA, June 1987.

[20] Boyd, I.D. and Stark, J.P.W., "Direct Simulation of Chemical Reactions," *Journal of Thermophysics and Heat Transfer*, Vol. 4 (3), 1990, pp. 391-393.

[21] Kewley, D.J. and Hornung, H.G., "Free-Piston Shock-Tube Study of Nitrogen Dissociation," *Chemical Physics Letters*, Vol. 25, No. 4, 1974, pp. 531-536.

[22] Candler, G.V., "On the Computation of Shock Shapes in Nonequilibrium Hypersonic Flows," AIAA Paper 89-0312, AIAA 27th Aerospace Sciences Meeting, Reno, NV, January 1989.

AIAA-92-4029

NUMERICAL SIMULATIONS OF UNSTEADY FLOW IN A HYPERSONIC SHOCK TUNNEL FACILITY

Jean-Luc Cambier, Susan Tokarcik
and Dinesh K. Prabhu
Eloret Institute
Palo Alto, CA

**AIAA 17th
Aerospace
Ground Testing Conference**
July 6-8, 1992 / Nashville, TN

For permission to copy or republish, contact the American Institute of Aeronautics and Astronautics
370 L'Enfant Promenade, S.W., Washington, D.C. 20024

NUMERICAL SIMULATION OF UNSTEADY FLOW IN A HYPERSONIC SHOCK TUNNEL FACILITY.

Jean-Luc Cambier [*], Susan Tokarcik [†], Dinesh K. Prabhu [‡]
Eloret Institute, 3788 Fabian Way, Palo Alto, California 94303

Abstract:

This paper describes the computational work being performed at Ames on the simulation of the 16" Shock Tunnel facility. The paper describes the approach used and shows some preliminary results for various flow transients. In particular, we describe the numerical problems encountered during the computation of these flows, and the methods used to resolve them. We also discuss the validity of some approximations used, notably concerning the reduction of the problem into problems of smaller dimensionality, or smaller size. We show how quasi-1D simulations can be used to help design experiments, or to better understanding the characteristics of the facility. An application to the design of a non-intrusive diagnostic is shown. The multi-dimensional flow transients computed include the shock reflection at the end of the driven tube, the shock propagation down the nozzle, and the breaking of the main diaphragm. The interaction between separate flow events will also be discussed.

I. Introduction

The Ames 16" facility, shown schematically in Figure 1, can be considered as a typical example of a shock-tunnel for hypersonic flows. The shock tunnel is about 70 meters long, composed of a driver section (17" diameter) filled with a light combustible mixture, and a long driven tube (filled with the test gas at low pressure). At the end of the tunnel is a supersonic nozzle 6 meters long (1 m diameter at the exit plane) and finally a test section. The complete operation of the facility typically results in test times of the order of 5 to 20 milliseconds: the time for the main shock to propagate from the main diaphragm to the end of the driven tube is of the order of 7 msec. After partial reflection at the end of the driven tube, the shock interacts with the incoming contact discontinuity (CD) which separates the test gas from the driver gas. For 'tailored' conditions, there is no wave reflected back from this interaction, and the flow between the CD and the nozzle is uniform and steady. More detailed descriptions of a shock tunnel operation can be found for example in ref. [1]. The test time is measured from the time the flow conditions in the stagnation region become steady, until the CD reaches the end of the driven tube, and the nozzle flow becomes contaminated with the driver gas. A flow 'quality' will be represented by the steadiness of the stagnated flow, the low level of contamination of the test gas by driver gas or impurities, as well as the peak conditions (pressure, enthalpy) attainable by the facility.

Numerical simulations are required to better understand the test flow conditions (temperature, mass fraction profiles, time dependence, etc..) and supplement the experimental knowledge: they are used also to improve the design of the experiments or to improve the tunnel operation characteristics. In order to satisfy these objectives, several aspects of the tunnel operation need to be simulated. Modeling the entire facility from the driver to the test section requires us to grid a physical length of about 50 meters; yet, important flow features such as shock and contact discontinuities (CD) should be resolved with good accuracy, i.e. a few mm in the axial direction. The spatial stiffness is then of the order of 10^4; this is a conservative estimate, since the boundary layers also need to be resolved in some cases, requiring grid spacing as low as tens of micrometers in the radial direction. The modeling of the shock-tunnel facility falls into the general category of *multiple scale* problems, and calls for appropriate special numerical methods which we will hint at in this paper.

The complete operation of the hypersonic facility also involves a large number of different physical processes at work, some of which are not well understood or are very difficult to compute. The combustion process in the driver gas requires a good description

---

[*] Senior Research Scientist, member AIAA. Mailing address: NASA Ames Research Center, MS 230-2, Moffett Field, California 94035.

[†] Research Scientist, member AIAA.

[‡] Research Scientist, member AIAA.

of the energy deposition and flame propagation; the main diaphragm rupture would require us to understand the material deformation up to the plasticity limit. The penetration of the jet of driver gas into the driven tube is a problem of 3D, turbulent, multiscale mixing. The temperatures are sufficiently high that some wall ablation takes place and contaminates the flow. Finally, radiative effects may need to be considered, and low density, thermal nonequilibrium gas models may be required in the nozzle expansion. A multiplicity of CFD tools must therefore be made available to study the effects of each of these phenomena.

The problem is compounded by the lack of crucial experimental data: such phenomena such as diaphragm rupture are difficult to observe, and only rough estimates of the process time and energy scales can be made available and approximately correlated with the experimental data. Ablation of the tunnel material is also a very complex physical process, which may depend on the microstructure of the material itself.

Solving this problem will require us to develop and test appropriate numerical techniques, decompose and reduce the problem accordingly, and develop and test various physical models. Simplification of the problem can be accomplished first by 'dimensional reduction', i.e. solving the problem in in a reduced number of dimensions. Quasi-1D simulations have low computational time and memory requirements, and therefore can be used for a large number of computations, such as those required for design and sensitivity studies. It will be important to verify the accuracy of these simulations, and to estimate the quality of information which can be obtained from them.

In a typical cartesian tradition, decomposition of the problem into several independent sections is usually attempted. This we regard as 'causality reduction'. This approach requires several approximations and simplifications, and its validity needs to be more clearly justified. For example, the time evolution of the flow in the test section clearly requires us to accurately compute the unsteady flow in the stagnation region, including gas/wall interactions, shock/boundary layer interactions. The shock/CD interaction is also very important, and this requires us to know very well the shape of the CD. Going back further, the shape of the CD will be influenced by the earlier process of flow establishment from the main diaphragm rupture and thereon. But the details of the diaphragm rupture will depend on the pressure rise in the driver gas, and this requires us to model first the turbulent flame propagation in the driver tube. The logical sequence of events, i.e. from driver tube combustion to flow expansion into the test chamber, is unfortunately the most difficult to compute, since it requires us to be able to model the most complex phenomena at first. Therefore we have to sacrifice some degree of detail in order to obtain practical answers in reasonable time. By causally reducing the problem, we loose accuracy but gain in efficiency: the method can still be used to examine the important physical effects (i.e. sensitivity studies) in an efficient way.

In this paper, we will discuss these methods and the preliminary results. The following questions must be addressed:

- what improvements in numerical techniques are required.
- how accurate are the results from reduced (1D) models.
- how significant are the causal influences of various sections of the tunnel.
- what physical phenomena are important and how to model them.

The last item on our list will not be discussed here. In this paper, we will concern ourselves primarily with the numerical techniques, and the evaluation of the approximations commonly made in shock-tunnel simulation. The obvious intent of the development of this numerical capability is to provide an array of numerical tools for better understanding of the facility operation, and the design of new test conditions and diagnostic procedures. The combined focus of both experimental and numerical tools leads to superior measurement capability, and is an approach practiced at NASA-Ames [2].

II. Numerical Techniques

We have already mentioned that the spatial and time stiffness can be quite large; fortunately the CFD community has developed an arsenal of techniques which can potentially be used to reduce the severity of the problem. First, we observe that the flow discontinuities are few and generally well localized: it is therefore unnecessary to simultaneously carry the same resolution requirements in all regions of the facility. We can rely on several techniques of dynamical

grid refinement to carry this task. Second, the problem can be approximately separated in three parts. The combustion process in the driver gas proceeds independently of the driven tube, and can be computed separately if necessary (throughout this paper, it will be simply modeled). Since the flow is mostly supersonic in the nozzle, there is no backward influence of the flow from the nozzle to the tubes. It is therefore adequate to compute at first the unsteady flow in the driver and driven sections, including the nozzle and up to the throat; the flow solution at the exit plane can be stored according to the required spatial and time accuracy, and used as unsteady inflow condition for the remainder of the facility, i.e. nozzle and test section. This allows us also to switch between different physical models (e.g. nonequilibrium thermodynamics) and different dimensionalities (3D versus 2D axi-symmetric or 2D versus 1D).

Another important question concerns the choice of numerical method: although we are interested in the unsteady flow motion, the flow time scales that need to be resolved may be large compared to the time scale from the stability limit of an explicit scheme. This is true especially for a clustered viscous grid. An implicit method, if time-accurate, can potentially be used for this problem as well. However, there is a huge cost associated with the inversion of the block-tridiagonal matrices from the LHS of the system of equations, especially when multiple species are present. Our experience showed that even when only two species are considered (driver gas/driven gas), the implicit method needs to be executed at a CFL number ≥ 5 for better performance than the explicit method. Due to the severe nature of the problem (pressure ratio, shock speed), this CFL value is generally too large for these transient flows. However, the viscous terms alone can be treated implicitely, and show greater stability than the convective terms: our method therefore performs an Operator Splitting between convection, viscous dissipation and chemistry. The viscous terms are treated implicitely, and the inversion of the 3×3 (in 2D) block tridiagonal matrices is sufficiently fast to be justified. The chemistry is also treated point-implicitely, and the algorithm is also very fast. When the chemistry is extremely stiff however, linearization errors will reduce the stability of the point-implicit algorithm. For example, let us consider air (79% N_2, 21% O_2) suddenly raised to 100 atm and 6000 °K: at constant volume, the system reaches equilibrium within a fraction of a microsecond. Attempting to solve implicitely the chemistry in one iteration and with a time step larger than $\simeq 2\ 10^{-8}$ sec would lead to very unstable and unphysical solutions. The initial evolution from the highly nonequilibrium state needs to be time-resolved more accurately: our algorithm sub-iterates (more precisely, 'sub-cycles') the chemistry, i.e. integrates over a given time interval Δt with variable steps δt. The sub-step is initially estimated from the rate of change of the species, then is stretched in a fixed proportion for the subsequent sub-iterations: $\delta t^{n+1} = (1+a)\delta t^n$, with $a \geq 0$. Each sub-iteration is solved point-implicitely. The change in temperature is also estimated at each sub-iteration from the change in chemical energy. Figure 2 shows a sample computation ($a = 0.5$) for this highly nonequilibrium case. The 'exact' time evolution is also shown. The integration intervals are $\Delta t = 5\ 10^{-7}$ seconds. One can see that the variable step solution is off in the equilibrium region until the end of the first integration interval, at which time the thermodynamic state of the gas is re-analyzed and a more accurate calculation of the temperature is performed. The sub-iterated solution then quickly matches the exact solution.

To maintain good accuracy, the relative changes in temperature estimated during the chemistry should be limited. A chemical time scale is therefore defined as the time during which the chemical reactions induce a relative change in temperature of $\simeq 5\%$[†] . The effect of chemistry on the flow dynamics occurs principally through the temperature change, and this time step limit provides us with a criterion for accurate coupling of the chemistry and flow dynamics. If there is no monitoring of the chemical time scale and no enforcement of this time step limit, an instability generally develops rapidly, especially in cases of stiff chemistry; this instability can occur for both a fully-coupled approach or the Operator-Splitting approach. The case of very stiff chemistry would seem therefore to be very inefficient: this corresponds basically to a very poor resolution of the chemical relaxation distance, such as the one behind the primary shock. However, it is possible to somewhat rescale the chemical time scale without changing the solution too much. Let us suppose that we want to resolve the flow dynamics on the order of a convective time-scale Δt_{conv}, but the chemistry is so stiff that accuracy and stability considerations restrict us to (for example) a global time scale $\simeq 0.01\Delta t_{conv}$. We can artificially rescale the chemistry by 10, and the stability limits lead us

---

[†] This number may be varied, according to the desired accuracy and/or the stability. It is our experience that in most cases, the maximum relative change allowed should be less than 10%.

to a time scale $0.1\Delta t_{conv}$, which we can better afford. This rescaling can be done locally, depending on the stiffness ratio: this will affect slightly the solution, for example by over-estimating the chemical relaxation length behind a shock, but the difference may be practically insignificant for very stiff cases. The technique is easily implemented by restricting the integration interval (it becomes $5\ 10^{-8}$ sec in our example): the insert in Figure 1 shows the results of this rescaling approach. We see that the original transients are still reproduced, and the solution still converge to the exact solution. This sub-iterated algorithm, with or without the rescaling option, is used in all our calculations.

The spatial stiffness can be solved by various techniques of dynamic grid adaption. In the driver tube, strong gradients and discontinuities exist only during the combustion process. After rupture of the main diaphragm, only weak gradients subside, and this section of the facility does not require high resolution. The spatial accuracy is required for the propagating shock and CD, down the driven tube. One possible technique is to dynamically compress and stretch the grid points to accumulate them in the required regions. This technique can work well in one dimension and is easy to implement: care must be taken however to prevent sudden jumps in spacings, or accuracy will be lost. The technique may become more problematic in two or more dimensions, as some flow features (including the CD) may have more complex shapes: the grid can become distorted, and can affect the solution. Another technique, pioneered by a group at Livermore [3], consists of adding smaller scale grids in regions of interest. These grids can be exact sub-scale replicas of some regions of the coarse, background grid: the flow variables can be transferred between grids in an exactly conservative way. This way, the grids are never distorted and their motion can be computed very quickly, with minimal overhead. An example is shown in Figure 3: the propagation of the primary shock and CD down the driven tube is computed in a one-dimensional model. A first calculation used a constant spacing grid, with about 1000 points for the whole tunnel. A second calculation used a background grid for the whole tunnel with 250 points, and a high resolution grid super-imposed on it: the latter moves along with the shock, with a sliding motion. The sub-scaled grid had a size of 800 grid points, and the scale ratio between the two grids was 20 to 1. Flow values within the background cells are computed by volume averaging of the sub-scaled cells present, if any. While both calculations used approximately the same number of points, it is clear that the second method has a much higher local resolution, and the sharpness of the CD is dramatically improved.

Another method, which we will be testing in the future, uses non conservation of the number of grid points. Unstructured grids can be manipulated to accumulate points in the regions of interest, either by grid displacement or by dynamic subdivision.

The singular axis was found to be another recurrent problem during the computation of flow transients: the simulation of the shock reflection at the end of the driven tube, for example, initially showed a strong conical shock structure near the axis with the apex of the cone leading the overall structure (see Figure 4). This peculiar formation can also be seen for example in the results of P. Jacobs [4]. This structure is possible only if a very intense and high velocity jet of gas is produced and maintained on the axis: this is a highly singular and unphysical behaviour. Close examination of the numerical results indeed showed an excessively large axial velocity component in a single cell close to the axis. Because this high velocity jet was present in one cell only, and did not show signs of diffusion, we were convinced that it is the result of a numerical error. A similar phenomenon can be observed also in the propagation of the main shock down the nozzle [5], and can be seen at the axis or in some cases near the walls. This phenomenon was observed only for axi-symmetric flows, and when a second-order accurate scheme (with minimal dispersion) was used. It was finally related to the aspect ratio of the grid cells: indeed, the problem disappeared when the aspect ratio of the grid cells was adjusted to lower the radial gradients. If the spacing is such that $\Delta x << \Delta r$, the flow features are smooth and accurate. If $\Delta x \geq \Delta r$ an instability *may* develop in some regions of the flow. We assume the problem comes from the axi-symmetric pressure correction term, which *is not* part of the monotonic (TVD) fluxes and acts as a non-conservative momentum source term. This pressure correction term is a result of the formulation of the Euler equations for an axi-symmetric problem, and can be easily visualized with the following finite-volume description. Let us consider a cell in a cylindrical geometry, described schematically in Figure 5. As one approaches the axis, the ratio of cell side surface to cell volume behaves as $1/\Delta x$ for the axial direction, while it is exactly 0 for the radial direction. There is a contribution to the radial momentum density from the pressure on the sides of the cells in the azimuthal direction. This contribution is proportional to $1/\Delta r$. It is

clear that when the cells are clustered near the axis, the contribution from the non-conservative momentum source term may become dominant, and therefore there is no guarantee that a non-oscillatory solution can still be obtained. The problem usually disappears when the grid is relatively coarse in the radial direction, near the axis, in which case the source term ceases to be the dominant contribution. This observation also applies to other cases, such as the computation of shock layers on blunt axi-symmetric bodies. In most unsteady cases or for steady flows, the radial gradients will be weak near the axis. One particular exception would be the propagation of a shock ring towards the axis: this is such the case in the reflection of the primary shock in the tunnel, from the upper section of the end wall. Figure 6 shows a time sequence for the same case as Figure 4, but for a grid coarsened near the axis: we see that the instability is effectively removed. A similar improvement can be obtained by reducing the spatial order of accuracy in that region.

The general effect of the grid structure or aspect ratio on the flow solution should never be underestimated, especially in the severe cases we are concerned with. Although we may see unstructured grids as a potentially useful tool for the flows of interest here, their effect on the flow solution will have to be carefully evaluated.

The flow expansion in the supersonic nozzle is one of the easier tasks to perform: the transient flow simulation is required to examine the steady flow establishment time in the test section, and to verify that the flow does not choke during that time. This is particularly relevant for large objects or for massive gas (fuel) injection. Since the nozzle is evacuated to very low pressure before the rupture of the secondary diaphragm, the flow propagating down the nozzle is preceded by a high velocity jet. The mean free path in that region can be quite large ($\simeq$ 3 mm for $P = 100$ milliTorr), and strictly speaking the Navier-Stokes equations cease to be valid in this low-density region prior to the shock. By attempting nevertheless to solve the flow dynamics with the Navier-Stokes equations, we are experiencing strong viscous effects which operate on a very short ($\simeq$ 10 pico-second) time scale. Although the viscous fluxes are computed implicitely, it is necessary for stability reasons to artificially reduce the strength of these viscous effects in that region. This is easily accomplished by using a numerical switch that effectively and smoothly removes the gradients on a scale smaller or comparable to the mean-free path during the calculation of the viscous fluxes. This switch will effectively reduce the spreading of the shock into the low density gas. The shock thickness will therefore be underestimated. The cutoff length scale can be adjusted arbitrarily: in Figure 7 we show the effect of the cutoff choice (0.1 versus 10 mean free paths) on the solution, for two cases of nozzle pressures. The change is dramatic for the first case (100 μTorr) and unnoticeable for the second (100 milliTorr). Nevertheless, for the latter case, which is also the case we will be using throughout the remainder, the viscous time scale is reduced by a factor of 5 by choosing the higher (10 m.f.p.) cutoff value.

Using all the modified techniques now at our disposition, we are able to sucessfully compute the transient flows in the nozzle and driven tunnel at the rupture of the secondary diaphragm (see Figure 6). Different grids were used for the driven tube and nozzle regions, and no subscaled grids were used for this particular case: both regions were coupled at each iteration. The results of the computation for the nozzle flow (Figure 8) are in good qualitative agreement with an experimental schlieren of a similar problem shown in Figure 9, taken from ref. [6]. Both show the curved leading shock, and a complex structure behind it, dominated by a Mach disk, itself supported by oblique shocks emanating from the nozzle walls. Although the initial conditions for these two flows are very different, the similarity between the two structures lead us to conclude that they are examples of a general pattern. Details of the conditions (pressures, geometry, etc..) may change the relative strength and position of the shocks, without modifying the overall configuration. A snaphost taken at later times would show that near the exit plane of the nozzle, the primary shock straightens out and becomes normal. If one was to perform an unsteady computation in the test chamber assuming a normal shock at the inflow, the calculation would be in error by leaving out the complex shock structure which propagates immediately behind the leading shock. This is shown for example in Figure 10, where a cone has been used as testing body.

III. Dimensional Reduction

When test times are large compared to the transients, it seems appropriate to compute the nozzle flow for the steady state, without having to perform the calculation time-accurately for tens of milliseconds. This allows us to use many numerical techniques to make this computation more efficient. We have done several such computations, solving for the

full Navier-Stokes equations, but for limited regions at a time. The computation proceeds on a subset of the whole nozzle grid, until convergence is obtained. The subset then moves further down the nozzle; the procedure is similar to the displacement of a 'window' along the flow direction. This procedure is half-way between a global calculation and the PNS method; although less efficient than the PNS method, it is more flexible and allows us to correctly treat embedded recirculation zones or other unexpected subsonic regions which may occur. It was observed that the convergence rate and the computation time are dominated by the chemistry in the boundary layer, and the downstream propagation of chemical changes in the low velocity sublayer. Although the calculation does not display severe instabilities such as may be the case for the transient flows, it is still desirable to coarsen the grid in the radial direction near the axis, to avoid spurious fluctuations in pressure.

The steady nozzle flow computations are usually done to obtain estimates of the flow conditions at the exit plane, in particular temperature, Mach number, pressure and species concentrations. Since it is generally assumed that the flow is nearly uniform at the exit plane, it seems that simple one-dimensional computations should be adequate. We have performed such computations using a quasi-1D version of our code, and compared the results. The effect of the boundary layer is expected to be the major contribution to any potential disagreements between the quasi-1D solution and the 2D axi-symmetric solution. This effect is taken into account by effectively modifying the nozzle profile and its area. By considering the inviscid core only, the quasi-1D method can approximately take into account the constricting effect of the boundary layer by assuming a new nozzle shape for which the effective radius is a constant fraction of the real nozzle radius. The dependence of some flow quantities on the effective nozzle area is shown in Figure 11. It is clearly apparent that the static pressure has the highest sensitivity to the effective nozzle area, and therefore to the boundary layer thickness. Temperature and species concentrations are less sensitive to the area variation, and additional uncertainties about the chemical rates or contaminants are likely to cloud the issues: the static pressure is therefore an important variable to measure at the nozzle exit. The comparison with the 2D axi-symmetric results is shown in Figure 12, where again the sensitivity of the static pressure is clearly demonstrated. The best agreement is obtained for an effective nozzle radius of 87% the real radius (i.e. a boundary layer thickness approximately 13% the nozzle radius). Notice also that the static pressure is the only variable that still displays significant radial fluctuations within the inviscid core, at the exit plane. A multi-point measurement of this variable is therefore doubly informative, as far as code validation is concerned. In Figure 13 we show the radial profile of Temperature and NO concentration at station code-named N3 (2.37 meters downstream of the throat) and the exit plane. All the species profiles are relatively unchanged between N3 and the nozzle exit, except atomic nitrogen N, which is present in very small amounts. Owing to the high reactivity of N, this result is not surprising: most of the chemistry is frozen before station N3, and this is especially true of NO. The temperature variation between N3 and the exit plane is therefore due to hydrodynamical effects only.

NO is a relatively important specie to measure (it effectively ties up a significant amount of oxygen and has a noticeable effect on ignition delays), and it can be done easily with a laser absorption method. A computational study of this diagnostic technique can also be done to help design the experiment. The computed high resolution spectrum of the $NO(\gamma)$ band system is shown in Figure 14, with and without the boundary layer. The intensity at peak absorption of the $(0,0)$ band changes by a factor of $\simeq 3$ when the boundary layer is removed. A precise measurement of the core flow must avoid the uncertainty caused by the boundary layer: this can be simply done by providing an optical wave guide that protects the beam from the boundary layer. Although this protrusion is likely to disrupt the flow, the effect may be small enough or irrelevant at the exit plane. We can now look at the effect of core flow variation by comparing the intensity for the 2D solution (without BL) and a quasi-1D solution. The result is plotted in Figure 15-a as the ratio of intensities between the two cases. Surprisingly, the error is less than 10% for the most sensitive lines. At the exit plane (Figure 15-b), the results are even better, with deviations less than 2%! This seems to indicate that this measurement can yield useful information on the core flow, without having to worry too much about details of the radial fluctuations within the inviscid core.

IV: Causality Reduction

In the previous section we have seen that dimensional reduction of the problem can still yield some useful results, and quasi-1D calculations can help design and understand the facility operation and exper-

imental diagnostic techniques. Some flow features are lost in this reduction process, for example the shock structure that propagates down the nozzle. If one were to compute the transient flow inside the test section, one would require a prior computation of the transient nozzle flow. This is an example of causal interaction between two different regions of the facility. The computation of the transient nozzle flow can be done by assuming constant stagnation conditions, or starting from a uniform shock impingement on the end wall of the driven tube. For later times, the propagation of the reflected shock in the driven tube must be followed accurately: this entails the interaction of the shock with the bounday layer and with the contact discontinuity. If this numerical simulation is done with sufficient detail, we can gather information on the effect of boundary layer and CD shape on pressure wave generation and flow contamination. The shape of the contact discontinuity may however depend on its early history, i.e. on the main diaphragm rupture itself. This is another example of causal interaction, which forces to model the diaphragm rupture and subsequent evolution, in order to at least estimate the effect on CD shape. This is another difficult problem which will require a lot of effort: the calculation done so far is only a first attempt at solving the problem, which helped us identify the areas where further improvement is necessary.

Although the opening and petaling of the steel diaphragm is a fundamentally 3-dimensional process, it is not required at this stage to include this complication. The problem is therefore reduced to a 2D axi-symmetric problem, and the diaphragm opening is reduced to a case of time varying boundary condition. The driver and driven tubes are gridded as two separate regions: between them, the boundary condition is set as a reflecting wall for some of the grid cells, and a patching condition for the grid cells within the opening. The distribution of patched/reflecting boundary points changes with time; in this first attempt, the grids are assumed fixed in time, i.e. the opening proceeds in steps, one grid point after another. If the grid had sufficent resolution in the radial direction, this would be a good approximation to a continuous process. Some effects are ignored in this approximation. First, the physical boundary (steel) between the two regions is changing in time, due to the distortion of the diaphragm (the petaling); its dynamics should be modeled as well, and this will require a major effort in the future. We also assumed that the diaphragm is initially vertical, while in reality it is to some extent assuming a hemispherical shape, due to the pressure rise in the driver tube. Since we are only interested at this point in testing the numerical capabilities, this is not a concern.

In Figure 16 we show the temperature contours of the flow transient, taken at three different times after the start of the opening of the main diaphragm. At 30 μseconds, the primary shock is just past the contracting section of the driven tube, immediately followed by the contact discontinuity and a hot layer of driver gas. The opening at that time is still small (about $1/6^{th}$ of the driven tube diameter). Notice that between the hot, sheared gas layer and the opening is a weak shock (blue contours in the figure) is emanating from the diaphragm opening. This is the result of the step in diaphragm opening: as one more cell of the driver section is put in contact with the driven tube, the sudden change in local boundary condition creates this weak shock. This purely numerical effect was difficult to estimate *a priori*, and is an interesting observation in itself: it forces us to reconsider the technique for future computations, in order to have a smoother, continuous opening. At a later time (54 μseconds), the primary shock has travelled further down the driven tube and significantly straightened. Oblique shocks reflected from the walls of the constricting section interact near the axis to form a strong mach disk. The shear layer has attached itself to the walls, and the driver gas behind the primary shock has developed a concave shape near the axis. At 70 μseconds, the primary shock is completely planar, the mach disk has shrunk, and a very complex flow structure follows the primary shock and CD. Since the stepwise diaphragm opening has produced spurious shocks, it is difficult to identify the real physical effects. Presumably, this structure is actually simpler (at least in this 2D approximation). We can safely assume that a few main conclusions can be drawn from this preliminary result:

- the primary shock becomes planar very rapidly ($\simeq 60\mu$seconds).
- a complex and unsteady flow structure, dominated by a mach disk, is formed behind the CD
- the CD itself develops a complex shape.

The last item can be more clearly demonstrated in Figure 17, which shows the CD and the main shock, for the same time sequence. It is clear from Figure 17-c that the CD is definitely non-planar; indeed, it is likely that from that moment on, the CD evolution will be dominated by Rayleigh-Taylor instabilities,

and will not recover an ideal, planar shape.

The remainder of the simulation, i.e. the full propagation of this structure down the whole length of the driven tube, would take a considerable amount of CPU, and has not yet been attempted. Future work will focus again on the diaphragm opening and on a numerical technique that more accurately describe it. It is important also to point out that this calculation is difficult for an additional reason: as the diaphragm opens, there is a strong jet of gas that flows through a small opening in a ideally reflecting surface. This jet has a tendency to entrain some flow around the opening, producing an artificial 'cavitation' near the surface. The same numerical phenomenon can be also observed occasionally near the base wall of a wedge in a hypersonic flow, for example. This numerical instability can be removed by enhancing the numerical diffusion in that region. This was done so in our case. This will also affect the diffusion of the driver gas into the driven tube, and therefore the extent of mixing and shape of the contact discontinuity. This transient flow must therefore be recomputed with special care.

Another example of causality relation concerns the influence of the combustion process in the driver and the flow in the driven tube. Pressure fluctuations are experimentally observed in the driver tube, which seems to indicate that the combustion is not a uniform process, and that some pressure waves are bouncing back and forth in the driver tube. These waves can travel down the driven tube after opening, and influence the pressure field in the stagnation region. This effect is demonstrated in Figure 18, where the pressure histories at two locations are compared with the computations: Figure 18-a shows the pressure history a few centimeters upstream of the main diaphragm, in the driver tube. Figure 18-b shows similar profiles near the end wall of the driven tube. Pressure fluctuations with a *sine* shape have been superimposed in the driver tube at the moment of diaphragm rupture; the amplitude of this fluctuation was chosen to match the experimental observation in the driver tube. These quasi-1D computations show a very good agreement with the experimental traces when the fluctuations (of the right phase) are superimposed. The agreement is notably much better than without these fluctuations (Figure 18-b). It is clear that the combustion process in the driver tube has a strong influence on the flow conditions in the stagnation region, and should also be modeled and better understood. These calculations were performed by G. Wilson at NASA-Ames, using a quasi-1D code: additional details on the modeling will be presented in the future [7].

These results are another example of the usefulness of dimensional reduction: it also shows that with some clever modeling, one can causally reduce the problem and retain an accurate description of the system. This should also help in understanding the conditions for better reproduction of test runs, and for more uniform flow conditions. This is another difficult task, which involves the modeling of energy deposition, initiation of deflagration and flame propagation. An effort in that direction is planned.

V: Conclusions and Future Plans

From these preliminary results, we can draw the following conclusions:

- The flow conditions are very severe and put enormous strain on the accuracy and stability of the current numerical techniques. Further research into the improvement of the numerical techniques is desirable.
- The validation of the CFD capabilities will require some difficult measurements, including high resolution video recording of the transient processes, such as secondary and main diaphragm rupture.
- The numerical modeling of the facility, even with simplistic assumptions (quasi-1D), can greatly benefit the design of experiments, diagnostic procedures, new test conditions, and understanding of the tunnel performance.
- The computation of separate regions of the facility treated as independent is an approximation at best. The influence of remote and past events on the overall flow structures is not negligible, and must be estimated. The separation of the facility flow into separate regions can be used for the estimation of various physical phenomena.

The most immediate challenge still concerns the opening of the main diaphragm. The preliminary results shown here suffer from an inadequate treatment of the unsteady boundary condition, and must be recomputed more accurately. Other challenges that await us concern the importance of various physical effects, such as shock-BL interactions at the end of the driven tube, and wall chemistry and ablation and resulting flow contamination. These three topics will be addressed in the future.

VI. References

[1] A. G. Gaydon & I.R. Hurle, "The Shock-Tube in High-Temperature Chemcal Physics", Reinhold Publ., 1963.

[2] J. Cavolowsky *et al*, 'Flow Characterization in the NASA Ames 16-inch Shock Tunnel', 28th Joint Propulsion Conference, Nashville, TN 1992. AIAA paper 92-3810.

[3] J. Bell et al., 'Adaptive Mesh Refinement on Moving Quadrilateral Grids', AIAA 9th Computational Fluid Dynamics Conference, Buffalo, N.Y. 1989. AIAA paper 89-1979.

[4] P.A. Jacobs, "Simulation of Transient Flow in A Shock Tunnel and a High Mach Number Nozzle", 4th Int. Symp. Comp. Fluid Dynamics, Davis, September 1991.

[5] M. Lewis, U. Maryland, private communication.

[6] M. Van Dyke, "An Album of Fluid Motion", p.171, Parabolic Press, 1982.

[7] G. Wilson, 'Time-Dependent Quasi-1D Simulations of High Enthalpy Pulse Facilities", to be presented at the AIAA 4th Int. Aerospace Planes Conference, Orlando, Dec. 1992.

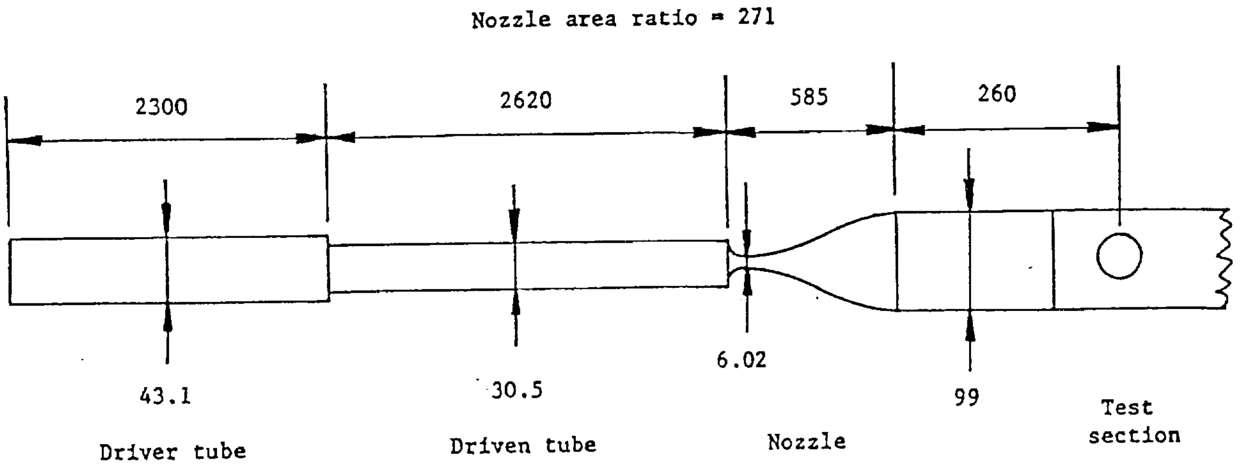

Figure 1: Schematic (not to scale) of Ames 16" Shock Tunnel facility. All dimensions are in cm.

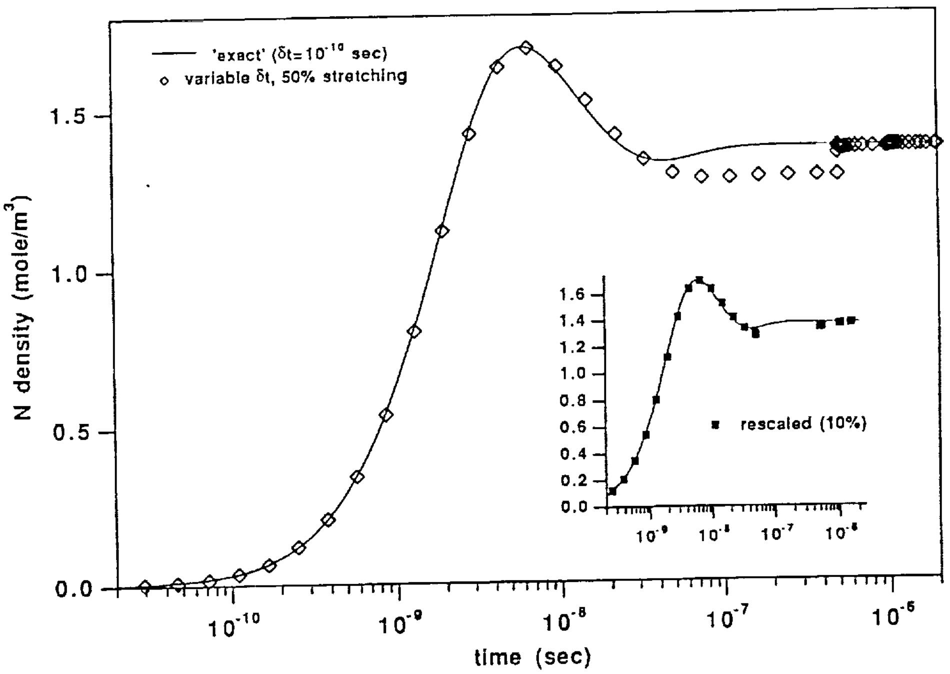

Figure 2: Computation of stiff chemistry. The open symbols are obtained when the implicit chemistry solver is sub-iterated with an increasingly large sub-step. The temperature change is also estimated at each sub-step. The integration proceeds until $\Delta t = 5\ 10^{-7}$ seconds, which is an assumed global time step. Deviations from the 'exact' solution at times greater than 10^{-7} seconds are due to an error in the estimate of temperature. As the first integration is terminated, a more accurate estimate of the temperature (including variations of the specific heat) is made, and the solution quickly converges to the correct one. The insert shows the effect of rescaling of the chemical time scale: here the integration proceeds only to 10% of the global time step. The integration during the second global step also quickly converges to the exact solution.

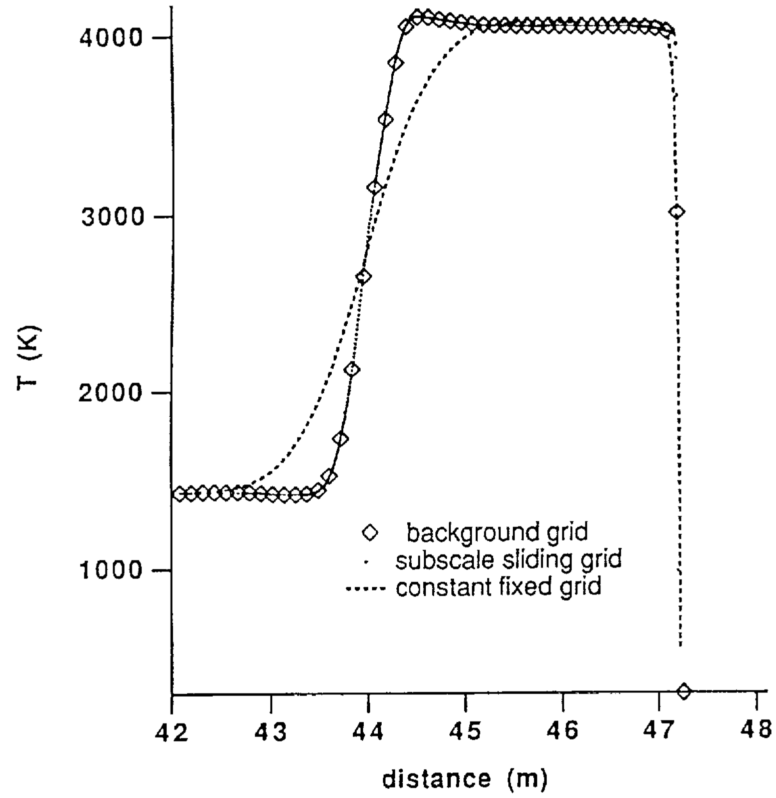

Figure 3: Grid subscaling performance. A constant fixed grid (1000 points) is compared with the results from a high density grid (800 points) moving along with the shock. This final profile, at the end of teh driven tube, shows the increase in resolution of the contact discontinuity. The high density ('subscaled') grid is a subset of the 'background' grid (250 points), and moves by steps equivalent to one cell spacing of the background grid. The transfer of information between the two grids proceeds by volume averaging, and is fully conservative.

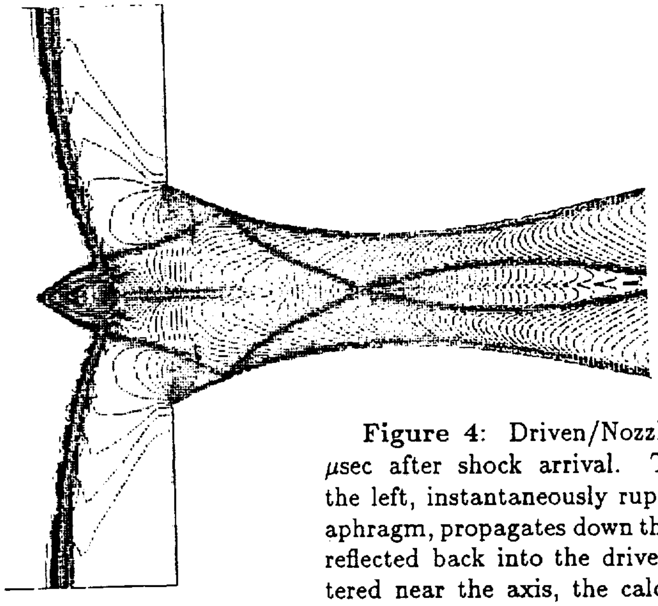

Figure 4: Driven/Nozzle flow transient at 80 μsec after shock arrival. The shock comes from the left, instantaneously ruptures the secondary diaphragm, propagates down the nozzle and is partially reflected back into the driven tube. Cells are clustered near the axis, the calculation id for inviscid, non-reacting flow, spatially 2^{nd}-order. The conical structure is believed to be an artifact from the numerical method.

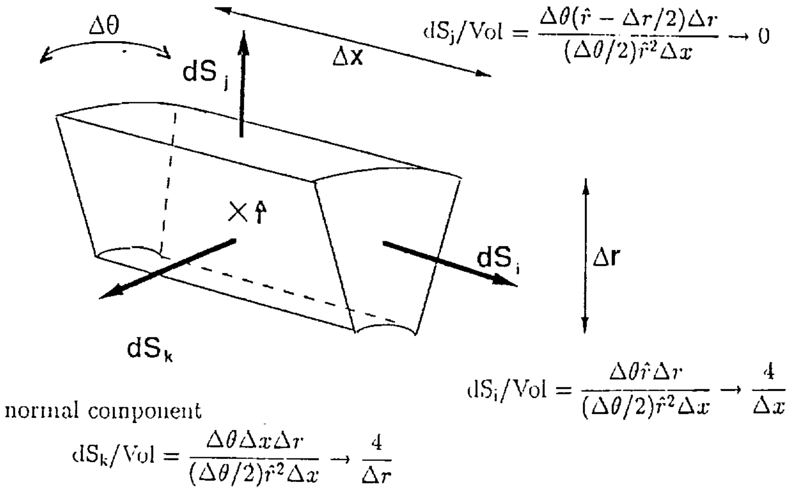

Figure 5: Schematic of finite-volume computational cell in cylindrical geometry. Surface to volume ratios are independent of the wedge angle. The momentum source term in the axi-symmetric formulation of the Euler equations is proportional to dS_k, and behaves as 1/Δr near the axis.

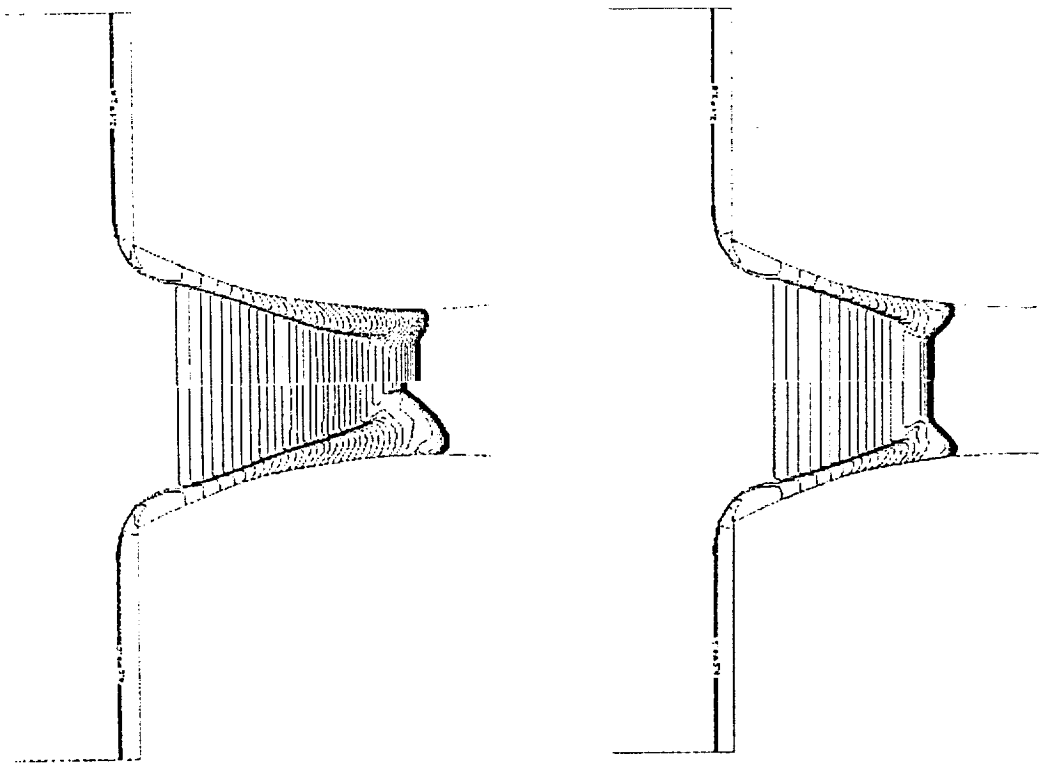

Figure 7: Effect of viscosity for low nozzle pressures. The top section shows the results for a cutoff of gradients at a scale comparable to 0.1 mfp. The bottom section uses a cutoff at 10 mfp. The case on the left is for a nozzle pressure of 100 μTorr, the case on the right is for 100 milliTorr (the experimental condition for the 16" shock tunnel). The cutoff allows greater stability and greater time steps in computing implicitely the viscous terms. The contours shown on the right hand side show that for our case of interest, the results are insensitive to the choice of cutoff.

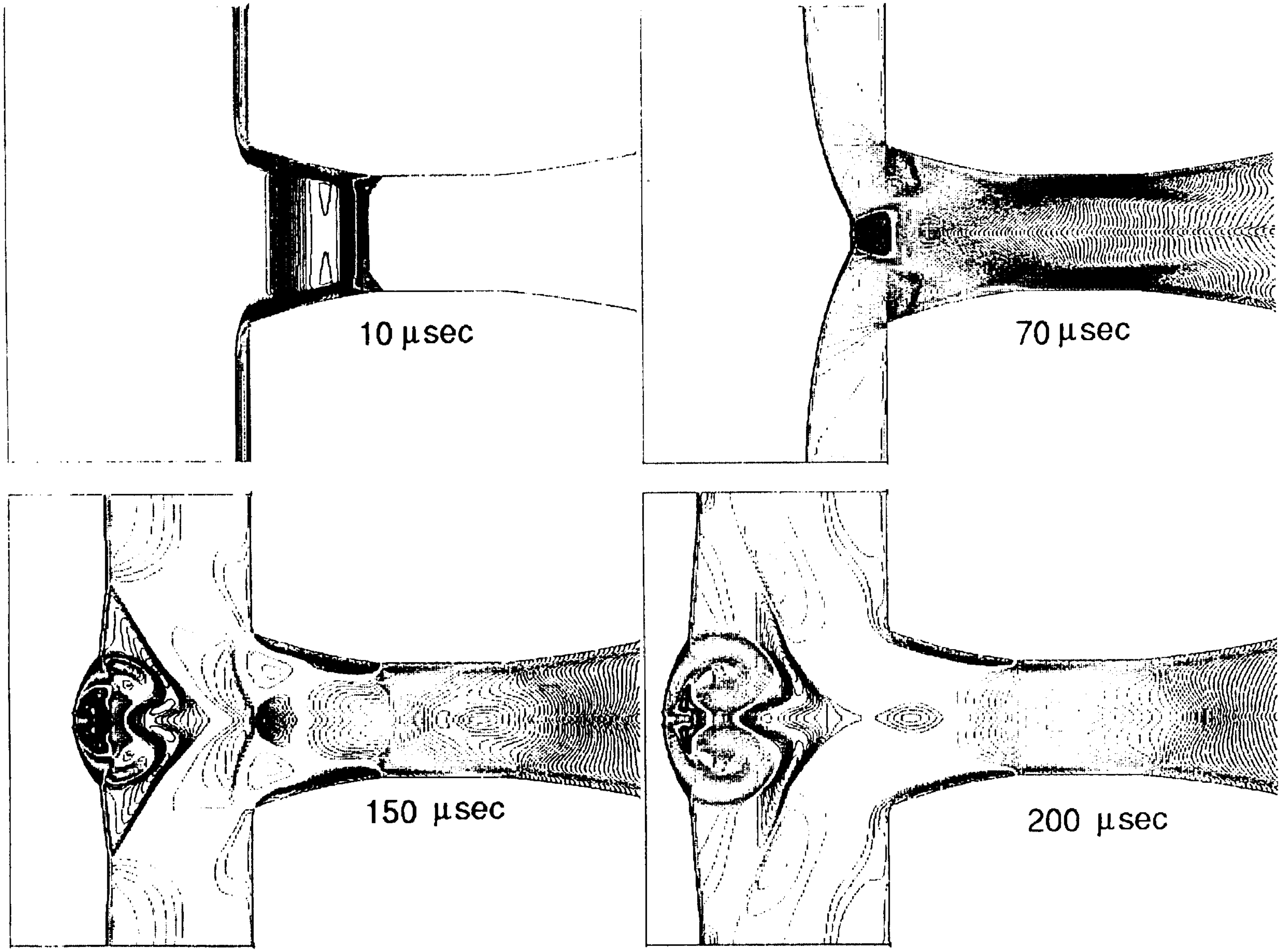

Figure 6: Driven/Nozzle flow transient. This computation is obtained after coarsening the grid in the radial direction near the axis. The shock convergence on the axis (70 μsec) now leads to a stable shock structure ('bubble') near the axis. The formation of an intense vortex is evident for 200 μsec. Plots at later times would show that the reflected shock becomes essentially planar at $\simeq 500\mu$sec, while the vortex structure persists.

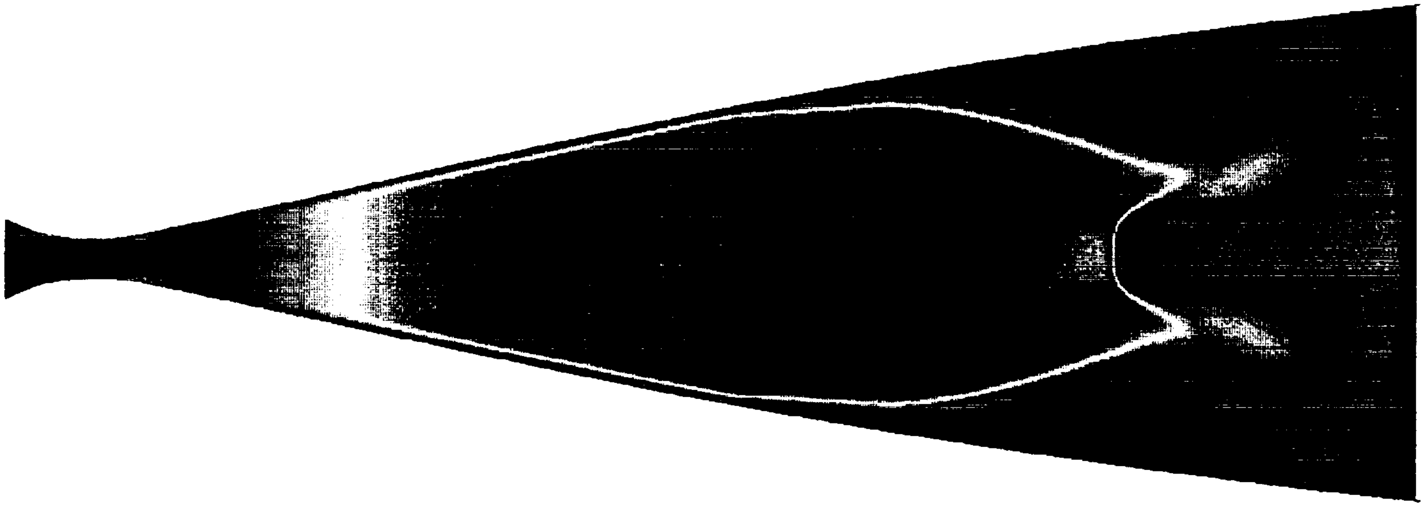

Figure 8: Nozzle flow transient (Mach contours). The curved primary shock can be identified on the right. Weak oblique shocks are emanating from the walls and converge to form a strong (upstream facing) mach disk on the axis, and reflect back. Strongly sheared flow is visible between the primary shock and the first oblique shocks. A contact discontinuity behind the primary shock has been numerically diffused beyond idenitification. A small vertical break in contours is due to an interpolation error by the graphics, between two different grids.

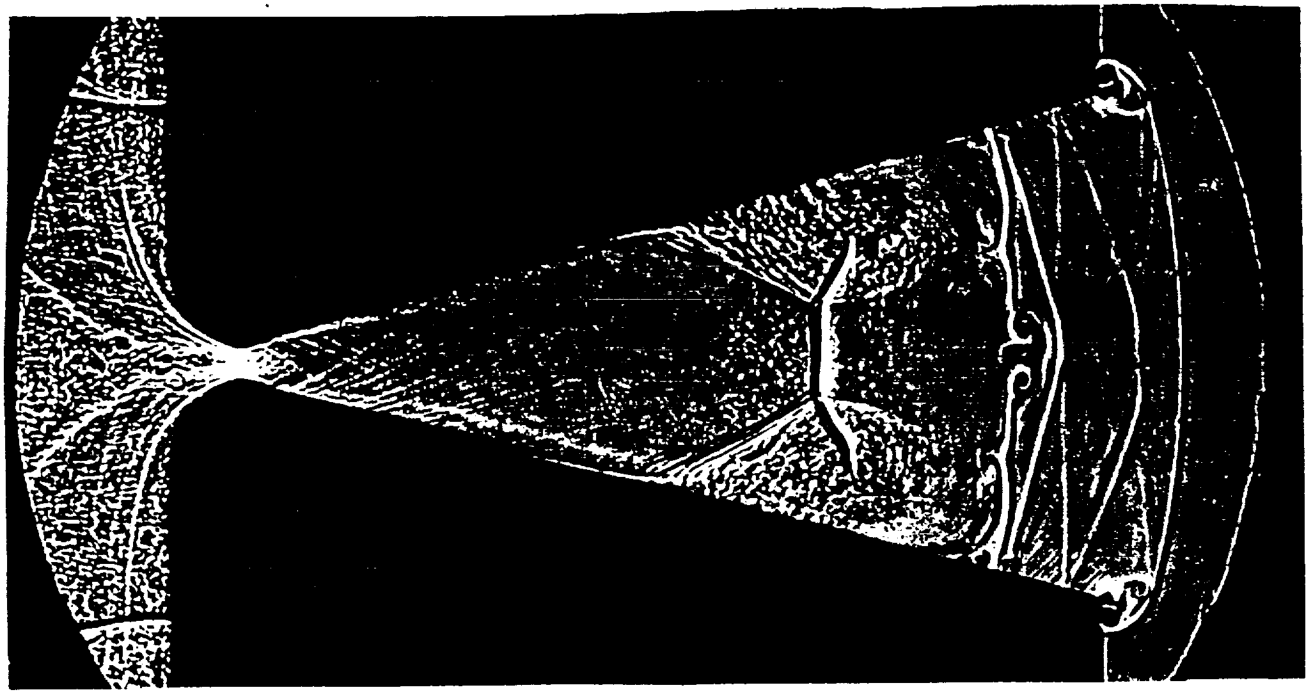

Figure 9:Experimental shadowgraph, taken from [6]. The upstream facing shock and the attached oblique shocks are clearly defined in this picture. Contact discontinuities are also very clear, and show strong vortices. All features of Figure 8 are contained in this picture.

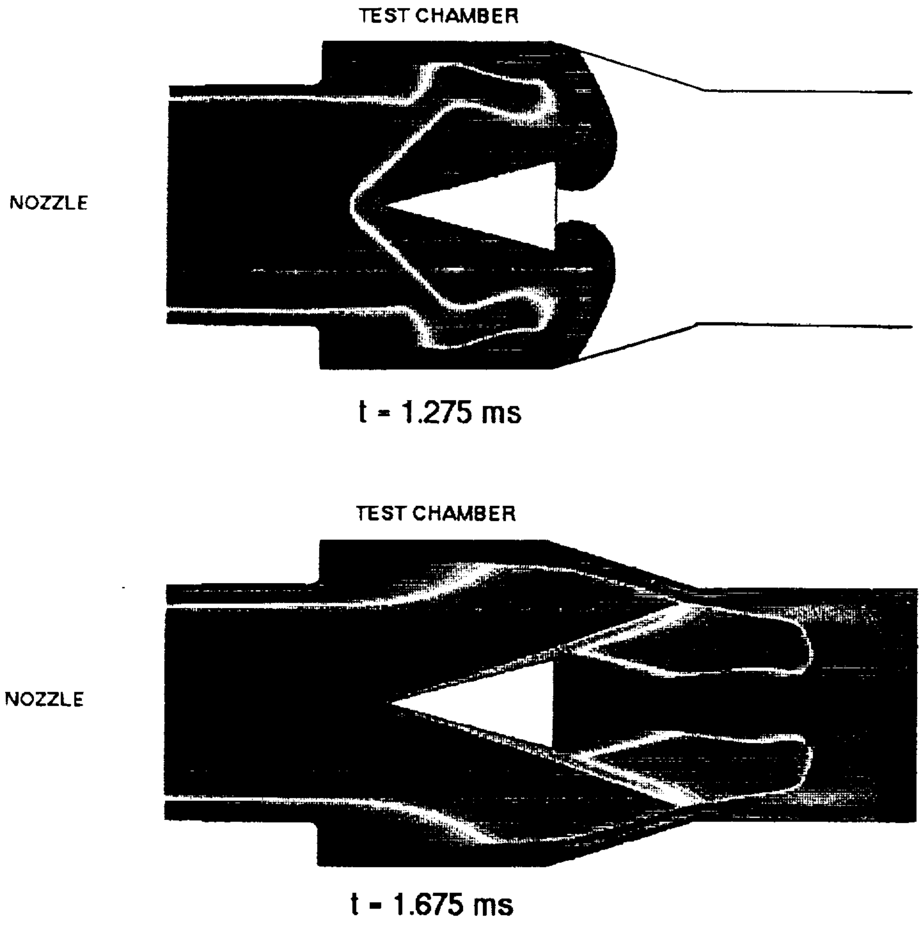

Figure 10: Interaction in test chamber (Mach contours). In this example, as the primary shock diffracts at the end of the cone, the remainder of the shock structure has just reached the apex of the cone. For this case, steady flow over the testing body is achieved within 400 μseconds.

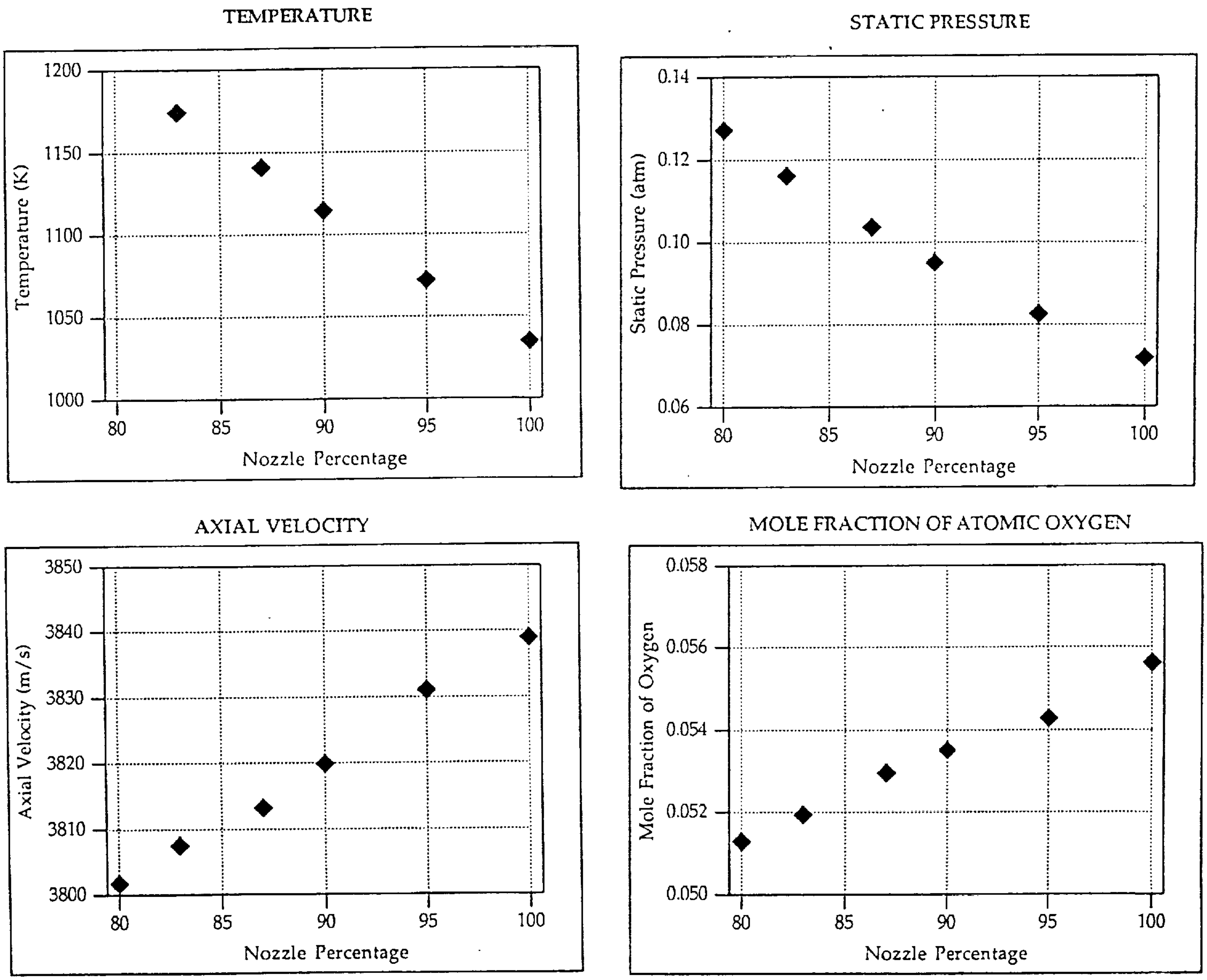

Figure 11: Sensitivity of various flow quantities to effective nozzle area. The nozzle shape is replaced by a modified nozzle contour from the throat on, by removing a fixed fraction of the radius (i.e. the 87% nozzle removes 13% of the radius), to account for the boundary layer. Examination of the plots shows that the static pressure is the most sensitive variable, and therefore the most useful variable to determine experimentally.

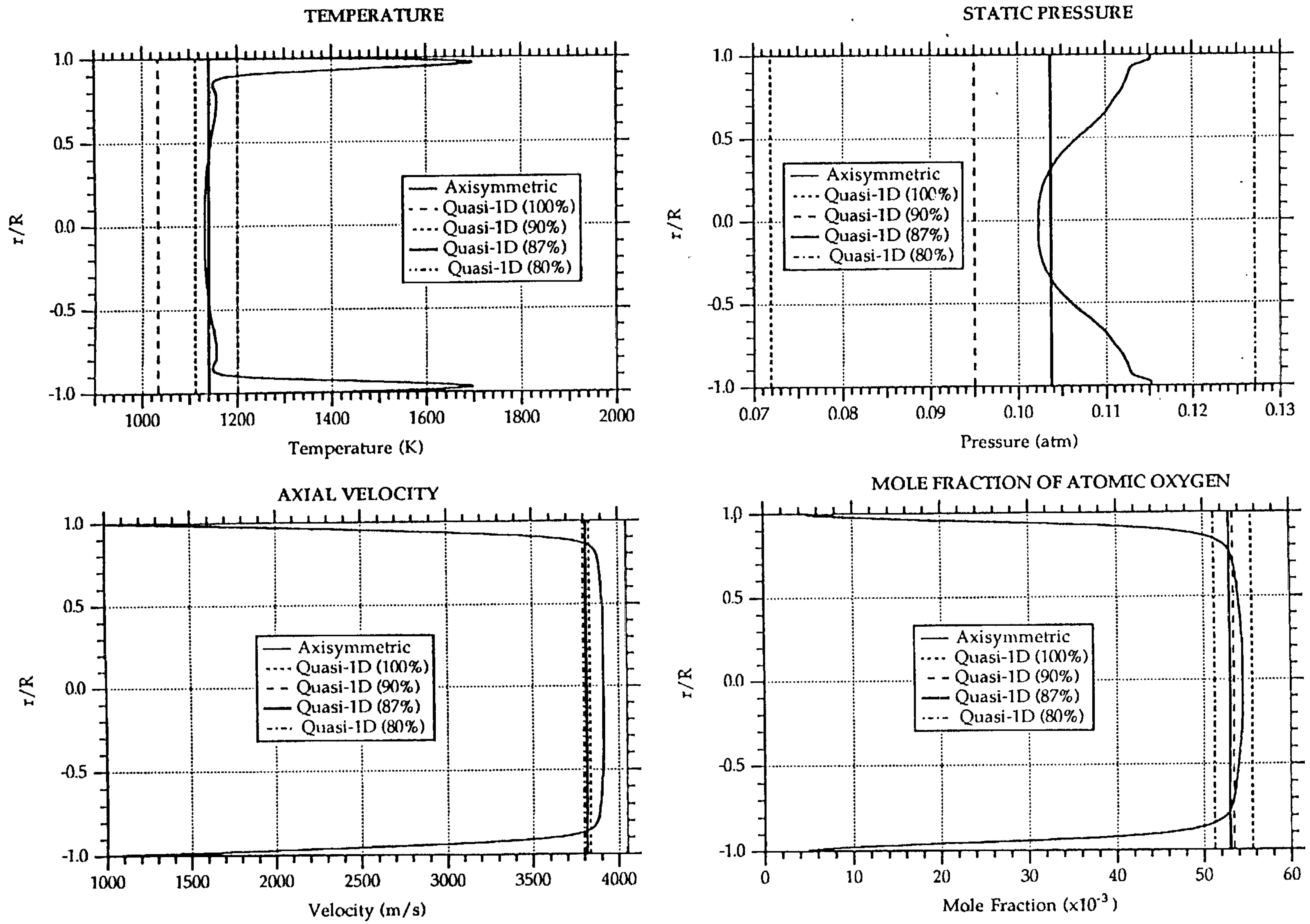

Figure 12:Comparison of quasi-1D solutions with 2D axi-symmetric solution. Except for the flow within the boundary layer, the agreement is very good for the 87% case. Most variables have a flat profile in the core region, except the static pressure. Again, measurement of the static pressure should yield some valuable information on the nozzle flow, and for code validation.

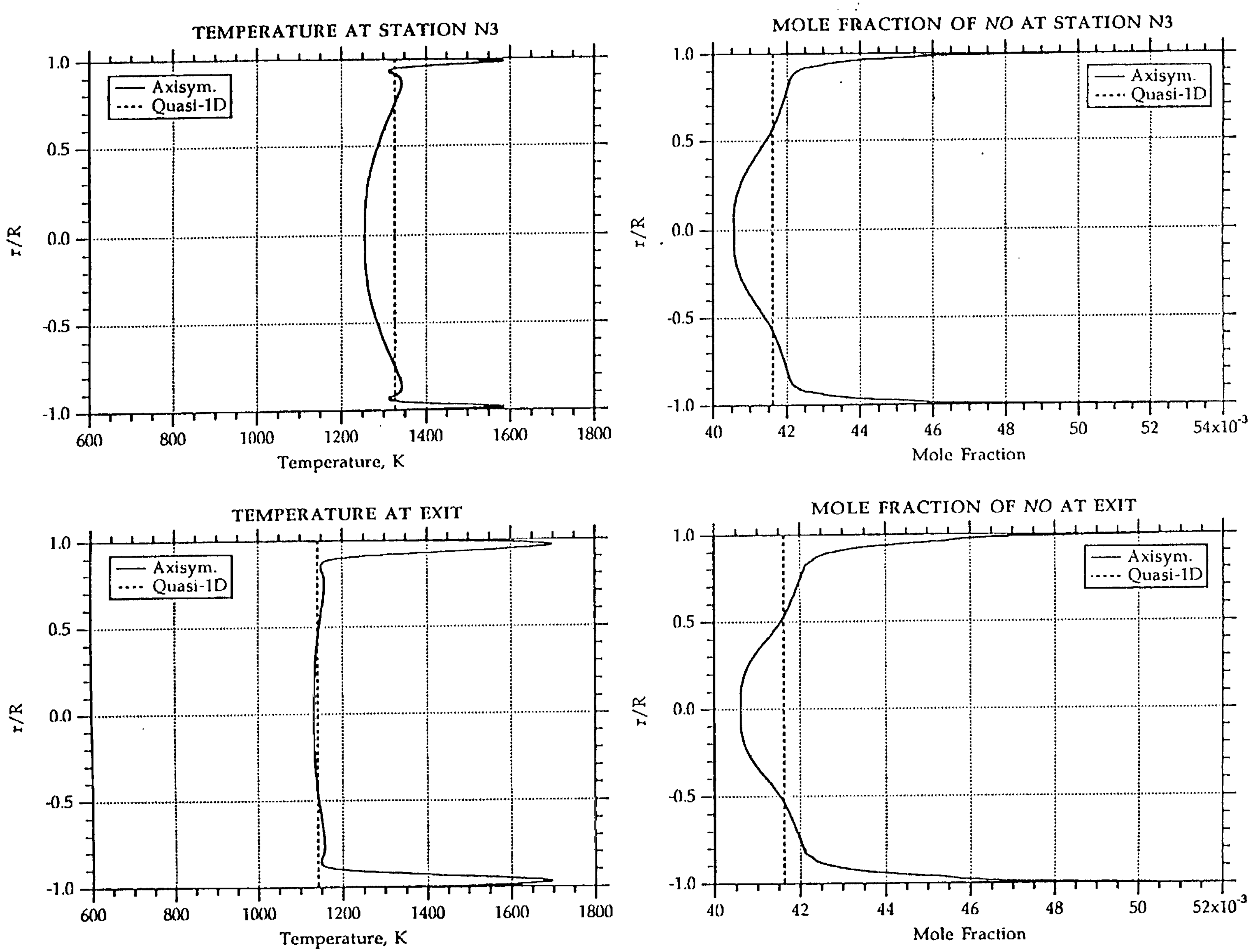

Figure 13: Temperature and *NO* mole fraction at two stations. There is still some significant core variation of the temperature at N3. The *NO* concentration profile remains essentially frozen, with most of the gradients in the boundary layer, as expected.

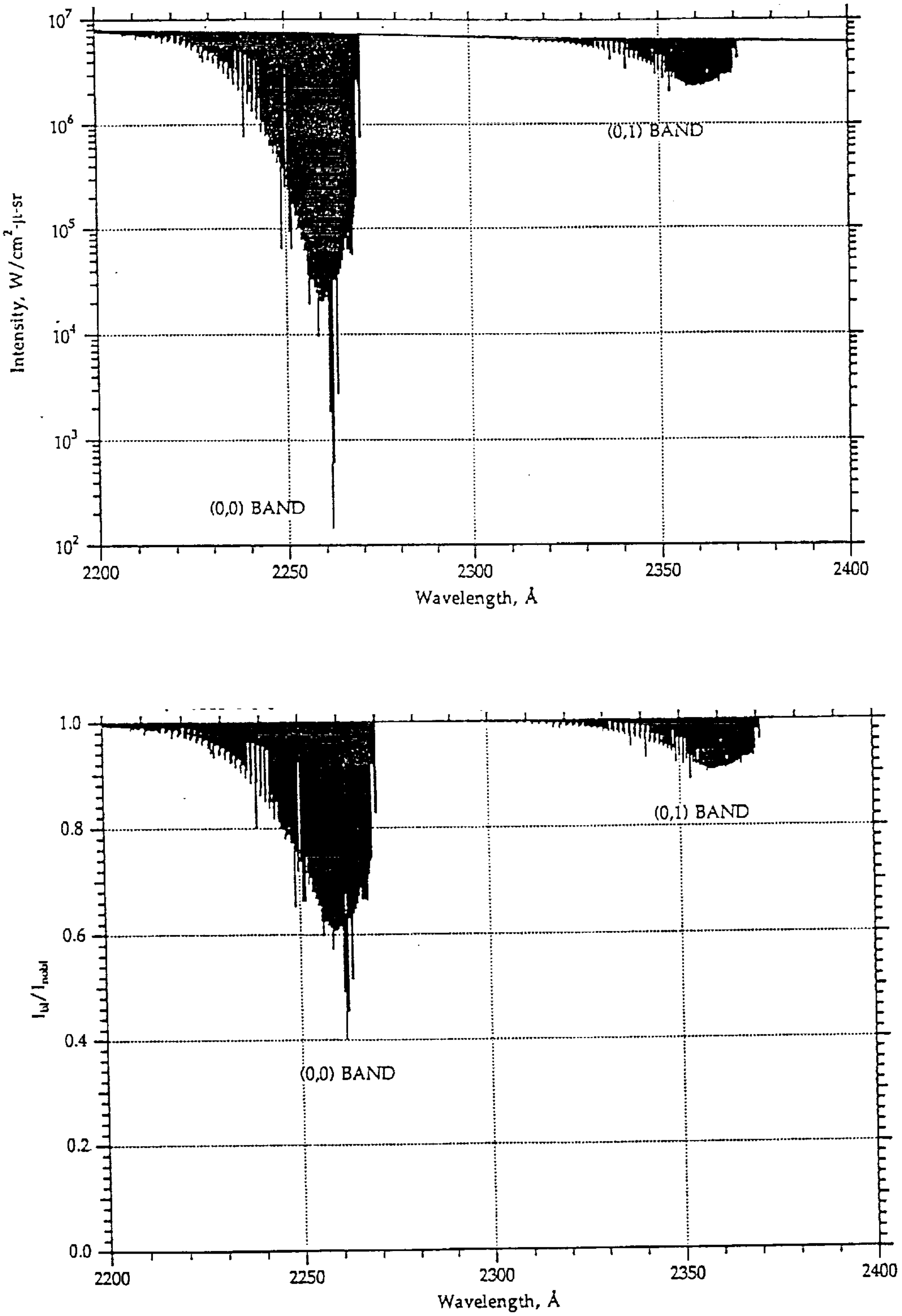

Figure 14: Computed Intensity at station N3, with and without the boundary layer. Figure 14-a (top), shows the intensity in absolute value, with the boundary layer included. Figure 14-b (bottom), shows the ratio of computed intensity *with* the boundary layer, versus the computed intensity *without* boundary layer. A similar plot for the exit plane would show a ratio at peak absorption of 0.2.

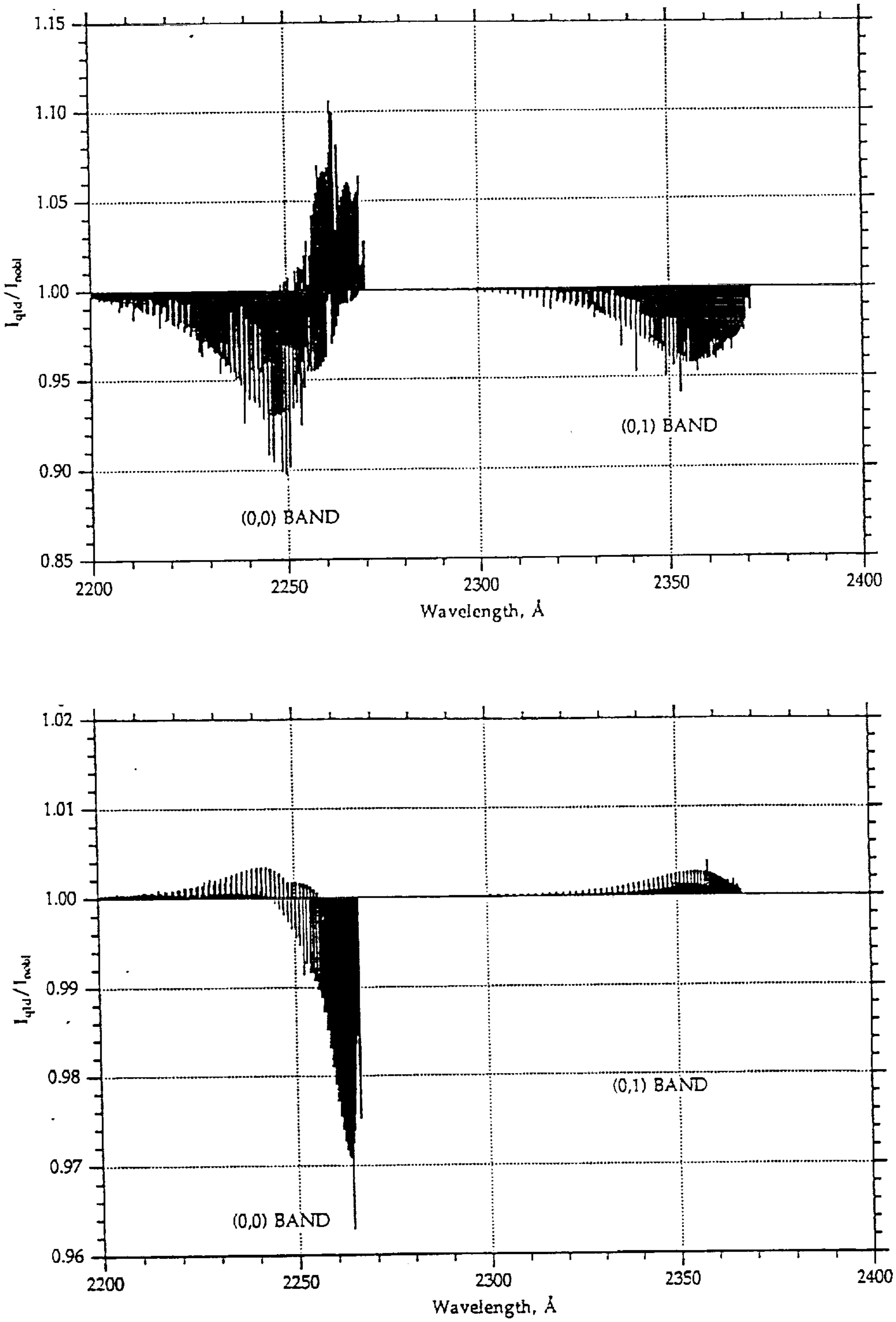

Figure 15: Comparison of quasi-1D and axi-symmetric cases (without BL). Figure 15-a (top) shows the ratio of the computed intensity for the quasi-1D solution (87%) versus the computed intensity for the 2D solution at station N3. Figure 15-b (bottom) shows a similar quantity for the exit plane.

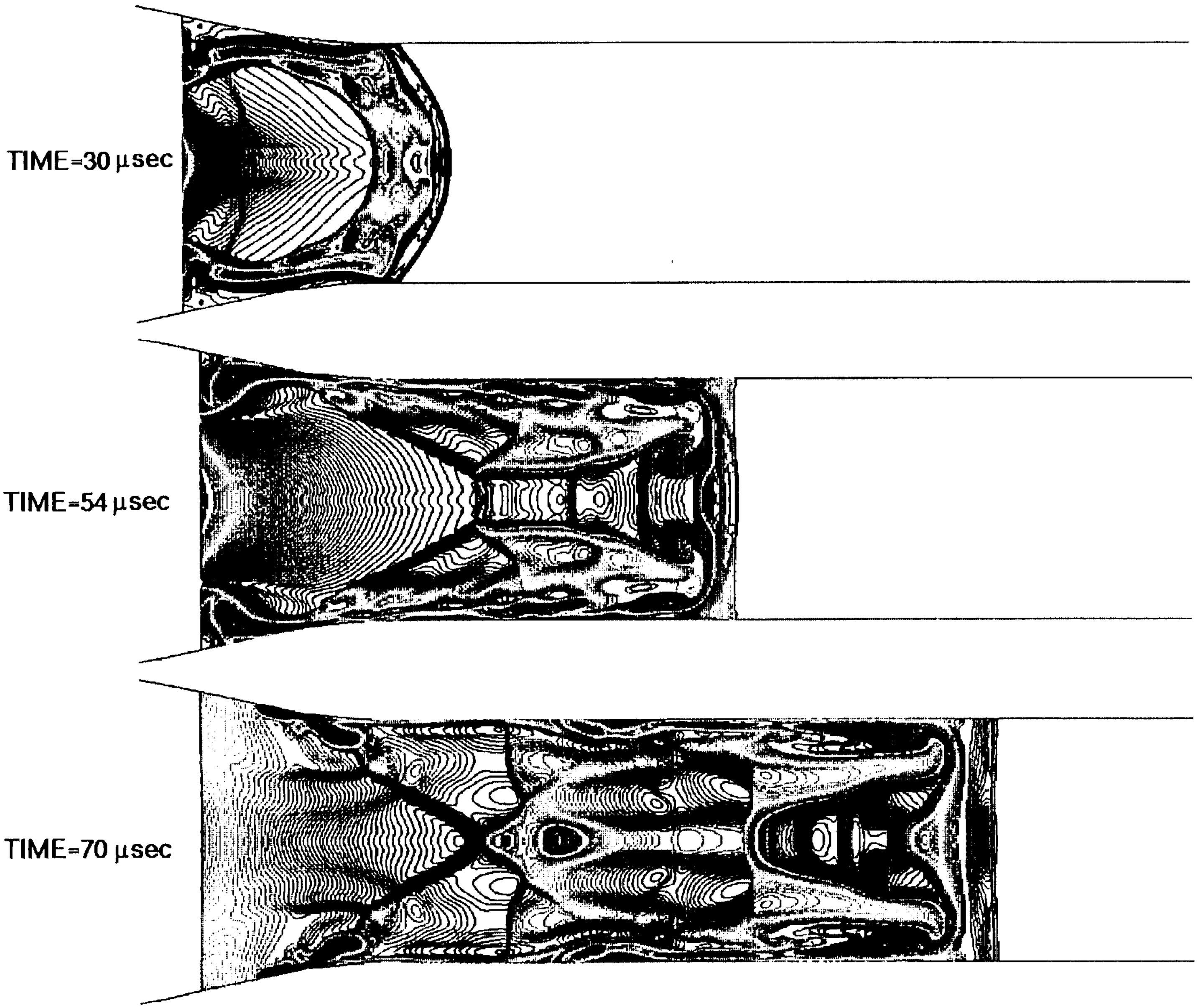

Figure 16: Flow transient at main diaphragm. Figure 16-a (top) taken at 30 μsec, Figure 16-b (middle) at 54 μsec, Figure 16-c (bottom) at 70 μ sec after start of diaphragm opening. The opening sequence has been set arbitrarily.

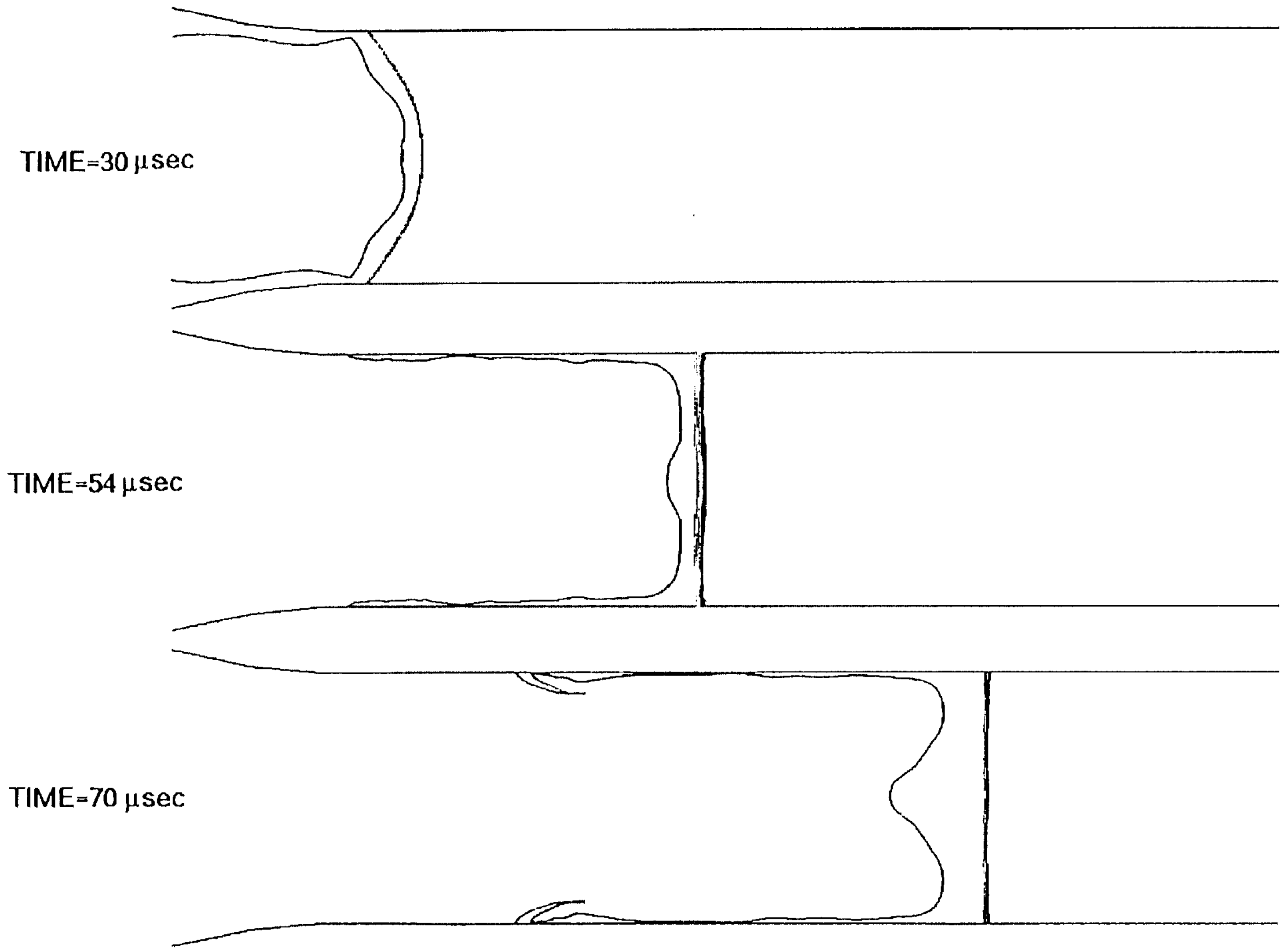

Figure 17: Shock and Contact Discontinuity for same time sequence as Figure 16.

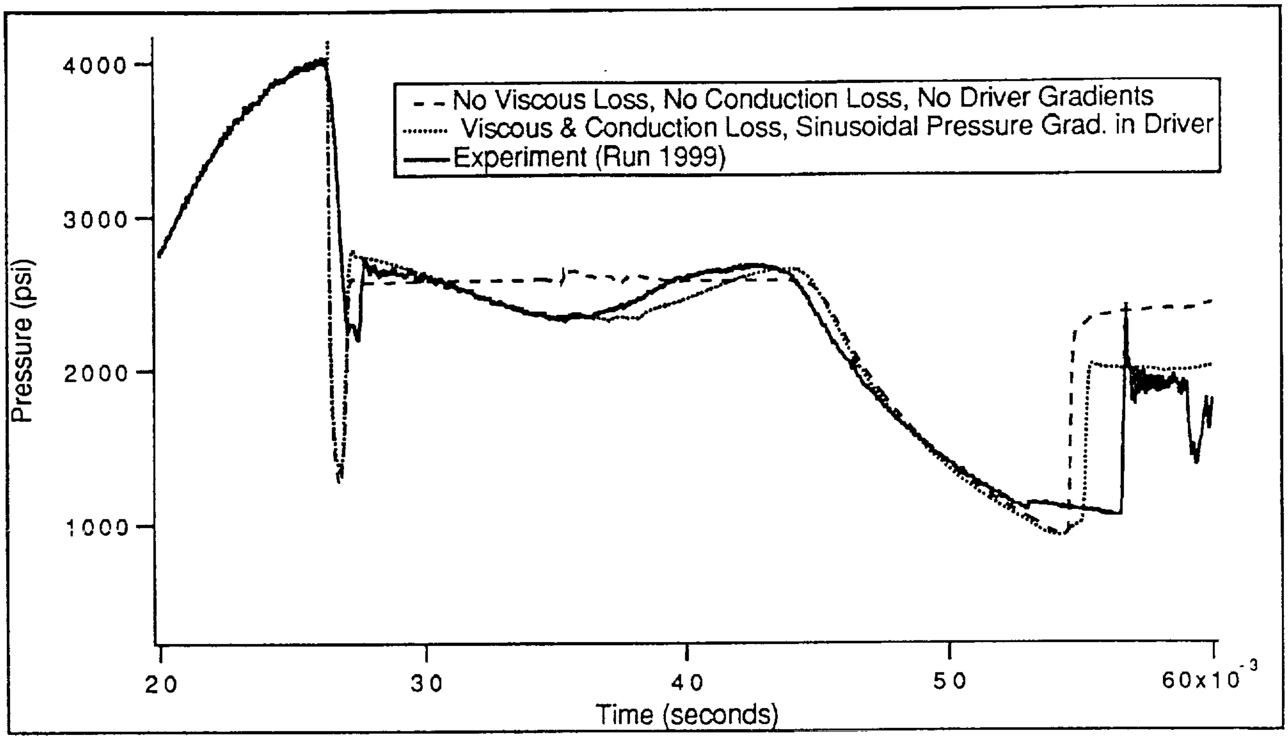

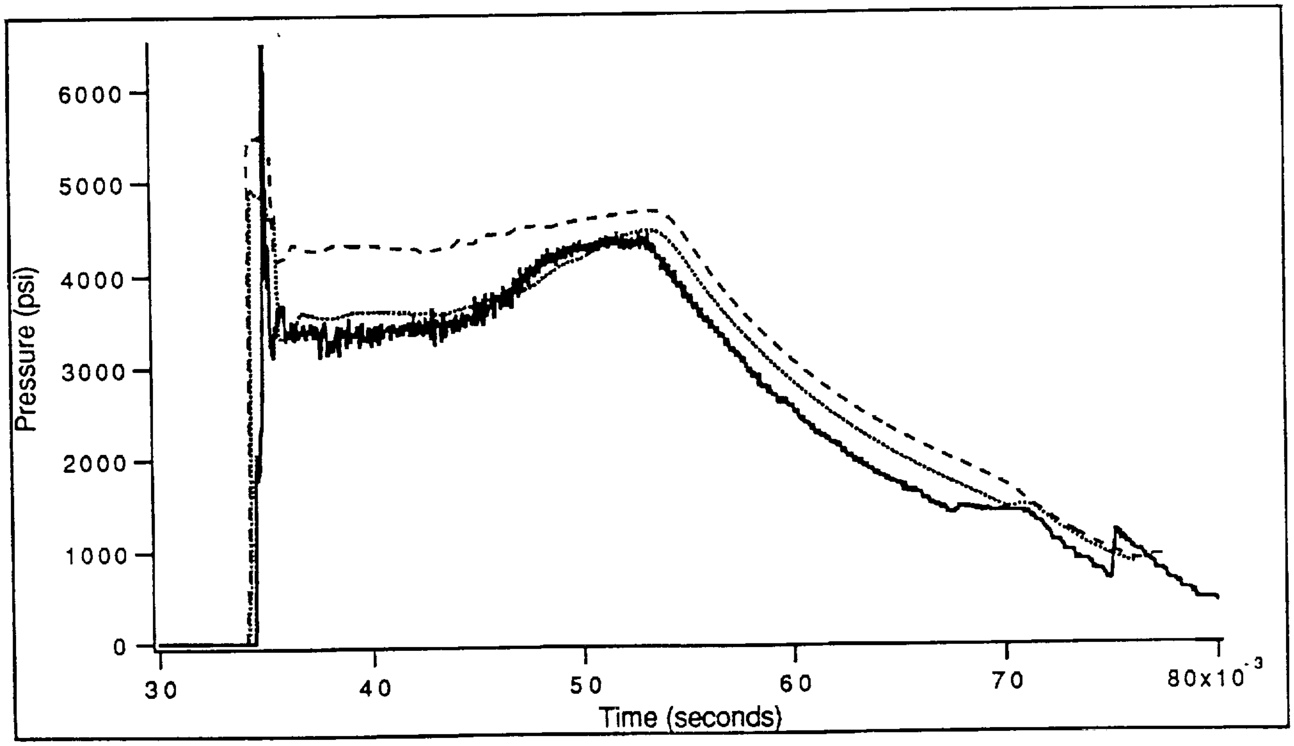

Figure 18: Comparison between experimental and computed pressure traces at two locations. Figure 18-a (top) shows the comparison at a few cm upstream of the main diaphragm in the driver tube. Figure 18-b (bottom) shows the traces for a point near the end of the driven tube. Significantly better agreement is obtained after assuming an *ad-hoc* pressure gradient within the driver tube, at the end of combustion.

AIAA-92-2971

Decoupled Predictions of Radiative Heating in Air Using a Particle Simulation Method

I. D. Boyd and E. E. Whiting
Eloret Institute
Palo Alto, CA 94303.

AIAA 23rd
Plasmadynamics & Lasers Conference
July 6-8, 1992 / Nashville, TN

DECOUPLED PREDICTIONS OF RADIATIVE HEATING IN AIR USING A PARTICLE SIMULATION METHOD

Iain D. Boyd* and Ellis E. Whiting*
Eloret Institute, 3788 Fabian Way
Palo Alto, California.

Abstract

The radiative emission along the stagnation streamline and the radiative heating at the stagnation point of a blunt-nosed vehicle entering the Earth's atmosphere at hypersonic speed are estimated using a particle simulation technique with decoupled radiation. The fluid mechanics of the weakly ionized flow is computed using the direct simulation Monte Carlo method, DSMC. Analysis of radiation is decoupled from the flowfield and is estimated using NEQAIR, a computer code written by Park. The results are compared with previous DSMC computations which employed a simplified, coupled radiation model. The effects of recent advances in modeling relaxation and dissociative behavior with the DSMC technique are assessed in terms of radiative emission. It is found that the introduction of the new models decreases the predicted total radiative heating at the stagnation point of the vehicle by a factor of 15. The DSMC approach is also compared with a continuum flow model: in each case prediction of radiation is decoupled from the flowfield. Similar sets of vibrational and chemical relaxation rates are employed in these simulations. Despite large differences in the computed flowfield, which exhibits strong thermo-chemical nonequilibrium, the total predicted radiative heating estimates agree within a factor of 2.

Introduction

The motivation for the present study arises from the requirement for accurate radiation estimates for hypersonic flight vehicles. These are necessary for adequate thermal protection of the spacecraft during entry into the Earth's atmosphere. A previous study for the Aeroassist Flight Experiment (AFE) has been reported by Whiting and Park[1] in which flowfield data were obtained using the Navier-Stokes equations at the lower altitudes traversed by the AFE during its sweep through the upper atmosphere. However, at higher altitudes, numerical difficulties were found in obtaining solutions. These difficulties are presumed to arise from the failure of the Navier-Stokes equations when the Knudsen number of the flow is too high.

The primary aim of the present study is to obtain radiation estimates using a particle simulation method for low-density, hypersonic flows in which strong effects due to thermo-chemical nonequilibrium are present and to compare the results with those from Ref. 1 for continuum flow. This is accomplished using the direct simulation Monte Carlo method (DSMC) to predict the one-dimensional flowfield along the stagnation streamline. The radiative emission is then computed using the computer code NEQAIR[2] with the radiation decoupled from the flowfield solution.

This is the first time that radiative heating has been estimated from DSMC computations using the approach in which radiation is decoupled from the flowfield solution. A new particle simulation code has been developed for the study. The code contains many recent developments which have improved considerably the modeling of thermo-chemical relaxation with the DSMC technique.

The new code is first evaluated through comparison against previously published particle computations of hypersonic, low-density, radiating flow. These previous DSMC computations employed simplistic thermochemistry models, and the effect of the introduction of the improved models is assessed. Additionally, comparison is made between the new code and continuum techniques for flow conditions corresponding to a trajectory point of the AFE vehicle. The continuum code

---

* Research Scientist. Mailing address:
NASA Ames Research Center, MS 230-2, CA 94035.

is SPRAP (Stagnation Point Radiation Program) written by Park[3] which solves the Navier-Stokes equations. Radiative emission for these continuum calculations is also decoupled from the flowfield solution.

Description of the Particle Simulation

The particle simulation code for computing one-dimensional shock waves in air is highly vectorized, and has been extended from the implementation for a reacting gas described by Boyd[4] to include electrons and ionizing reactions. An eleven species (N_2, N, O_2, O, NO, N_2^+, N^+, O_2^+, O^+, NO^+, E^-) real air model is employed. The code contains many recent modeling developments which have improved the ability of the DSMC technique to simulate thermochemical relaxation phenomena.

The code simulates rotational[5] and vibrational[6] energy exchange using probability functions which are evaluated using the energy of each collision. These represent an improvement on previous models in which constant probabilities were applied. The code employs the Vibrationally-Favored Dissociation model of Haas and Boyd[7] and a corresponding recombination model.[4] From the DSMC simulation, it is assumed that the vibrational and electronic temperatures of the gas are equal for the purposes of computing the radiative emission. Therefore, it is expected that the improved physical models employed in the DSMC code may affect significantly the total radiative heating predicted.

The introduction of electrons into the code requires special consideration. Due to their very low mass, the collision rates associated with electrons are about two orders of magnitude higher than those associated with the heavy species which occur in air. This requires the use of a numerical time-step which is two orders of magnitude smaller than would be employed were the electrons absent from the flowfield. In the present implementation, this problem is solved by using a time-step based on the heavy species to move the particles through the flowfield, and then subdividing the time-step into one hundred sub-steps to perform the collisions. Charge-neutrality is enforced throughout the flowfield by forcing each electron to remain in the same computational cell as the ion with which it was initially formed. While this is physically unrealistic, this approach should not affect the prediction of radiative emission to any great extent. Also, any charged particles which collide with the cold surface of the vehicle are assumed to recombine to the neutral species. The special considerations described here for simulating charged species add a significant numerical overhead to the calculations (although the DSMC code is still highly vectorized). This overhead is minimized by initially running the DSMC code without the charged species until a steady state is reached. The ionizition and charge-exchange reactions are then turned on, and the system is allowed to reach a new steady state, before sampling of flow variables begins.

Two different sets of chemical rate data are employed in the DSMC code. The first corresponds to that used by Moss *et al.*.[8] This set was implemented without coupled vibration-dissociation. In addition, for each reaction, the reverse rate expressions were determined by evaluating the electronic partition functions in the equilibrium constants at a fixed temperature. The second set of rate constants is based on those employed by Whiting and Park in the continuum code SPRAP. In their analysis, the reverse reaction rates are obtained by evaluating temperature-dependent curve fits for the equilibrium constant. The curve fits take the following form proposed by Park[3]:

$$K_e(T) = exp(A_1 + A_2 ln(z) + A_3 z + A_4 z^2 + A_5 z^3)$$

where the A_i are constants and z=10000/T. Unfortunately, this form for the equilibrium constant is not mathematically convenient for implementation in the DSMC chemistry models.

The goal of this part of the present study is to evaluate differences in the chemical models employed in the continuum and particle methods. To limit the number of factors involved in these comparisons, it is the aim to maintain consistency between the relaxation rates employed in the solution techniques. Therefore, a form for the equilibrium constant which takes the traditional Arrhenius form is fit as a function of temperature to Park's expression. This approach has been very successfully applied by Boyd and Gökçen[9] to the ionizing reactions for N_2. By achieving good correspondence between the two sets of chemical rate constants, very good agreement was obtained for flow solutions to hypersonic shock-waves in N_2 using particle and continuum methods. For air, good agreement is generally obtained between the new DSMC expressions and Park's results over the temperature range of interest, i.e. from 10,000 to 20,000 K.

Description of NEQAIR

The code employed to estimate the radiative emission from the flowfield solution is called NEQAIR and was developed originally by Park.[2] NEQAIR calculates the nonequilibrium electronic excitation of the species in the flow and the radiation emitted by those species. A principal assumption made in the code is that the quasi-steady state (QSS) model may be used to determine the population of each electronic state of a species after the species density is found from the reacting-flow solution.

The QSS model assumes that the individual rates of populating and depopulating each electronic state are much faster than the rate of change of the population of the state itself. Thus, the population of a state is given by the difference of two large numbers that are about equal. This assumption is not valid in the flow immediately behind the shock wave where the populations of the excited states are low and increasing rapidly. However, as the excited states become populated, the species begin to emit radiation, and by the time the radiation reaches a significant level, the assumption is reasonably valid.

As the QSS model is applied after the chemistry portion of the calculation is completed, the electronic excitation processes are assumed to be independent of the chemical reactions. This simplifies the calculation enormously. The QSS model allows a separate effective electronic temperature to be defined for each excited electronic state. These temperatures are defined by comparing the population of an excited state to the population of the ground state. At each flowfield data point, the QSS model implemented in NEQAIR employs the translational and vibrational temperatures from the DSMC or continuum simulation. In addition, the QSS model assigns many temperatures for electronic excitation (one for each excited electronic state of every species).

In the estimation of radiative emission from the flowfield solution, NEQAIR is executed over 12 different spectral regions which are listed in Table 2. These have been determined by Whiting and Park[1] to be those which make significant contributions to the total radiative heating for hypersonic flows of air. The following molecular bands have been included: N_2^+ (1-), N_2 (1+), N_2 (2+), N_2 (BH1), NOβ, NOγ, O_2 (SR).

The ultimate test of such codes is how well the results compare with experiment. Park[10] has compared calculated radiative results with shock-tube, ballistic-range, and Earth-entry data covering a wide range of flight conditions and finds good agreement, generally within a factor of two.

Results and Discussion

This section is divided into three sub-sections. In the first, comparison is made between the new code and DSMC computations reported previously by Moss *et al.*.[8] A number of different comparisons are made to examine the ability of the new code to reproduce exactly the results of Ref. 8 using the same physical model and chemical reaction rates. Specifically, the DSMC code employs constant rotational and vibrational collision numbers of 5 and 50, and the chemical reaction rates from Ref. 8 with the degree of vibration-dissociation coupling set to zero. The second subsection investigates the effects of employing the improved physical models. For this purpose, the DSMC code employs variable rotational and vibrational collision numbers, vibrationally-favored dissociation, and the new chemical rate constants derived from the continuum expressions. In the third sub-section, comparison is made between the DSMC code using the new models and the continuum computations of Ref. 1.

Comparison with Previous Results Using Old DSMC Models

The new code is first assessed through comparison with DSMC computations presented by Moss *et al.*[8] for the AFE at an altitude of 78 km (the flow conditions are given in Table 1). The free-stream temperature and Knudsen number were 188 K and $1.2\text{x}10^{-3}$ respectively. For compatability with the study reported in Ref. 8, constant rotational and vibrational collision numbers of 5 and 50 are employed. Also, the chemical reaction rates from Ref. 8 are used, the degree of vibration-dissociation coupling is set to zero, and the shock standoff distance is specified as 0.110 m from the body. A total of 1,000 computational cells and over 100,000 simulated particles are employed in each of the calculations reported in the current work.

The temperatures computed in the present study (lines) are compared with data taken from Ref. 8 (symbols) in Fig. 1. It is clear that significant thermal nonequilibrium effects are present. In comparison to the profiles from Ref. 8, the present temperatures are slightly higher. This effect is at least partially due to the absence of radiative cooling in the current work.

The mole fractions of the major species computed in the present study (lines) are compared with data taken from Ref. 8 (symbols) in Fig. 2. The present study is in very good agreement with the solutions from Ref. 8. In addition to the general form of the computed profiles shown in Figs. 1 and 2, the peak electron temperature of about 18,000 K and the maximum electron mole fraction of about 0.013 are in good correspondence to the results of Ref. 8.

The radiative emission along the stagnation streamline given by NEQAIR for the present DSMC flowfield solution is shown in Fig. 3. This profile compares quite well with the profile given in Ref. 8, although the peak value is somewhat larger in the present study. Integration of the spontaneous emission along the streamline to the body gives a one-dimensional radiative flux of 64.8 $kW/m^2/sr$, which is about a factor of 1.6 greater than the result of Moss *et al.*. The difference may partly be accounted for in terms of radiative cooling which is omitted in the present calculations by estimating radiative emission decoupled from the flowfield. Considering the significant differences in the radiation models employed in the two studies, the agreement is acceptable.

The radiative heating at the stagnation point due to the radiative flux given above is found using a spherical cap model[1]. First, the infinite slab result is obtained for the total radiative heating flux at the stagnation point by multiplying the one-dimensional value by 2π for the optically thin gas part of the spectrum, and by π for the self-absorbing regions. The spherical cap result is then computed as about 80% of the infinite slab value[1]. This procedure gives a total radiative heating value of about 340 kW/m^2, which is a very high value. This value is even higher than the convective heating rate reported in Ref. 8 as 248 kW/m^2.

The contributions to the total radiative heating made by the various spectral regions which are analyzed are listed in Table 3 under Old Model. The reasonable agreement found between the present DSMC results and those obtained in Ref. 8 for the radiative flux, indicates that the decoupled approach to radiation assumed in this study is an appropriate solution method for these flow conditions. In addition, analysis of the rate of loss of energy from the flowfield showed that only about 0.2% was due to radiative emission. This confirms that simulation of radiation coupled to the fluid mechanics is unnecessary for these flowfields.

Comparison of Old and New DSMC models

Having established that the new DSMC code provides solutions which are similar to previous studies, when using similar models, it is appropriate to assess the effect on the radiative emission by the introduction of the improved physical models. Specifically, variable rotational and vibrational collision numbers, vibrationally-favored dissociation, and the new chemical rate constants derived from the continuum expressions are implemented. The translational and vibrational temperatures computed with the DSMC code using the old and new models are shown in Fig. 4 for the same conditions considered in the previous subsection. The relaxation zone is much larger with the improved models. Note that the vibrational mode using the new model does not equilibrate with the translational mode until the body surface is reached. This is due mainly to the use of the variable vibrational collision number. This quantity is a strong function of temperature, and only reaches a maximum of about 50 at the peak translational temperature. For most of the stagnation streamline, the vibrational collision number is greater than 100 which reduces significantly the rate of equilibration of the vibrational mode.

The species which radiate most energy in the ultraviolet region of the spectrum (0.11-0.18μ m) are atomic nitrogen and oxygen. The variation in the mole fractions for these species is shown in Fig. 5. With the new, improved models, the rise in N and O due to dissociation is retarded significantly due to the use of the vibrationally-favored dissociation models and the lower vibrational temperatures. The strongest radiator above 0.2 μm is N_2^+ and its variation in mole fraction computed with the old and new DSMC models is compared in Fig. 6. The rise in N_2^+ is faster with the old models although behind the shock the two solutions show general agreement.

The profiles of radiative emission are compared in

Fig. 7. The peak emission obtained with the new models is significantly lower than that computed with the previous models due to the lower electronic temperature, which is set equal to the vibrational value in NEQAIR. The computed three-dimensional integrated radiative heating at the stagnation point is only about 23.4 kW/m^2 for the new model which is a factor of about 15 smaller than that predicted by the old model. The contributions to the total radiative heating made by the various spectral regions which are analyzed using NEQAIR are listed in Table 3 under New Model. The very large difference obtained in the radiative heating estimates using the old and new thermochemistry models demonstrates the sensitivity of the calculations to the physical models.

Comparison with Continuum Results

The DSMC code using the new models is applied to the flow conditions examined by Whiting and Park[1], which are given in Table 1. These are slightly different from those investigated in Ref. 8. The most important difference involves the shock standoff distance which is significantly larger in Ref. 1 (0.188 m) than in Ref. 8 (0.110 m). The freestream temperature is 188 K and the Knudsen number is $1.7x10^{-3}$. The DSMC computations again employed the energy-dependent probabilities of rotational and vibrational energy exchange, and the vibrationally-favored dissociation model discussed by Boyd.[4] The vibrational and chemical rate constants are made consistent with those employed in the continuum simulation as discussed earlier.

The continuum results taken from Ref. 1 were computed using SPRAP which was developed by Park.[3] This code computes the viscous, one-dimensional, continuum flow behind an infinitely thin normal shock wave using the approach described in Ref. 3. The solution for the one-dimensional, uniform area duct may then be transformed to represent the flow along the stagnation streamline of a spherical body. The initial flow conditions immediately behind the shock are determined from the Rankine-Hugoniot shock-jump relationships, assuming that the vibrational temperature remains at the free-stream value. A viscous shock layer treatment is applied for computation of the boundary layer which forms next to the cold wall of the vehicle. It is assumed that the flow in the boundary layer is chemically frozen with a ratio of specific heats equal to 11/9. Further, the wall is assumed to be noncatalytic for the dissociation reactions and fully catalytic for the ionization reactions. In this approach, a two-temperature dissociation model is used in generating the reacting flow behind the normal shock wave. This model equates the molecular rotational temperature to the kinetic temperature of the atoms and molecules, and also equates the electron kinetic and electronic temperatures to the molecular vibrational temperature. In the two-temperature model, all molecules have the same vibrational temperature, the degree of ionization is small, and the chemical reactions occur in the ground states of the atoms and molecules.

The computed temperature profiles are compared in Fig. 8. The two-temperature continuum approach provides a translation-rotation value, and a vibration-electron-electronic value. The particle DSMC approach provides separate values for the translational, rotational, and vibrational energy modes and equates the electronic temperature to the vibrational temperature to calculate the radiation.

The temperature profiles exhibit many differences. The DSMC solution shows considerable shock thickness and structure which is omitted in the continuum calculation. In the DSMC computation, there is a significant region of the shock where the translational and rotational modes are not equilibrated, thereby casting doubt on the validity of the continuum two-temperature approach at least at these low densities.

The rise in vibrational temperature predicted by DSMC is slower than that computed in the continuum simulation. Further, the DSMC method predicts a higher degree of nonequilibrium between the vibrational mode and the translational and rotational modes all along the stagnation streamline. The reasons for these differences in the two solutions are not clear at this point. The factors involved include differences in simulating viscosity, thermochemistry, and transforming a one-dimensional calculation into a stagnation streamline flow. These factors need to be investigated more thoroughly.

The mole fractions of atomic nitrogen and oxygen computed with the continuum method and the DSMC code for these conditions are compared in Fig. 9. Generally, the agreement is quite good except within the shock wave itself which is omitted in the continuum code. In the continuum technique, it is assumed that no chemical reactions occur upstream of the shock standoff location. The DSMC computation indicates that significant chemical activity does take place through the shock. This is due to the finite thickness of the shock-wave and to diffusion effects. Thus, the rise in atomic mole fractions computed by DSMC preceeds the continuum results by a significant distance. The profiles computed by the two methods then follow similar paths until the last few centimeters next to the body, where the continuum code assumes the flow to be chemically frozen. The variation in mole fraction of N_2^+ computed with the two techniques is shown in Fig. 10. The rise in N_2^+ predicted by DSMC occurs in the thick shock-front and therefore leads the continuum solution. Behind the shock, the DSMC results provide a higher concentration of N_2^+ than the continuum data.

The spontaneous radiative emission profiles obtained from the continuum and DSMC solutions are compared in Fig. 11. The peak emission obtained with the new DSMC models is significantly lower than that computed with the continuum method, due to the smaller electronic (vibrational) temperature.

The integrated radiative heating at the stagnation point computed with the DSMC calculation is about 47 kW/m^2 while the continuum solution gives a value of 75.5 kW/m^2. The contributions to the total radiative heating made by the various spectral regions are listed in Table 4.

Despite the large differences observed in the flowfield solutions, it is interesting to note that the continuum and DSMC total radiative heating estimates lie within a factor of 2 of each other. It is also worth noting that by increasing the shock standoff distance from 0.110 m (from Ref. 8) to 0.188 m (from Ref. 1) the total radiative heating predicted by the new DSMC thermochemistry models is doubled, indicating nearly linear scaling between these two quantities.

For the sake of completeness, the flow conditions investigated in Ref. 1 were also computed with the old DSMC thermochemistry models. The difference in flow quantities computed with the old and new models was similar to those shown in Figs. 4 through 6. The flow quantities were again interpretted in terms of total radiative heating at the stagnation point using NEQAIR. The solution obtained with the old DSMC thermochemistry models gave a radiative heating which was ten times higher than that predicted with the new models.

Concluding Remarks

A new approach has been evaluated for predicting the radiative heating of a blunt-body entering the Earth's atmosphere. In this approach, the fluid mechanics of the flow along the stagnation streamline was predicted using a particle method (the direct simulation Monte Carlo method, DSMC), which is decoupled from the radiative emission.

Comparison was made with a previous DSMC calculation which employed outdated thermochemistry models together with a simplified, coupled radiation model. For the purpose of this comparison, the present DSMC computation also employed the old DSMC thermochemistry models. These two very different approaches gave agreement to within a factor of 2 for the total radiative heating at the stagnation point. This is viewed as acceptable considering the differences between the radiation models employed. The decoupled approach gave the higher value which was attributed in part to the absence of radiative cooling.

For the same flow conditions, the use of new DSMC thermochemistry models led to a decrease by a factor of 15 in the total radiative heating at the stagnation point. This drastic reduction in heating illustrates the sensitivity of the computed data to the physical models employed in the simulations. It is proposed that the new thermochemistry models, which have been successfully evaluated in previous studies, should provide more realistic simulation results. This decrease in radiative heating indicates that it is not necessary to couple radiation to the fluid mechanics under these flow conditions. To attain greater confidence in the numerical simulations, it is clear that experimental data is required for the validation of these physical phenomena.

A further comparison of the new DSMC chemistry models with a continuum calculation gave agreement within a factor of 2 for the total radiative heating, despite considerable differences in the flowfield solutions. The main conclusion of this study is that there remains a large degree of uncertainty in the application of state-of-the-art numerical methods for the prediction of radiative heating to hypersonic vehicles flying in low-density regions of the Earth's atmosphere. Considering the importance of such heating to many future aerospace projects, there is a need for continued numerical and experimental investigation in this area.

Acknowledgement

Support (for I.D.B.) by NASA (Grant NCC2-582) is gratefully acknowledged.

Table 1. Freestream conditions.

Source	Altitude	U_∞ (m/s)	ρ_∞ (kg/m^3)
Ref. 8	78 km	9110	2.75×10^{-5}
Ref. 1	80 km	9756	2.05×10^{-5}

Table 2. Spectral regions analyzed with NEQAIR.

Region (μm)	Description	Absorption
0.1130-0.1140	N atomic lines	Yes
0.1160-0.1170	N atomic lines	Yes
0.1170-0.1180	N atomic lines	Yes
0.1195-0.1205	N atomic lines	Yes
0.1240-0.1250	N atomic lines	Yes
0.1294-0.1314	N and O atomic lines	Yes
0.1315-0.1325	N atomic lines	Yes
0.1323-0.1333	N atomic lines	Yes
0.1405-0.1415	N atomic lines	Yes
0.1490-0.1500	N atomic lines	Yes
0.1740-0.1750	N atomic lines	Yes
0.2000-2.0000	Molecular lines	No

Table 3. Total radiative heating (in kW/m^2) using DSMC for the flow conditions from Ref. 8.

Region (μm)	Old Model	New Model
0.1130-0.1140	3.11	0.08
0.1160-0.1170	4.19	0.16
0.1170-0.1180	2.30	0.08
0.1195-0.1205	6.07	0.21
0.1240-0.1250	3.65	0.14
0.1294-0.1314	8.23	0.24
0.1315-0.1325	3.16	0.23
0.1323-0.1333	2.37	0.07
0.1405-0.1415	3.13	0.28
0.1490-0.1500	11.94	0.72
0.1740-0.1750	19.30	2.21
Sub-Total	67.5	4.42
0.2000-2.0000	272.2	19.0
Total	339.7	23.4

Table 4. Continuum and DSMC contributions (in kW/m^2) of the various spectral regions to the total radiative heating at the stagnation point for the flow conditions from Ref. 1 at an altitude of 80 km.

Region (μm)	Continuum	New Model
0.1130-0.1140	0.44	0.20
0.1160-0.1170	0.76	0.50
0.1170-0.1180	0.32	0.27
0.1195-0.1205	0.84	0.46
0.1240-0.1250	0.92	0.40
0.1294-0.1314	0.76	1.13
0.1315-0.1325	0.76	0.61
0.1323-0.1333	0.52	0.19
0.1405-0.1415	0.84	0.70
0.1490-0.1500	2.84	1.65
0.1740-0.1750	5.36	4.73
Sub-Total	14.4	10.8
0.2000-2.0000	61.1	36.2
Total	75.5	47.0

References

[1] Whiting, E.E. and Park, C., "Radiative Heating at the Stagnation Point of the AFE Vehicle," NASA Technical Memorandum 102829, November 1990.

[2] Park, C., "Nonequilibrium Air Radiation (NEQAIR) Program: User's Manual," NASA Technical Memorandum 86707, 1985.

[3] Park, C., "On Convergence of Computation of Chemically Reacting Flows," AIAA Paper 85-0247, January 1985.

[4] Boyd, I.D., "Analysis of Vibration-Dissociation-Recombination Processes Behind Strong Shock Waves of Nitrogen," *Physics of Fluids A*, Vol. 4, No. 1, 1992, pp. 178-185.

[5] Boyd, I.D., "Analysis of Rotational Nonequilibrium in Standing Shock Waves of Nitrogen," *AIAA Journal*, Vol. 28, No. 11, 1990, pp. 1997-1999.

[6] Boyd, I.D., "Rotational and Vibrational Nonequilibrium Effects in Rarefied Hypersonic Flow," *Journal of Thermophysics and Heat Transfer*, Vol. 4, No. 4, 1990, pp. 478-484.

[7] Haas, B.L. and Boyd, I.D., "Models for Vibrationally-Favored Dissociation Applicable to a Particle Simulation," AIAA Paper 91-0774, AIAA 29th Aerospace Sciences Meeting, Reno, NV, January 1991.

[8] Moss, J.N., Bird, G.A. and Dogra, V.K., "Nonequilibrium Thermal Radiation for an Aeroassist Flight Experiment Vehicle," AIAA Paper 88-0081, AIAA 26th Aerospace Sciences Meeting, Reno, NV, January 1988.

[9] Boyd, I.D. and Gökçen, T., "Evaluation of Thermochemical Models for Particle and Continuum Simulations of Hypersonic Flow," AIAA Paper 92-2954, AIAA 27th Thermophysics Conference, Nashville, Tennessee, July 1992.

[10] Park, C., "Assessment of Two-Temperature Kinetic Model for Ionizing Air," Journal of Thermophysics and Heat Transfer, Vol. 3, No. 3, 1989, pp. 233-244.

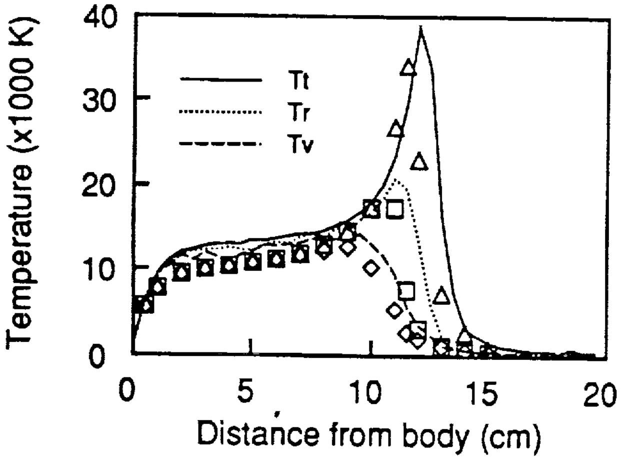

Fig. 1. Temperature profiles along the stagnation streamline: comparison of present calculatons and Ref. 8 using the old DSMC thermochemistry models.

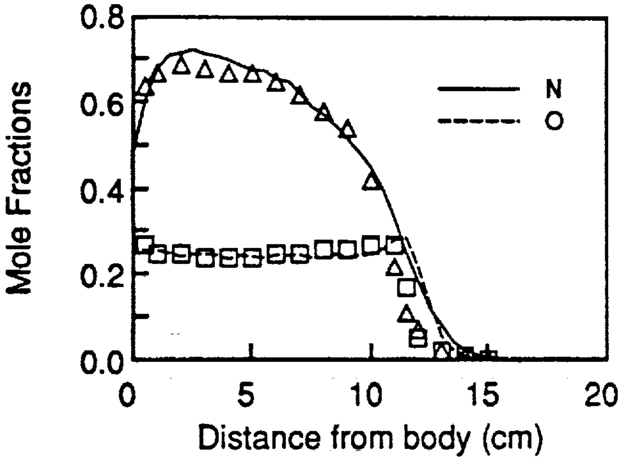

Fig. 2. Profiles of atomic species mole fractions: comparison of present calculatons and Ref. 8 using the old DSMC thermochemistry models.

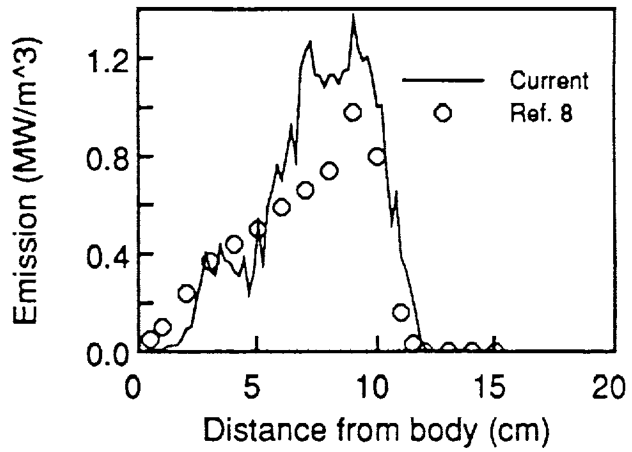

Fig. 3. Profiles of radiative emission along the stagnation streamline: comparison of present calculatons and Ref. 8 using the old DSMC thermochemistry models.

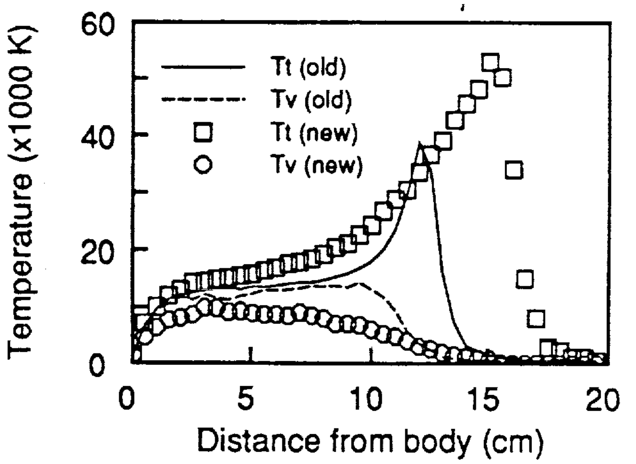

Fig. 4. Temperature profiles along the stagnation streamline: comparison of the old and new DSMC thermochemistry models.

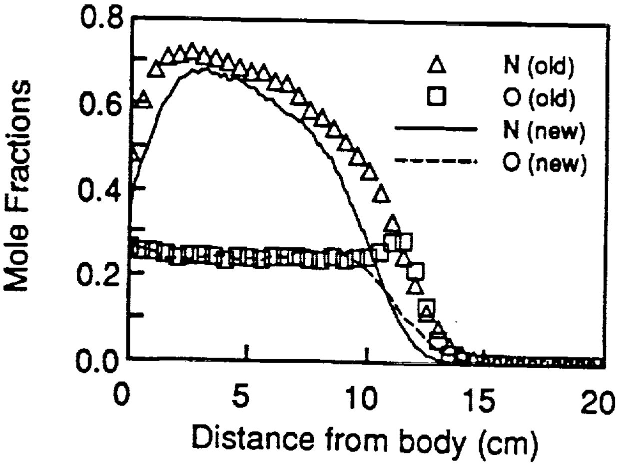

Fig. 5. Profiles of atomic species mole fractions along the stagnation streamline: comparison of the old and new DSMC thermochemistry models.

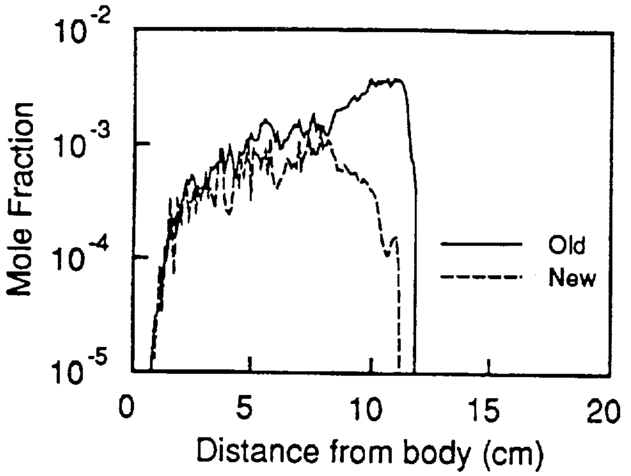

Fig. 6. Profiles of N_2^+ mole fraction along the stagnation streamline: comparison of the old and new DSMC thermochemistry models.

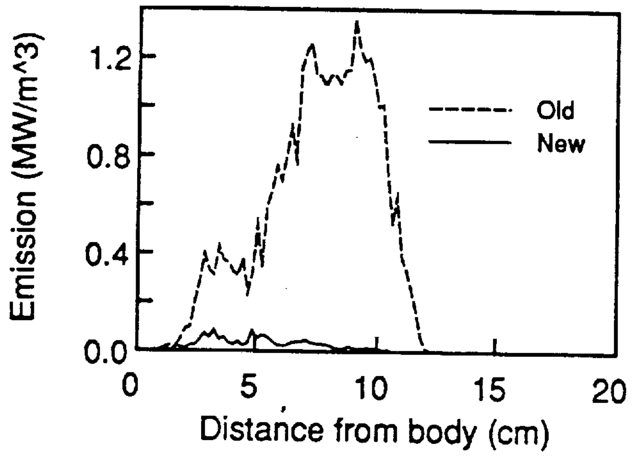

Fig. 7. Profiles of radiative emission along the stagnation streamline: comparison of the old and new DSMC thermochemistry models.

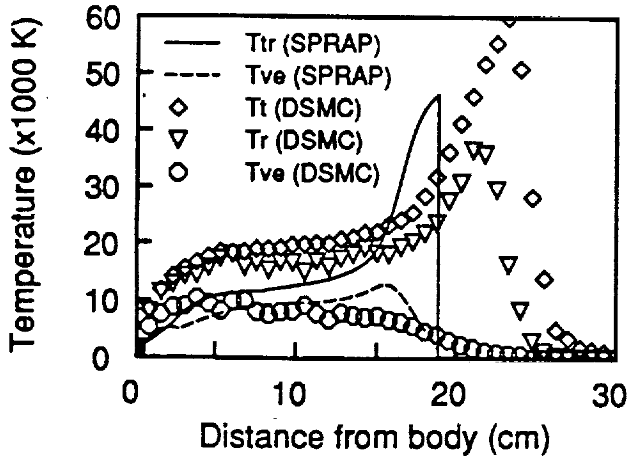

Fig. 8. Temperature profiles along the stagnation streamline: comparison of continuum and DSMC calculations using the new thermochemistry models.

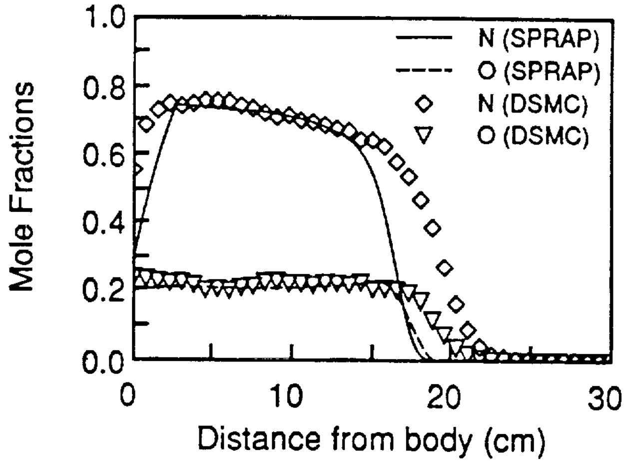

Fig. 9. Profiles of atomic species mole fractions: comparison of continuum and DSMC calculations using the new thermochemistry models.

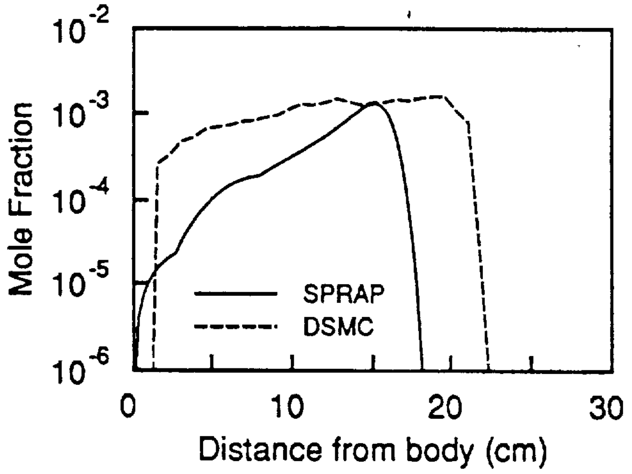

Fig. 10. Profiles of N_2^+ mole fractions: comparison of continuum and DSMC calculations using the new thermochemistry models.

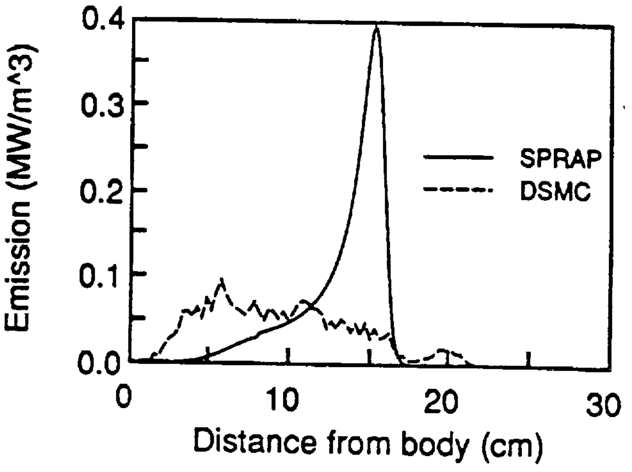

Fig. 11. Profiles of radiative emission: comparison of continuum and DSMC calculations using the new thermochemistry models.

AIAA-92-5096

Time-Dependent Quasi-One-Dimensional Simulations of High Enthalpy Pulse Facilities

G. Wilson,
Eloret Institute,
Palo Alto, CA

AIAA FOURTH INTERNATIONAL AEROSPACE PLANES CONFERENCE
1 - 4 DECEMBER 1992/ORLANDO, FL

For permission to copy or republish, contact the
American Institute of Aeronautics and Astronautics
The Aerospace Center • 370 L'Enfant Promenade, SW • Washington, DC 20024-2518

TIME-DEPENDENT QUASI-ONE-DIMENSIONAL SIMULATIONS OF HIGH ENTHALPY PULSE FACILITIES

Gregory J. Wilson*
Eloret Institute
3788 Fabian Way
Palo Alto, California 94303

Abstract

The purpose of this paper is to present a numerical methodology for simulating the time-dependent reacting flow inside the entire length of several types of high enthalpy pulse facilities. The numerical approach uses a finite-volume TVD scheme for the quasi-one-dimensional Euler equations coupled with finite-rate chemistry on a moving mesh. A Riemann solver is incorporated for tracking contact discontinuities. Several numerical difficulties encountered in simulating pulse facility flows are discussed and the numerical techniques chosen to overcome these problems are presented. Comparisons of experimental and computational pressure traces are made for three different experimental facilities; the NASA Ames electric arc driven shock tube facility (from cold driver shots), the NASA Ames 16 inch combustion driven shock tunnel, and the HYPULSE expansion tube. The comparisons help validate the numerical methodology and add to the understanding of the flow inside these facilities. Differences between the quasi-one-dimensional solutions and the experiments are used to suggest improvements that multi-dimensional simulations might provide.

Introduction

The high enthalpy pulse facilities considered in this work are experimental apparatus designed to create hypersonic flow. The term "pulse" is used because these facilities are capable of creating the desired flow conditions for only short periods of time (on the order of milliseconds). The present work investigates shock tubes, shock tunnels (without pistons), and expansion tubes which represent only a few of the many different types of pulse facilities. At the core of each of these facilities is a shock tube, which makes the current methodology applicable to several devices.

A primary motivation for simulating the flow inside a high enthalpy pulse facility is to help predict important operating characteristics such as the stagnation properties and the chemical composition of the test flow which are often difficult to measure. Knowing these quantities is important for interpreting the experimental data obtained from these facilities. For example, the shape/angle of shock waves or the ignition properties in a combustor can be affected by test gas that has become contaminated or dissociated during the operating sequence of a facility. Numerical simulations that are able to quantify such effects can make the experimental data more valuable. They can also be used to investigate ways to increase a facility's performance or operating envelope.

Computing the unsteady flow inside a high enthalpy pulse facility is challenging because the flow can be significantly influenced by strong shock waves, gas interfaces, high temperature effects, chemical kinetics, and viscous interactions. In addition to these complexities, there is often a large disparity of length scales. For example, a facility may be tens of meters in length while the length scales of some of the physical phenomena such as the chemical kinetics may be less than a millimeter. This requires finding a way to resolve the small scale physics while still economically simulating the large scale flow.

Because of the large length scales of the facilities being considered in this work (in one case over 50 m), an unsteady quasi-one-dimensional compressible flow formulation has been adopted. The lower computational requirements of the one-dimensional approach compared to multi-dimensional simulations allows the computations to be advanced over long distances in a practical amount of computer time and also allows for the use of a relatively complicated gas model.

Several recent works have also used one-dimensional simulations to look at high enthalpy pulse facilities.

---

*Research Scientist, Member AIAA. Mailing address: NASA Ames Research Center, MS 230-2, Moffett Field, CA 94305

Groth *et al.*[1] used a sophisticated gas model to compute the complete unsteady performance of an impulse tunnel. Their work clearly shows the usefulness of one-dimensional simulations of a complete facility. However, that work differs from the present research because instead of having gas interfaces, the facility that they simulated uses a piston to separate the driver gas and test gas. As a result, several of the primary physical phenomenon and numerical concerns are different. Another work by Maus *et al.*[2] contains quasi-one-dimensional simulations of a free-piston shock tunnel using a Lagrangian scheme.

The numerical approach taken in this work has been to solve the unsteady quasi-one-dimensional Euler equations coupled to a detailed finite-rate chemistry model. An upwind TVD scheme is used to compute the bulk of the flowfield and a Riemann solver is included for tracking gas interfaces. This hybrid scheme is applied on a moving mesh. One goal of this work is simply to investigate whether this kind of approach can consistently predict some of the detailed flow features within large facilities that operate by rupturing diaphragms. There are concerns that the deformation and instabilities of contact discontinuities are so severe and unpredictable that the current approach with its simplifications and ideal treatment of the gas interfaces may not be helpful. With this overall objective in mind, some of the finer points of the physical modeling have been kept relatively simple and show what is possible rather than what is best. For instance, viscosity and heat conduction models are not as sophisticated as they might be and the provision for vibrational nonequilibrium is included in the fluid equations but is not utilized.

This work begins by presenting and discussing several numerical difficulties, which are considered to be common to simulations of high enthalpy pulse facilities. This is followed by a description of the mathematical and numerical formulation. Then, numerical computations are compared to experimental data from a shock tube, a shock tunnel, and an expansion tube. In addition to validating the numerical approach, these simulations demonstrate the physical understanding that can be gained with quasi-one-dimensional modeling. Specifically, the computations are used to predict the following phenomena: the influence of initial conditions on the interaction of the reflected shock with the contact discontinuity (tailoring behavior); the influence of pressure non-uniformities in the driver section (a situation often seen in combustion drivers) on the reflected shock region; and the influence of a finite diaphragm opening time on the chemical composition of expansion tube test conditions.

Numerical Issues

Two numerical issues encountered in this work are discussed in this section so that the reasons for adopting the present numerical scheme can be understood. One issue is the performance of numerical schemes on a flow started by instantaneously removing a diaphragm which separates two regions with a very large pressure difference, and the other is the smearing of gas interfaces by numerical diffusion.

All the pulse facilities considered in this work begin by bursting a diaphragm which separates a high pressure driver section from a low pressure driven section. One-dimensional simulations of the unsteady flow created by this type of initial condition are not uncommon and plots of the resulting shock, contact discontinuity, and expansion fan are often presented in the literature when the merits of a numerical scheme are being investigated.[3,4,5] These investigations, however, are usually for relatively low pressure ratios across the diaphragm (ratios less than 10). Initial pressure ratios in a hypersonic pulse facility may be over 10000 in which case it has been found that special care must be taken.

Figure 1 shows temperature profiles from simulations of a perfect gas in a 2 meter shock tube which began with driver conditions of 1 atm and 300K and driven conditions of .1 atm and 300K (initial pressure ratio 10). The computations were made using Harten and Yee's upwind TVD scheme[4] at CFL number 0.65 on several different equally-spaced grids. All of the solutions are similar with the major difference being the degree of resolution of the contact discontinuity (and to a smaller extent the sharpness of the shock). The similarity of the solutions and their convergence toward a single solution gives confidence in the accuracy of the computations. In contrast, Figure 2 depicts temperature profiles resulting from the same initial conditions except that a driver pressure of 1000 atm was used (initial pressure ratio 10000). Under these conditions, the solution changes significantly with each refinement of the mesh and even a 3200 point grid is unable to support an accurate solution. In this case, not only does the resolution of the features change with the grid, but the shock propagation speed changes as well. Investigations with several first and second-order schemes including a Riemann solver resulted in similar results with the conclusion that higher grid resolution is required at the diaphragm as the initial pressure ratio is increased.

This conclusion is supported by using a highly clustered grid at the diaphragm for just the initial part of the solution. To avoid the small time step and high cost that a fine spacing imposes, the grid spacing is allowed to expand as the solution progresses until an equally-spaced grid is attained. The temperature profiles with an initial spacing of 2.5 μm at the diaphragm location (a 400,000 point equally-spaced grid would be required to get this spacing) are shown in Figure 3 for grids of 200, 400, and 3200 points along with the equally-spaced 3200 point solution from Figure 2. The plot shows that with the initial clustering the propagation speed of the various features becomes nearly the same for all the grids and that a very accurate solution is reached more quickly than on the equally-spaced grid (it is not shown but an 800 point solution is nearly the same as the 3200 point solution).

The other numerical issue mentioned above is the smearing of gas interfaces by numerical diffusion. The smearing increases as the grid becomes coarser and also increases as the distance the interface travels becomes greater. The latter property is a concern when the length of the facility being simulated becomes large. When an interface is poorly resolved, the resulting artificial diffusion can lead to nonphysical spikes or valleys near the interface (see Figure 2) and if species concentrations change across the interface, nonphysical mass transfer can occur. Such behavior can pose additional problems if chemical kinetics are being included in the simulation because nonphysical chemical reactions may occur.

Although some numerical algorithms produce less interface smearing than others, all are less than satisfactory without the presence of a fine grid in the region of the interface. However, this increases the mesh size and reduces the time step. Another way to avoid the problem is to track the contact discontinuity and eliminate the interface smearing completely. This approach is particularly well suited to one-dimensional problems because the interface cannot become distorted and so the tracking algorithm can remain relatively simple. Given these observations, a tracking scheme was developed for this work. The scheme utilizes the same TVD method for all of the flowfield except at gas interfaces where a Riemann solver is used. The details of the scheme are given later.

Results using the tracking scheme on the case with a pressure ratio of 10000 are presented in Figure 4 on grids of 200 and 400 points. Also included in the figure is the well resolved 3200 point solution from Figure 3. The solutions obtained with the tracking scheme also utilize initial clustering at the diaphragm since the tracking algorithm does not remove the requirement for high resolution at this location when there are high pressure ratios. As before, the minimum spacing is increased as the solution proceeds. The effectiveness of tracking the contact discontinuity is clearly seen. There is no smearing of the contact discontinuity and both the 200 and 400 point solutions closely match the 3200 point solution without tracking. The points are plotted for the 200 point solution showing that there are no points within the gas interface. The scheme with front tracking required a reduced time step for the first 50 time steps but otherwise was run at the same CFL number.

Not all of the improvement from the interface tracking seen in Figure 4 is due to the removal of numerical diffusion across the contact discontinuity. Some of the improvement is simply due to increased grid resolution at the interface. By moving the mesh with the interface, the initial clustering at the diaphragm follows the interface. Therefore, a side benefit to tracking the contact discontinuity is that it provides an easy way to concentrate grid points where they are needed.

Governing Equations

The fluid dynamic equations for the quasi-one-dimensional Euler equations with chemical and vibrational nonequilibrium and approximations for viscous and heat-conduction losses are written in the following form:

$$\frac{\partial U}{\partial t} + \frac{1}{S}\frac{\partial FS}{\partial x} = W, \tag{1}$$

where the state vector, U, the convective flux vector, F, and the source vector, W, are defined as follows:

$$U = \begin{pmatrix} \rho_1 \\ \rho_2 \\ \vdots \\ \rho_{ns} \\ \rho u \\ E_v \\ E \end{pmatrix} F = \begin{pmatrix} \rho_1 u \\ \rho_2 u \\ \vdots \\ \rho_{ns} u \\ \rho u^2 + p \\ u E_v \\ u(E+p) \end{pmatrix} W = \begin{pmatrix} w_1 \\ w_2 \\ \vdots \\ w_{ns} \\ A + F_{wall} \\ w_v \\ Q_{wall} \end{pmatrix} \tag{2}$$

The variable S represents the cross sectional area of the duct and is a known function of x. The other terms are the density of each species ρ_i with $\rho = \sum_{i=1}^{ns} \rho_i$, the pressure p, the velocity components u and v, the vibrational energy per unit volume E_v, and the total energy per unit volume E. The source terms w_i represent the production or destruction of species i through chemical reactions, and the term w_v is the source term for vibrational energy. The source term A is due to area changes and F_{wall} and Q_{wall} represent the losses in momentum and energy due to viscosity and heat conduction per unit volume, respectively.

The pressure is given by the equation of state for a thermally perfect gas mixture,

$$p = \sum_{i=1}^{ns} \frac{\rho_i}{M_i} RT, \tag{3}$$

where R is the universal gas constant and M_i is the molecular weight of species i. The total energy is written as

$$E = \sum_{i=1}^{ns} \rho c_{v_i} T + E_{v+el} + \frac{1}{2}\rho(u^2 + v^2) + \sum_{i=1}^{ns} \rho_i h_i^\circ, \tag{4}$$

In Equation (4), the first term is the sum of translational and rotational energies per unit volume for each species (c_v is the translational and rotational specific heat). The second term E_{v+el} contains the sum of the vibrational energies for all the species containing vibrational modes plus the sum of the energy in the excited electronic modes. The vibrational and electronic modes are assumed to be in thermal equilibrium at a vibrational-electronic temperature T_v. The vibrational energies are computed assuming harmonic oscillators with corrections for anharmonic effects applied to species that may be present in large mass fractions and have significant anharmonic terms (N_2, O_2, H_2, and H_2O). Electronic modes are included for only O_2, O ,and N. The last two terms in Equation (4) are the kinetic energy and the chemical energy per unit volume. The thermodynamic data are from the JANAF tables.[6]

The vibrational source term w_v is in the form of Landau-Teller relaxation. In this work, very fast relaxation rates are specified so that the gas is essentially in thermal equilibrium (i.e. $T_v = T$) at all times. The source term due to area changes A is written

$$A = \frac{p}{S}\frac{\partial S}{\partial x}.$$

The source term modeling the boundary layer frictional loss F_{wall} is written in the following form

$$F_{wall} = -\frac{4f}{D}\frac{\rho u|u|}{2}$$

where f is a friction coefficient and D is the tube diameter. The rate of heat transfer to the gas from the wall Q_{wall} is given by

$$Q_{wall} = \frac{\alpha}{D}(T_{wall} - T)$$

where T_{wall} is the wall temperature and α is a heat-transfer coefficient. The expressions for F_{wall} and Q_{wall} are very simple and the coefficients in this work are adjusted by making comparisons to experiment for one case and then using those coefficients for all other cases. A more complex treatment of these terms is found in Groth *et al.*.[1] In whatever way these terms are defined, they are still engineering approximations for multi-dimensional phenomena and probably need to be "tuned" for each particular facility that is investigated. The application of these kinds of simple models to flows that have large boundary layers in relation to the tube diameter may not work at all (i.e. a satisfactory model for the low density, high velocity flow in the acceleration section of an expansion tube has not been found for this work).

Chemistry Model

The chemistry mechanism is based on the hydrogen-air combustion mechanism (including the species and reactions within the hydrogen peroxide and NO_x supplements) recommended by the NASP rate committee.[7] The hydrogen species are included for the purpose of simulating facilities with combustion drivers. In addition, helium is included since this light gas is often used in pulse facilities. The complete set includes 14 species (He, N_2, O_2, H_2, NO, OH, NO_2, HNO, HO_2, H_2O, H_2O_2, N, O, H) and 32 reactions, each of which may proceed forward or backward. Helium is added as an inert species with a third body efficiency in termolecular reactions of 1.0. An air reaction mechanism is obtained by setting the species containing hydrogen to negligible levels.

The equilibrium constants for each of the reactions are calculated from standard Gibbs free energy for each species which, in turn, are obtained from the NASA Lewis polynomials for thermochemical data found in Appendix 2 of the NASP rate committee report. These polynomials are valid from 200 to 6000 K.

Plots extrapolated to 7000 K show that the polynomials are still well behaved out to this temperature; however, curve fits to higher temperatures are necessary. Note that these curve fits are used only for computing the equilibrium constants for the purpose of finding backward rate constants. Internal energy values do not rely on these curves, instead they are computed in the manner explained in the previous section.

Numerical Method

The gas dynamic equations are solved by using an explicit finite-volume form of the Harten-Yee upwind TVD scheme[4] which gives second-order spatial and temporal accuracy. Tracking of gas interfaces and a moving grid are incorporated for the reasons described in the section on numerical difficulties. The combined TVD/tracking scheme is relatively straightforward. The upwind TVD algorithm is used to calculate the flux across all of the interior cell sides except for at gas interfaces where a Riemann solver is applied (see Figure 5). Tracking other features such as shocks is not necessary because modern flux-splitting or flux-differencing methods capture these features quite well. The Riemann solver provides the local fluid velocity at an interface so that the cell side associated with the interface can be moved with it (i.e. it is tracked). As the interface moves, all the other points in the computational domain are moved in an organized way so that a distributed mesh is retained. Several minor changes are required to the TVD algorithm to account for changes in the inviscid flux due to the motion of the grid. Note that with the approach just outlined, a contact discontinuity behaves as any other interior part of the simulation (i.e. waves are allowed to pass through the interfaces).

Because it is prescribed that there is no mass flux across an interface, only two quantities need to be calculated by the Riemann solver. These two quantities are the local fluid velocity and the local static pressure. The inviscid flux vector at the contact discontinuity F_{cd} is written:

$$F_{cd} = (0, 0, \ldots, 0, p^*, 0, p^* u^*) \tag{5}$$

where p^* and u^* are supplied by the Riemann solver and the cell side is translated at the velocity u^*. These two quantities are generally the first two quantities computed by such a solver and only constitute a fraction of the computational work usually associated with such a solver. Therefore, there is little, if any, increase in cost introduced by the interface tracking.

The procedure for the Riemann solver to obtain u^* and p^* was taken from Jacobs[8] and generalized for a multicomponent mixture. A MUSCL interpolation is used to achieve a higher order spatial accuracy. A modification is made in the TVD scheme for the cell sides adjacent to a gas interface so that the computational stencil does not cross the interface. The effect of the Riemann solver, which is first-order in time, on temporal accuracy has not been formally established. No noticeable change in accuracy has been observed by incorporating it with the second-order upwind TVD algorithm. Tests of temporal accuracy were made by comparing solutions with and without tracking at various CFL numbers.

The motion of the computational mesh is dictated by both the motion of gas interfaces and the requirement to have very fine grid initial spacing at diaphragm locations. Because interfaces are tracked, cells initially associated with a region of gas (such as the driver or driven gas) remain associated with that region. Therefore, when the driven section is compressed by the incident shock, the cells become compressed too. This has the positive result of producing a fine mesh at the reservoir region of a shock tube or shock tunnel. However, in some cases, the grid spacing can become so small (and the time step so small) that the solution becomes very expensive. In such cases, the difficulty can be avoided by turning off the tracking and the grid motion (reverting to the TVD scheme on a fixed grid for all cells) when a reasonably fine grid has been created. In this way, the driven section grid is allowed to become fine enough to satisfactorily "capture" any gas interfaces but not so fine as to make the time step unpractical.

The source term due to the area change is treated in an explicit manner, however, the source terms representing the finite-rate chemical kinetics and vibrational relaxation are often large and make the algorithm too stiff to be advanced explicitly. To avoid this stiffness, a fully-coupled point-implicit treatment of these source terms is implemented. The extra cost of inverting a singe block matrix at each cell is more than offset by the increase in the size of the time step that this allows.

Shock Tube Simulation

The first pulse facility considered is the NASA Ames electric-arc driven shock tube facility.[9,10] This facility has several different configurations and has a large hypervelocity operating range using its arc-driver; however, in this work, several shots using a cold helium driver with nitrogen in the driven section are simulated. These shots were made with a cylindrical driver of .76 m (2.5 feet) in length and 10 cm (3.93 inches) in diameter. The driven section was 4.02 m (13.17 feet) long with the same diameter as the driver. A single self-break diaphragm separated the driver and driven gases.

Three different run conditions are simulated. All of the shots had a nominal 3.96 MPa (575 psi) cold helium driver. The initial nitrogen driven pressures were different for each shot. Driven tube pressures of 300 torr, 100 torr, and 20 torr were used which resulted in incident shock speeds of approximately 1250 m/sec, 1550 m/sec, and 1950 m/sec, respectively. The initial conditions prescribed for the simulations were the same with the additional specification of a driver and driven tube temperature of 300 K (the experimental driver pressure was not known). The temperatures behind the reflected shock range between 1400-4500 K, so the vibrational excitation and dissociation of the nitrogen driven gas is important. Figure 6a-c shows experimental and computed sidewall pressure traces 2.5 cm upstream of the driven section endwall. Each of the plots has the same scaling so that the relative changes caused by the different driven tube pressures can be easily identified. The source terms for viscosity or heat conduction were turned off to demonstrate what kind of results can be expected from purely inviscid one-dimensional flow. Each of the simulations used 350 points (half in the driver and half in the driven section) and required approximately 5 minutes of CPU time on a single processor on the NASA Ames Cray Y-MP.

Several of the major events are labeled in the Figure 6. These include the passage of the incident and reflected shocks, the arrival of the rarefaction wave (which has reflected off the opposite end of the facility), and the presence of reflected waves off the contact discontinuity. Agreement between the experiments and the computations is relatively good. Certainly, the general changes in the pressure traces due to reflected-shock/contact-discontinuity interaction (in off-tailored conditions) are captured for all three cases. As expected, the experimentally measured features associated with the the contact discontinuity (such as waves which have interacted with it) are smeared because the interface is non-planar and diffuse while the same features in the simulations are sharp because the interface is tracked. The position of the pressure transducer within the boundary layers further contributes to the smearing of the experimentally observed features. Shock/boundary-layer interaction of the reflected shock is large and the one-dimensional formulation cannot capture such effects. The overshoot just after the arrival of the reflected shock is from the lambda shock formed at the foot of the reflected shock (see Figures 6b,c). The 20 torr driven case is expected to be influenced most by boundary layer effects because the shock speeds are highest and the density is the lowest. This is the case in which the largest differences are seen between the experiment and the computation.

As an aid to understand the features seen in the pressure traces, a computed x-t diagram of density contours for the 20 torr case is presented in Figure 7. Note that a vertical line of data from this plot yields a trace at a given location. Included in the figure is an enlargement of the driven section endwall. The enlargement shows the reflected shock being partially transmitted through the contact discontinuity and partially reflected back toward the endwall. This occurs several times and each successive interaction further slows the interface down until it is brought to rest. This type of off-tailored interaction (with reflected shocks) is referred to as an overdriven case.

Shock Tunnel Simulation

The next facility considered is NASA Ames 16-inch combustion-driven shock tunnel.[11,12] In a shock tunnel the high-pressure, high-temperature region of stagnated gas (created at the end of a shock tube by the reflection of the incident shock) is expanded through a nozzle to obtain supersonic/hypersonic flow. Figure 8 contains a schematic of the facility. The driver and driven tubes are 21.3 m (70 feet) and 25.9 m (85 feet), respectively. The inside diameter of the driver tube is 43.18 cm (17 inches) and the inside diameter of the driven tube is 30.48 cm (12 inches). The name of the tunnel is derived from the 16-inch naval guns which were used to construct the driver. The nozzle is 5.9 m (19.35 feet) in length and the Mach number at the nozzle exit varies between 5 and 7.

The driver tube is operated by burning a mixture of hydrogen and oxygen with helium or nitrogen added as a diluent. The mixture is ignited by heating thin wires strung down the length of the driver with a voltage discharge from a capacitor bank. Post-burn pressures are typically between 300 and 600 atm. A single self-break diaphragm is used which is designed to rupture near the peak of the pressure rise. The driven section is usually filled with air between 100 and 300 torr which provides incident shock speeds around 3 km/sec. The high pressure and temperature reservoir created when this shock reflects off the endwall lasts for 10-30 msec and can produce 2-10 msec of uncontaminated flow depending on the conditions.

The simulations presented for this facility will concentrate on the effect that the driver conditions can have on the reservoir. Many combustion driven pulse facilities have found that it is very difficult to experimentally produce uniform burning of the mixture which then causes non-uniform post-burn driver conditions.[13] Sometimes these non-uniformities can be severe; however, a burning procedure has been developed for the NASA Ames shock tunnel that produces only mild pressure oscillations (10-15% of the post-burn pressure) that are reproducible in amplitude and phase from shot to shot.

Figure 9 shows pressure traces from a relatively low pressure condition in which the diaphragm was purposely kept from breaking (i.e. a closed driver shot). The traces correspond to the three pressure transducer locations in the driver depicted in Figure 8 (DR1, DR2, and DR3). They all show a pressure rise due to combustion over the first 20 ms followed by oscillations at the post-burn pressure. The traces reveal that when the pressure reaches a maximum at one end of the tube, it is at a minimum at the other end. The pressure in the center of the driver remains fairly constant. This type of behavior is caused by the driver gas translating in one direction down the tube, coming to a rest, and then translating back again.

The pressure traces in the closed driver experiment were used to find an approximate model for the flow in the driver. It was found that at the point in time when the diaphragm region (DR3) experiences a pressure maximum, that the driver flowfield can be modeled by a sinusoidal pressure and density distribution (with a constant temperature) superimposed on the average post-burn conditions as plotted in Figure 10. The fluid is assumed to be at rest throughout the driver at this point and the amplitude of the sine wave is deduced from the experiments. Using the approximate flowfield shown in Figure 10 as initial conditions for a closed driver simulation results in the pressure traces shown in Figure 11. These computed traces have good qualitative agreement with the experimental traces shown in Figure 8. The pressure waves steepen with time and the middle trace has twice the frequency of the end traces.

Having established some of the qualities of the driver, the conditions and results for an particular shot are presented. The case of interest used a pre-burn driver mixture of

$$2H_2 + 1.17O_2 + 9.36He$$

at a pressure and temperature of 740 psi and 300 K. The driven section was filled with air at 220 torr. Although the pre-burn conditions are well known, the simulations require the post-burn pressure, temperature, and species mass fractions as the initial conditions. Obtaining these conditions by simulating the time dependent ignition and combustion of the mixture is a multi-dimensional problem beyond the capabilities of a one dimensional formulation. Therefore, post-burn equilibrium conditions corresponding to the pre-burn mixture are found using a code called STANJAN.[14] By this method, the ideal post-burn pressure and temperature for the mixture above are 430 atm (6300 psi) and 2690 K. As a correction to the ideal conditions, a pressure and temperature of 90% of these values were used in the simulation. This particular loss value has been found to work well over a wide range of facility operating conditions and accounts for losses due to phenomena such as heat-conduction during the 20 ms burning process, lateral waves, and energy absorbed by the diaphragm rupture.

Figure 12a,b show experimental and computed pressure traces at locations just upstream of the diaphragm (DR3) and next to the driven tube endwall (DN5). The figure includes one simulation that began with a uniform driver and one that began with the sinusoidal pressure distribution shown in Figure 10. This initial sinusoidal pressure distribution with a maximum occurring at the diaphragm location when the diaphragm ruptures was deduced from the experimental traces which show that this is almost always the case (it is logical that the diaphragm breaks while experiencing a pressure peak). The time basis for the simulations and the experiment were aligned by placing the start of the simulation at the pressure drop corresponding to the diaphragm rupture at DR3 (at approx. 29 ms).

It can be seen that the initial conditions that include the driver pressure gradients give a much better overall agreement with the experiment and reveal how the driver pressure oscillations effect the pressure in the reservoir. Such a finding would be difficult without a simulation of the whole facility.

The sharp drop and then rise in pressure seen at DR3 immediately after the diaphragm break is due to the rapid area change between the driver and driven tube (the area changes by almost a factor of 2). The drop exists in both the experimental and simulated traces but is much larger in the computations. The large differences between the experiment and simulations may exist in the diaphragm region because of two dimensional and viscous effects caused by the area change. It was found that having rapid area changes increased the required number of grid points for a smooth solution. These simulations used 600 points and required approximately 40 minutes of CPU time on the NASA Ames Cray Y-MP. Solutions with 1200 points gave nearly the same results.

The viscous coefficient was set so that the simulations would duplicate the attenuation of the incident shock as measured by pressure transducers located down the length of the driven tube. It was found that a single value of this coefficient was adequate for a variety of facility operating conditions. The coefficient for heat loss was set so that closed driver simulations would predict a pressure loss over time similar to that observed in experiments (see Figure 9). Only one value of the heat-conduction coefficient was used for a variety of conditions. With the heat-conduction coefficient set in this way, the simulations showed that heat-conduction was not a relatively important aspect of the modeling for this particular facility.

Results for the nozzle region of the facility are not included, except for a few comments, because of space constraints. Including the nozzle region of the facility is simply done by including the area changes associated with the nozzle. Corrections to the nozzle geometry must be included to account for the effect of the large boundary layers in the nozzle.

Expansion Tube Simulation

A unique feature of the expansion tube among different types of pulse facilities is that it theoretically avoids stagnating the flow within the facility and, therefore, avoids any excitation and dissociation of the test gas. If this can be done, experimental conditions matching the freestream conditions seen by a flight vehicle can be produced.[15] Figure 13 depicts the components and ideal operating sequence (using an x-t diagram) of the HYPULSE expansion tube which was previously the NASA Langley expansion tube.[16,17] It is composed of the following three sections: a driver, an intermediate section (containing the test gas), and an acceleration section. For the particular case considered here, the driver was 2.44 m (8.01 feet) in length, the intermediate section was 7.49 m (24.57 feet), and the acceleration tube was 14.62 m (47.96 feet). The diameter of the driver is 16.51 cm (6.5 inches) and the diameter of the intermediate and acceleration sections is 15.24 cm (6 inches). The facility is driven by compressed helium, and the gas mixtures and pressures in the intermediate and acceleration tube are varied to achieve the prescribed test conditions. Typical test times are from 200 to 600 microseconds.

As in the previous facilities, the operation of the expansion tube begins by rupturing a diaphragm (in this facility a double diaphragm) separating the driver gas from the test gas. An incident shock wave travels into the test gas, compressing it. At the end of the intermediate tube, a secondary diaphragm is encountered and is ruptured. This creates a second incident shock and a second expansion both of which travel down the acceleration tube. The secondary expansion is propagating upstream into the test gas but is convected downstream in the supersonic flow. The unsteady expansion of the test gas creates the high velocity test conditions. Data is taken at the end of the acceleration tube in the gas between the secondary contact discontinuity and the tail of the secondary expansion. In this ideal operating sequence, no stagnation regions are created and, thus, there are no high-temperatures to dissociate the test gas.

Several numerical simulations are presented for the HYPULSE facility at a single operating condition. One simulation is for the ideal operating conditions as explained above and the others investigate the effects of a delayed opening of the secondary diaphragm. This latter situation is studied because there is clear evidence from the pressure transducers positioned near the secondary diaphragm that the diaphragm does not open instantaneously. Several works have studied the effect of the finite opening time on test flow properties such as wall pressure, pitot pressure, and velocity.[16,18] However, the effect of this behavior on the flow quality with regard to species concentrations has not been studied in detail. A delay in the diaphragm opening causes the primary shock to reflect off the diaphragm and create a small stagnation region of hot gas in the intermediate tube (the test gas). This will produce dissociation of the test gas which could impact the quality of the flow. The finite-rate chemistry capability in the present code allows the amount of dissociated species in the test flow created from such non-ideal behavior to be estimated. The finite opening time of the diaphragm is simulated by noting the time of arrival of the primary shock at the secondary diaphragm and then instantaneously removing the diaphragm when a specified time has elapsed (i.e. 10 microseconds). No viscous or heat-conduction source terms are included because the validity of these terms is questionable for the high speed, low density flow in the acceleration tube. Some indication of the character and size of the viscous phenomena which occur inside the acceleration tube is shown in the axisymmetric computations of Jacobs[19] who simulated the HYPULSE facility using a perfect gas code.

For the particular HYPULSE conditions of interest here, the driver was filled with unheated helium and both the intermediate and acceleration section contained air. The reported initial driver pressure was 37.9 MPa (5500 psi), the intermediate section pressure was 3426 Pa (.497 psi), and the acceleration section pressure was 7.2 Pa (.001 psi). These same values were used in the simulations. The initial temperatures used in the simulations were 380K, 292K, and 292K for the driver, intermediate, and acceleration sections, respectively. The temperature of the driver was not measured in the experiments but is known to be somewhat higher than room temperature because of Joule-Thomson and compression heating.[16] A driver temperature of 380K was adopted because this temperature produced primary shock speeds in the intermediate tube that were close to those measured in the experiment.

Figure 14 contains an x-t diagram of the logarithm of density for the flow within the expansion tube with a 10 microsecond opening time for the secondary diaphragm. This flow can be compared to the ideal x-t diagram in Figure 13. The enlargement of the secondary diaphragm region depicts the incident shock reflected by the rigid diaphragm and shows that the reflected shock is very quickly weakened by the secondary rarefaction after the diaphragm is removed. However, as seen in the full scale diagram, the reflected shock is still able to cause a significant disturbance when it reaches the primary interface. Part of the wave is transmitted through the interface and part is reflected in the form of the shock. This kind of interaction is observed and computed in Miller and Shinn.[18]

Figure 15 contains a experimental wall pressure trace for the conditions mentioned above.[20] Figure 16 contains computed pressure traces at the test section for the ideal case with no delay in the opening of the secondary diaphragm, a case with a 10 microsecond delay, and a case with a 25 microsecond delay. The computed pressure values are slightly higher than the experimental values which is expected since no viscous correction (no shock attenuation) is included in the simulation. All of the computations give similar pressure traces except for the presence of a shock that has reflected off the primary interface for the 25 microsecond case. For longer opening times (not shown), this reflected shock overtakes the test flow and effects the test time. These results match the experimental observations of Miller and Shinn[18] which were made by increasing the secondary diaphragm thickness to experimentally increase the opening time. In their work, the wall pressures were not greatly effected by the diaphragm thickness, but others quantities such as pitot pressure did change.

A further validation of the computations is made by comparing experimental[21] and simulated pressure traces from a location 3 inches downstream of the secondary diaphragm found in Figures 17 and 18, respectively. The pressure spike in Figure 17 which occurs just after the passage of the secondary shock is caused by the finite diaphragm opening. Note that computed trace with an instantaneous diaphragm opening has no pressure spike. Similar experimental plots for different gases and diaphragm thicknesses are found in Miller.[16] As the diaphragm opening time is increased, the size of the disturbance increases. Even with the very simple model for the opening time used in this work, the qualitative features of the disturbance compare well with the experiments. A quantitative comparison of the magnitude and the length of time of the disturbance can be used to estimate the size of an "equivalent opening time" using the current model. In this way, the typical opening time present in the experiments appears to be between 10 and 25 microseconds.

Figure 19 contains traces of O mass fractions from the simulations. The large amount of monatomic oxygen immediately behind the secondary shock is caused by the very high acceleration gas temperature behind the secondary shock. The region of the test gas is behind the secondary interface and is labeled in the figure. For the ideal case there is very little dissociation, as expected. However, for both the 10 and 25 microsecond opening times there is a significant amount of dissociation in the test gas. The computed traces of NO mass fractions, which are not shown here, show that this molecule is present in significant amounts, as well.

The high mass fractions of dissociated species in the test flow originate at the secondary diaphragm from dissociation behind the reflected primary shock. The high temperatures and pressures behind the reflected shock bring the gas to the equilibrium conditions almost immediately. These high mass fractions persist until the test region because the secondary expansion freezes the chemical composition before full recombination can occur. The simulations indicate that because the expanded test flow originates from gas immediately adjacent to the secondary diaphragm, the area affected by a reflected shock does not have to be large to significantly impact the test conditions provided by the facility.

The computations presented here were calculated with a mesh of 1400 points. Nearly identical results were obtained with 700 point and 2800 point grids. Solution times for the 1400 point mesh were approximately 20 minutes on the NASA Ames Cray Y-MP.

It is recognized that much more could be said about the expansion tube simulations and better modeling could be made in several areas: a more sophisticated diaphragm opening model could be used (the rupture process is surely a multi-dimensional phenomenon), boundary layer effects could be taken into account, and finite-rate vibrational relaxation could be incorporated. However, the current results agree with experiments closely enough to suggest that significant concentrations of dissociated species may be created in the test gas for even relatively small finite opening times of the secondary diaphragm and suggest that further investigations should be carried out.

Conclusion

A quasi-one-dimensional methodology for numerically simulating the flow inside high enthalpy pulse facilities was presented. The numerical formulation solves the Euler equations with 14 species equations with fully-coupled finite-rate chemistry. A moving mesh and tracking of gas interfaces were included to overcome some of the numerical difficulties associated with these types of flows. The value of simulating the flow inside a complete facility using the current numerical approach was demonstrated by computing the flows through three different types of pulse facilities. A simulation of a helium driven shock tube showed that computations can be used to predict the off-tailored behavior of shock tubes and tunnels. Computations of the flow through the NASA Ames 16-Inch combustion driven shock tunnel showed the influence of non-uniformities in the driver section on the reservoir conditions. Finally, the effect of finite secondary diaphragm opening times on the chemical composition of the test flow in the HYPULSE expansion tube were investigated.

Acknowledgements

Support was provided by a grant from NASA to Eloret Institute (NCC2-420). Computer time was provided by the NAS Facility and by the Central Computing Facility at NASA Ames Research Center. The author also gratefully acknowledges the cooperation, insight and data provided by Dr. Surrendra Sharma and Walter Gillespie for the NASA Ames arc-driven shock tube, Dr. Mark Loomis, Dr. David Bagdanoff, and Dr. John Cavolowski for the NASA Ames 16-Inch shock tunnel, and Oussama Rizkalla for the GASL expansion tube. The author also thanks Dr. Chul Park and Myles Sussman for their valuable input.

References

[1] Groth, C. P. T., Gottlieb, J. J., and Sullivan, P. A.,"Numerical Investigation of High-Temperature Effects in the UTIAS-RPI hypersonic Impulse Tunnel," *Can. Journal of Physics*, Vol. 69, pp 897-918, 1991.

[2] Maus, J., Laster, M., and Hornung, H.,"The G-Range Impulse Facility A High-Performance Free-Piston Shock Tunnel," AIAA-92-3946, July 1992.

[3] Sod, G. A.,"A Survey of Several Finite Difference Methods for Systems of Nonlinear Hyperbolic Conservation Equations," *Journal of Computational Physics*, Vol. 27, pp. 1-31, 1978.

[4] Yee, H.C.,"A Class of High-Resolution Explicit and Implicit Shock-Capturing Methods," NASA TM 101088, February, 1989.

[5]Harten, A. and Hyman, J. M.,"Self-Adjusting Grid Methods for One-Dimensional Hyperbolic Conservation Laws," *Journal of Computational Physics*, Vol. 50, pp 235-269, 1983.

[6]"JANAF Thermochemical Tables," *Journal of Chemistry Reference Data*, Vol. 14, Suppl. 1, 1985.

[7]NASP Rate Constant Committee, "Hypersonic Combustion Kinetics," NASP TM-1107, May 1990.

[8]Jacobs, P. A.,"Single-Block Navier-Stokes Integrator," NASA Contract No. NAS1-18605, July 1991.

[9]Sharma, S. P. and Park C.,"Operating Characteristics of a 60- and 10 cm Electric Arc-Driven Shock Tube - Part 1: The Driver," *Journal of Thermophysics and Heat Transfer*, Vol. 4, No. 3, pp. 259-265, 1990.

[10]Sharma, S. P. and Park C.,"Operating Characteristics of a 60- and 10 cm Electric Arc-Driven Shock Tube - Part 2: The Driven Section," *Journal of Thermophysics and Heat Transfer*, Vol. 4, No. 3, pp. 266-272 , 1990.

[11]Bogdanoff, D.W., Zambrana, H. A., Cavolowsky, J. A., Newfield, M. E., Cornelison, C. J., and Miller, R. J.,"Reactivation and Upgrade of the NASA Ames 16 Inch Shock Tunnel," AIAA Paper 92-0327, January, 1992.

[12]Cavolowsky, J. A., Loomis, M. P., Bogdanoff, D.W., Zambrana, H. A., Newfield, M. E., and Tam, T. C.,"Flow Characterization in the NASA Ames 16-Inch Shock Tunnel," AIAA Paper 92-3810, July, 1992.

[13]Belanger, J. and Hornung, H. G.,"A Combustion Driven Shock Tunnel to Complement the Free Piston Shock Tunnel TAIAA Paper 92-3968, July, 1992.

[14] STANJAN Chemical Equilibrium Solver, (c) Stanford University. v3.90 IBM-PC.

[15]Trimpi, R. L.,"A Preliminary Theoretical Study of the Expansion Tube, A New Device for Producing High-Enthalpy Short-Duration Hypersonic Gas Flows," NASA TR R-133, 1962.

[16]Miller, C. G.,"Operational Experience in the Langley Expansion Tube With Various Test Gases," NASA TM 78637, Dec. 1977.

[17]Tamagno, J., Bakos, R., Pulsonetti, M., and Erdos, J.,"Hypervelocity Real Gas Capabilities of GASL's Expansion Tube (HYPULSE) Facility," AIAA Paper 90-1390, June, 1990.

[18]Shinn, J. L. and Miller, C. G.,"Experimental Perfect-Gas Study of Exapansion-Tube Flow Characteristics," NASA TP 1317, 1978.

[19]Jacobs, P. A.,"Numerical Simulation of Transient Hypervelocity Flow in an Expansion Tube," NASA CR 189615 (also ICASE Report 92-10).

[20]Calleja, J. and Tamagno, J.,"Calibration of HYPULSE for Hypervelocity Air Flows Corresponding to Flight Mach Numbers 13.5, 15, and 17" General Applied Science Laboratories, Inc., TR 335, February, 1992.

[21]Rizkalla, O.,GASL, Private Communication, October, 1992.

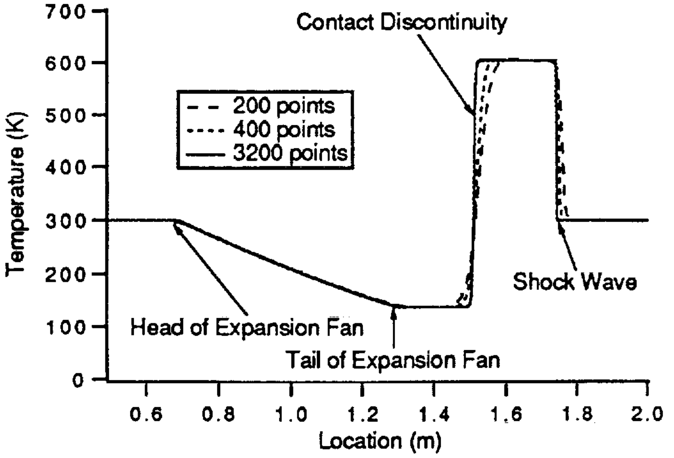

Fig. 1 Shock tube temperature profile; initial pressure ratio= 10, equally-spaced grid.

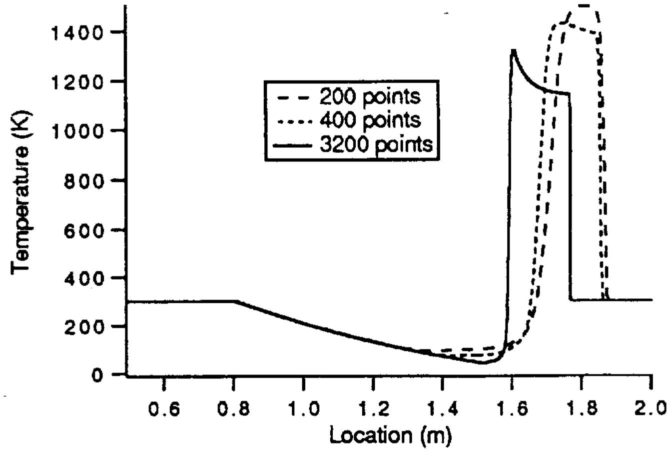

Fig. 2 Shock tube temperature profile; initial pressure ratio= 10,000, equally-spaced grid.

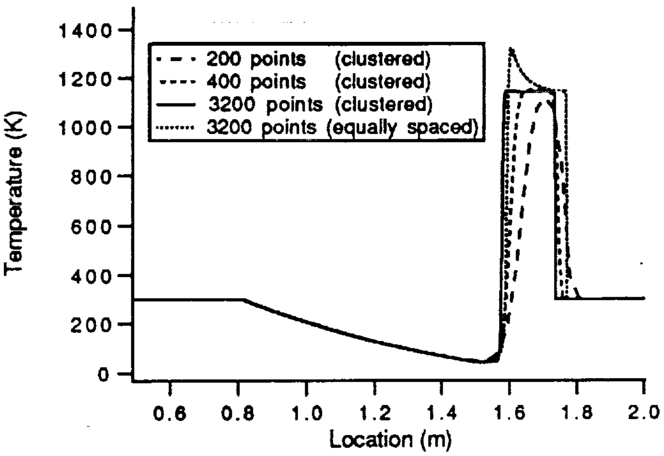

Fig. 3 Shock tube temperature profile; inital pressure ratio= 10,000, initial grid clustering.

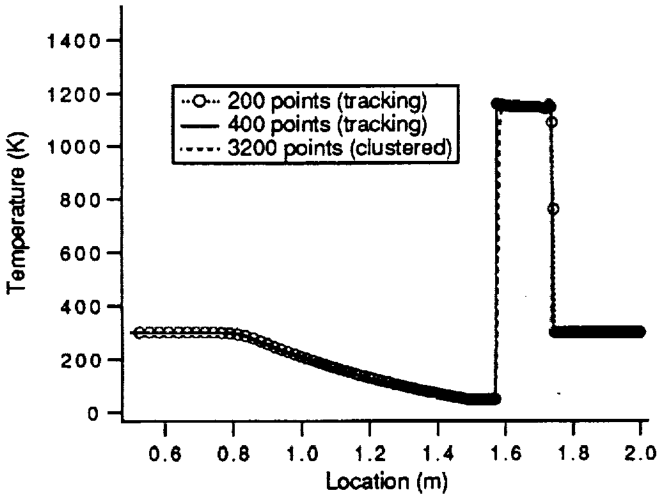

Fig. 4 Shock tube temperature profile; inital pressure ratio= 10,000, tracking and initial grid clustering.

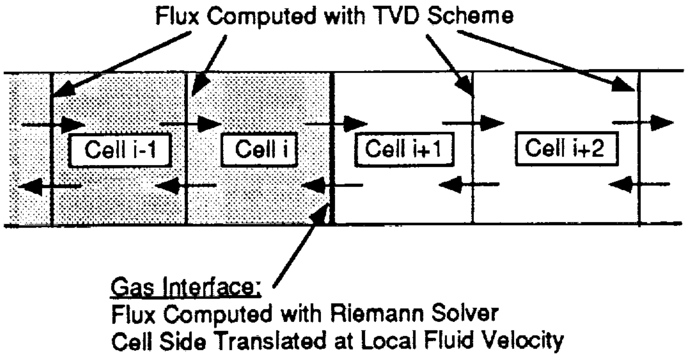

Fig. 5 Schematic of finite volume cells near a gas interface to illustrate the inviscid flux calculations.

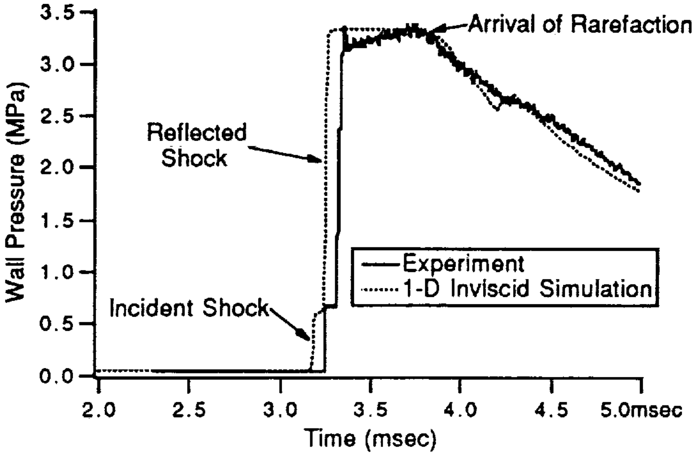

Fig. 6a Pressure trace comparison between experiment and computation for 300 torr case.

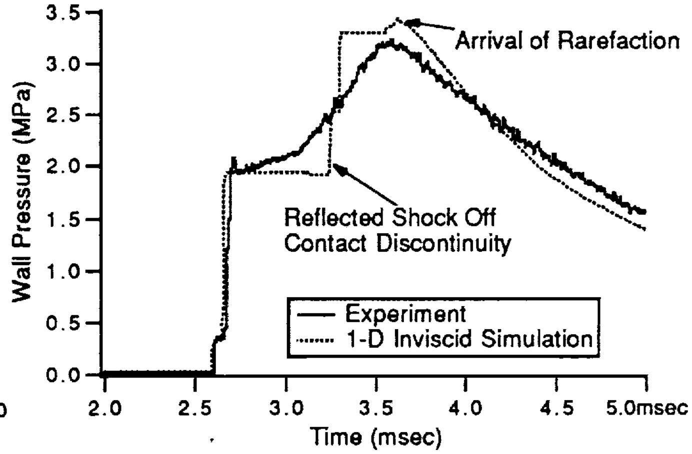

Fig. 6b Pressure trace comparison between experiment and computation for 100 torr case.

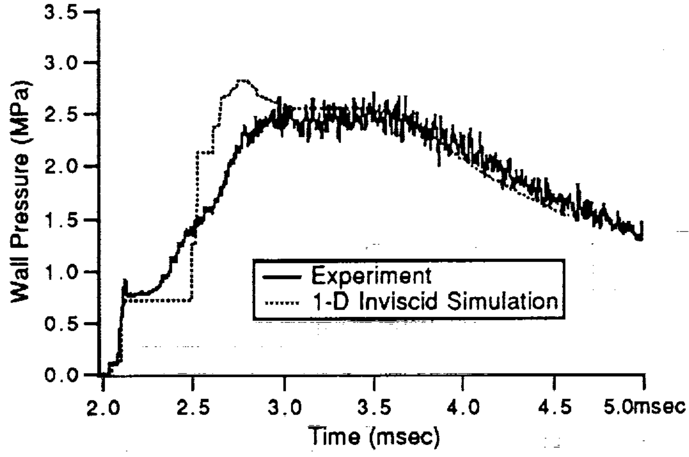

Fig. 6c Pressure trace comparison between experiment and computation for 20 torr case.

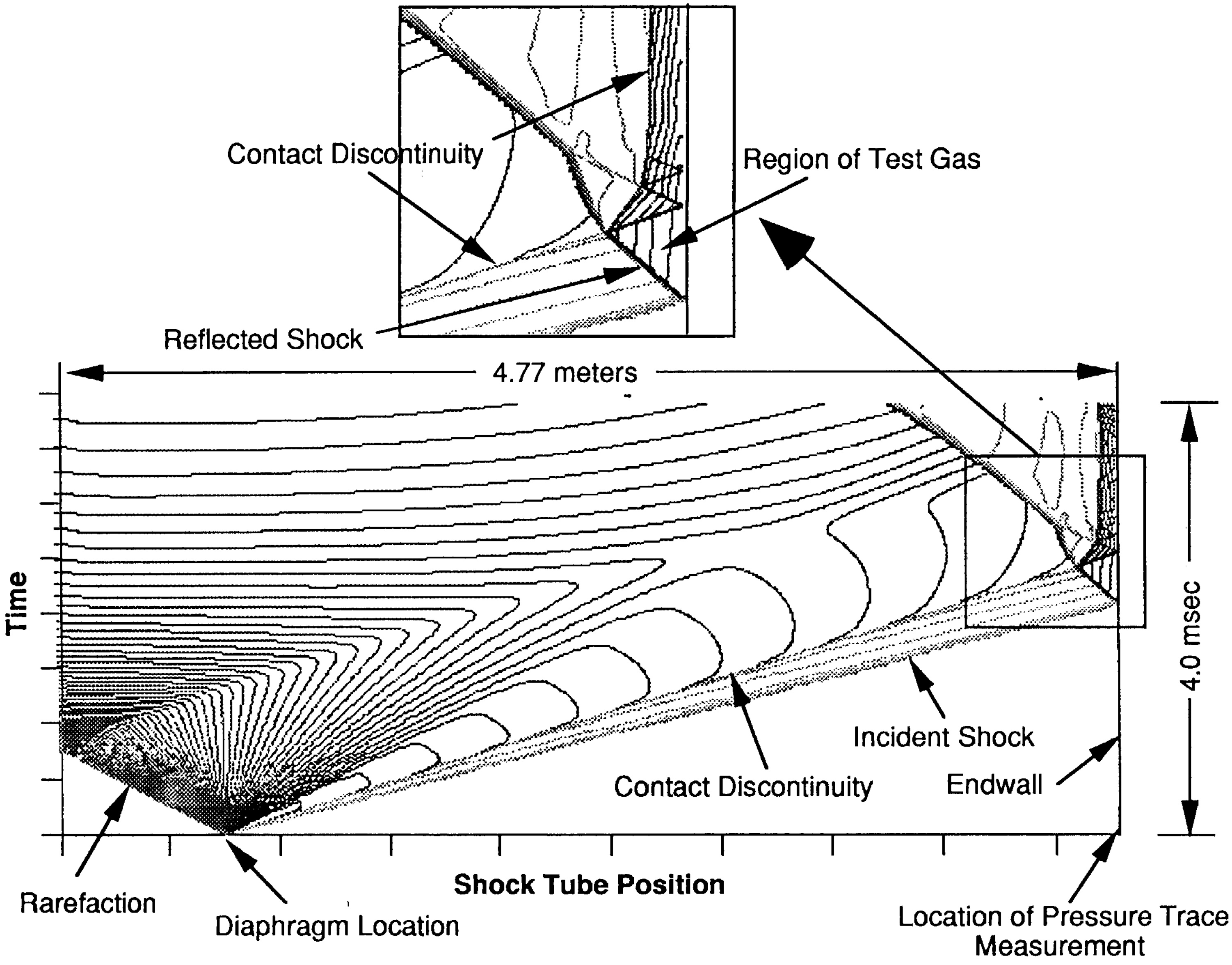

Figure 7: Computed x-t diagram of temperature contours for the 20 Torr driven case.

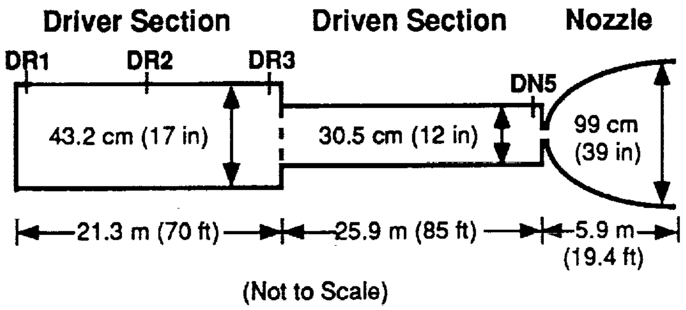

Fig. 8 Schematic of the NASA Ames 16-Inch Shock Tunnel.

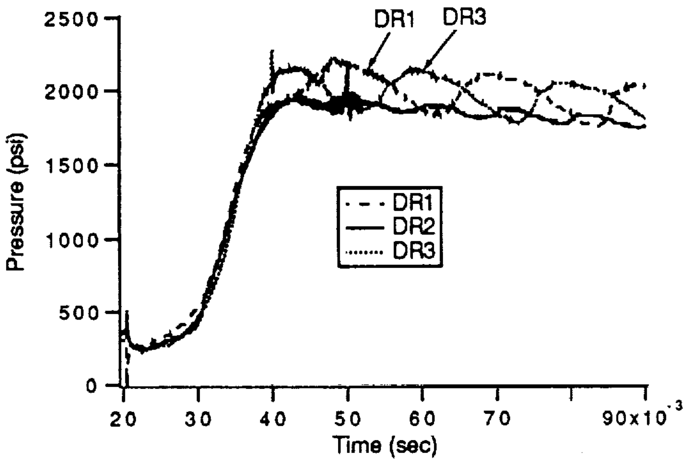

Fig. 9 Experimental pressure traces for a closed driver shot.

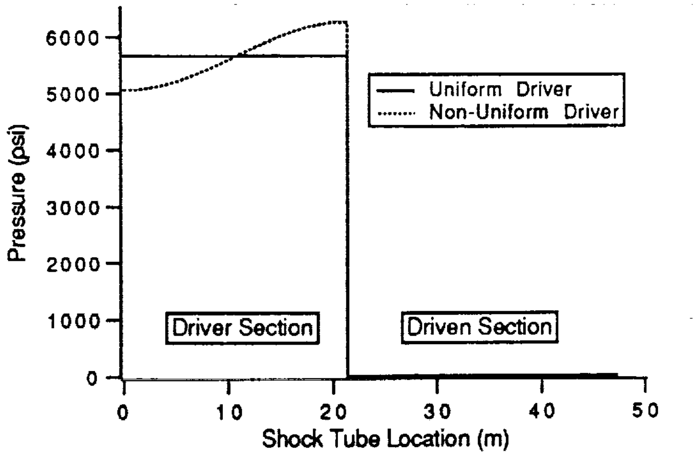

Fig. 10 Inital pressure distribution with a uniform and a non-uniform driver.

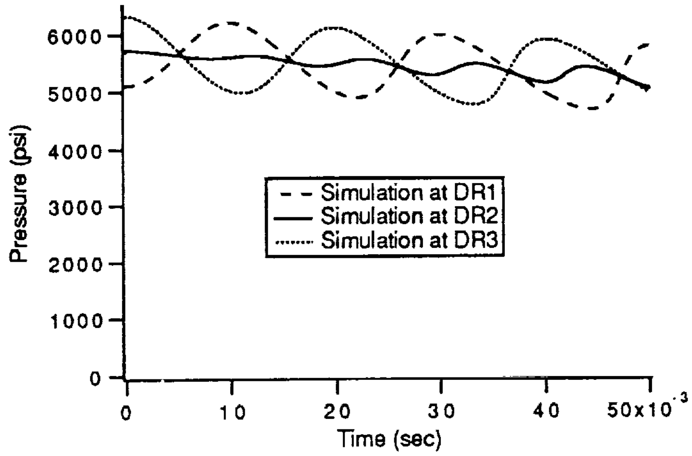

Fig. 11 Computed pressure traces for a closed driver shot with inital driver pressure gradients

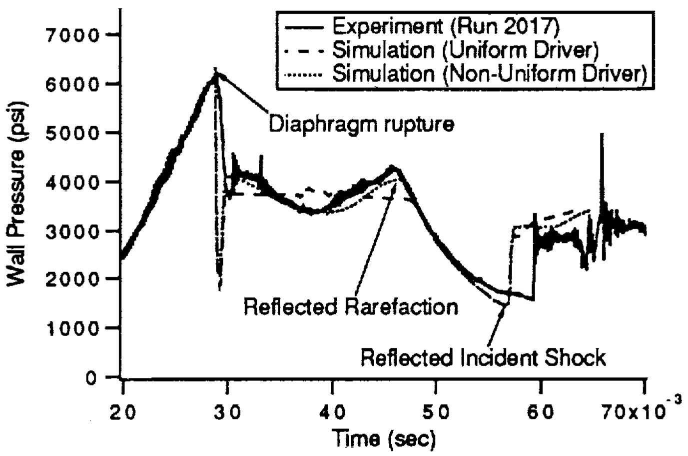

Fig. 12 Comparison of experimental and computed pressure traces at DR3 (near diaphragm).

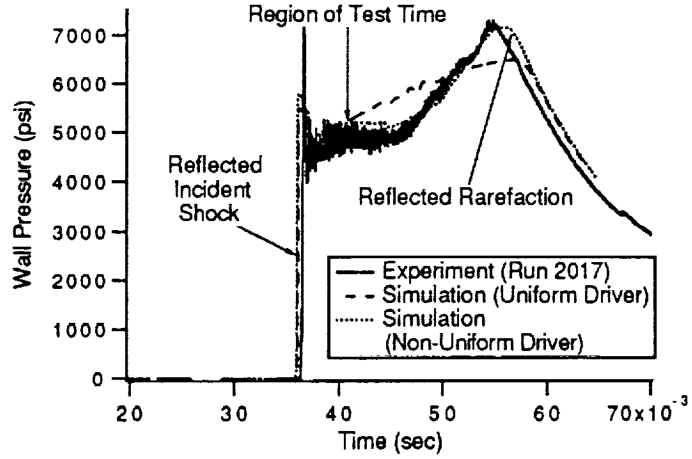

Fig. 13 Comparison of experimental and computed pressure traces at DN5 (near driven section endwall).

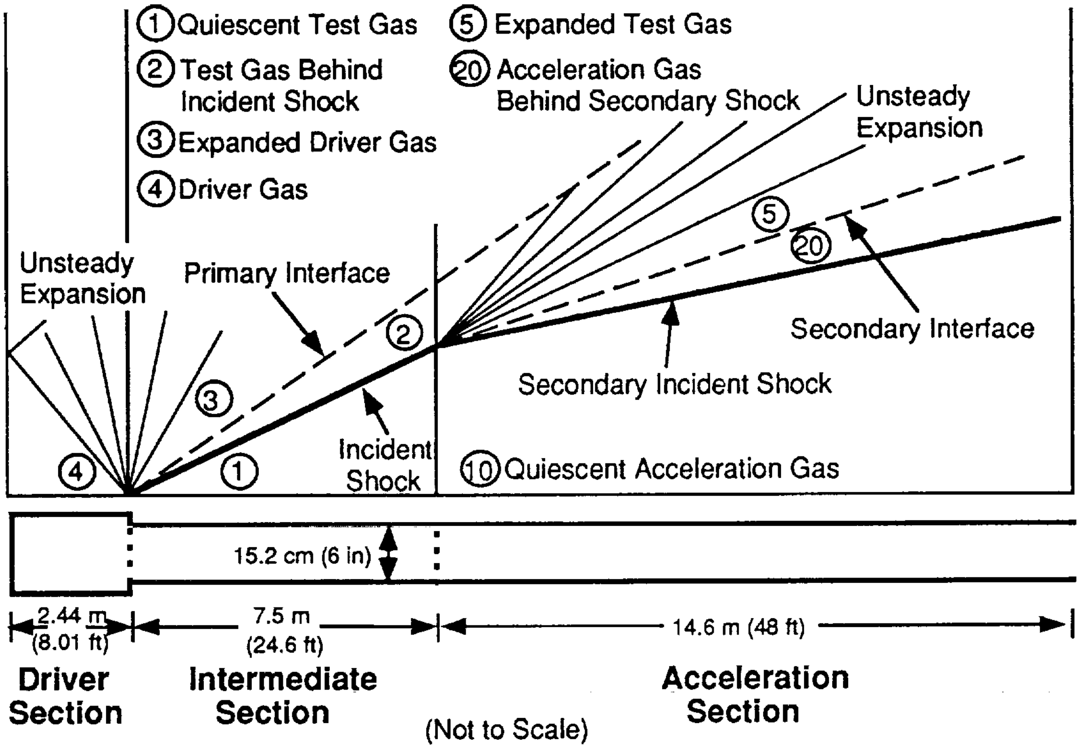

Figure 13: HYPULSE Expansion Tube.

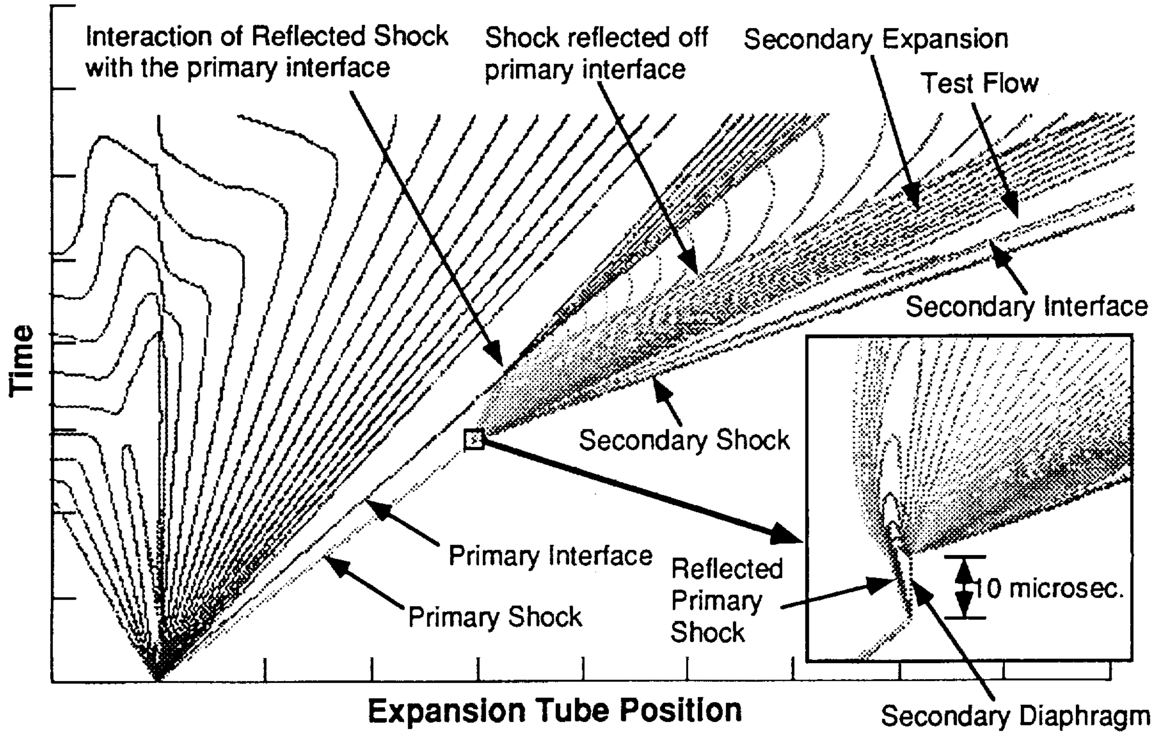

Figure 14: Computed x-t diagragm of the logarithm of density for the Mach 17 HYPULSE conditions with a 10 microsecond delay of the secondary diaphragm.

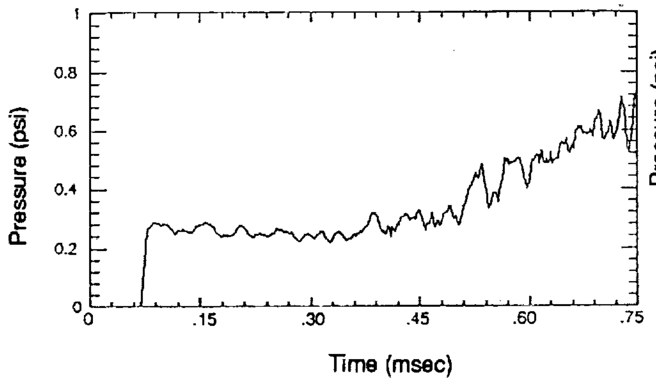

Fig. 15 Experimental expansion tube pressure trace at the test position.

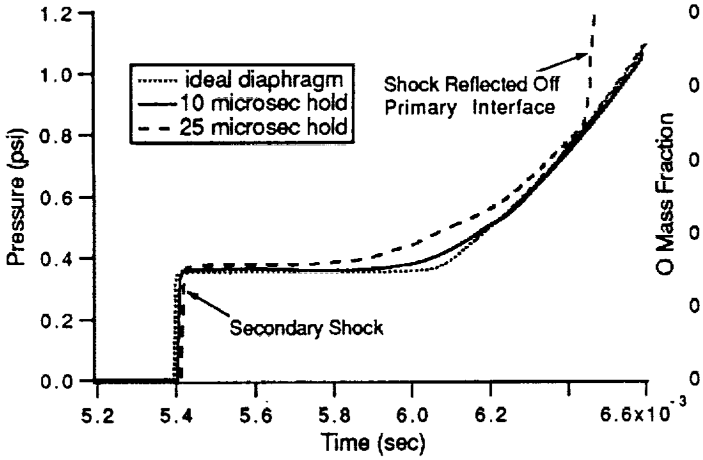

Fig. 16 Computed expansion tube pressure traces at the test location.

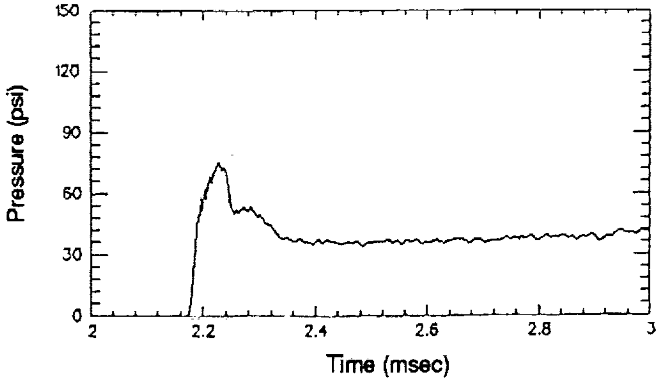

Fig. 17 Experimental pressure trace 3.0 inches downstream of the secondary diaphragm.

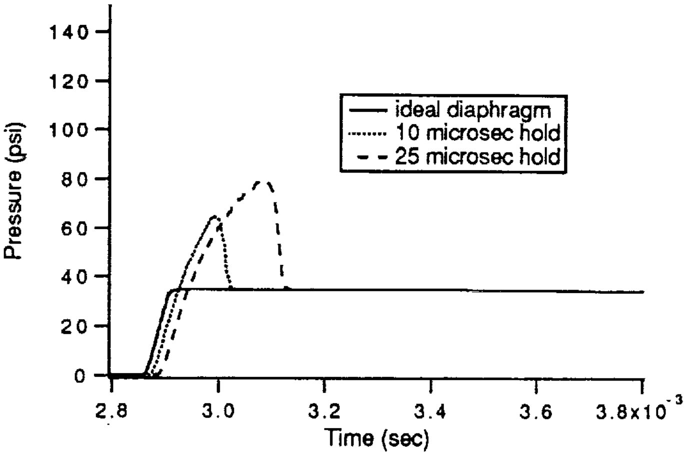

Fig. 18 Computed pressure traces 3.0 inches downstream of the secondary diaphragm.

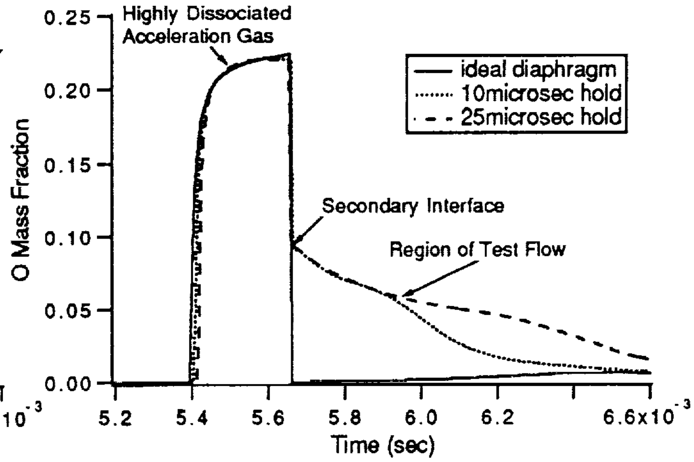

Fig. 19 Computed mass fractions of O molecules at the test location.

VALIDATION OF THREE-TEMPERATURE NOZZLE FLOW CODE NOZ3T

Seung-Ho Lee, Eloret Institute, Palo Alto, CA
and
Chul Park, NASA Ames Research Center, Moffett Field, CA

Abstract

A computer code NOZ3T which calculates one-dimensional flows of partially dissociated and ionized gases in an expanding nozzle developed earlier is validated in this work by comparing with three sets of existing experimental data. The code accounts for the differences among the translational-rotational, vibrational, and electron-electronic temperatures. Certain reaction rates are assumed to be controlled by vibrational and electron-electronic temperatures. The calculations are compared with: the electron temperature and number density data taken in a shock tunnel at CALSPAN during the 1960s, the mass-spectrometric data taken in an arc-jet wind tunnel at AEDC during the 1960s, and the spectroscopic data taken in an arc-jet wind tunnel at Ames Research Center recently. The results show that the three sets of data can be numerically reproduced by using the code. Typically, vibrational temperature is slightly higher than translational-rotational temperature, and electron-electronic temperature is considerably higher than vibrational temperature. Atomic oxygen concentration at the end of expansion is significantly smaller than that calculated by the conventional one-temperature model.

Method

A computer code NOZ3T has been developed in Ref. 1. This code enables one-dimensional calculation of a flow expanding through a convergent-divergent nozzle in the dissociated and ionized regime. It accounts for three temperatures, that is, translational-rotational, vibrational, and electron-electronic. The interactions among these three temperatures are calculated generally using the model described in Ref. 2. However, three different innovations have been made. First, the forward rates for the reactions

$$N_2 + O \rightarrow NO + N$$

$$NO + O \rightarrow O_2 + N$$

are assumed to be determined by the electron-electronic temperatures. This is because these reaction rates are controlled mostly by the concentration of electronically-excited O-atoms. Second, radiative loss is accounted for. Third, reactions involving NO_2 and N_2O are accounted for.

Results

Ames Arc-Jet Data - An experiment has been conducted recently at NASA Ames Research Center to determine temperature of the freestream flow in the test section of an arc-jet wind tunnel. The tunnel was operated at the stagnation chamber pressure of 2.5 atm, and enthalpy of about 45 MJ/kg. Emissions from the Gamma and Delta bands of

NO molecules are measured spectrographically in the test section. The results showed that the rotational temperature is about 600 K, the vibrational temperature is about 900 K, and the electronic temperature is about 7000 K for the experimental condition. The code NOZ3T is run to numerically reproduce these measured values. By dividing the vibrational relaxation time value of Millikan and White by 10^7, the observed values are reproduced numerically by the NOZ3T code.

CALSPAN shock tunnel data - The temperature and number density of electrons had been measured along an expanding nozzle of a shock tunnel at CALSPAN (Refs. 3 to 5). The experimental data are reproduced by NOZ3T. The comparison between the measured and the calcualted values is given in Figs. 1 to 3. As seen in these figures, NOZ3T can reproduce the experimental data fairly well. Here again, vibrational temperature is higher than the translational temperature, and electron-electronic temperature is higher than vibrational temperature.

AEDC arc-jet data - Concentration of O, N, N_2, O_2, and NO had been measured in the test section of an arc-jet wind tunnel at AEDC (Refs. 6 and 7). Using the NOZ3T code, the measured data have been numerically reproduced. Comparison between the experimental and the theoretical results is given in Figs. 3 to 6. In these figures, the solid curves represent the theoretical values obtained using the conventional one-temperature model. As seen in these figures, one-temperature model is not able to reproduce the measured data. The present three-temperature model can reproduce the data fairly well. It is important to note that measured concentrations of atomic oxygen is less than those calculated by the one-temperature model. The three-temperature model correctly predict this trend.

Conclusions

Using NOZ3T code, it is possible to numerically reproduce the three existing experimental data in which the nonequilibrium thermochemical state of the gas has been determined at the exit of a hypersonic nozzle. Generally, vibrational temperature is higher than translational-rotational temperature, and electron-electronic temperature is higher than vibrational temperature. Concentration of atomic oxygen is less than that calculated by the conventional one-temperature model in typical environments.

References

[1] Park, C., "Estimation of Excitation Energy of Diatomic Molecules in Expanding Nonequilibrium Flows," AIAA Paper 92-0805, January 1992.

[2] park, C., *Nonequilibrium Hypersonic Aerothermodynamics,* John Wiley and Sons, 1990.

[3] Dunn, M. G., and Lordi, J. A., "Measurement of Electron Temperature and Number Density in Shock Tunnel Flows, Part 2. NO^+ + e Dissociative Recombination Rate in Air," AIAA Journal, Vol. 7, 1969, pp. 2099-2104.

[4] Dunn, M. G., and Lordi, J. A., "Measurement of N_2^+ + e Dissociative Recombination in Expanding Nitrogen Flows," AIAA Journal, Vol. 8, 1970, pp. 339-345.

[5]Dunn, M. G., and Lordi, J. A., "Measurement of O_2^+ + e Dissociative Recombination in Expanding Oxygen Flows," AIAA Journal, Vol. 8, 1970, pp. 614-618.

[6]MacDermott, W. N., and Marshall, J. G., "Nonequilibrium Nozzle Expansions of Partially Dissociated Air: A Comparison of Theory and Electron-Beam Experiments," AEDC-TR-69-66, July 1969.

[7]MacDermott, W. N., and Dix, R. E., "Final Results of On-Line Spectrometric Analysis of Nonequilibrium Airflows," AEDC-TR-71-23, February 1971.

FIGURE CAPTIONS

Figure 1. Comparison between the experimental data and the present calculation for shock tunnel flow with nitrogen; settling chamber conditions: p = 17.1 atm, T = 7200 K (Ref. 4)

Figure 2. Comparison between the experimental data and the present calculation for shock tunnel flow with oxygen; settling chamber conditions: p = 25 atm, T = 4950 K (Ref. 5)

Figure 3. Comparison between the experimental data and the present calculation for shock tunnel flow with air; settling chamber conditions: p = 25 atm, T = 7200 K (Ref. 3)

Figure 4. Comparison between the experimental data and the present calculation for arc-jet flow with air; nitrogen and oxygen atoms (Ref. 6 and 7).

Figure 5. Comparison between the experimental data and the present calculation for arc-jet flow with air; nitric oxide (Ref. 6 and 7).

Figure 6. Comparison between the experimental data and the present calculation for arc-jet flow with air; nitrogen and oxygen molecules (Ref. 6 and 7).

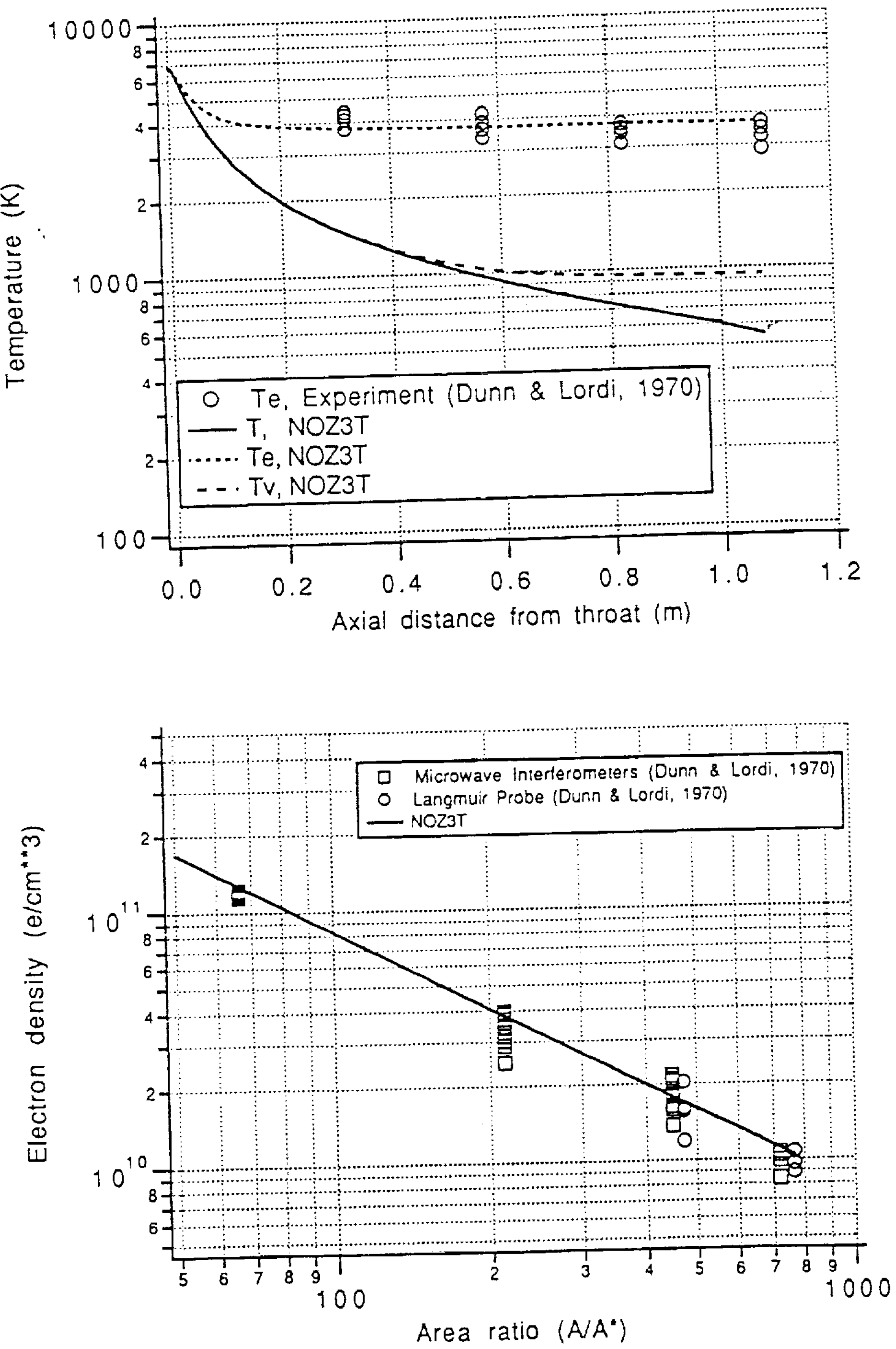
10000
8
6
4
2
1000
8
6
4
2
100
Temperature (K)
0.0
0.2
0.4
0.6
0.8
1.0
1.2
Axial distance from throat (m)
○ Te, Experiment (Dunn & Lordi, 1970)
T, NOZ3T
Te, NOZ3T
Tv, NOZ3T
4
2
10^{11}
8
6
4
2
10^{10}
8
6
Electron density (e/cm**3)
5
6
7
8
9
100
2
3
4
5
6
7
8
9
1000
Area ratio (A/A*)
□ Microwave Interferometers (Dunn & Lordi, 1970)
○ Langmuir Probe (Dunn & Lordi, 1970)
NOZ3T

Fig. 2

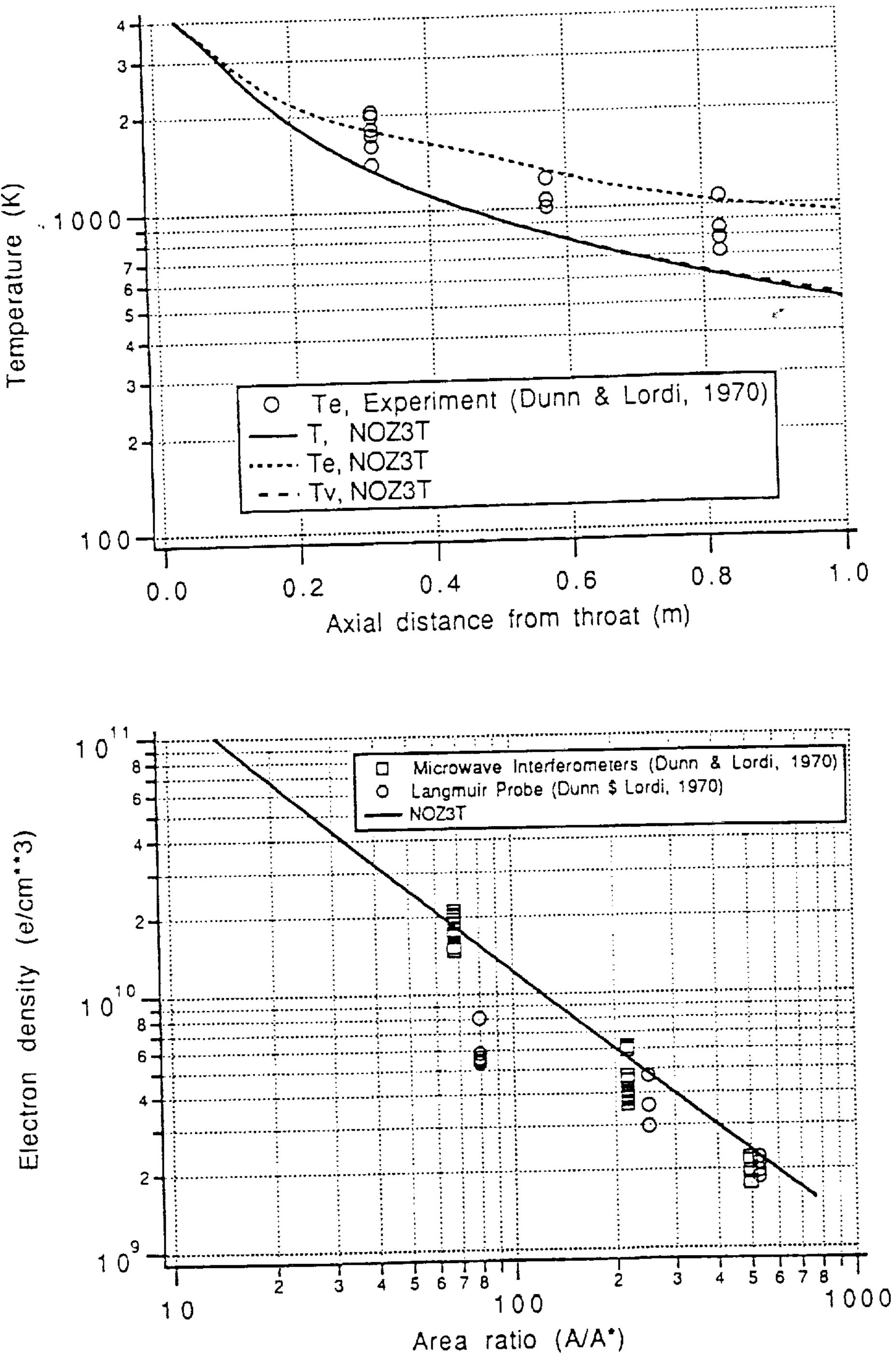

Temperature (K)
100
1000
2
3
4
5
6
7
0.0
0.2
0.4
0.6
0.8
1.0
Axial distance from throat (m)
○ Te, Experiment (Dunn & Lordi, 1970)
T, NOZ3T
Te, NOZ3T
Tv, NOZ3T
Electron density (e/cm**3)
10^{9}
10^{10}
10^{11}
10
100
1000
Area ratio (A/A*)
□ Microwave Interferometers (Dunn & Lordi, 1970)
○ Langmuir Probe (Dunn $ Lordi, 1970)
NOZ3T

Fig. 2

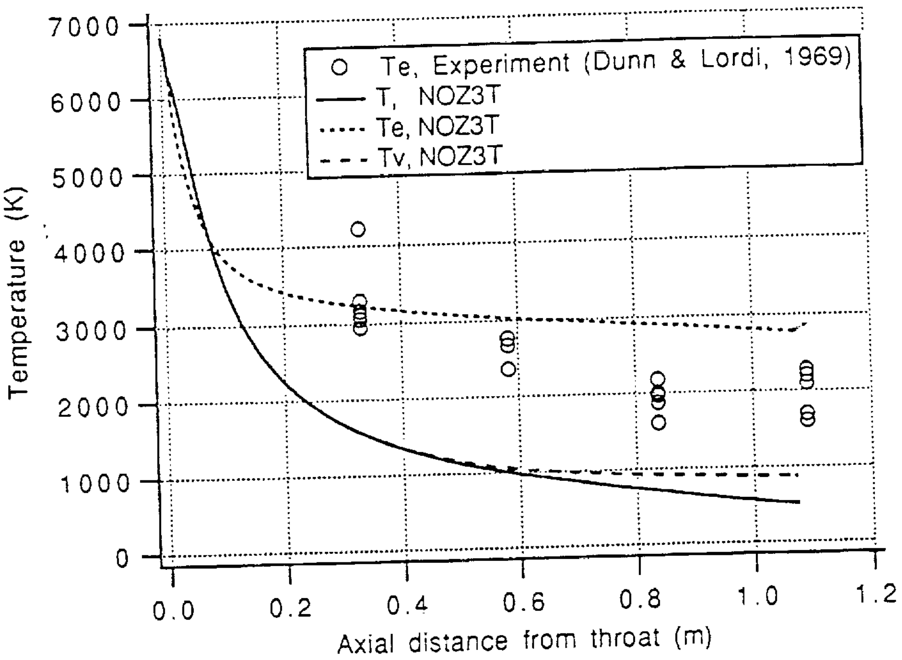
Temperature (K)
7000
6000
5000
4000
3000
2000
1000
0
0.0
0.2
0.4
0.6
0.8
1.0
1.2
Axial distance from throat (m)
○ Te, Experiment (Dunn & Lordi, 1969)
T, NOZ3T
Te, NOZ3T
Tv, NOZ3T

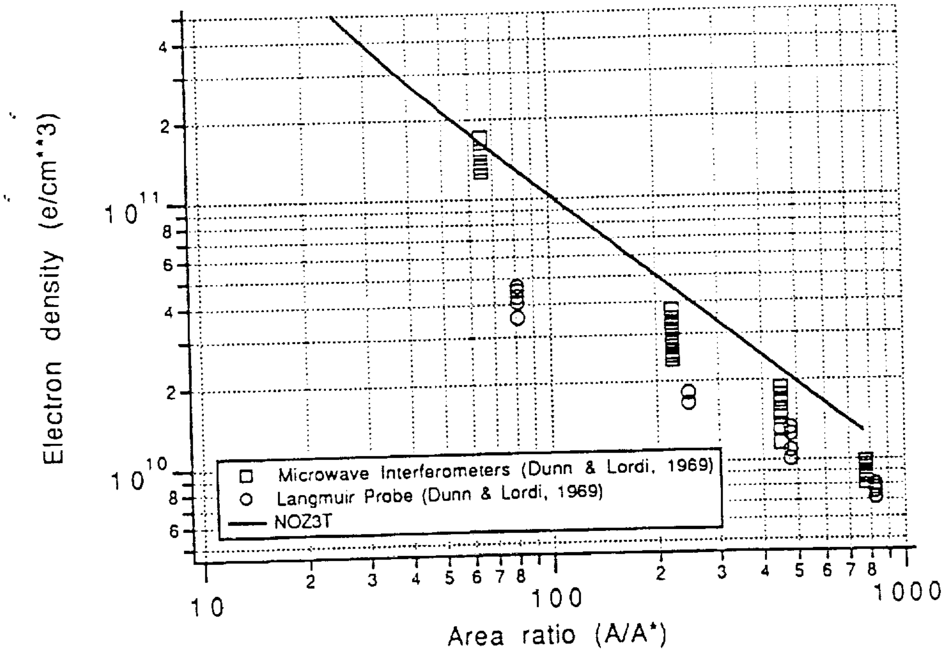
Electron density (e/cm**3)
4
2
10^11
8
6
4
2
10^10
8
6
10
2
3
4
5
6
7
8
100
2
3
4
5
6
7
8
1000
Area ratio (A/A*)
□ Microwave Interferometers (Dunn & Lordi, 1969)
○ Langmuir Probe (Dunn & Lordi, 1969)
NOZ3T

Fig. 3

aii

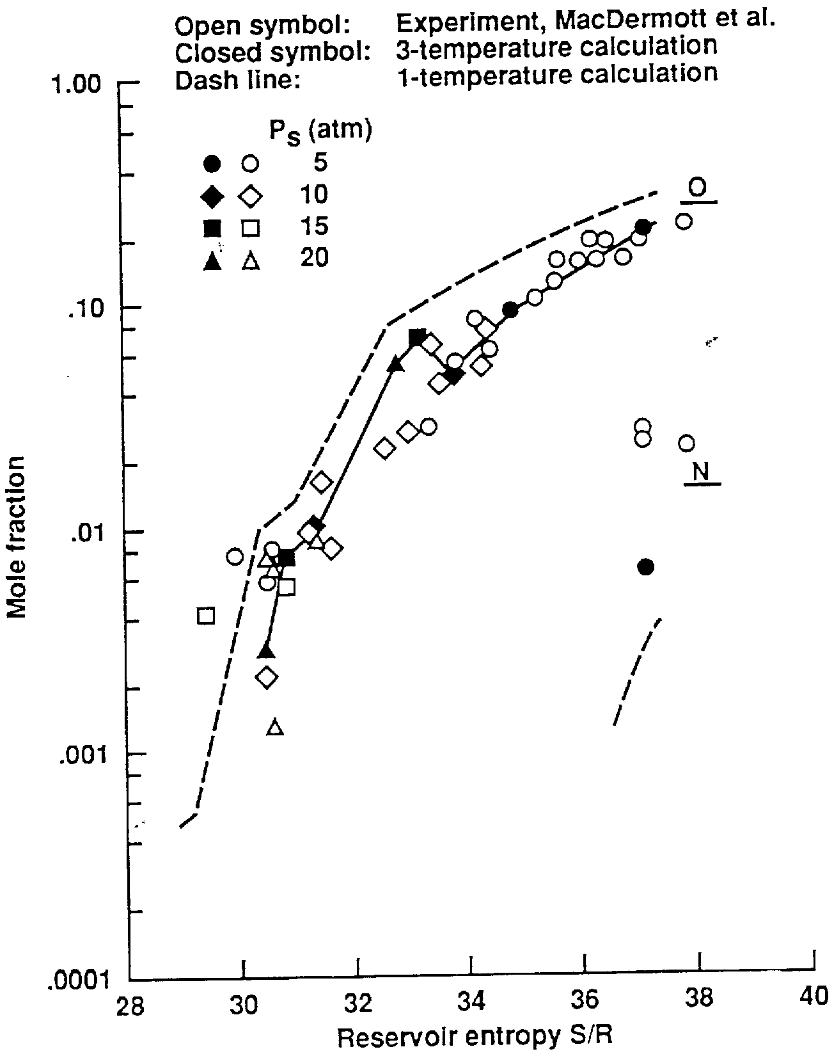

Open symbol: Experiment, MacDermott et al.
Closed symbol: 3-temperature calculation
Dash line: 1-temperature calculation
P_S (atm)
● ○ 5
◆ ◇ 10
■ □ 15
▲ △ 20
O
N
Mole fraction
1.00
.10
.01
.001
.0001
28
30
32
34
36
38
40
Reservoir entropy S/R

Park-3

Fig. 4

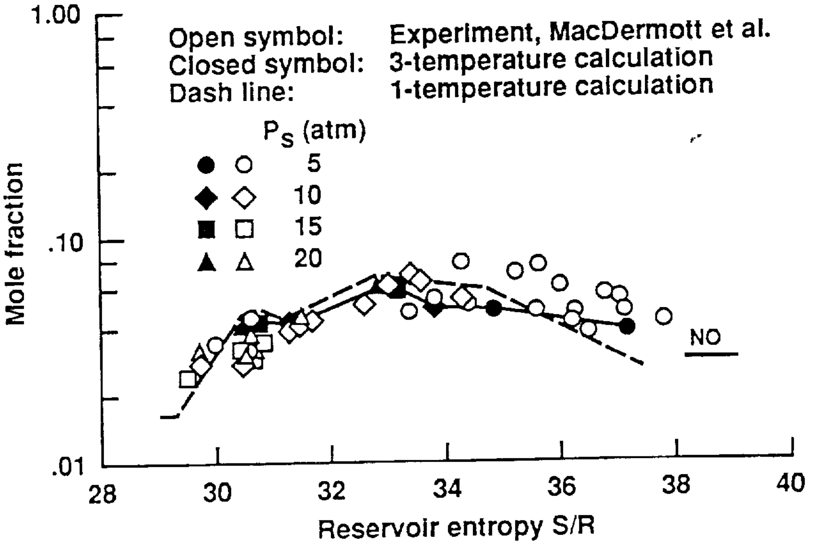
1.00
.10
.01
Mole fraction
Open symbol: Experiment, MacDermott et al.
Closed symbol: 3-temperature calculation
Dash line: 1-temperature calculation
P_S (atm)
● ○ 5
◆ ◇ 10
■ □ 15
▲ △ 20
NO
28
30
32
34
36
38
40
Reservoir entropy S/R

Park-2

Fig. 5

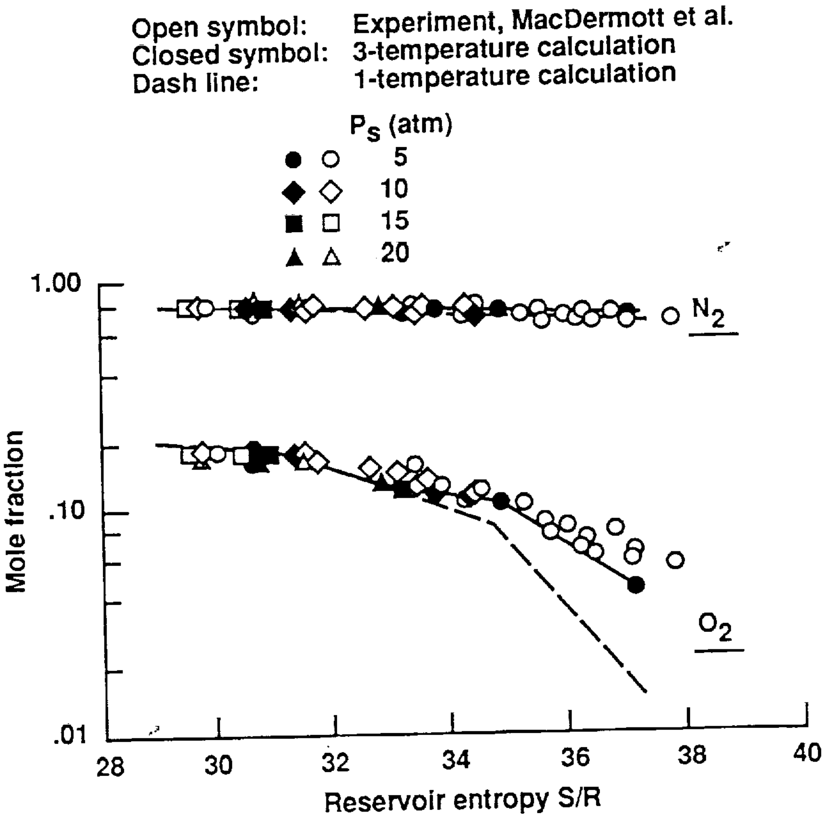
Open symbol: Experiment, MacDermott et al.
Closed symbol: 3-temperature calculation
Dash line: 1-temperature calculation
P_S (atm)
● ○ 5
◆ ◇ 10
■ □ 15
▲ △ 20
1.00
.10
.01
Mole fraction
28
30
32
34
36
38
40
Reservoir entropy S/R
N_2
O_2

Park-1

Fig. 6

AIAA 93-0037

Computational Study of a Lunar Return Aerobrake Concept

S. (Tokarcik) Polsky and E. Venkatapathy
Eloret Institute
Palo Alto, CA 94303

M. Tauber
NASA Ames Research Center
Moffett Field, CA 94035

31st Aerospace Sciences Meeting & Exhibit

January 11-14, 1993 / Reno, NV

For permission to copy or republish, contact the American Institute of Aeronautics and Astronautics
370 L'Enfant Promenade, S.W. Washington, D.C. 20024

Computational Study of a Lunar Return Aerobrake Concept

Susan (Tokarcik) Polsky*and Ethiraj Venkatapathy†
Eloret Institute, Palo Alto, CA 94303

Michael Tauber#
NASA Ames Research Center
Moffett Field, CA 94035

Abstract

The flow field around a proposed lunar return aerobrake is examined computationally assuming viscous, laminar flow and utilizing an effective γ approach to incorporate real-gas effects. The flow fields for three cases are calculated with both an axisymmetric and a three-dimensional formulation. The three vehicle configurations have braking panels extended 50°, 55°, and 60° to the inflow (zero lift configurations). The resulting axisymmetric and 3-D flow fields are examined, and it is shown that despite complexities in the 3-D flow field, the total drag coefficients calculated from modified axisymmetric results are very close to those obtained from the 3-D solutions. The aerobrake is shown to achieve total drag coefficients as high as 8.4 for a vehicle with panels deflected to 60°.

Introduction

An aerobrake uses aerodynamic forces, in place of rocket propulsion, to decelerate and maneuver, thereby achieving orbital modifications or entry into the atmosphere. The aerobrake concept examined here is intended for lunar return missions (11 km/sec entry velocity). It is designed so that, in a stowed configuration, it can be launched into space using the proposed National Launch System (NLS) or the Space Shuttle which has a payload bay capacity of 4.57m x 18.28m.

Nomenclature

A	reference area, $\pi d^2/4$, m^2
C_D	total drag coefficient, $D/q_\infty \cdot A$
D	drag, N
d	diameter, m
L	lift, N
M	mass, kg
q_∞	dynamic pressure, N/m^2
r	radius, m
δ	panel deflection angle
γ	specific heat ratio, C_p/C_v

Vehicle Design

An aerobrake is required to generate large amounts of drag. Therefore, this initial design study concentrates on the prediction of the drag capabilities of the proposed vehicle. The aerobrake vehicle, shown in Fig. 1, is composed of an hemi-ellipsoidal nose (forebody), a nearly cylindrical main-body, and four large, flat panels. The panels are used mainly as braking surfaces; however they are independently adjustable so that lift can be generated for maneuvering within the atmosphere to alleviate deceleration loads and heating. Desirable L/Ds for lunar return are 0.25 to 0.3. The panels can be stowed in the launch vehicle with zero deflection, and the maximum width and length of the panels is limited by the size of the launch vehicle's payload bay. Initially, a vehicle with four braking panels is examined. The optimum number of panels has yet to be determined, and future work may address this design feature. The panels can be deployed at variable angles to the freestream depending on the amount of drag required. Three panel deflection angles are examined in order to study how the panel angle affects the total drag coefficient.

The radius of the main-body increases from the forebody to the end of the main body. However, parts of the main body are flattened to provide a long hinge line for attachment of the panels. Tapering of the lower portion of the panels and the flattening of the main body allow for a long hinge line so that loads on the panels can be distributed along the hinge line without unduly reducing the volume of the vehicle.

---

* Research Scientist, Member AIAA. Mailing Address: NASA Ames Research Center, MS 230-2, Moffett Field, CA 94035

† Research Scientist, Member AIAA.

Research Scientist, Associate Fellow, AIAA.

The panels are made large to yield a low ballistic coefficient, $M/C_D \cdot A$. This permits the vehicle to decelerate at higher altitudes thereby reducing deceleration, structural loads and heating rates. The hemi-ellipsoidal nose shape was chosen to maximize drag and minimize heating to the forebody region. The payload capacity of the aerobrake is estimated to be 10,000 kg, and it has a total volume of about 150 m^3. The empty weight of the aerobrake is assumed to be 6500 kg, and the entry weight is 16,500 kg.

Approach

For initial design purposes, a general understanding of the over all flow field characteristics and the drag producing capabilities of the aerobrake is required. For this initial study, all four panels are maintained at the same deflection angle (zero lift configuration), and three panel orientations are examined: δ=50°, 55°, and 60°. The range of panel angles was chosen based on past drag brake studies[2] which showed that for similar vehicles with no gaps in the braking surfaces, these deflection angles yielded the highest drag while maintaining good flow quality and relatively low heating rates.

The freestream (flight) conditions used for this study (see Table 1) correspond to the peak pressure point along an aerobrake trajectory. A ballistic coefficient, β=250, and a maximum lift to drag ration, L/D=0.25, were assumed to calculate a lifting trajectory for the aerobrake. For the β and entry mass assumed, the corresponding C_D is approximately 4. The L/D for this trajectory is not held constant, and the maximum g-loading for this trajectory is 8.3gs.

Note that for all calculations requiring a reference area, the area is based on the largest main body diameter (d=4.572 m).

The flow fields for these cases are calculated assuming a laminar boundary layer and an ideal gas having an effective constant specific heat ratio. It is also assumed that the pressure in the base flow region is very low and will not affect that calculation of total drag coefficient. The panels create compression corners that, at the hypersonic speeds examined, will cause the flow to massively separate. Because of the separation, Newtonian flow or other inviscid methods are not applicable to this problem, and full Navier-Stokes solvers are required.

A large portion of the aerobrake trajectory is dominated by real-gas effects. These effects are approximated by incorporating an effective value of the specific heat ratio, γ, in the code. This method has been shown to be suitable for the calculation of drag and lift coefficients of blunt bodies in real-gas flows.[1,2] At the chosen flight conditions the stagnation pressure is nearly 0.4 atm; therefore the flow is assumed to be in chemical and thermal equilibrium. An effective specific heat ratio, γ, of 1.21 was used[3] based on the flight conditions.

Because the panels are flat and portions of the main-body are flattened, the aerobrake geometry is three dimensional. However, it is very nearly axisymmetric, and therefore, an axisymmetric geometry is used as a first approximation to reduce the time required for the flow field computations. The axisymmetric geometry is created by generating a body of revolution using a panel symmetry line. The surface pressure field for this axisymmetric geometry is then computed. The calculation of drag is a function of the vehicle geometry as well as the surface pressure field. Therefore, to better estimate the drag on the 3-D vehicle using the axisymmetric results, the axisymmetric pressure field is applied to the actual 3-D geometry. In this way, the flatness of the panels, the flattened portions of the main body, and the gaps between the panels are taken into account. The drag coefficient that is calculated by integrating the axisymmetric pressure field over the 3-D geometry is then referred to as a "modified" axisymmetric value.

In addition, solutions are also computed using the actual three-dimensional geometry. This geometry contains one octant of symmetry (45° from the middle of a panel to the middle of a gap region); therefore, only one eighth of the full configuration is needed for the three-dimensional calculations.

Numerical Methods

Two different CFD codes were used to calculate the axisymmetric flow around the aerobrake. The first code is an axisymmetric solver developed by Candler.[4] This is a finite-volume code that uses Steger-Warming flux-vector splitting and Gauss-Seidel line relaxation to solve the Navier-Stokes equations. This code has been used previously for similar studies of hypersonic drag brakes.[2]

The second code that was used is a 3-D solver, FL3D, developed by Venkatapathy.[5] This is a finite difference code that uses a three-dimensional, implicit time marching Navier-Stokes solution procedure. This code has previously been applied to axisymmetric and three-dimensional nozzle-plume and blunt body flows[5]. The numerical method is a LDU-ADI scheme with Roe's averaging and MUSCL differencing. High order spatial accuracy is achieved by constructing MUSCL extrapolation of flow variables with a differentiable limiter. Roe averaged upwind fluxes are constructed and the flux-difference from the higher order fluxes are used in this formulation. The LDU-ADI algorithm is a diagonal algorithm requiring minimal CPU per iteration and is applicable to steady flows. Both the codes are ideal-gas solvers which incorporate an effective value of γ.

Since no experimental data exist for the present flow field, solutions from the two codes were compared against one another to assure that the flow fields are calculated consistently. The flow field solutions for an axisymmetric aerobrake with panels at 50° were used for the comparison. The general flow structures, including the size of the separation bubble caused by the panels, compared well, and the differences in calculated surface pressures were less than 1%. The size of the separation region is important because it affects the efficiency of the braking panels. The pressure within a separated region remains essentially constant even when part of that region is a compression surface such as the base of a panel. Therefore, the portion of the panel contained within the separated region contributes little to the total drag.

For each set of panel angles, an axisymmetric and a 3-D solution were calculated. Although the 3-D solver could be used to calculate the axisymmetric solutions as well as the 3-D solutions, the axisymmetric solver was used because of its speed and convenience. Each axisymmetric solution was started from the same initial conditions and required approximately 10-15 minutes of CPU time on a Cray Y-MP. The first 3-D solution, the 50° panel case, was started from a blunt cone solution and required approximately 1.75 hours of CPU time. Subsequent 3-D solutions were started from the most similar preexisting 3-D solution. For example, the solution from the 50° panel case was used as the initial conditions for the 55° panel case. This reduced the CPU time to approximately 45 minutes.

The grids used are 63x47x61 for the 3-D calculations and 63x61 for the axisymmetric calculations. A representative axisymmetric grid is shown in Fig. 2. For the axisymmetric calculations, a solution-adapted[6] grid technique was used to refine the major flow features. Although 3-D grid adaptation is possible with the same procedure, it was concluded that solution adaptation of the 3-D grid was not necessary. This conclusion is based on the axisymmetric results which showed that although the flow features became more distinct, the calculated drag coefficient changed very little from the non-adapted cases. For the 3-D calculations, symmetry is taken advantage of and only one octant (45°) of the full 3-D geometry is computed. The surface grid for the 3-D calculations, shown in Fig. 3, consists of half of a panel and half of a gap region. The forebody of the aerobrake is truly axisymmetric at the zero angle of attack cases considered here and is not influenced by the downstream flow. Therefore there is no need to compute the nose region using a 3-D formulation. The portion of the flow field that is actually computed by the 3-D solver begins at the end of the forebody, and the inflow is fixed to the values from the axisymmetric solution. This reduces the grid size for the 3-D calculations to 46x47x61.

The outflow boundary conditions used for the gap region of the 3-D geometry are of concern because a portion of this region may be recirculating, subsonic flow. The supersonic portions of the outflow are extrapolated from interior points. The pressure is fixed across the subsonic region to the pressure that exits just as the flow becomes supersonic. The remaining flow variables are then extrapolated. Fixing the pressure across the subsonic region is a fairly good assumption because the pressure within separation bubbles remains relatively constant. This is indeed the case for the portion of the separation region which affects the aerobrake surface pressure.

Results and Analysis

Colored pressure contours for a representative axisymmetric solution at $\delta=50°$ are shown in Fig. 4. The pressure contours reveal that the peak pressure on the panels occurs in the region where the forebody shock interacts with the shock formed off the panel. The separation and reattachment regions are also indicated. Notice that the separation region is quite large. Consequently the pressure on the panel surface remains low within the separation zone and only begins to substantially increase downstream of the reattachment point.

A comparison of the axisymmetric and 3-D calculations of surface pressure is made for an aerobrake with panels at 50° (see Fig. 5). Although the axisymmetric solution shows a somewhat higher peak pressure on the panel, the surface pressure profiles look very similar indicating that, at least along a panel centerline of the 3-D geometry, the axisymmetric solution comes very close to the 3-D case. However, for either case it is noteworthy that the multiple shock interaction (see Fig. 4) increases the peak pressures on the panels by about a factor of 2 over the Newtonian impact theory value of nearly 23 kPa.

The limitations of the axisymmetric solution become apparent when numerically simulated surface oil flow for the 3-D solution is examined (see Fig. 6). The surface pressure on the body is indicated by colors; dark blue is the lowest pressure, essentially freestream, and white the highest. The oil flow is shown in yellow. The separation on the main body indicated by the convergence of oil flow lines is largest in the center of the panel regions and decreases only slightly in the centers of the gap regions. The patterns of the oil flow indicate that a complex, multiple vortex structure exists within the separated region.

Particle traces constrained to a panel center plane are shown in yellow in Fig. 7. The particle traces indicate the size of the separated region and show more clearly than the surface oil flow the extent of the separation on the panels. Almost half of the panel length is contained within the separation region. The effect of the separation on the panels is demonstrated by the painted surface pressure contours which show a very low pressure within the entire separated region. A cut away of the outer shock region is shown in this figure as a solid surface. The effect of the separation on the outer shock surface is indicated by the slight bulging of the surface in the region of the separation. Because of the panel-gap geometry, the shock structure in the flare region is truly three dimensional. It retains a conical shape in the gap regions and bulges out in the panel regions where it reflects off the panels. The shock stand off distance on the panels is greatest at the center of the panels. As the flow expands around the edge of the panels, the shock curves and the stand-off distance decreases. This causes the peak pressure on the panels to shift off the center line to a position approximately midway between the panel center and the edge.

Particle traces constrained to a gap center plane are shown in Fig. 8. The particle traces terminate at the end of the computational domain. The separation in the gap region remains relatively large and, as is indicated by the traces, the recirculation region extends into the base area where the flow field has not been calculated. The flow at the outflow boundary of the computational domain remains mostly supersonic even within the separation, therefore, the extrapolated boundary conditions applied at the outflow region are adequate. However, the effect of the base flow region on the main body is not captured by this representation.

It is assumed that the base flow region has very little affect on the total drag that is calculated for the vehicle, since the pressure in that region is relatively low. However, because of the gaps, the base flow may have some effect on the main body, and it is not clear what these effects may be. To capture the base flow region properly, the flow behind the aerobrake needs to be calculated for a distance equivalent to approximately four times the panel's vertical height. This corresponds to the approximate distance required for the flow to reattach (if the reattachment point is not contained within the computational domain, the error is not eliminated). Increasing the grid size to incorporate the necessary base flow region would increase the solution time substantially. The major drag producing areas of the vehicle are on the panels where the shock-shock interaction occurs. It is unlikely that including the base flow region in the calculation would affect this part of the flowfield. Therefore, the increase in solution time needed to calculated the base flow region is not warranted in this initial study.

A comparison of the total C_D calculated for the modified axisymmetric and 3-D solutions for 50°, 55°, and 60° flare angles is shown in Fig. 9. Here the term "modified" indicates that the axisymmetric C_D is computed by first distributing the axisymmetric surface pressure field across the 3-D geometry, thus taking into account that there are gaps and that the panels are flat. This configuration is then used to calculate the "modified" axisymmetric C_D. The most notable feature of this comparison is that, although the axisymmetric solution is incapable of computing the complex flow field revealed by the 3-D solutions, the total drag coefficient calculated for the modified-axisymmetric and 3-D solutions are very close. This suggests that, for this particular panel-gap geometry, it is not necessary to compute a full 3-D solution in order to calculate drag coefficient. However, it is not clear from this study whether the relationship between the axisymmetric and 3-D results would be maintained if the gap size was changed, if the total number of panels was increased or decreased, or if the panel angles were different from those examined here. For the cases considered, the general structure of the flow fields did not change substantially with the changes in panel angle.

The main purpose of the panels is to increase the total drag of the vehicle. Figure 10 shows how the (modified) drag coefficient changes along the vehicle's length for all three panel deflection angles. The base of the panels is at x=11.23 m. Because the vehicle's main body is cylindrical for these axisymmetric cases, the main body does not contribute anything to the total drag, and the C_D curve is flat in this region. The curve does not begin to rise until x=15m. This indicates that approximately (15m-11.23m=) 3.77m or 53.5% of the panels are contained within the separation region and contribute little to the total drag.

The total drag coefficient of the vehicle without the panels is C_D=0.886. The vehicle with panels at deflection angles of 50°, 55°, 60° achieves total drag coefficients of 5.84, 7.24, and 8.39, respectively. This corresponds to an increase in total C_D between 560% and 847% above the no-panel configuration. Also note that the total C_D increases 24% from the 50° deflection case to the 55° deflection case, and the increase from the 55° to 60° case is 16%. The resulting changes in the vehicle's ballistic coefficient are shown in Fig. 11.

The amount of the total C_D increase can be tailored by changing the panels' lengths and deflection angles. The panels' length would be fixed for a specific mission category (i.e. lunar return or mars return) and the total C_D variation needed during a specific mission would be achieved by changing the deflection angles.

The effects of turbulence were not examined in this study; however a turbulent boundary layer tends to decrease the separation bubble size thus causing the total drag to increase. Therefore, the laminar calculations of drag coefficients are conservative estimates.

Conclusions

The 3-D calculations of a proposed lunar return aerobrake show that a major portion of the main body as well as the braking surfaces are contained within a large, complex separated flow region. Despite the complexity of the 3-D flow field, modified axisymmetric solutions predicted total drag coefficients very close to those that were calculated from the 3-D solutions for aerobrakes with panels at 50°, 55° and 60° angles.

It was shown that, for the panel deflection angles and panel length examined here, the total drag coefficient could be increased to as much as 8.4 times the C_D of the same vehicle without panels. The increase in total C_D that is required for a given mission can be achieved by changing the lengths and deflection angles of the panels. It was also shown that Newtonian impact theory predicted a peak panel pressure one half of that calculated by the present methods showing that the Navier-Stokes method was indeed necessary.

Questions were raised concerning the possible effects of the base flow region and also whether the agreement between the axisymmetric and 3-D calculations would be maintained for similar aerobrakes with different panel configurations. These questions will be examined in future work

References

1 Yates, L.A. and Venkatapathy, E., "Trim Angle Measurements in Free-Flight Facilities," AIAA Paper 91-1632, June 1991.

2 Tokarcik, S.A., Venkatapathy, E., Candler G., Palmer, G., "Computational Flow Predictions for Hypersonic Drag Devices," AIAA Paper 91-3303, Sept. 1991.

3 Jorgensen, L.H., "Charts of Isentropic Exponent as a Function of Enthalpy for Various Gases in Equilibrium," NASA SP-3020, 1965.

4 Candler, G., "The Computation of Weakly Ionized Hypersonic Flows in Thermo-Chemical Nonequilibrium," Ph.D. Dissertation, Dept. of Aeronautics and Astronautics, Stanford University, Stanford, CA, 1988.

5 Venkatapathy, E., Feiereisen, W.J., and Obayashi, S., "Computational Studies of Hard Body and 3-D Effects in Plume Flows," AIAA Paper 89-0129.

6 Davies, C. and Venkatapathy, E., "A Simplified Self-Adaptive Grid Method, Sage,"NASA TM-102198, Oct. 1989.

altitude	56.6 km
velocity	9082 m/s
density	$4.751\text{x}10^{-4}$ kg/m^3
pressure	35.0 N/m^2
temperature	256.6 K
wall temp.	2700 K

Table 1 Flight altitude, velocity, and ambient conditions

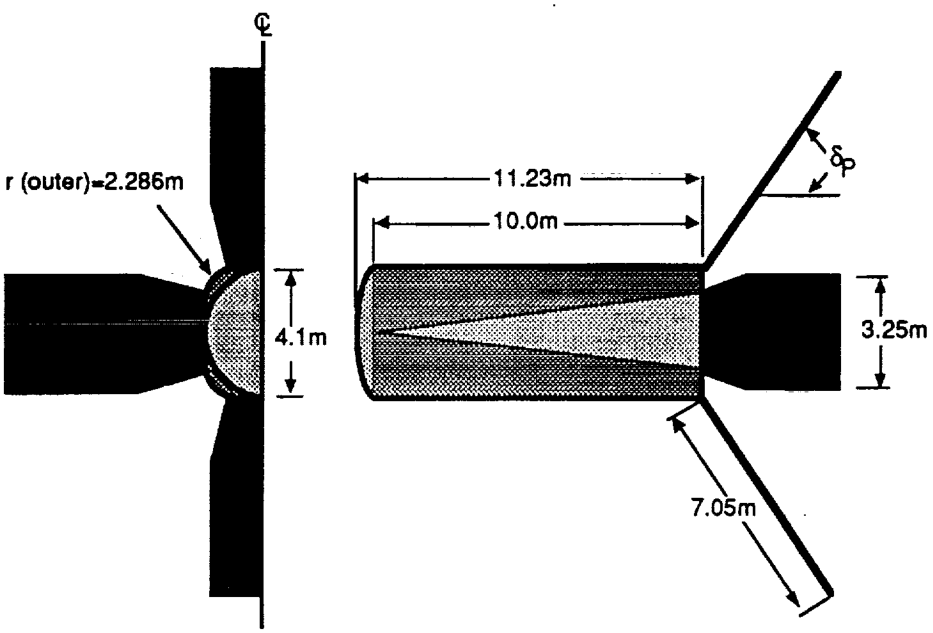

Figure 1. Lunar return aerobrake configuration

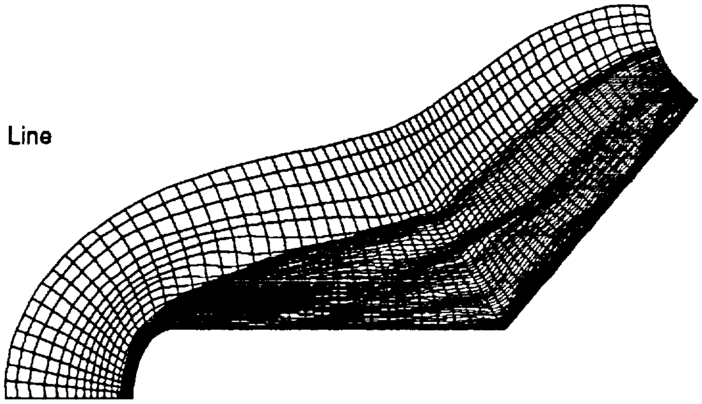

Figure 2. Solution adapted computational grid for axisymmetric calculations

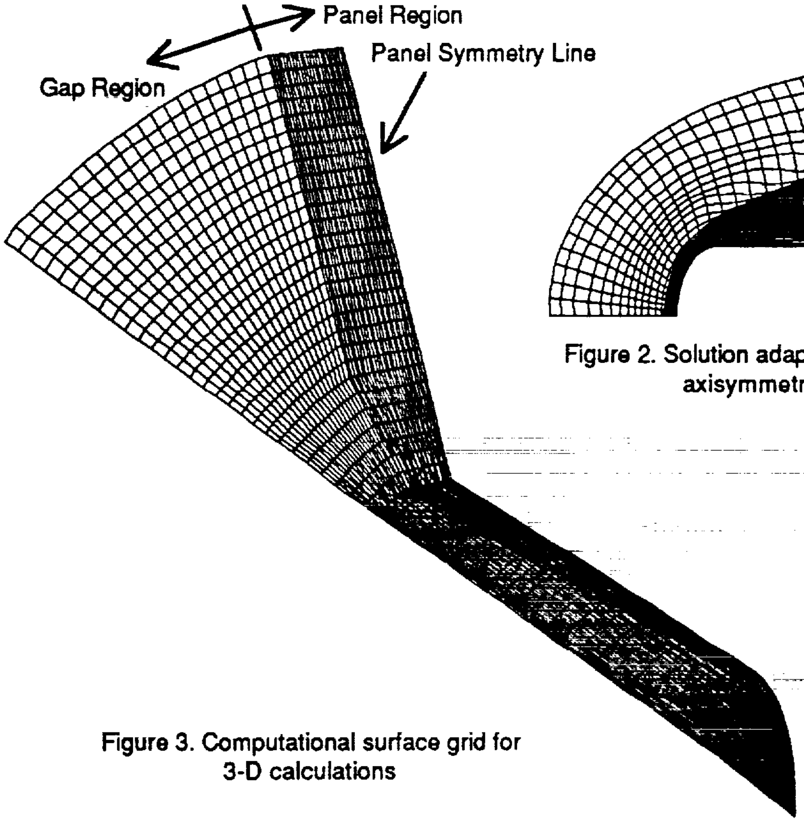

Figure 3. Computational surface grid for 3-D calculations

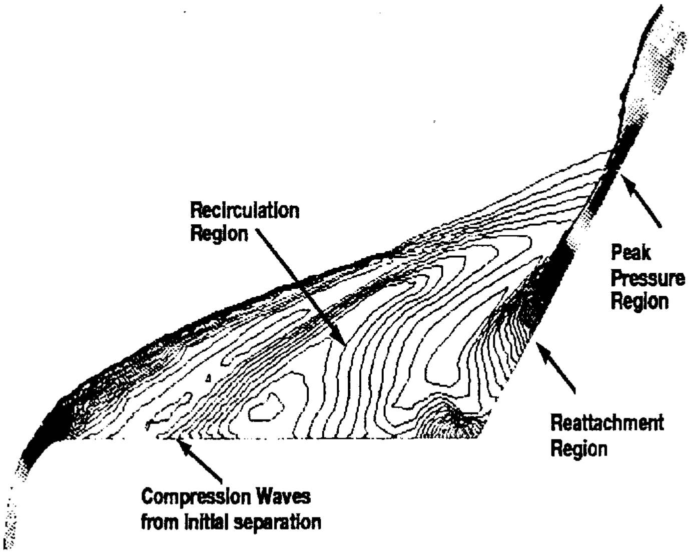

Figure 4 Pressure contours for axisymmetric, δ=50° geometry

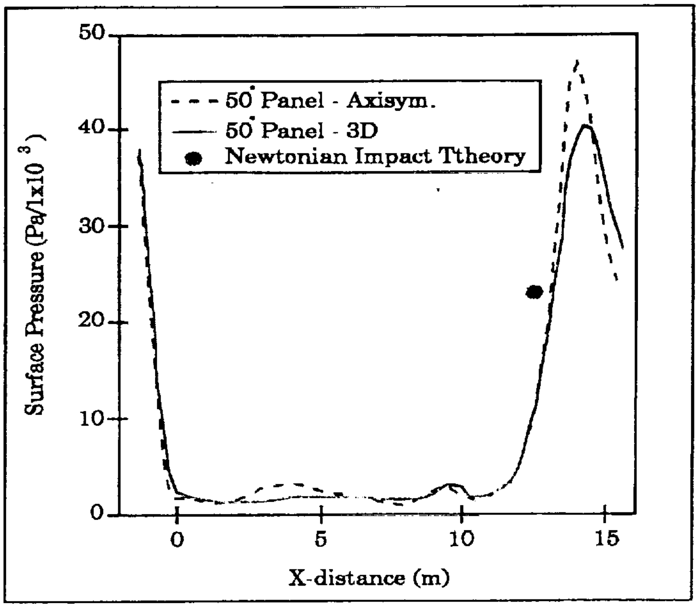

Figure 5 Surface pressure comparison

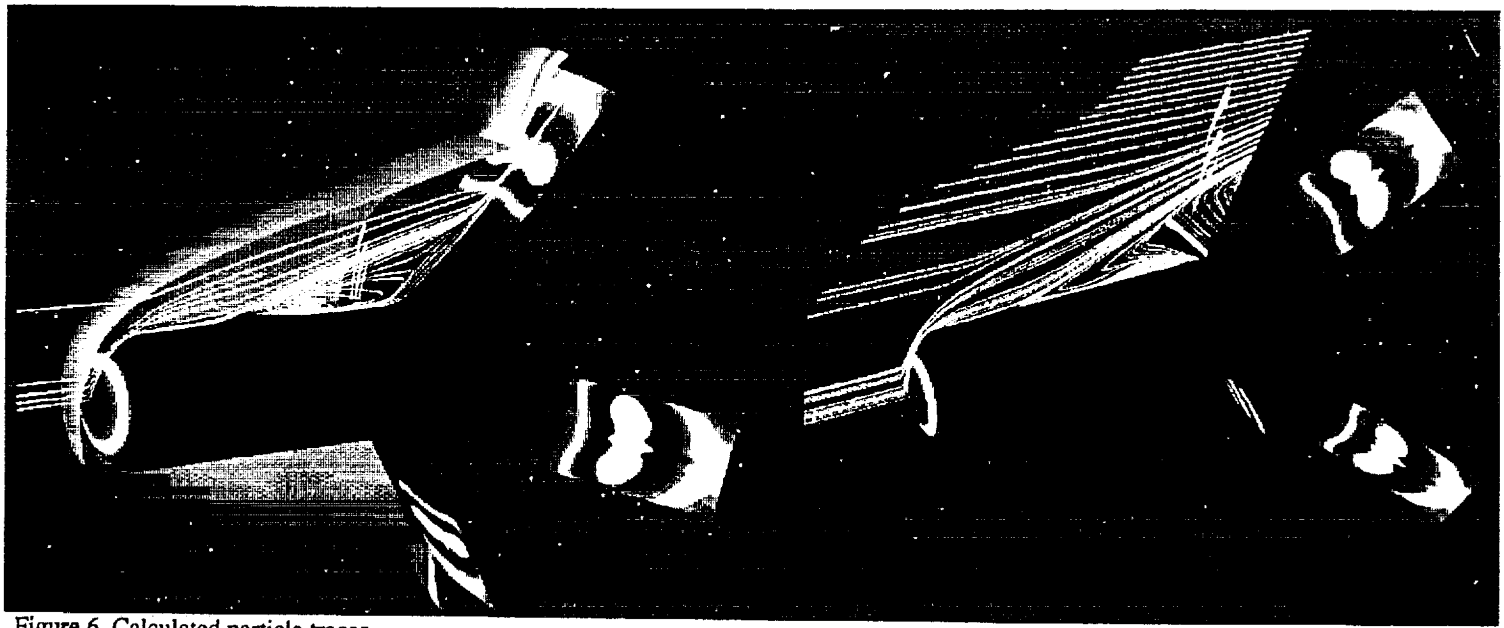

Figure 6 Calculated particle traces constrained to a panel symmetry line, surface pressure, and outer shock surface for δ=50°

Figure 7 Calculated particle traces constrained to a gap symmetry line and surface pressure for δ=50°

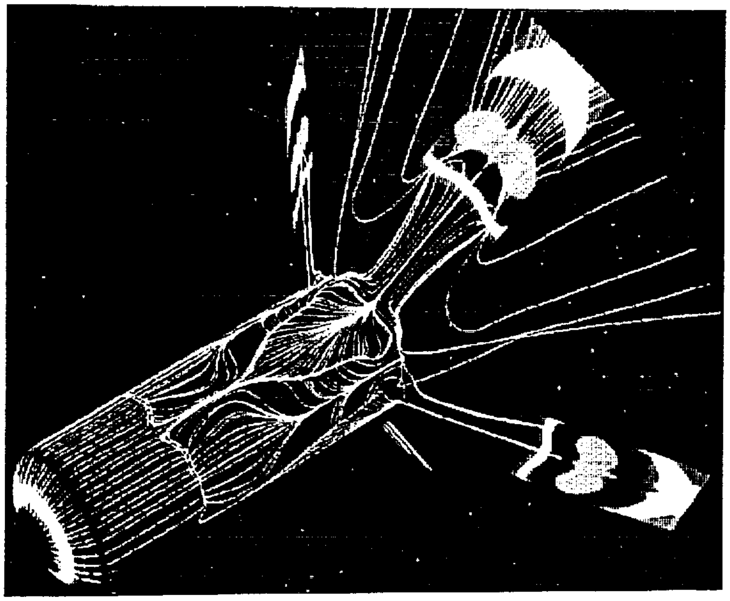

Figure 8 Calculated surface oil flow and surface pressure for δ=50°

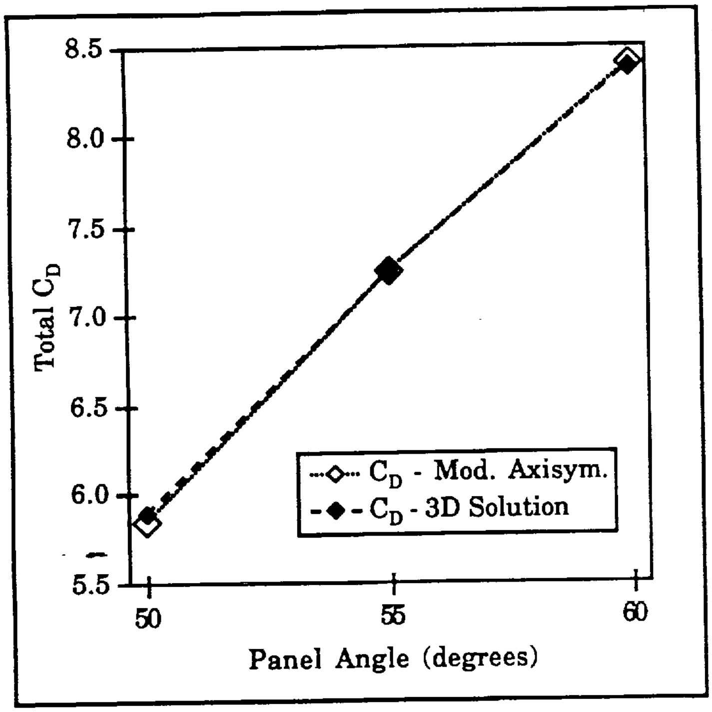

Figure 9 Total drag coefficient comparisons between axisymmetric and 3-D calculation

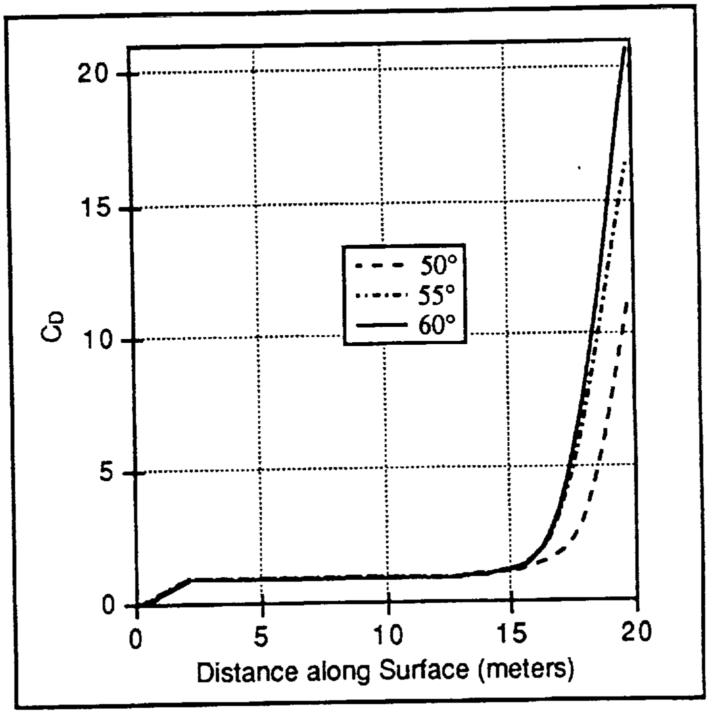

Figure 10 Variation of drag coefficient down the length of the vehicle for three panel deflection angles

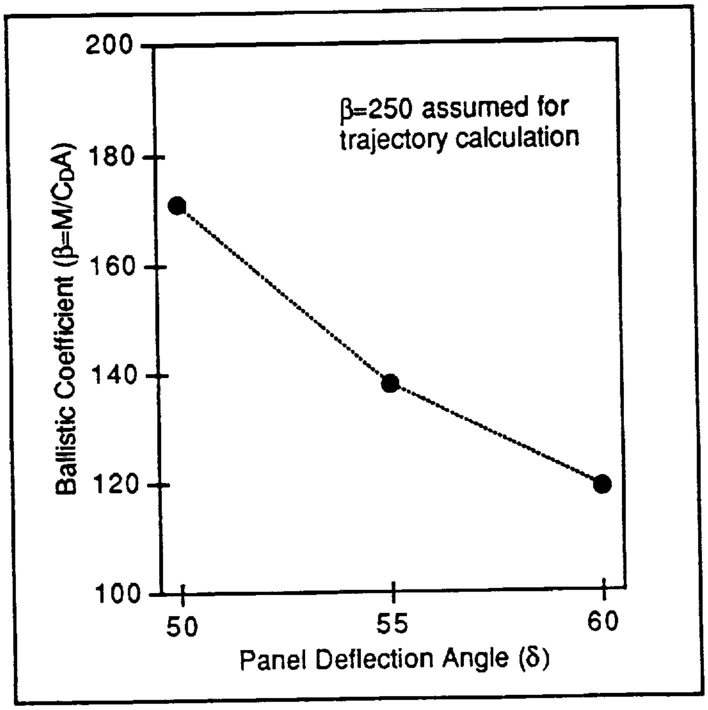

Figure 11 Change in ballistic coefficient due to panel deflection

AIAA-93-0480

Time-Dependent Simulations of Reflected-Shock/Boundary Layer Interaction

Gregory J. Wilson
Eloret Institute, Palo Alto, CA

Surendra P. Sharma
NASA-Ames, Moffett Field, CA

Walter D. Gillespie
Stanford University, Stanford, CA

31st Aerospace Sciences Meeting & Exhibit
January 11-14, 1993/Reno, NV

TIME-DEPENDENT SIMULATION OF REFLECTED-SHOCK/BOUNDARY LAYER INTERACTION

Gregory J. Wilson*
Eloret Institute, 3788 Fabian Way, Palo Alto, California 94303

Surendra P. Sharma**
NASA Ames Research Center, Moffett Field, CA

Walter D. Gillespie***
Stanford University, Stanford, CA

Abstract

An initial numerical/experimental investigation has been done to better understand multi-dimensional flow phenomena inside pulse facilities. Time-dependent quasi-one-dimensional and axisymmetric numerical simulations of complete shock tube flow are compared with experimental pressure traces recorded at the NASA Ames electric-arc driven shock tube facility (from cold driver shots). Of particular interest is the interaction between the reflected shock wave and the boundary layer. Evidence of the shock bifurcation caused by this interaction is clearly seen in the present experimental data. The axisymmetric simulations reproduce this phenomenon and demonstrate how this interaction can provide a mechanism for driver gas to contaminate the stagnation region. The simulations incorporate finite-rate chemistry, a moving mesh and laminar viscosity.

I. Introduction

The duration of the test time provided by a shock tube or shock tunnel is always less than the theoretical value. In fact, it is not uncommon for the test time to be only a fraction of what might be ideally expected. The usual reason for this decrease is the early arrival (or contamination) of driver gas in the stagnation region, although there may also be other causes such as the arrival of the rarefaction wave reflected off the driver end of the shock tube. Since accurately knowing the experimental conditions provided by such facilities is important, many investigations have been carried out to understand and quantify the physical mechanisms which cause shortened test times. Several of these mechanisms are schematically presented in Figure 1 and include deformation of the contact discontinuity caused by the diaphragm rupture process,[1] mass transfer of the driven gas into the boundary layer,[2] contact discontinuity diffusion and instabilities,[3-5] and shock/boundary layer interaction after reflection of the incident shock off the end wall.[6-18] Non-ideal performance may also be caused by the shock tube/tunnel geometry. For example, Jacobs[19] and Cambier *et al.*[20] have numerically predicted the formation of a vortex created during the reflection of the incident shock off an end wall which includes a nozzle entrance. This vortical flow may enhance the mixing of the driver and driven gases in shock tunnels.

It is not clear which of the mechanisms mentioned above limits test times most and it may be that the dominant mechanism varies with the experimental facility or the run conditions. There is a large amount of evidence, however, that suggests that the reflected-shock/boundary layer interaction is often a major contributor to the contamination process. It is well established that under many conditions the reflected shock will interact with the boundary layer causing it to bifurcate near the wall (see Figure 2). Mark[6] developed a model to predict the characteristics of the bifurcation and the conditions under which it will occur. He showed that the flow in the energy deficient boundary layer has a stagnation pressure that is less than the stagnation pressure behind the normal reflected shock and is prevented from passing under the reflected shock. Instead, it separates and collects in a bubble of gas next to the wall. Davies[8,9] used Mark's model to show that the bifurcated shock structure provides a mechanism for driver gas contamination of the stagnation region. It can be seen in Figure 2 that the

---

*Research Scientist, Member AIAA. Mailing address: NASA Ames Research Center, MS 230-2, Moffett Field, CA 94305

**Research Scientist. Associate Fellow AIAA.

***Graduate Student, Member AIAA.

gas which encounters the oblique shocks at the foot of the bifurcated shock retains a higher velocity than the gas which encounters the normal shock. The result is a jet of gas near the wall. Clear experimental evidence of this wall jet can be seen in the recent color schlieren photographs of Kleine *et al.*[12] which include features such as the rolling up of the wall jet as it encounters the end wall. Davies showed that when the bifurcated shock structure of Figure 2 interacts with the contact discontinuity, cold driver gas is propelled by this jet toward the end wall and into the driven gas. He and others such as Bull and Edwards[10] have done experiments which measured the time of arrival of the cold driver gas, Davies by heat-transfer gages and Bull and Edwards by "tagging" the driver gas with an infrared active gas. Both found that measured values of the arrival time of driver gas in the stagnation region were in agreement with the analytical theory of Davies. An interesting experimental work by Ligong *et al.*[14] attempted to reduce driver gas contamination using boundary layer suction to eliminate the wall jet.

In the absence of optical data, the presence of shock bifurcation can be inferred from side-wall pressure measurements. Experiments show that the passage of the reflected shock is not accompanied by a sharp rise but by a rise of about one half the expected value followed by a small plateau or drop in pressure. The post-reflection pressure is then achieved after a pressure overshoot (see Figure 3). Sanderson[15] used Mark's model with a small modification to explain how the bifurcated foot causes these pressure trace features. The presence of reflected-shock/boundary layer interaction can also be deduced by noting the change of the reflected shock speed compared to theory.[6,16,17]

The description of reflected-shock/boundary layer interaction presented above is adequate to explain much of what is observed experimentally in shock tubes. However, more complicated flow structures such as a pseudo-shock (or shock train) can develop when the shock/boundary layer interaction is strong. Matsuo *et al.*,[16] Strehlow and Cohen,[17] and Brossard and Charpentier[18] all show schlieren photographs of the formation of multiple shocks after the reflection of the incident shock. The effect of these multiple shocks on driver gas contamination has not been studied.

There have been very few multi-dimensional simulations of shock tubes and shock tunnels that resolve wall viscous effects and none of them have looked at the contamination of the stagnation region with driver gas through the wall jet mechanism proposed by Davies. The reason for this is surely related to the small time steps caused by the fine grid needed to resolve boundary layers and the resulting high cost of propagating the flow features down the length of a shock tube at those small step sizes. Jacobs[21] has simulated expansion tube flow of a perfect gas including the boundary layer. Cambier *et al.*[20] looked at several isolated multi-dimensional phenomena including the diaphragm rupture process. Several other works have simulated reflected-shock/boundary layer interaction by considering only the end wall region of a shock tube and assuming a boundary layer profile for the inflow.[12,22]

The approach taken in this work is to develop a numerical methodology for time-dependent axisymmetric simulations of the flow inside the NASA Ames electric-arc driven shock tube (cold driver shots without the arc-driver) starting from diaphragm rupture. The numerical scheme is based on experience gained from time-dependent quasi-one-dimensional simulations for pulse facilities.[23] The high cost of resolving the boundary layers and simulating the flow through the entire facility is minimized by an efficient use of grid points, highly vectorized code, and an implicit treatment of the viscous terms. Experimental data is obtained from the facility for comparison to the simulations. Starting the simulations with the diaphragm rupture allows the position of the contact discontinuity and the boundary layer development to be computed. This, in turn, makes it possible for phenomena such as the reflected shock/boundary layer interaction and the reflected-shock/contact discontinuity interaction to be investigated numerically. Of particular interest is the ability of the simulations to predict the driver gas contamination by the wall jet mechanism proposed by Davies. In this work, the contact discontinuity is assumed initially to be planar and the boundary layer is treated as laminar. Comparisons of the axisymmetric simulations with quasi-one-dimensional solutions help illustrate the pressure trace features captured by the axisymmetric solutions.

II. Experimental Facility

The NASA Ames electric-arc driven shock tube facility.[24,25] has several possible configurations and has a large hypervelocity operating range using its arc-driver. However, this work only considers experiments using a cold helium driver with nitrogen in the driven section. These shots were made with a cylindrical driver of .76 m (2.5 feet) in length and 10 cm (3.93 inches) in diameter (see Figure 4). The driven section was 4.02 m (13.17 feet) long with the same diameter as the driver. A single self-break diaphragm separated the driver and driven gases.

For the current experiments the instrumentation consisted of pressure transducers flush mounted at two positions on the shock tube walls. One location was .0254 m from the driven tube end wall and the other was .445 m from the end wall. The transducers were PCB Piezotronics, Inc. Model 113A21 with a circular surface area .218 inches in diameter. They have a rise time of 1 microsecond. Heat-transfer data has also been collected at the same instrument locations and will be used in future work.

III. Numerical Method and Gas Model

The gas dynamic equations for both the quasi-one-dimensional and the axisymmetric simulations are solved by using an explicit finite-volume form of the Harten-Yee upwind TVD scheme[26] which gives second-order spatial and temporal accuracy. The gas model includes the three major species present in the shock tube for the present experiments (N_2, N, and He) and accounts for finite-rate chemical processes. A separate equation for vibrational energy is included so that vibrational nonequilibrium effects can be assessed. The present work, however, enforces thermal equilibrium. The full Navier-Stokes viscous terms are included in the axisymmetric simulations.

In the quasi-one-dimensional computations, a tracking scheme is used for the contact discontinuity to avoid the numerical difficulties associated with resolving this feature as it moves large distances.[23] The tracking scheme is not used in the axisymmetric simulations so that mixing of the the driver and driven gases can occur during the interaction of the reflected shock with the contact discontinuity. Instead, the axisymmetric simulations cluster grid points at the contact discontinuity to minimize numerical diffusion and convect this clustered grid with the gas interface as it travels down the driven tube. This approach has the additional benefit of compressing all of the cells associated with the driven tube into the end wall region of the shock tube as the driven gas is compressed thereby providing a fine axial mesh during the shock reflection.

Because time accuracy is required, the global time step is dictated by the smallest required time step in the computational domain. The solutions for both the one-dimensional and axisymmetric solutions are advanced at a CFL number less than 1 based on the inviscid gas dynamics. In the boundary layer of the axisymmetric simulations, this CFL number can be significantly larger than the stability bound required by the viscous terms. To avoid the more limiting time step dictated by the viscous terms, they are treated implicitly. This requires a block tri-diagonal matrix inversion along each line of cells normal to the wall. The cost of this inversion is more than offset by the greater allowable time step. It is believed that the time accuracy of the solution is not significantly effected by this approach and without it the simulation becomes impractical. The source terms representing the finite-rate chemical kinetics and vibrational relaxation are also treated implicitly. This implicit treatment reduces the formal time accuracy to first order.

IV. Results

All of the numerical work in this paper is compared with a single experimental condition in the NASA Ames electric-arc driven shock tube. The initial condition for the experiment was 3.96 MPa (575 psi) cold helium in the driver and 100 torr nitrogen in the driven section. This resulted in an incident shock speed of approximately 1490 m/sec. The temperature in the driver was not measured and so is not known precisely.

To illustrate the general character of the flow in the NASA Ames electric-arc driven shock tube with the cold helium driver, a computed x-t diagram of temperature contours from a one-dimensional simulation is given in Figure 5. The x-t diagram is for a flow at a higher shock speed than the conditions mentioned above, but the flow is qualitatively similar. This figure clearly shows the time-varying positions of the incident shock, contact discontinuity, and rarefaction. Included in Figure 5 is an enlargement of the end wall region of the driven section showing the reflected shock being partially transmitted through the contact discontinuity and partially reflected back toward the end wall. This reflection occurs several times and each successive interaction further slows the interface down until it is brought to rest. This type of off-tailored interaction (with reflected shocks) is referred to as an over-driven case. Note that a vertical line of data from this plot yields a trace over time at a given location.

Figure 6a shows experimental and computed one-dimensional sidewall pressure traces .0254 m upstream of the driven section end wall. There are two one-dimensional simulations included in the figure to show the sensitivity of the solutions to the initial conditions. Each of the simulations used 350 points with half in the driver and half in the driven section. Both have the same the initial conditions except that the driver temperature is 300 K in one case and 330 K in the other. A driver pressure of 3.45 MPa (500 psi) was chosen for both simulations to produce approximately the same shock speed as measured in the experiment. The required driver pressure for the computations is less than that used in the experiments because there are losses in the experiment due to the diaphragm rupture and viscous effects. The shock speeds for the 300 K and 330 K driver cases are 1495 M/sec and 1529 m/sec, respectively. The driver at 300 K produces a smaller incident shock speed compared the driver at 330 K and nearly matches the measured experimental shock speed. The driver at 300 K also slows the arrival of the rarefaction off the opposite end of the facility by reducing the speed of sound in the driver. Note that a relatively small change in the initial conditions has a significant effect on the pressure traces. Because the exact time of the experimental diaphragm rupture is not known, the experiments and computations are temporally aligned at the shock arrival time at the location .445 m from the driven tube end wall.

Several of the major events are labeled in the Figure 6a. These include the passage of the incident and reflected shocks, the arrival of the rarefaction, and the presence of reflected waves off the contact discontinuity. The general changes in the pressure traces due to off-tailored interactions with the contact discontinuity are captured fairly well with the one-dimensional approach. As expected, the experimentally measured features associated with the contact discontinuity (such as waves which have interacted with it) are smeared because the interface is non-planar and diffuse while the same features in the simulations are sharp because the interface is tracked. The overshoot in the experimental trace just after the reflected shock is from the bifurcation of the reflected shock as explained by Sanderson.[15]

Figure 6b contains the pressure traces from the experiment and the two one-dimensional simulations for the location .445 m upstream of the driven tube end wall. The main feature to consider in this figure is the arrival time of the reflected shock at this station. Both one-dimensional simulations significantly under predict the reflected shock speed compared to the experiment. The disagreement is expected because the reflected shock is significantly influenced by the shock/ boundary layer interaction on the shock tube walls and because the one-dimensional simulations cannot account for this phenomenon. Figure 6b also shows that the reflected shock speed is more strongly affected by the shock tube initial conditions than the incident shock (the 300 K and 330 K cases are quite different).

Axisymmetric simulations were then performed for the 100 torr case using a driver pressure of 3.45 MPa (500 psi) and a driver temperature of 330 K. It is seen from the one-dimensional simulations that the 300 K driver temperature would give better agreement with experiment but the expensive axisymmetric simulations were done before the experimental data was gathered. Two different meshes are used for the axisymmetric investigations both of which contained 700 points along the length of the tube (350 each in the driver and driven sections) and 112 points between the tube centerline and an outer wall. The two meshes differ in the grid spacing used at the wall. The points were exponentially clustered near the wall with a minimum spacing of .075 mm at the wall for one case and .0375 mm for the other case. These solutions will be referred to as the "coarse" and "fine" solutions, respectively. Both cases used a larger wall spacing of .15 mm in the driver section and in the first half of the driven tube. The specified finer spacing was present in the final .75 meters of the driven tube after being linearly reduced from the larger spacing. This approach eased the computational cost by allowing a larger time step early in the solution and also by allowing the same starting solution to be used for both computations since the grid was identical for approximately one half of the driven tube. As mentioned before, the solutions assumed an initially planar contact discontinuity and laminar viscosity. A constant wall temperature of 300 K was also specified.

Figure 7 shows computed density and velocity contours of the end wall region shortly after the reflection of the incident shock on the fine grid solution (the contact discontinuity is still far upstream at this point in the simulation). The contours are very similar to the schematic diagram in Figure 2. The boundary layer ahead of the reflected shock is quite thin and contains approximately 16 points. There is a region of separated, recirculating flow under the shock bifurcation. A slight curvature of the normal shock which is observed in experiments is also perceivable in the simulation. Along the wall in the stagnation region there is a layer of higher velocity fluid that curls up when it encounters the end wall. This feature compares quite favorably with the schlieren pictures of Kleine *et al.*[12]

Figure 8a shows temperature contours of the end wall region a short time *before* the the reflected shock interacts with the contact discontinuity. The driver gas is easily distinguished with temperature because it is much cooler than the driven gas. Note that the contact discontinuity is still planar. Because the boundary layer in this portion of the tube has had a longer time to develop compared to the end wall region, it is thicker and contains approximately 30 mesh points. The reflected-shock/boundary layer interaction has significantly changed since the time at which Figure 7 was recorded. Although the familiar shock bifurcation is still present, there is now a secondary shock structure behind the original reflected shock. This phenomenon appears similar to the pseudo-shock structure mentioned in the introduction. The separated flow region under the foot of the reflected shock has expanded so that it extends from the front foot of the shock bifurcation to the area under the secondary shock. Even with the modified structure of the pseudo-shock there is still a wall jet originating at the oblique shock of the bifurcated foot and extending all the way to the end wall. The jet is visible with temperature contours because the temperature rise experienced by the gas passing through the oblique shocks of the bifurcated foot is 100-200K less than the rise experienced by the gas passing through the normal reflected shock.

Figure 8b shows temperature contours a short time *after* the reflected shock interacts with the contact discontinuity. The figure indicates that the bifurcated shock structure significantly deforms the contact discontinuity. Hot driven gas in the separated region under the shock bifurcation has been carried into the driver gas while the driver gas that passed through the oblique shocks of the foot region has begun to penetrate into the driven gas (i.e. it is part of the wall jet). There is also the additional feature of a reflected shock due to the overtailored conditions.

Figure 9 contains temperature contours from a time later than in Figure 8. The flowfield has become even more complicated. The penetration of the driver gas along the walls is now clearly seen and the bubble of separated flow under the bifurcated shock has carried hot driven gas with it far from the end wall.

Figure 10a,b repeats the experimental data and the 1-D results with the 330 K driver of Figure 6 and adds the results from the two axisymmetric simulations. Figure 10a is from .445 m upstream of the end wall and Figure 10b is .025 m from the end wall (the order is reversed compared to Figure 6). As was mentioned for Figure 6b, the 1-D formulation is unable to account for the shock/boundary layer interaction and predicts a slower reflected shock arrival time at the pressure transducer location. The axisymmetric solutions include this phenomenon (with a laminar shock/boundary layer interaction) and predict a faster reflected shock speed and closer agreement to the experiment. Strehlow and Cohen[17] also reported that the reflected shock speed was increased by the presence of the shock bifurcation. By considering the relative change produced in Figure 6b by using a driver at 300 K rather than at 330 K, it is presumed that even better agreement with experiment would result by using the lower driver temperature in the axisymmetric simulation. Another factor that may influence the comparison between the experimental and simulated reflected shock speeds is the character of the boundary layer. The presence of a turbulent boundary layer in the experiment would cause a growth of the bifurcated shock different than the growth computed with the laminar viscosity assumption.

The general features of the pressure traces obtained near the end wall from the one-dimensional and axisymmetric solutions in Figure 10b are fairly similar. One difference is the presence of small oscillations in the computed axisymmetric pressure traces (particularly after the tailoring wave arrives). When looking at the many flow features created in the stagnation region in Figures 8 and 9, it is easy to understand that any reflected waves interacting with these features would produce very complicated pressure patterns. Figure 10b also allows an opportunity to compare the experimental and computed pressure traces created by the passage of the bifurcated shock. An enlargement of this region is presented in Figure 11.

Figure 11 reveals that there are several significant differences between the experimental and the computations. The largest discrepancy is the large computed pressure drop under the bifurcated foot where the experiments show more of a pressure plateau. This discrepancy is reinforced by the fact that going from the coarse grid to the fine grid increased the size of the computed pressure drop. The explanation for this difference is not known. It is interesting to note, however, that the experimental pressure traces presented by Sanderson[15] show a drop in pressure under the separated region (comparable to the current simulations) and that similar behavior is sometimes observed in the current experimental apparatus under different initial conditions. These observations support the physical nature of a pressure drop as well as the the ability of the transducers to capture such a phenomenon. Another difference between the experiment and the axisymmetric simulations is the size of the pressure overshoot after the separation bubble. Part of the disagreement can be attributed to the width of the pressure transducer (.21 inches). Both the pressure drop mentioned previously and the overshoot are created by features which are smaller than the width of the transducer so that some smearing of the experimental data is probably occurring. To illustrate possible influence of the transducer size, Figure 12 repeats the pressure trace in Figure 11 for the fine grid axisymmetric solution and also contains a pressure trace created by integrating the computed pressure over the surface of the transducer and dividing by the total transducer surface area. Some smearing in the computed traces is produced by this averaging but significant differences between the computations and the experiment remain.

There is room for improvement in the current simulations. While sufficient resolution has been achieved in the boundary layers for computing laminar velocity profiles, the thermal boundary layer is not sufficiently resolved. Future work will explore more formally examine the time accuracy of treating the viscous terms implicitly. The accuracy of treating *inviscid* terms implicitly will also be investigated. It is hoped that if an implicit time step at a CFL number greater than 1 based on the inviscid terms can be used for the small cells near the wall (while still retaining time accuracy in the regions away from the wall), then a much finer wall spacings and lower computational cost may be possible. Better resolution may explain some of the differences seen in this work between the experiments and computations.

The knowledge gained through the present research will be used to design experiments so that data can be acquired for validation of the predicted pseudo-shock structures and the arrival of driver gas in the stagnation region. Initial attempts at measuring this latter phenomenon will be done with heat-transfer measurements. Further studies will also allow many of the phenomena investigated analytically and experimentally by earlier works to be investigated numerically. These topics include shock bifurcation growth rates and the effects of turbulent boundary layers.

Conclusions

Axisymmetric simulations of the NASA Ames electric-arc driven shock tube have been done which include the wall boundary layer. The computed results have been compared with experimental data. These simulations have allowed the wall jet created by the reflected-shock/boundary layer interaction to be investigated numerically for the first time. These simulations support earlier analytical and experimental work which indicate that this mechanism can contribute to the reduction of the usable test time by allowing the driver gas to contaminate the stagnation region. It was also shown that even before any driver gas contamination, the wall jet creates a layer of lower temperature gas on the shock tube walls which might effect the interpretation of temperature measurements in the stagnation region. These results reinforce the fact that the stagnation region in shock tubes and shock tunnels is a region of complex flow phenomena. There were discrepancies between the experimental and computed pressure traces under the bifurcated foot of the reflected shock. The differences may be due to a lack of grid resolution or turbulent boundary layers.

The present results show that multi-dimensional simulations of shock tubes and tunnels are expensive but also valuable. An implicit treatment of the viscous terms was required to make the simulations practical. The lessons learned from this initial work are being used to determine future experimental and computational directions for the purpose of better understanding shock tube flows. Future experimental work will include gathering data at more locations to help verify the prediction of pseudo-shocks and the use of heat transfer and visual data to further study the driver gas contamination process.

Acknowledgements

Support for G. J. Wilson was provided by a grant from NASA to Eloret Institute (NCC2-420). Computer time was provided by the NAS Facility and by the Central Computing Facility at NASA Ames Research Center. The authors also gratefully acknowledge Myles Sussman's advice on implementation of the TVD scheme.

References

[1]Outa, E., Tajima, K., and Hayakawa, K., "Shock Tube Flow Influenced by Diaphragm Opening (Two-Dimensional Flow near the Diaphragm)," Proc. 10th Int. Symp. on Shock Waves and Shock Tubes, 1975, pp. 312-319.

[2]Mirels, H., "Shock Tube Test Time Limitations Due to Turbulent-Wall Boundary Layer," *AIAA Journal*, Vol. 2, Jan. 1964, pp. 84-93.

[3]Hooker, W. J., "Testing Time and Contact-Zone Phenomena in Shock-Tube Flows," *Physics of Fluids*, Vol. 4, Dec. 1961, pp. 1451-1463.

[4]Markstein, G. H., "Flow Disturbances Induced Near a Slightly Wavy Contact Surface or Flame Front Traversed by a Shock Wave," *J. Aeronaut. Sci.*, Vol. 24, 1957, pp. 238-239.

[5]Besnard, D. and Haas, J. L., "Two-Dimensional Simulation of Contact Surface instabilities in Shock-Tubes," 17th Symposium of Shock Tubes and Waves, 1990, pp.296-301.

[6]Mark, H., "The Interaction of a Reflected Shock Wave with the Boundary Layer in a Shock Tube, " NACA TM 1418, March, 1958.

[7]Holder, D. W., Stuart, C. M., and North, R. J., "The Interaction of a Reflected Shock with the Contact Surface and Boundary Layer in a Shock Tube," Aeronautical Research Council 22-891, Sept., 1961.

[8]Davies, L., "The Interaction of a Reflected Shock Wave with the Boundary Layer in a Shock Tube and its Influence on the Duration of Hot Flow in the Reflected-Shock Tunnel. Part I," Aeronautical Research Council-CP-880, 1966.

[9]Davies, L., "The Interaction of a Reflected Shock Wave with the Boundary Layer in a Shock Tube and its Influence on the Duration of Hot Flow in the Reflected-Shock Tunnel. Part II," Aeronautical Research Council-CP-881, 1967.

[10]Bull, D. C. and Edwards, D. H., "An Investigation of the Reflected Shock Process in a Shock Tube," *AIAA Journal*, Vol. 6, Aug. 1968, pp. 1549-1555.

[11]Davies, L. and Wilson, J. L., "Influence of Reflected Shock and Boundary-Layer Interaction on Shock-Tube Flow," *Phys. of Fluids* , Vol. 12, Suppliment I, 1969, pp. I-37 - I-43.

[12]Kleine, H., Lyakhov, V. N., Gvozdeva, L.G. and Gronig, H., "Bifurcation of a Reflected Shock Wave in a Shock Tube," Proc 18th Int. Symp. on Shock Waves and Shock Tubes, 1991, pp. 261-266.

[13]Stalker, R. J., and Crane, C. A., "Driver Gas Contamination in a High-Enthalpy Reflected Shock Tunnel," *AIAA Journal*, Vol. 16, March, 1978, pp.277-279.

[14]Ligong, X., Gourlay, C. M., and Stalker, R. J., "Reduction of Driver Gas Contamination in a Reflected Shock Tube by Boundary Layer Suction," Proc 16th Int. Symp. on Shock Waves and Shock Tubes, 1987, pp. 637-643.

[15]Sanderson, R.J., "Interprepation of Pressure Measurements Behind the Reflected Shock in a Rectangular Shock Tube, " *AIAA Journal*, Vol.7, July 1969, pp. 1370-1372.

[16]Matsuo, K., Kage, K., and Kawagoe, S., "The Interaction of a Reflected Shock Wave with the Contact Region in a Shock Tube," *Bull. of the JSME*, Vol. 18, No. 121, July, 1975.

[17]Strehlow, R. A. and Cohen, A., "Limitations of the Reflected Shock Technique for Studying Fast Chemical Reactions and Its Applications to the Observation of Relaxation in Nitrogen and Oxygen," *The Journal of Chemical Physics*, Vol. 30, No. 1, Jan. 1959, pp. 257-265.

[18]Brossard, J. and Charpentier, N.,"Experimental Study of Shock Wave Reflection in a Narrow Channel," Proc. 15th Int. Symp. on Shock Waves and Shock Tubes, 1985 pp. 163-169.

[19]Jacobs, P. A.,"Simulation of Transient Flow in a Shock Tunnel and a High Mach Number Nozzle," NASA CR 187606 (also ICASE Report 91-60).

[20]Cambier, J.L., Tokarcik, S., and Prabhu, D. K., "Numerical Simulations of Unsteady Flow in a Hypersonic Shock Tunnel," AIAA 17th Aero. Ground Testing Conf., Nashville, TN, 1992, AIAA Paper-92-4029.

[21]Jacobs, P. A.,"Numerical Simulation of Transient Hypervelocity Flow in an Expansion Tube," NASA CR 189615 (also ICASE Report 92-10).

[22]Yakano, Y., "Simulations for Reflected Shock Waves in Combustible Gas in Shock Tubes," Proc. 18th Int. Symp. on Shock Waves and Shock Tubes, 1991, pp. 869-874.

[23]Wilson, G.J., "Time-Dependent Quasi-One Dimensional Simulations of High Enthalpy Pulse Facilities," AIAA 4th Int. Aerospace Planes Conf., Orlando, FL, Dec. 1992.

[24]Sharma, S. P. and Park C.,"Operating Characteristics of a 60- and 10 cm Electric Arc-Driven Shock Tube - Part 1: The Driver," *Journal of Thermophysics and Heat Transfer*, Vol. 4, No. 3, pp. 259-265, 1990.

[25]Sharma, S. P. and Park C.,"Operating Charac-

teristics of a 60- and 10 cm Electric Arc-Driven Shock Tube - Part 2: The Driven Section," *Journal of Thermophysics and Heat Transfer*, Vol. 4, No. 3, pp. 266-272 , 1990.

[26] Yee, H. C., "A Class of High-Resolution Explicit and Implicit Shock-Capturing Methods," NASA TM 101088, Feb., 1989.

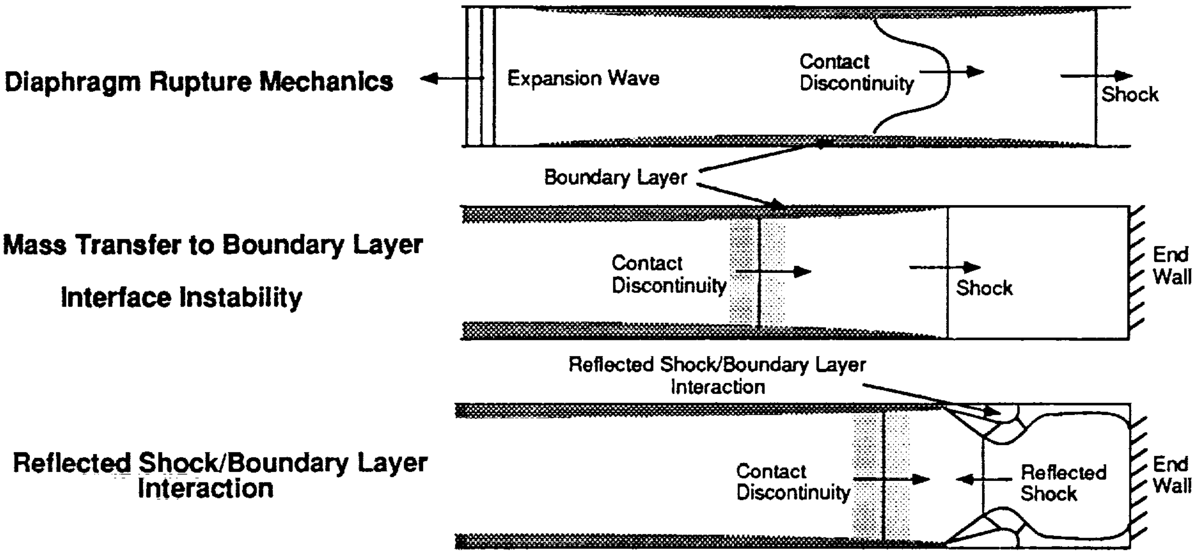

Fig. 1 Schematic diagram of multi-dimensional phenomena in shock tubes that lead to reduced test times.

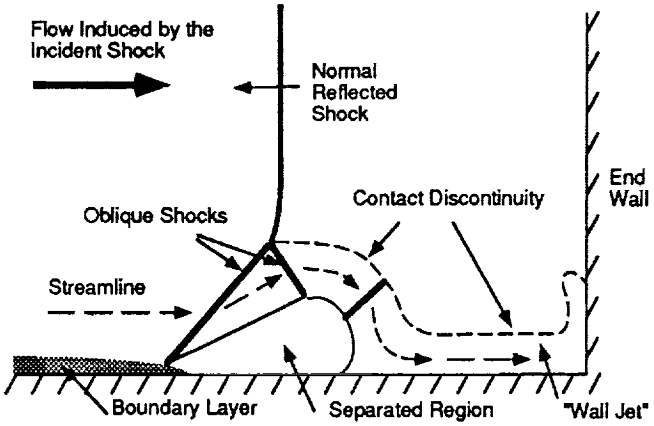

Fig. 2 Schematic diagram of the interaction of the reflected shock with the boundary Layer.

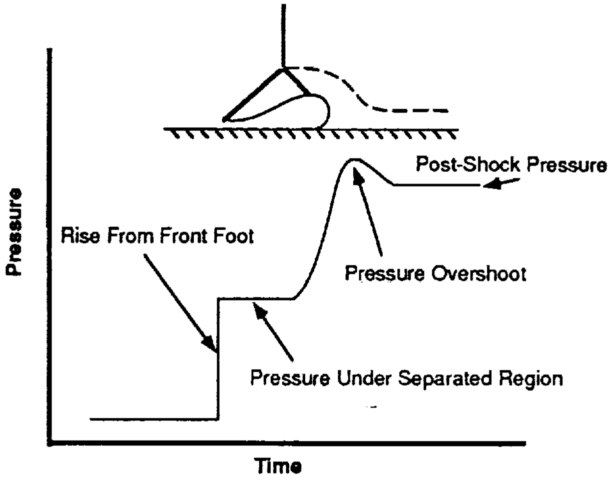

Fig. 3 Schematic diagram of the pressure trace under a bifurcated shock.

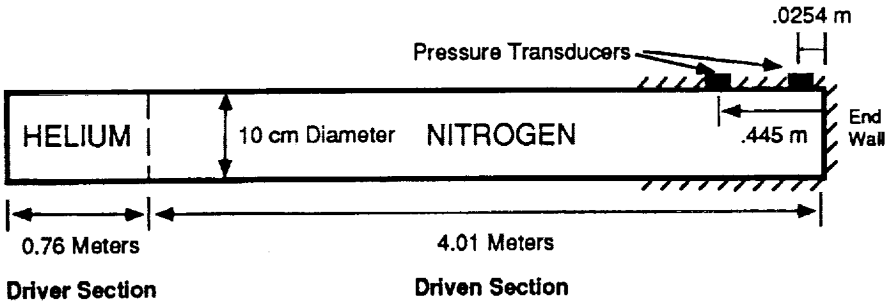

Fig. 4 Geometry and instrumentation for the NASA electric-arc driven shock tube.

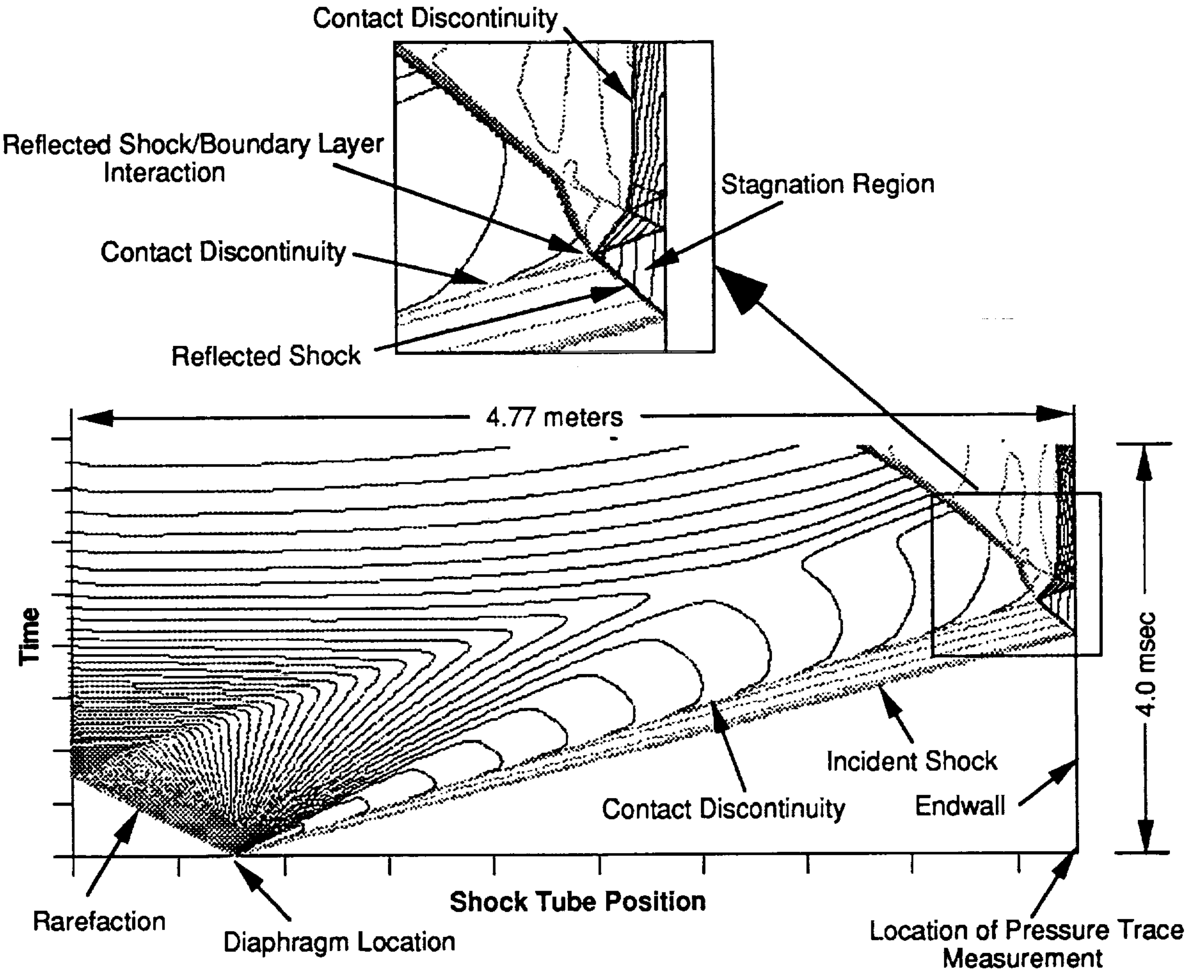

Fig. 5 Computed x-t diagram of temperature contours for a one-dimensional simulation of the NASA Ames electric-arc driven shock tube.

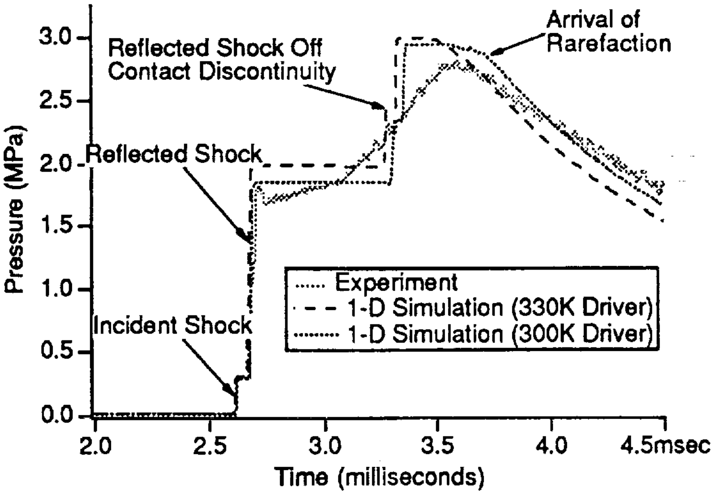

Fig. 6a Experimental and computed pressure traces .0254 m from the driven tube end wall.

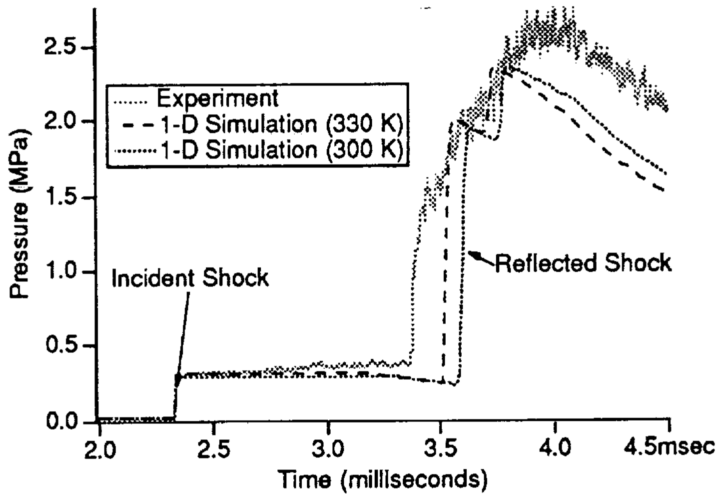

Fig. 6b Experimental and computed pressure traces .445 m from the driven tube end wall.

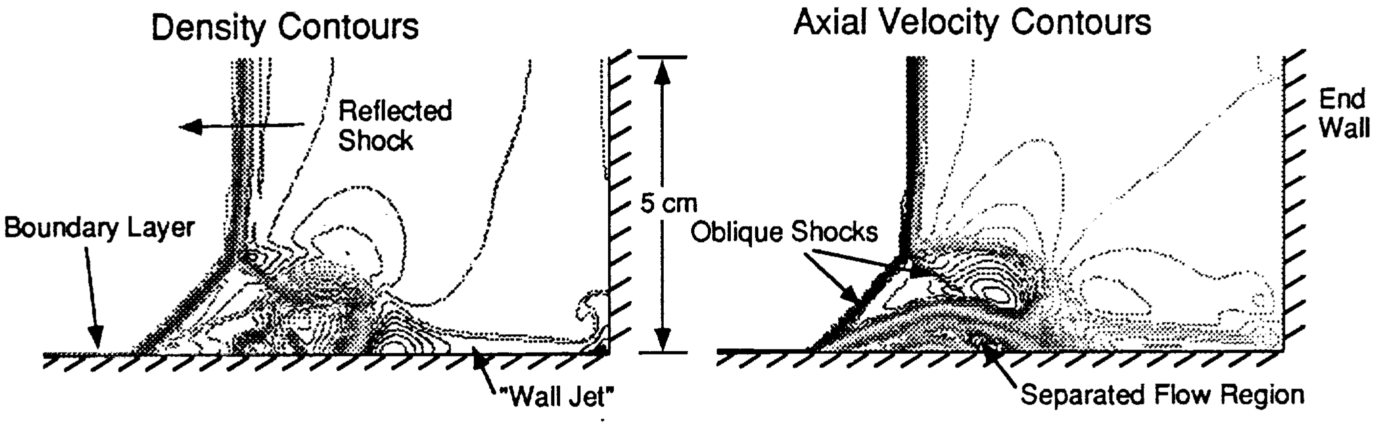

Fig. 7 Density and axial velocity contours showing the computed reflected shock/boundary layer interaction (t = 2.74 msec). Compare to the schematic diagram in Figure 2.

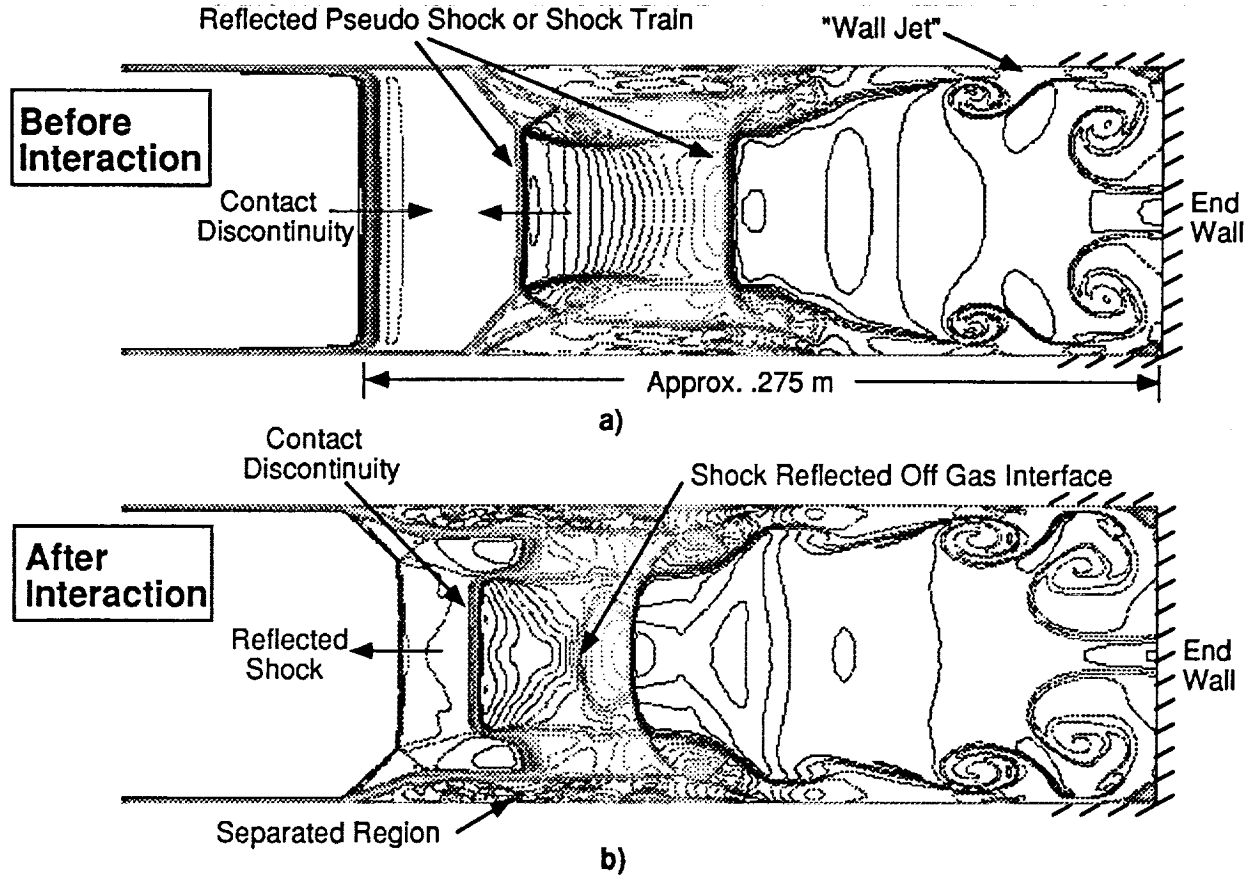

Fig. 8a,b Computed temperature contours before and after the interaction of the bifurcated reflected shock wave with the contact discontinuity: a) t = 3.00 msec b) 3.06 msec.

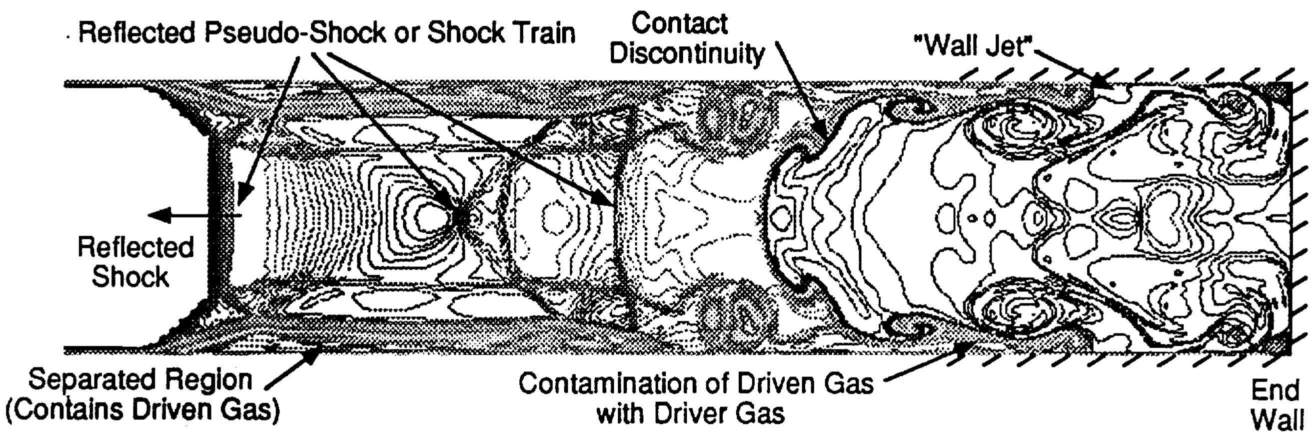

Fig. 9 Computed temperature contours after the interaction of the reflected shock with the contact discontinuity (t = 3.25 msec).

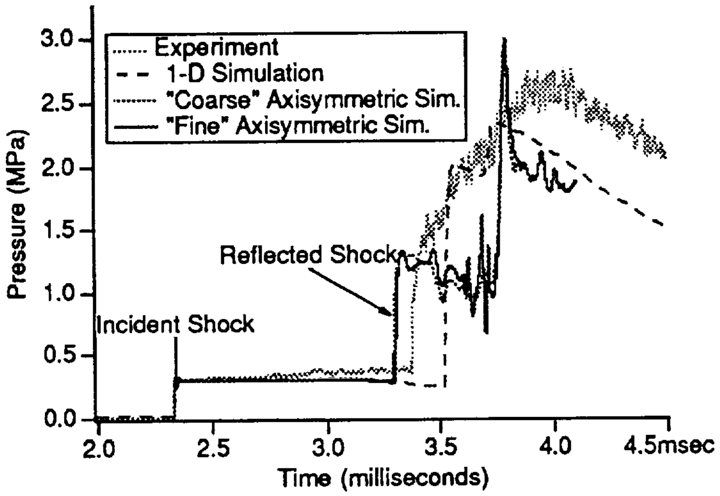

Fig. 10a Experimental and computed pressure traces .445 m from the driven tube end wall.

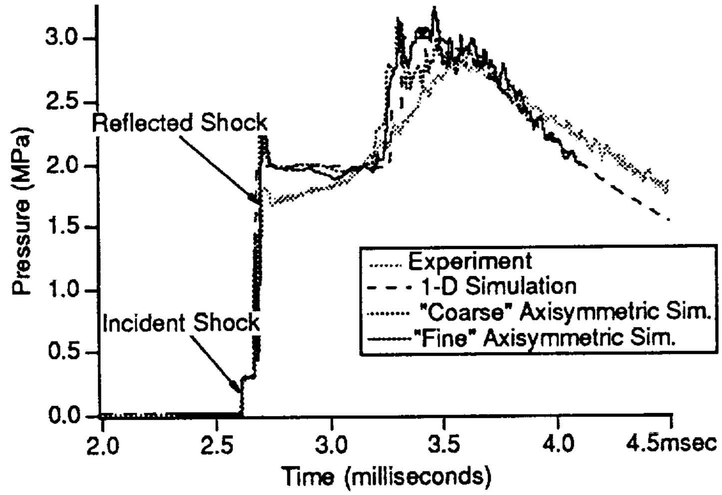

Fig. 10b Experimental and computed pressure traces .0254 m from the driven tube end wall.

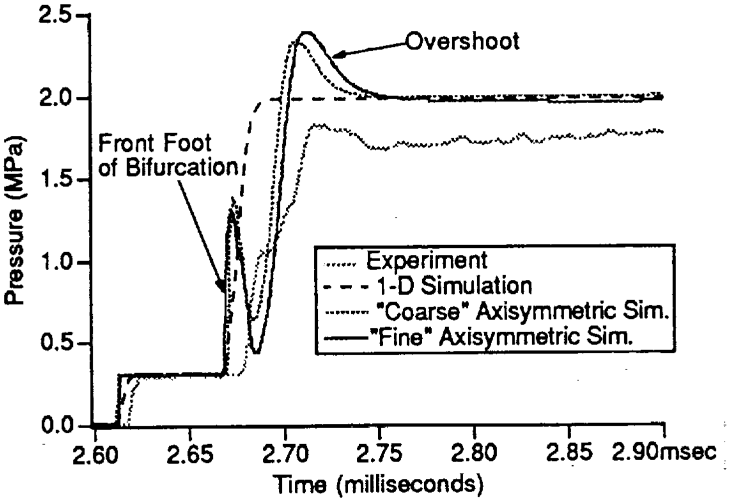

Fig. 11 Enlargement of Figure 10b showing the passage of the bifurcated reflected shock.

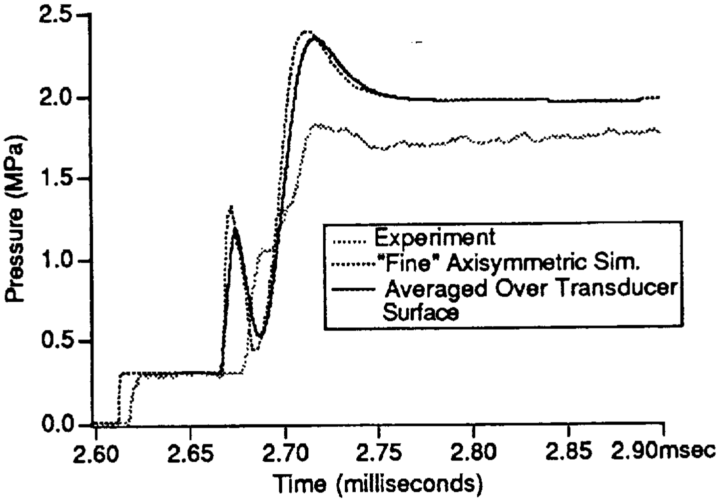

Fig. 12 Computed pressure trace showing the effect of the pressure transducer surface.

Computational Study of a Lunar Return Aerobrake Concept

Abstract for 31st Aerospace Sciences Meeting
Jan 11-14, 1993, Reno, NV

Susan Tokarcik*, Ethiraj Venkatapathy†, and Mike Tauber#

Abstract

The flowfield around a proposed lunar return aerobrake is computationally examined using both axisymmetric and three-dimensional formulations. Aerobrake configurations with four panel-shaped braking surfaces at 50°, 55°, and 60° to the freestream are calculated and the complex nature of the three dimensional flowfield is examined. It is shown that, despite the complexity of the three dimensional flowfield, the axisymmetric solutions give results very similar to the three-dimensional solutions for total drag coefficient. The full paper will examine the effect of changing the width of the braking surfaces on the relationship between the axisymmetric and three-dimensional calculations for drag.

Introduction

Future space exploration holds many exciting possibilities not the least of which are manned and unmanned missions to other planets. For this type of exploration, a lunar base may be employed as a way station for personel and equipment between the target planet and Earth. Transportation from a lunar base to Earth can be accomplished by an aerobraking vehicle. The lunar return aerobrake concept examined here is essentially a blunt nosed cylinder that uses four large, flat panels as braking and control surfaces, Fig. 1. The nose of the aerobrake is an ellipsoid so that drag from the nose region is maximized and heating is minimized. The radius of the body increases linearly from the beginning of the main body,where the nose ends, to the end where the panels attach. The main body is flattened where the panels attach such that the width of the main body in that region is equal to the nose diameter. The tapering of the lower portion of the panels and the flattening of the main body allow for a long hinge line so that the bending loads on the panels can be distributed along the hinge without unduly reducing the volume of the vehicle. The four panels are extended at angles of attack to the flow and are independently adjustable so that desired angles of attack and lift to drag ratios can be achieved ($L/D \approx 0.3$ for lunar return). The panels are large so that the ballistic coefficient (M/C_DA) is reduced thereby reducing the total heating to the vehicle. However the width of the panels is limited so that they can be stowed at 0° deflection while inside the launch vehicle. The payload capacity of the aerobrake is estimated to be 10,000 kg and the total volume to be 150 m^3. The vehicle is designed such that it could be launched from Earth aboard the proposed National Launch System (NLS), and it can also fit within the Space Shuttle payload bay (4.57 m x 18.28 m).

A large portion of the aerobrake trajectory will be dominated by real-gas effects. These effects can be approximated for initial design purposes by using an ideal-gas assumption which incorporates an effective value of specific heat ratio, γ. This method has been shown to be suitable for the calculation of drag and moment coefficients of bodies in real-gas flows.[1,2] The trajectory point chosen for the study corresponds to the peak pressure trajectory point, Table 1. At these freestream conditions the stagnation pressure is nearly 0.4 atm. and the flow is assumed

---

* Research Scientist, Eloret Institute, Mailing Address: NASA Ames Research Center MS 230-2, Moffett Field, CA 94035. AIAA Member.

† Research Scientist, Eloret Institute. AIAA Member.

Research Scientist, NASA Ames Research Center. AIAA Associate Fellow.

to be in chemical and thermal equilibrium. Therefore, the effective value of γ, γ=1.21, is chosen to be the specific heat ratio that corresponds to equilibrium conditions at the given speed and altitude.

Numerical Methods

The laminar flow about an aerobrake with all four panels at three different orientations, consisting of 50°, 55°, and 60°, is examined computationally. Because of the flat panels and the flattened portion of the main body, the aerobrake has only one octant symmetry (45° from the middle of a panel to the middle of a gap region). Therefore, a code that is capable of solving a three-dimensional (3-D) problem is required. However, the geometry is very nearly axisymmetric and can be estimated by creating a body of revolution using a line that runs from the nose of the aerobrake down the center of a panel. For this approximated geometry, an axisymmetric solver can be used. Solutions are computed for both the 3-D geometry as well as the axisymmetric geometry. Although the axisymmetric case runs much faster it has the disadvantage that the gaps that exist between the panels are neglected and the braking surface becomes a solid cone shape. Therefore, the effect of the gaps on the aerobrake flow cannot be examined using the axisymmetric geometry.

Two different CFD codes were used to calculate the axisymmetric flow around the aerobrake. The first code is an axisymmetric solver developed by Candler.[3] This is a finite-volume code that uses flux-vector splitting and Gauss-Seidel line relaxation to solve the Navier-Stokes equations. This code has been used previously for similar studies of hypersonic drag brakes.[2] The second code used is a 3-D solver, FL3D, developed by Venkatapathy.[4] This is a finite difference code that uses a three-dimensional, implicit time marching Navier-Stokes solution procedure. This code has previously been applied to axisymmetric and three-dimensional nozzle-plume and blunt body flows. The numerical method is a LDU-ADI scheme with Roe's averaging and MUSCL differencing. High order spatial accuracy is achieved by constructing MUSCL extrapolation of flow variables with a differentiable limiter. Roe averaged fluxes are constructed and the flux-difference from the higher order fluxes are used in this formulation. The LDU-ADI algorithm is a diagonal algorithm requiring minimal CPU per iteration and is applicable to steady flows, and the ADI sweeps of this formulation are quite efficient. Both the codes are ideal-gas solvers which can incorporate an effective value of γ.

Since no experimental data for this type of flowfield exist, the two codes were compared against each other to assure that the flowfields are calculated in a consistent manner. The codes were used to calculate the flowfield around an axisymmetric aerobrake with panels at 50°. The general flow structure, including the size of the separation bubble caused by the panels, compared well, and the differences in calculated surface pressures were less than 1%. The size of the separation region is important because it impacts the efficiency of the braking panels. The pressure within a separated region remains essentially constant even when part of that region is a compression surface such as the base of a panel. Therefore, the pressure increase that would exist if no separation occurs is not realized due to the separation.

For each set of panel angles, an axisymmetric and a 3-D solution were calculated. Although the 3-D solver could be used to calculate the axisymmetric solutions as well as the 3-D solutions, the axisymmetric solver was used because of its speed and convenience. Each axisymmetric solution was started from the same initial conditions and required approximately 10-15 minutes of CPU time on a Cray Y-MP. The first 3-D solution, the 50° panel case, was started from a blunt cone solution and required approximately 1.75 hours of CPU time. Subsequent 3-D solutions were started from the most similar preexisting 3-D solution. For example, the solution from the 50° panel case was used as the initial conditions for the 55° panel case. This reduced the CPU time to approximately 45 minutes.

The grids used are 61x47x63 for the 3-D calculations and 61x63 for the axisymmetric calculations. A representative axisymmetric grid is shown in Fig. 2. For the axisymmetric calculations, a solution-adapted[5] grid technique was used to refine important flow features. This technique will also be used for future 3-D calculations. For the 3-D calculations, symmetry is taken

advantage of and only one octant (45°) of the full 3-D geometry is computed. The surface grid for the 3-D calculations is shown in Fig. 3. Because the nose of the aerobrake is truly axisymmetric at the zero angle of attack considered here and is not influenced by the flow downstream, there is no need to compute the nose region using a 3-D formulation. Therefore, the portion of the flowfield that is actually computed by the 3-D solver begins at the main body. The inflow of the 3-D calculation is fixed to the values from the axisymmetric solution for the nose region. This reduced the grid size for the 3-D calculations to 46x47x63.

The assumption is made that the base flow region has very little affect on the total drag on the vehicle, since the pressure in that region is relatively low. However, because of the gaps, the base flow may have some effect on the main body. It is not clear what these effects may be, and a study of the full flowfield including the base flow is reserved for future work.

Results and Analysis

A comparison of the axisymmetric and 3-D calculations of surface pressure is made for an aerobrake with panels at 50°, Fig. 4. Although the axisymmetric solution shows a somewhat higher peak pressure on the panel, the surface pressure profiles look very similar indicating that, at least along that one line of the 3-D geometry, the axisymmetric solution comes very close to the 3-D solution. However, the limitations of the axisymmetric solution become apparent when simulated surface oil flow for the 3-D solution, Fig. 5, is examined. The surface pressure on the body in Fig. 5 is indicated by colors; dark blue is the lowest pressure, essentially freestream, and white the highest. The oil flow is show in yellow. The separation on the main body is largest in the center of the panel regions and decreases only slightly to the smallest size in the centers of the gap regions. The patterns of the oil flow indicate that a complex, multiple vortex structure exists within the separated region. This structure will be examined to a greater extent in the full paper.

Particle traces constrained to the plane that lies on the center of a panel are shown in yellow in Fig. 6. The particle traces indicate the size of the separated region and show more clearly than the surface oil flow the extent of the separation on the panels. Almost half of the panel length is contained within the separation. The effect of the separation on the panels is demonstrated by the painted surface pressure contours which show a very low pressure within the entire separated region. A cut away of the outer shock region is shown in this figure as a solid surface. The effect of the separation on the outer shock surface is indicated by the slight bulging of the surface in the region of the separation. Because of the flare-gap geometry, the shock structure in the flare region is truly three dimensional. It retains a conical shape in the gap regions and bulges out in the panel regions where it reflects off the panels. The shock stand off distance on the panels is greatest at the center of the panels. As the flow expands around the edge of the panels, the shock curves and the stand off distance decreases. This causes the peak pressure on the panels to shift off the center line to a position approximately midway between the panel center and the edge.

Particle traces constrained to the plane that lies in the center of a gap region are shown in Fig. 7. The particle traces terminate at the end of the computational domain. The separation in the gap region remains relatively large and, as is indicated by the traces, the recirculation region extents into the base area where the flowfield is not calculated. The flow at the outflow of the computational domain remains supersonic even within the separation, therefore, the extrapolation boundary conditions applied at the outflow region are valid. However, the effect of the base flow region on the main body is not captured by this representation.

The area of a circle with a radius equal to the outer radius of the base of the aerobrake main body is used as the reference area for calculating drag coefficients For the axisymmetric solutions, the total C_D is computed by calculating the drag assuming the panel to be solid and then subtraction out the portion of the drag that is produced where the gaps occur in the 3-D geometry. Since the 3-D flares are flat and not rounded as is assumed for the axisymmetric solution, the flare size for the axisymmetric solution is determined by assuming that the width of the flare is the base of a triangle with its vertex at the symmetry line. The angle opposite the base

of the triangle is then used to determine the arc length of the "axisymmetric flare". The tapered portion of the 3-D flare is assumed to be straight for the axisymmetric calculations.

A comparison of the total C_D calculated for the axisymmetric and 3-D solutions for 50°, 55°, and 60° flare angles is shown in Fig. 8. The most notable feature of this comparison is that, although the axisymmetric solution is incapable of computing the complex flowfield revealed by the 3-D solutions, the total drag calculated for the axisymmetric and 3-D solutions are very similar. This suggest that, for this type of geometry, it is not necessary to compute a full 3-D solution in order to calculate drag. Presently, calculations are being performed to compare different "flare-to-gap" ratios in order to determine whether the similarity between the axisymmetric and 3-D drag calculations is maintained. For these calculations, the flat-flare 3-D geometry is replaced by a geometry that would be axisymmetric if there were no gaps between the braking surfaces. This is done so that a one to one comparison of drag can be made between the 3-D and axisymmetric solutions. The results form these calculations will be given in the full paper.

Conclusions

The 3-D calculations of a proposed lunar return aerobrake show that a large portion of the main body as well as the braking surfaces are contained within a large, complex separated region. Despite the complexity of the 3-D flowfield, axisymmetric solutions predicted total drag coefficients very close to those calculated from the 3-D solutions for aerobrakes with panels at 50°, 55° and 60°. It is presently being determined whether different "flare-to-gap" ratios, i.e. different flare widths, will change the relationship between the axisymmetric and 3-D calculations of drag.

References

[1] Yates, L.A. and Venkatapathy, E., "Trim Angle Measurements in Free-Flight Facilities," AIAA Paper 91-1632, June 1991.

[2] Tokarcik, S.A., Venkatapathy, E., Candler G., Palmer, G., "Computational Flow Predictions for Hypersonic Drag Devices," AIAA Paper 91-3303, Sept. 1991.

[3] Candler, G., "The Computation of Weakly Ionized Hypersonic Flows in Thermo-Chemical Nonequilibrium," Ph.D. Dissertation, Dept. of Aeronautics and Astronautics, Stanford University, Stanford, CA, 1988.

[4] Venkatapathy, E., Feiereisen, W.J., and Obayashi, S., "Computational Studies of Hard Body and 3-D Effects in Plume Flows," AIAA Paper 89-0129.

[5] Davies, C. and Venkatapathy, E., "A Simplified Self-Adaptive Grid Method, Sage," NASA TM-102198, Oct. 1989.

altitude	56.6 Km
velocity	9082 m/s
density	$4.751\text{x}10^{-4}$
pressure	35.0 N/m^2
temperature	256.6 K
wall temperature	2700 K

Table 1 Freestream Conditions

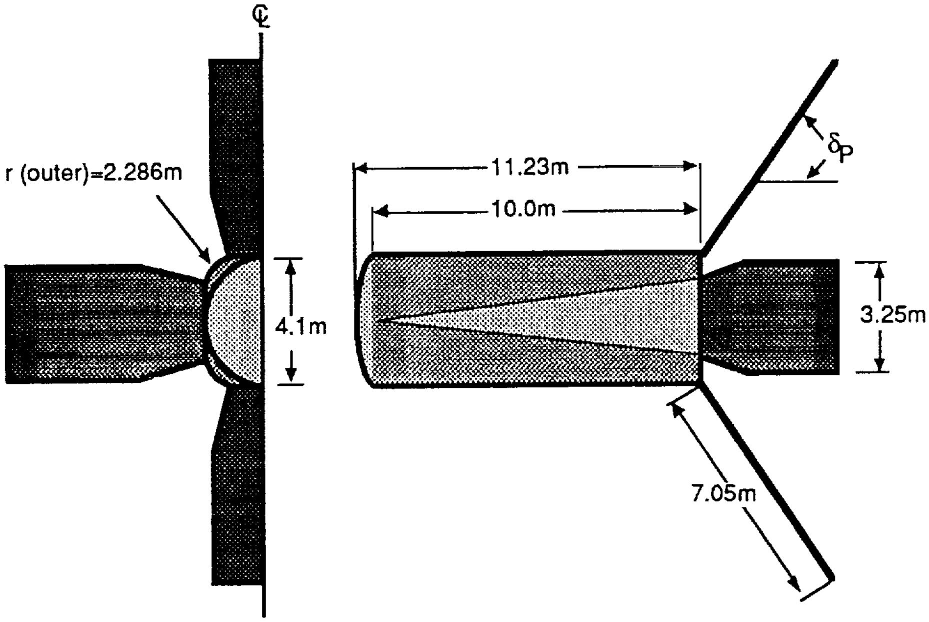

Figure 1. Lunar Return Aerobrake Concept

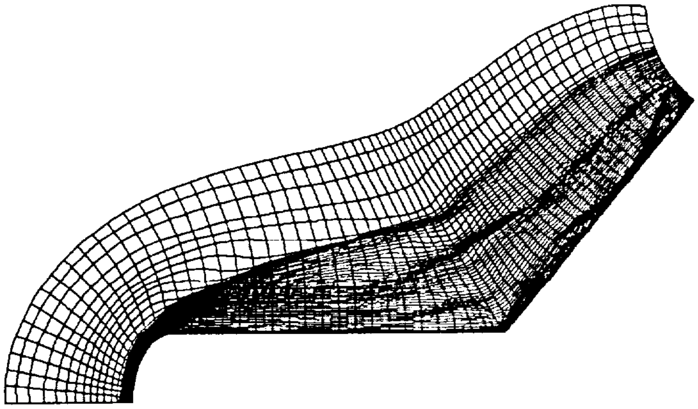

Figure 2. Solution Adapted Computational Grid for Axisymmetric Calculations

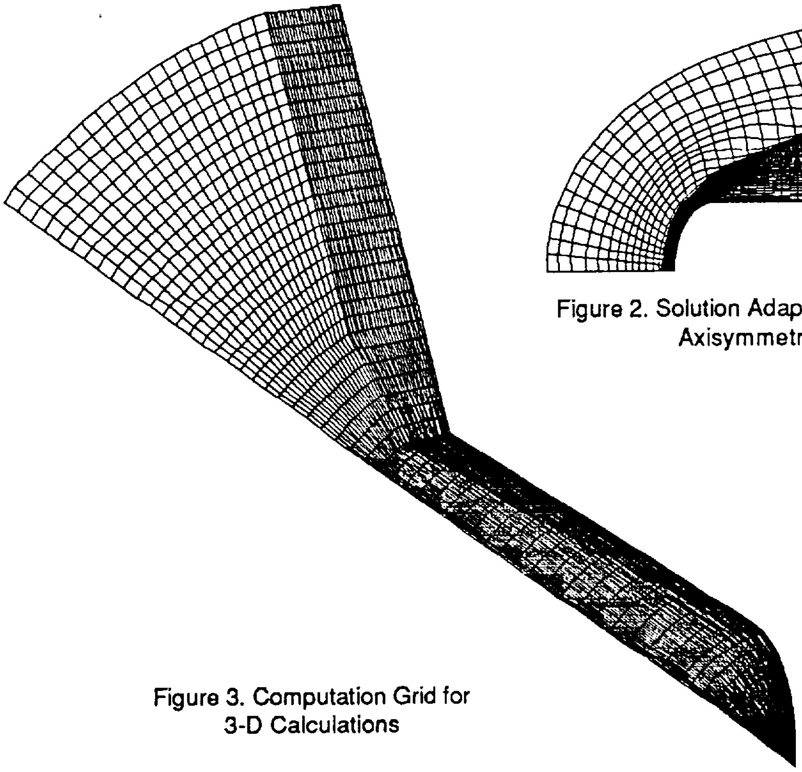

Figure 3. Computation Grid for 3-D Calculations

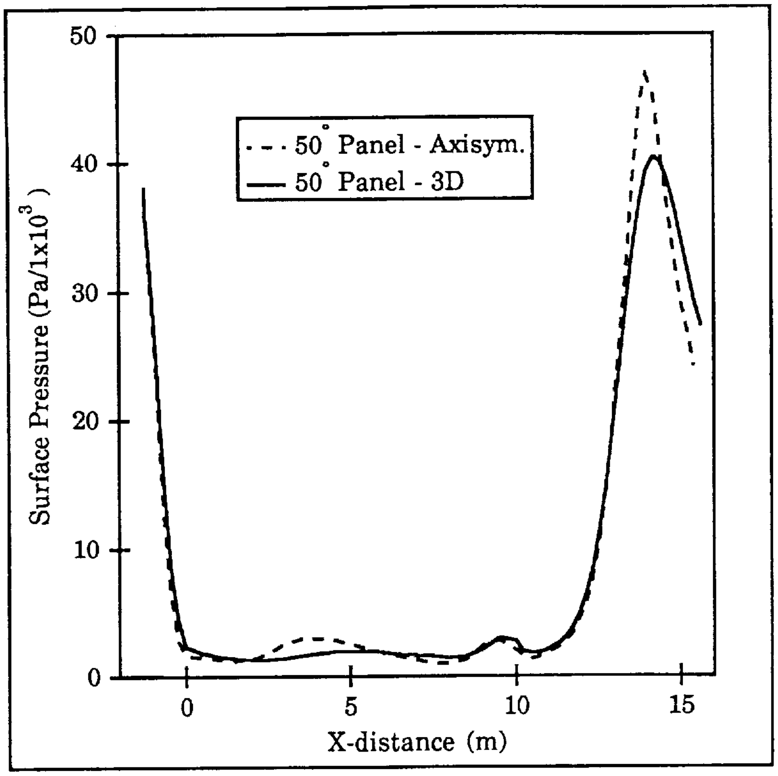

Figure 4 Surface Pressure Comparison

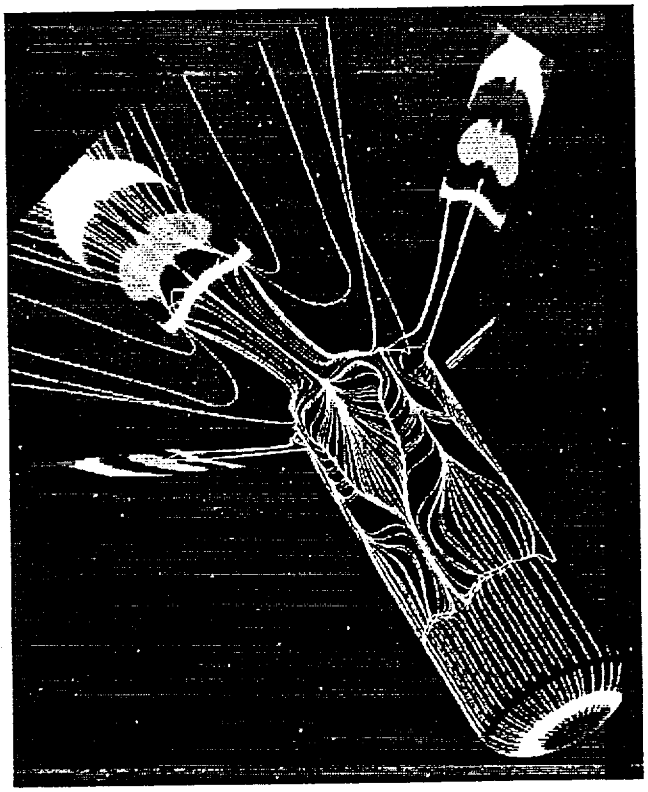

Fig 5

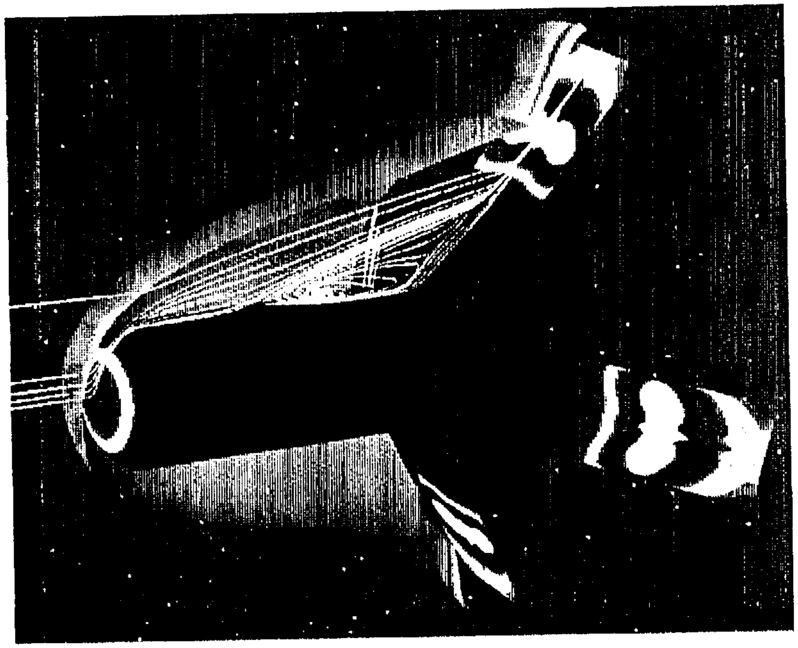

Fig. 6

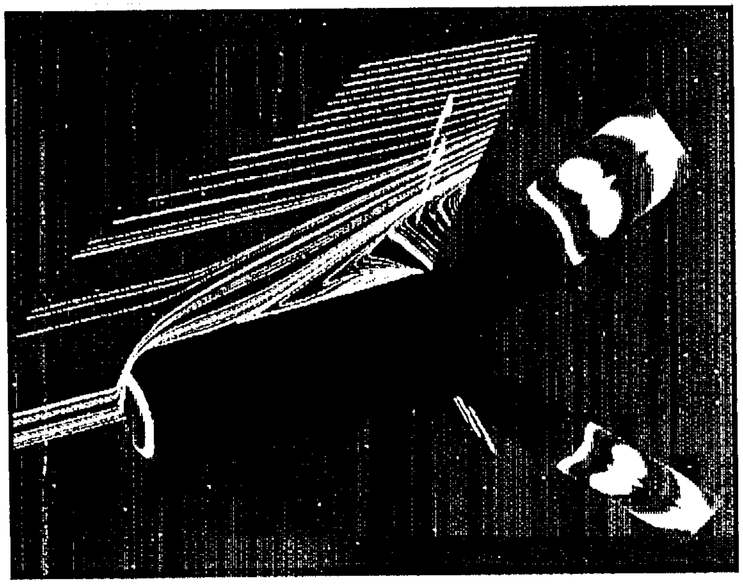

Fig 7

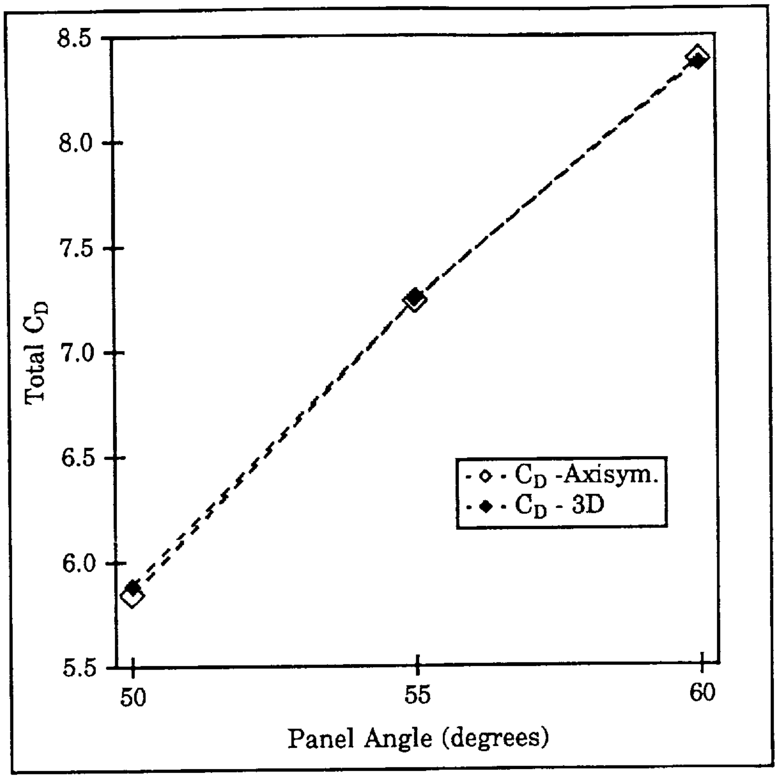

Figure 8 C_D Comparisons

Numerical Study of the Transient Flow in the Driven Tube and the Nozzle Section of a Shock Tunnel

Susan Tokarcik and Jean-Luc Cambier
Eloret Institute

ABSTRACT

The initial flow in the NASA Ames 16" shock tunnel is examined numerically. A finite-volume total variation diminishing (TVD) scheme is used to calculate the transient flow in the region of the driven-tube/nozzle interface. The flow is assumed to be inviscid and non-reacting. Two types of calculations are presented: a series assuming that the flow is axisymmetric, and a calculation assuming the flow is two dimensional. The differences between the 2-D and the axisymmetric flows are examined. The axisymmetric solutions predict that a vortical structure is formed in the driven-tube/nozzle interface region and propagates into the driven tube along with the reflected shock. Several parameters are examined in order to determine their effect on the vortex structure: 1) varying throat size, 2) changing the shape of the juncture between the driven tube and the nozzle, and 3) changing the shape of the driven tube's end wall.

INTRODUCTION

The Ames 16" facility, shown schematically in Figure 1, can be considered as a typical example of a shock tunnel for hypersonic flows. The shock tunnel is about 70 meters long and is composed of a driver section (17" diameter) filled with a light combustible mixture, a long driven tube (filled with the test gas at low pressure), a supersonic nozzle, and finally a test section. The test times of this facility are typically 5 to 20 milliseconds, and the time for the main shock to propagate from the main diaphragm to the end of the driven tube is on the order of 7 millisec. The shock partially reflects at the driven tube end-wall bursting the second diaphragm and initiating flow in the nozzle. The reflected shock eventually interacts with the contact discontinuity (CD) which separates the test gas from the driver gas. More detailed information about shock tunnel operations can be found in ref. [1]. The test time is measured from the time the flow conditions in the nozzle stagnation region become steady, until the CD reaches the end of the driven tube, and the nozzle flow becomes contaminated with the driver gas.

The initial, unsteady flow in the shock tunnel is important because it directly affects the quality of the resulting test flow. Because the initial flow is difficult to examine experimentally, numerical analysis is used to simulate the start-up process. Recent numerical studies, ref. [2] and ref. [3], have predicted that the flow in the region of the driven tube and nozzle interface is quite complex. A particularly important feature is a vortex system which is formed in the center of the driven tube. This vortex may have an impact on the quality of the test flow as well as the overall test time; it is therefore examined in more detail in this study.

NUMERICAL ANALYSIS

A finite-volume, explicit, total variation diminishing (TVD) scheme developed by Cambier is used to calculate the flow which is assumed to be inviscid and non-reacting. The code has first order as well as second order spatial accuracy capabilities. Most calculations were performed using second-order accuracy; calculation which used first-order accuracy are noted as such. This code has been employed previously to calculate similar transient flows, see ref. [2].

90 deg Expansion Corner Flow

A validating exercise was performed to show that the code is capable of adequately resolving transient flows which are highly vortical in nature. A schematic sketch of the shock tube experiment, which was conducted by Mandella [4], and Mandella and Bershader [5] is shown in Figure 2. The shock tube, which has a 5cm x 5cm cross section, produced a planar shock wave with a Mach number $M_S=2.0$. The end of the shock tube was open to ambient conditions. Two parallel plexi-glass plates were attached to the end of the shock tube in order to keep and shock wave and the rest of the flow field two dimensional. The planar shock wave starts to diffract as soon as it leaves the shock tube and forms a curved shock wave. The experimental interferogram (Figure 3) show that, as the shock wave propagates into the test section, vortices are formed in the vicinity of each of the 90 deg expansion corners. Also seen are the contact surface, slipstream, and Prandtl-Meyer fan which interact with the vortices.

Figure 4 shows computed density contours at approximately the same time as the experimental interferogram. Comparing the two figures demonstrates that the computations are able to predict all the major flow features mentioned above with good accuracy.

Shock Tunnel Driver/Nozzle Flow

The starting conditions used for all the shock tunnel calculations correspond to the point in time when the main shock has reached the driven tube's end wall and the secondary diaphragm has ruptured. The flow conditions in the driven tube at this initial point are calculated taking into account chemistry and correspond to the conditions for a main shock with a speed of 12 km/sec and a driver tube pressure of 6000 lbs/sq. in: P=50.76 ATM, T= 3674 K, U=2710 m/s, $N=0.6042\times10^{-4}$, O=0.04091, $N_2=0.7341$, $O_2=0.1456$, NO=0.07934 (unit of mole fraction). The initial conditions in the nozzle correspond to air with a 79% N_2 and 21% O_2 mixture at a pressure of 1.3×10^{-4} ATM and a temperature of 298 K. As mentioned earlier, chemical reactions are not considered in this study, and the flow is assumed to be chemically frozen.

As was mentioned earlier, the initial flow in the region of the driven-tube/nozzle interface is quite complex. Numerical calculations have predicted that a vortex forms at the center line of the driven tube and propagates with the reflected shock into the driven tube. The vortex can cause the reflected shock to bulge at the center line (Figure 5) which may cause premature contamination of the test gas by the driver gas thus decreasing the test time.

Several aspects of the calculated transient flow are examined: 1) the effects of the numerical method on the resulting flow field, 2) the effects of geometry, 3) the effects of time (how the flow field changes as the reflected shock and vortex structure continues to propagate into the driven tube and 4) an axisymmetric versus two-dimensional flow field.

(Note: the full paper will also examine the interaction of a bulging, reflected shock with a CD.)

Numerical Effects

Two components of the numerical technique are examined: 1) grid effects and 2) first order versus 2nd order spatial accuracy. Figure 6a shows a second-order solution on a uniform grid at a time t=80 µsec after shock arrival at the driven tube's end wall (80 µsec from starting the calculation). This figure shows that the reflected shock has formed a coned shaped at the centerline. Figure 6b shows a solution at the same time (and same accuracy), however the aspect ration of the grid is $\Delta X:\Delta Y=3:1$. In other words, the grid is clustered at the axis. Comparing these two figures it becomes evident that the jetting effect at the axis has been aggravated by the aspect ratio of the grid. This peculiar formation can also be seen in the results of P. Jacobs, ref. [3]. This structure is possible if an intense and high velocity jet of gas is produced and maintained on the axis, which is a highly singular and unphysical behavior. One explanation of this phenomenon, which is described in ref. [2], is that the jetting is caused by the numerical representation of the singular axis in the axisymmetric formulation. It was assumed in ref. [2] that the problem arose from the axisymmetric pressure correction term which is not part of the monotonic (TVD) fluxes and acts as a non-conservative momentum source that behaves as $1/(\Delta r)$ near the axis. Therefore clustering points near the axis (thus accentuation the $1/(\Delta r)$ term) aggravates the jetting. However, further study has shown that the jetting phenomenon can also occur off the axis as well as in solutions which have two-dimensional formulations. Therefore, although the pressure correction term is still believed to be a contributing factor in the axis problem, it has become clear that there is still an, as yet, unknown cause for the jetting in other cases.

Despite not fully understanding the cause of the problem, it has been determined that coarsening the grid in the radial direction alleviates the problem in all instances. Figure 6c show the same case as computed in Figures 6a and 6b, however the grid aspect ratio has been changed so that $\Delta X:\Delta Y=3:1$ (near the axis). Comparing Figures 6a, 6b and 6c shows that the unphysical jetting effect, which is present in both the $\Delta X:\Delta Y=3:1$ and the uniform grid, is eliminated in the third solution by the proper choice of grid aspect ratio.

Another way to somewhat alleviate the jetting problem is to compute the solution using only first order spatial accuracy. This essentially causes the numerical scheme to become more dissipative which in turn mitigates the jetting effect. Using a first order formulation does have some serious consequences, however. Figures 7a and 7b compare two solutions, each at t=200 µsec and each on the same $\Delta X:\Delta Y=1:3$ grid. The first solution employed first-order spatial accuracy while the second used second-order accuracy. These figures show that as the reflected shock continues to propagate down the driven tube, the dissipative, first-order scheme loses any trace of the vortex structure while the second-order solution clearly shows that the vortex structure not only remains but has increased in size. Therefore, it is clear that the study of this transient flow must be conducted using at least second-order accuracy and employing grids which are coarsened in the radial direction. All flow solutions presented in the remainder of the study employ the latter two criteria.

Effects of Geometry

Assuming that all major numerical effects have been removed from the problem, the effects of changing the geometry in the driven-tube/nozzle interface region is now studied. Several parameters are examined: 1) changing the throat size, 2) changing the shape of the juncture between the two sections, and 3) changing the shape of the driven tube's end wall.

The area ratios of the nozzle throats examined are A/A*=100, A/A*=190, and A/A*=570. Figures 8a, 8b, and 8c show temperature contours for these three throat sizes at t=120 µsec. A comparison of the temperature contours indicates that, while the flows within the nozzle sections are somewhat different in each case (in particular, the shock interaction in the subsonic portion of the throat is intensified by the smaller throats), the vortex structures in the driven tubes are identical. Therefore, it is concluded that the size of the throat has at most a minimal affect on the formation of the vortex in the driven tube.

The affect of the size of the aperture at the end of the driven tube is now examined. The size of the hole in the driven tube was increased by 35%, Figure 9, and the flow was recomputed for the A/A*=190 throat. The temperature contours show that for this case the flow in the nozzle section is unaffected, and the flow is the driven tube is somewhat affected. The central vortex structure is unchanged, however the length of the "arms" on either side of the central vortex have increased causing an overall size increase of 16% over the case discussed above (which is significantly less than the 35% increased in aperture height). From this it can be concluded that increasing the aperture height increases the overall size of the affected area of the reflected shock, however the increase is not one to one.

Another change that can be made to the driven-tube/nozzle juncture is rounding the interface. Rounding the interface resulted in an aperture which was slightly larger that the 35% increase case discussed above. Again, the overall structure and size of the central vortex was unchanged, however the size of the affected area increased significantly (43% larger than for the original geometry). Another important difference was that the center vortex observed in this case protruded slightly further into the driven tube than for any of the other cases (all of which protruded to the same distance). Also, the flow field in the nozzle section is affected in this case. In the subsonic portion, the shocks emanating from the juncture corners are no longer present, and compression waves have appeared downstream of the throat.

The last geometric change that is examined is altering the shape of the end-wall of the driven tube. Figure 10 shows how the end-wall has been angled outward from the juncture so that it is no longer vertical and, again, the juncture between the two section is rounded. This flow field (t=120 µsec) looks considerably different than those examined so far; there are strong shocks in both the subsonic and supersonic portions of the nozzle, and the character of the vortex structure has changed. The overall vortex structure is much larger than for the original geometry, and the central structure extends significantly further into the driven tube than for any of the other cases. Also, the central vortex itself is significantly larger than in the other cases where the height of the overall structure changed but the central structure remained virtually unchanged.

For the bulging of the reflected shock to be of importance it would have to persist as the shock continued to travel up the driven tube to the CD where the bulge would cause the driver gas to be prematurely mixed with the test gas. The original A/A*=190 case was continued for a significant time (t= 400μsec), and it was found that the vortices did appear to dissipate as the reflected shock continued to propagate down the driven tube. Therefore, the likelihood of premature mixing will depend on how much time elapses before the CD and the reflected shock interact.

A question that arises is whether the formation of the vortex is an axisymmetric phenomenon. Figures 11a and 11b show temperature contours for a 2-D calculation using the original A/A*=190 geometry at t=120 μsec and t=160 μsec. For the two-dimensional cases, the centerline vortex does not form; furthermore, the portion of the reflected shock near the centerline actually lags behind the rest of the shock. Even at t=160 μsec the centerline region of the shock has not caught up with the rest of the shock.

The behavior of the flow field for a three-dimensional formulation may be presented in the full paper.

CONCLUSIONS

It was found that refining the grid in the radial direction (such that $\Delta x:\Delta y > 1$ produced an unphysical, jetting behavior in the solution. A partial explanation was given, and changing the grid aspect ratio such that $\Delta x:\Delta y \geq 3$ was presented as a solution to the jetting problem. Spatially first order accurate solutions were found to be too dissipative to resolve the vortex structure in the driven tube.

Several geometry changes were made to both the nozzle section and the driven tube to determine their effect on the flow field. It was found that 1) changing the throat area had an unobservable effect on the flow in the driven tube and relatively minor effects on the nozzle flow, 2) increasing the height of the aperture in the driven tube increased the size of the overall vortex structure; however the size increase was not one to one and the size of the core structure was unchanged, 3) rounding the juncture between the nozzle and driven sections caused the size of the vortex structure to increase markedly, and also caused the reflected shock to bulge slightly more 4) changing the shape of the driver tube's end-wall such that it was no longer vertical caused a more intense vortex to form in the driver tube which caused a significantly larger bulge in the reflected shock, and 5) the vortex structure eventually dissipated at the reflected shock continued to propagate into the driven tube.

Solutions assuming that the flow was two dimensional showed no that no vortex existed in the driven tube, and the reflected shock near the centerline actually lagged behind the rest of the shock instead of protruding ahead of it.

REFERENCES

[1] A. G. Gaydon & I. R. Hurle, "The Shock-Tube in High-Temperature Chemical Physics," Reinhold Publ., 1963.

[2] J.-L. Cambier, S. Tokarcik, & D. Prabhu, "Numerical Simulation of Unsteady FLow in a Hypersonic Shock Tunnel Facility," AIAA Paper No. 92-

4029, presented at the AIAA 17th Aerospace Ground Testing Conference, Nashville, TN, July, 1992.

[3] P. A. Jacobs, "Simulation of Transient Flow in a Shock Tunnel and a High Mach Number Nozzle," 4^{th} Int. Symp. on Computational Fluid Dynamics, Davis, Sept., 1991.

[4] M. Mandella, "Experimental and Analytical Studies of Compressible Vortices," Ph.D. thesis, Dept. of Applied Physics, Stanford University, Stanford, Ca, 1987.

[5] M. Mandella & D. Bershader, "Quantitative Study of Compressible Vortices: Generation, Structure and Interaction with Airfoils," AIAA Paper No. 87-0328, Jan. 1987.

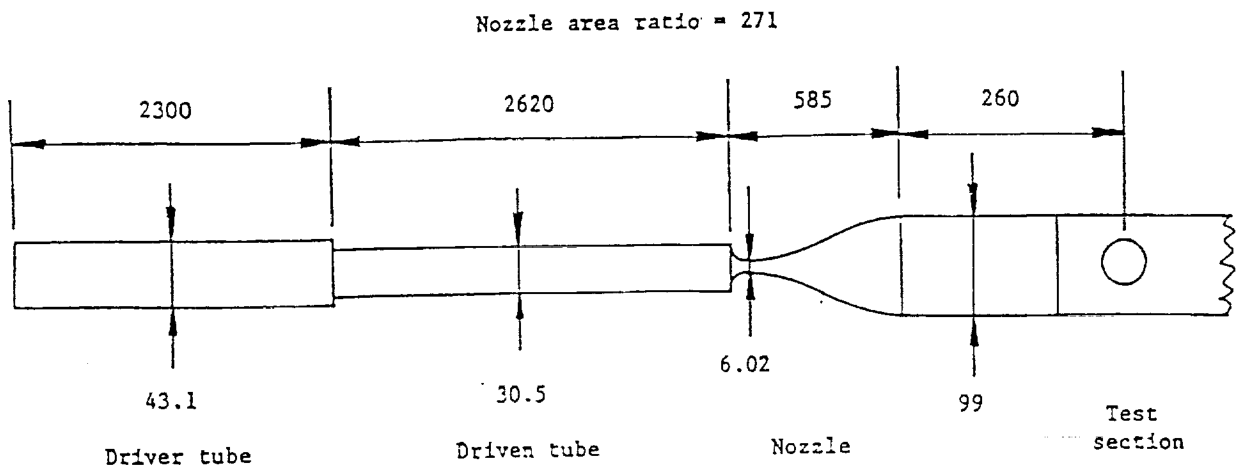

Fig. 1 Schematic of the Ames 16" Shock Tunnel Facility

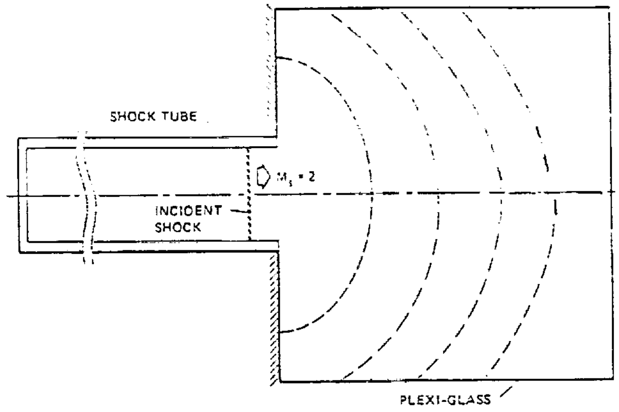

Fig. 2 Schematic of the Shocktube Experiment by Mendella and Bershader

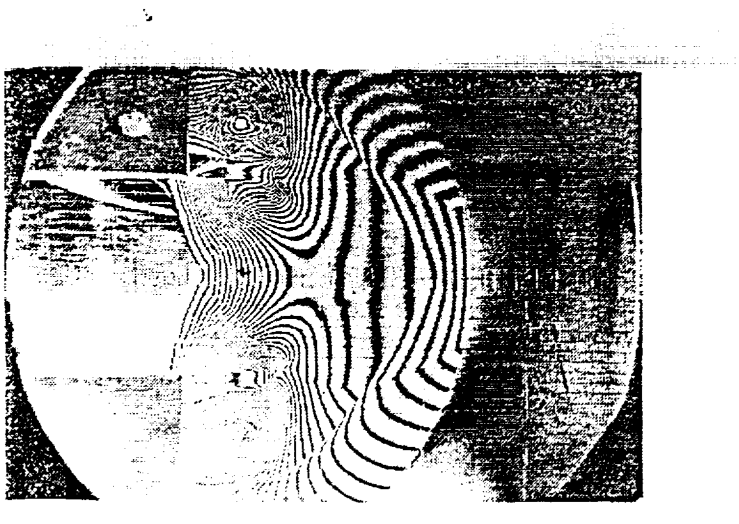

Fig. 3 Experimental Interferogram of Flow Around 90 deg Expansion Corners

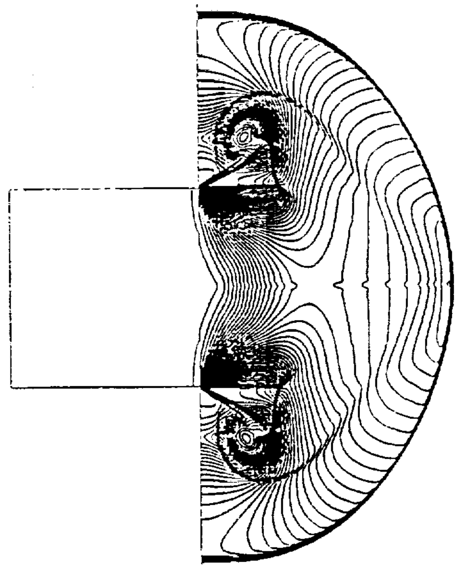

Fig. 4 Calculated Density Contours of Flow Around 90 deg Expansion Corners

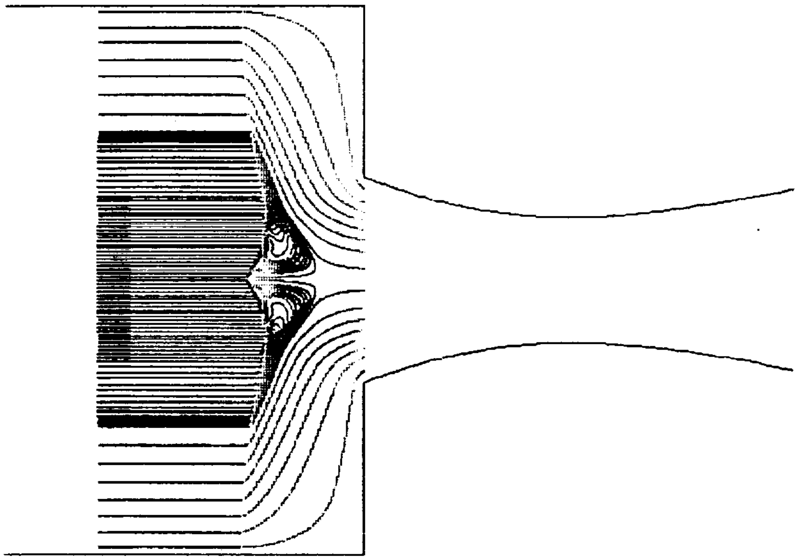

Fig 5. Particle Traces Colored by Pressure Demonstrate the Existence of a Vortex System At the Center of the Driven Tube which Causes the Center Portion of the Reflected Shock to Bulge Upstream.

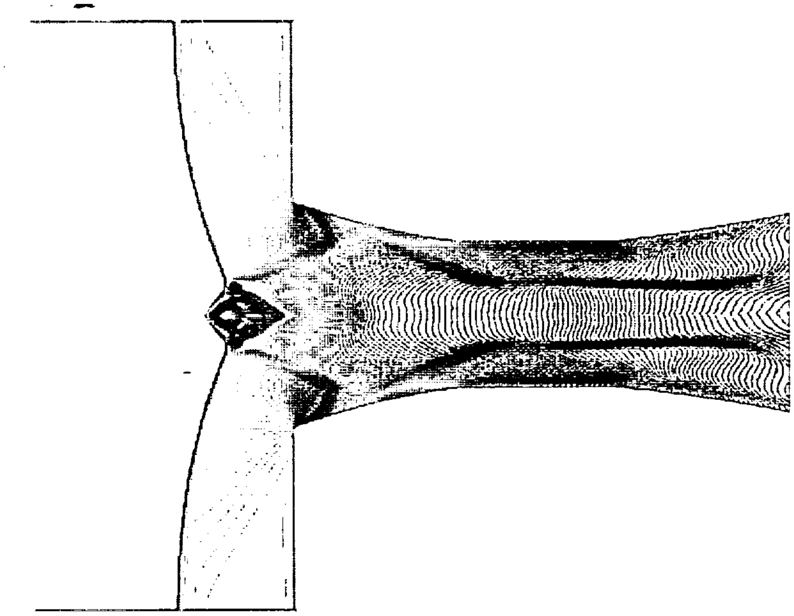

Fig. 6a Temperature Contours at time=80μsec Computed on a Uniform Grid with 2nd Order Spacial Accuracy

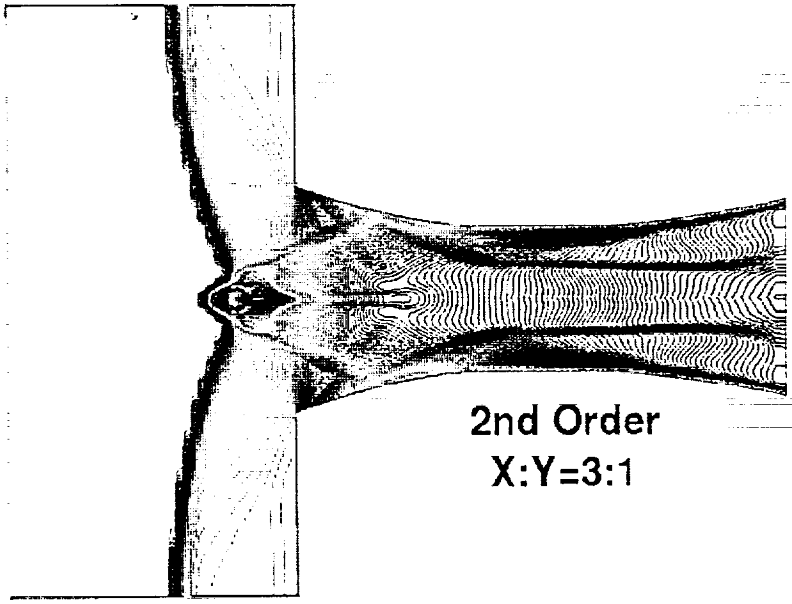

Fig. 6b Temperature Contours at time=80μsec Computed on a Grid with Aspect Ratio Δx:Δy=3:1

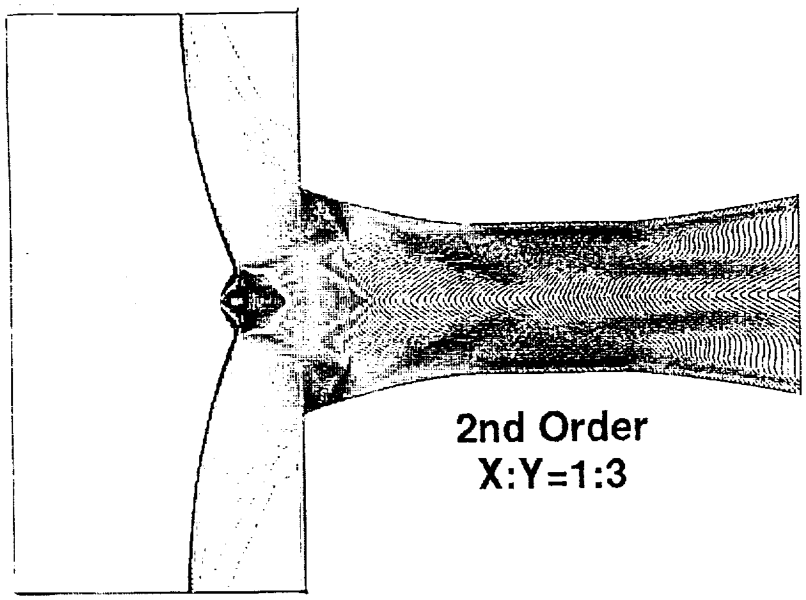

Fig. 6c Temperature Contours at time=80μsec Computed on a Grid with Aspect Ratio Δx:Δy=1:3

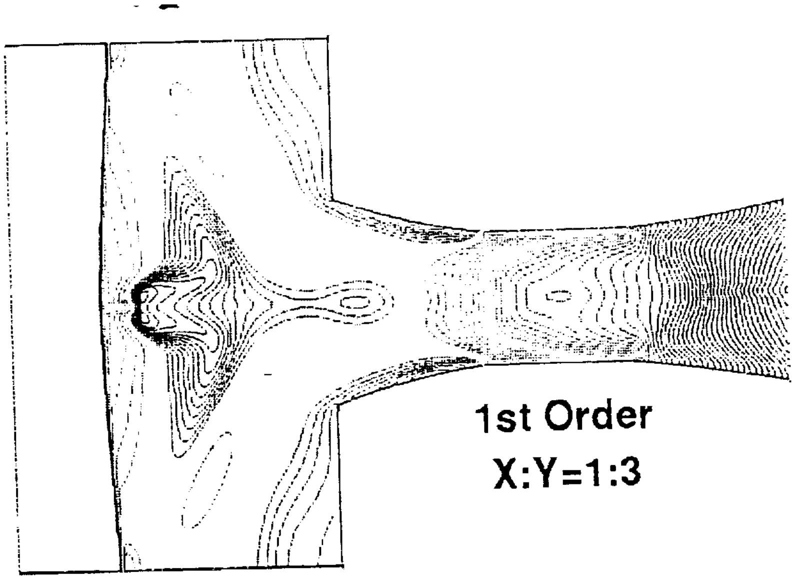

Fig. 7a Temperature Contours at time=120μsec Computed on a Grid with Aspect Ratio Δx:Δy=3:1 and 1st Order Spacial Accuracy

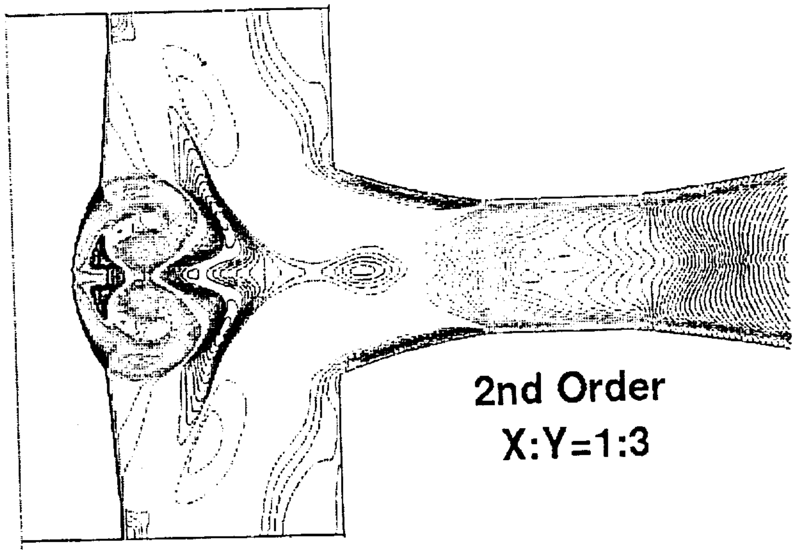

Fig. 7b Temperature Contours at time=120μsec Computed on a Grid with Aspect Ratio Δx:Δy=3:1 and 2nd Order Spacial Accuracy

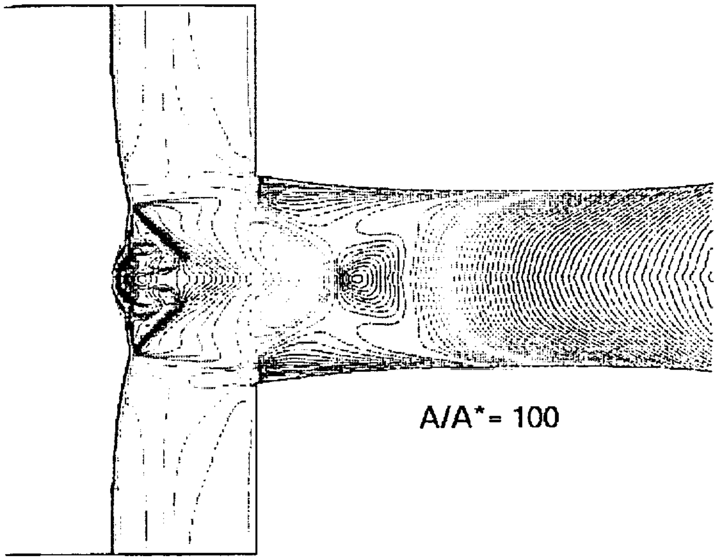

Fig. 8a Temperature Contours at time=120μsec Computed on a Grid with Aspect Ratio $\Delta x:\Delta y=3:1$ and 2nd Order Spacial Accuracy for a Large Throat Size

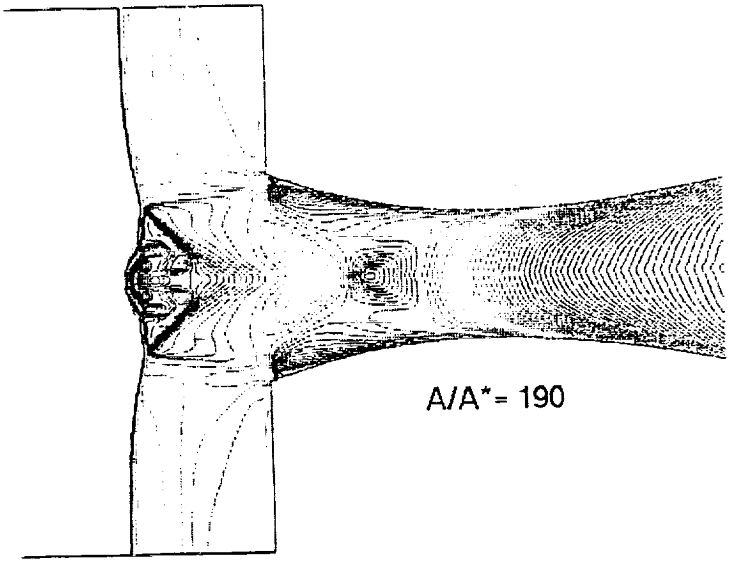

Fig. 8b Temperature Contours at time=120μsec Computed on a Grid with Aspect Ratio $\Delta x:\Delta y=3:1$ and 2nd Order Spacial Accuracy for a Medium Throat Size

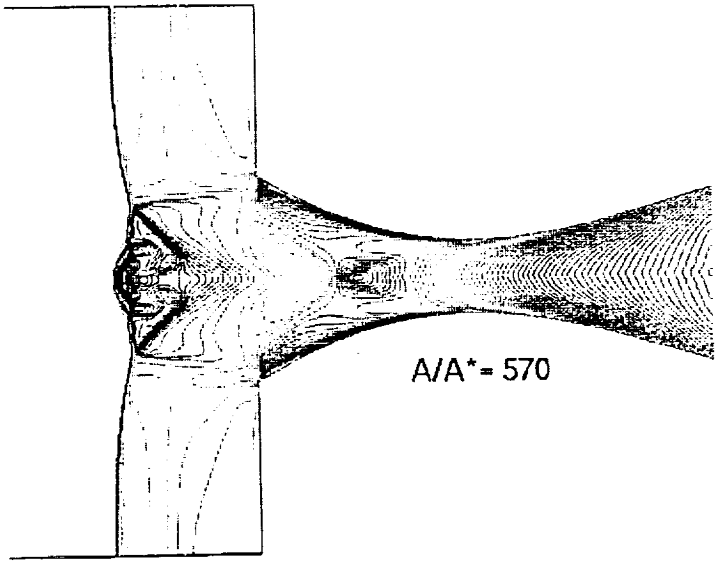

Fig. 8c Temperature Contours at time=120μsec Computed on a Grid with Aspect Ratio $\Delta x:\Delta y=3:1$ and 2nd Order Spacial Accuracy for a Small Throat Size

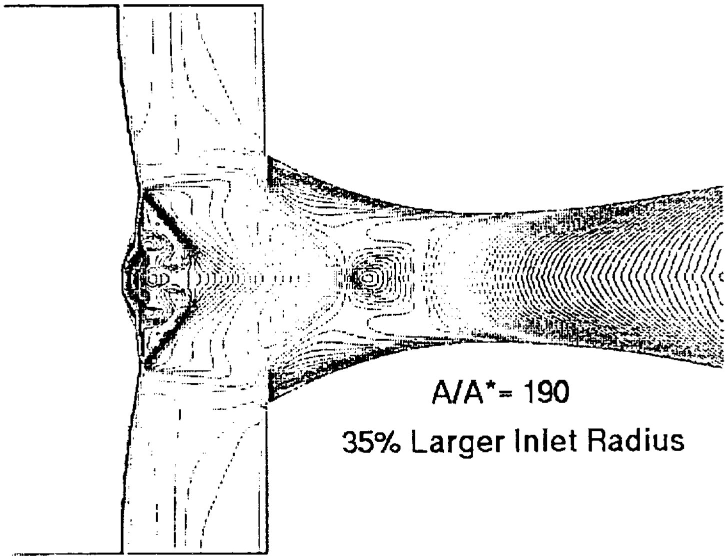

Fig. 9 Temperature Contours at time=120μsec Computed for a Geometry with a 35% Larger Aperature in the Driven Tube End Wall

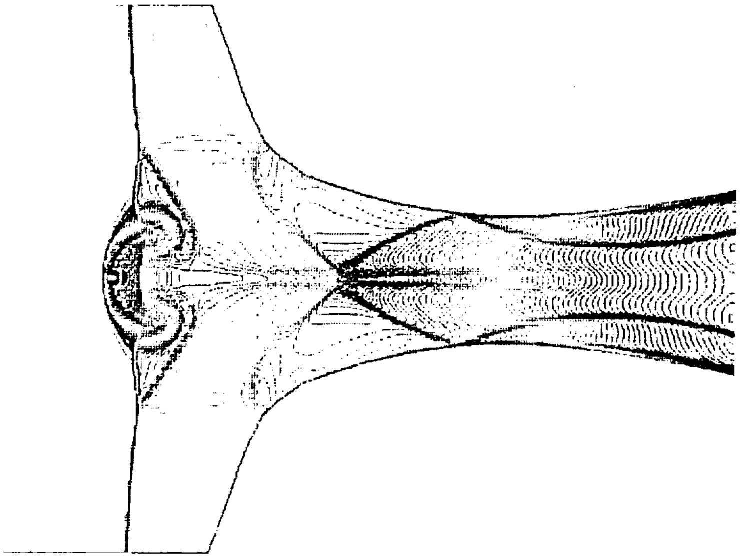

Fig. 10 Temperature Contours at time=120μsec Computed for a Driven Tube with a Non-Vertical End Wall

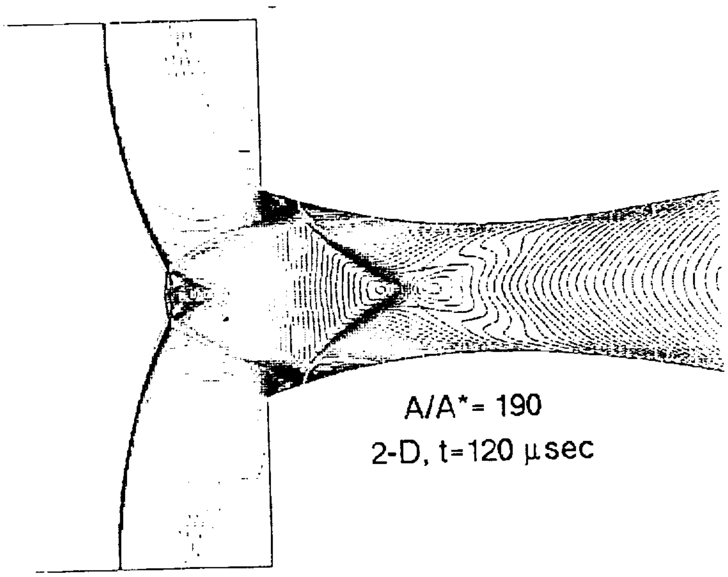

Fig. 11a Temperature Contours at time=120μsec Assuming That the Flow is Two Dimensional

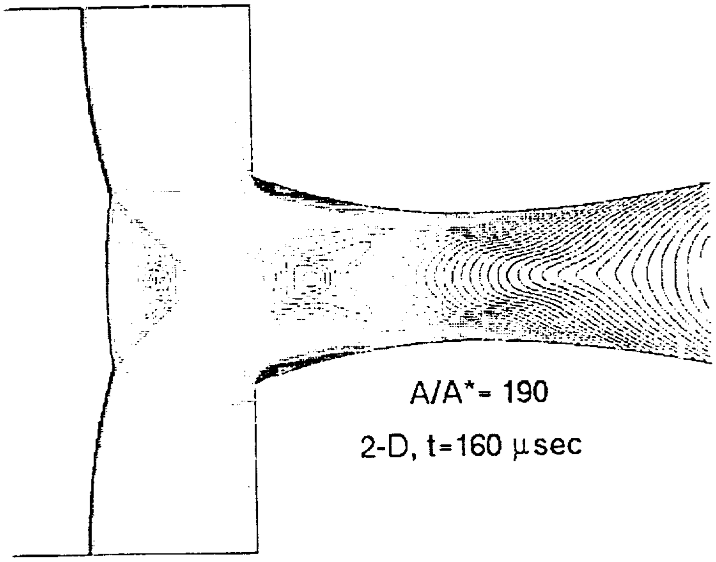

Fig. 11b Temperature Contours at time=160μsec Assuming That the Flow is Two Dimensional

AIAA JOURNAL
Vol. 31, No. 2, February 1993

Computation of Unsteady Shock-Induced Combustion Using Logarithmic Species Conservation Equations

Gregory J. Wilson*
Eloret Institute, Palo Alto, California 94303
and
Myles A. Sussman†
Stanford University, Stanford, California 94305

Numerical simulations are used to investigate periodic combustion instabilities observed in ballistic-range experiments of blunt bodies flying at supersonic speeds through hydrogen-air mixtures. The computations are validated by comparing experimental shadowgraphs with shadowgraphs created from the computed flowfields and by comparing the experimentally measured instability frequencies with computed frequencies. The numerical simulations use a logarithmic transformation of the species conservation equations as a way to reduce the grid requirements for computing shock-induced combustion. The transformation is applied to the Euler equations coupled to a detailed hydrogen-air chemical reaction mechanism with 13 species and 33 reactions. The resulting differential equations are solved using a finite volume formulation and a two-step predictor-corrector scheme to advance the solution in time. Results are presented and compared for both a flux-vector splitting scheme and an upwind TVD scheme. The computations add insight to the physical processes observed in the experiments and the numerical methods needed to simulate them. The usefulness of the ballistic-range experiments for the validation of numerical techniques and chemical kinetic models is also demonstrated.

Introduction

BALLISTIC-RANGE experiments performed in the 1960s and early 1970s[1-7] provide excellent data for studying the coupling between supersonic fluid dynamics and nonequilibrium chemical kinetics as well as for evaluating combustion flow codes. In these experiments, small projectiles were fired at supersonic speeds into a variety of premixed combustible mixtures. Shadowgraphs of the flowfields exhibit two distinguishing features: one is the bow shock ahead of the projectile and the other is an energy-release front created by the ignition of the heated mixture behind the bow shock. Both features can be seen in Fig. 1 in the shadowgraph by Lehr[5] of a steady ballistic-range experiment at Mach 6.46. The region between the bow shock and the energy-release front is called the induction zone, and it exists because there is an ignition delay caused by chemical nonequilibrium. The induction zone is characterized by near-constant values (the postshock values) of temperature, density, pressure, and velocity. The size of the induction zone is determined by the fluid speed downstream of the shock and the ignition time corresponding to the postshock conditions. When ignition occurs, the energy is released over an interval much shorter than the ignition delay time and appears as a discontinuity that is referred to as the energy-release front. Across the energy-release front the pressure is nearly constant, the temperature rises, and the density drops. This can be seen in the shadowgraph where the shift from light to dark across the bow shock corresponds to the density increase across the shock whereas the shift from dark to light across the energy-release front indicates a drop in density.

Depending on the conditions of the experiment, one will observe either steady or unsteady flow. Projectile speeds greater than the detonation wave speed tend to induce steady flows whereas speeds less than the detonation wave speed can produce unsteady flows. The unsteady flows are characterized by two different regimes. One is called the regular regime, and the other is called the large disturbance or irregular regime. All of the unsteady simulations presented in this work are in the regular regime (see Alpert and Toong[7] for more on the large disturbance regime). Figures 2a and 2b show an unsteady ballistic-range experiment with the same freestream conditions as in Fig. 1 except that the projectile speed is Mach 4.79. The shadowgraphs reveal remarkable high-frequency oscillations. The frequency of the instability is approximately 720 kHz as deduced from the projectile speed and counting the number of oscillations that occur over a known distance. Figures 2a and 2b are from the same ballistic-range shot but show different view angles. The view axis of Fig. 2a is perpendicular to the

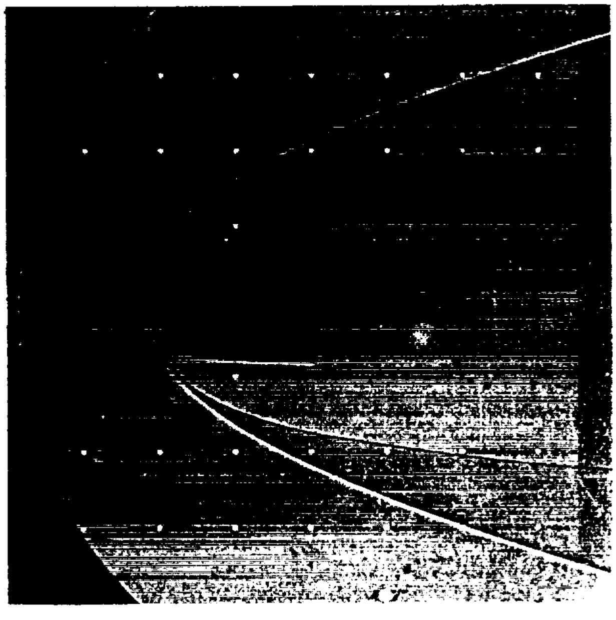

Fig. 1 Shadowgraph of a spherical nose projectile moving at Mach 6.46 in a stoichiometric hydrogen-air mixture (courtesy of H. F. Lehr).

Received Dec. 19, 1991; revision received July 20, 1992; accepted for publication July 24, 1992. Copyright © 1992 by the American Institute of Aeronautics and Astronautics, Inc. All rights reserved.

*Research Scientist; mailing address, NASA Ames Research Center, MS 230-2, Moffett Field, CA 94305. Member AIAA.

†Graduate Student, Department of Aeronautics and Astronautics. Student Member AIAA.

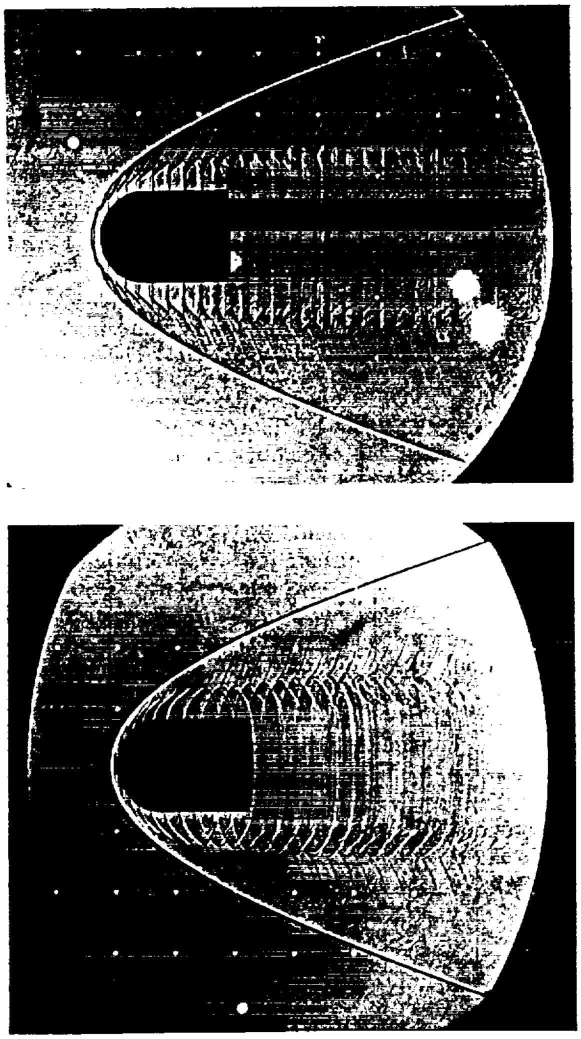

Fig. 2 Shadowgraph of a spherical nose projectile moving at Mach 4.79 in a stoichiometric hydrogen-air mixture: a) side view, b) off-axis view (courtesy of H. F. Lehr).

flight axis, and Fig. 2b is off axis and reveals some of the three-dimensional structure of the flowfield. Although complex in many ways, the physics of these ballistic-range flows are predominantly driven by reaction kinetics and convection phenomena; therefore, the complications and uncertainties of diffusion and mixing are removed from the problem. As a result, differences between the experimental data and numerical simulations can be attributed either to numerical errors or to improperly modeled chemical kinetics.

An earlier work by Wilson and MacCormack[8] focused on the steady ballistic-range experiments and demonstrated the physical and numerical modeling requirements for accurate computations of these flows. It was shown that a primary requirement is adequate resolution in the induction zone between the bow shock and the energy-release front. Fine grid resolution is needed because the mass fractions of the important radical species change exponentially in this region. Adaptive grid techniques offer one way to efficiently distribute points; however, such techniques are not always adequate. The induction zone may cover such a large region of the flowfield that grid requirements still remain large. Furthermore, the small grid spacings in the adapted regions may result in undesired time step limitations. Additional difficulty is added by the presence of the complex flow structures seen in the unsteady ballistic-range cases because there is no primary direction for adapting.

As an alternative to adapting the grid, the simulations presented in this paper use the logarithmic transformation of the species conservation equations presented by Sussman and Wilson.[9] Other researchers have realized the potential advantages of such an approach because the exponential growth of the radical mass fractions that occurs in the induction zone can be accurately represented with fewer points if a logarithmic transformation is used. The formulation of Sussman and Wilson is unique because it can be implemented in modern shock-capturing computational fluid dynamics (CFD) schemes.

The use of the logarithmic transformation allows accurate simulations of both steady and unsteady ballistic-range experiments on grids more coarse than have been used in prior works.[8,10] The reduction in grid size, and thus computational resources, permits the use of a detailed chemical model, which enables direct comparisons of the simulations to the experiments to be made for the first time. In particular, measured oscillation frequencies are compared with those predicted by the computations.

The simulations in this work add insight into the combustion instabilities observed in ballistic-range experiments and allow previously proposed mechanisms for the instabilities to be assessed. In particular, this work considers the wave interaction mechanism of McVey and Toong[6] and the modified mechanism proposed by Matsuo and Fujiwara.[10] McVey and Toong developed their mechanism by using experimental data and analytical calculations. Matsuo and Fujiwara used modern computational fluid dynamics techniques, fine grids, and a two-equation, two-step combustion model to do qualitative simulations that led them to propose their modified mechanism. In addition to adding greater physical understanding, the current method also provides a tool to validate and possibly "tune" proposed chemical kinetic models.

The chemical kinetic model used in this paper can be found in Wilson and MacCormack.[8] It is the mechanism proposed by Jachimowski[11] containing 13 chemical species and 33 reactions except that one of the reaction rate expressions (the expression most influential for ignition times) has been replaced by an expression recommended by another source. This modification was found by Wilson and MacCormack[8] to give better agreement with experiment. Additional details on the chemical kinetics are found in Wilson.[12]

Logarithmic Form of the Species Conservation Equation

This section gives an overview of the logarithmic transformation of the species conservation equations as presented by Sussman and Wilson.[9] The transformation is based on the definition

$$\pi_s \equiv \rho \ln\left(\frac{\rho_s}{\rho}\right) \equiv \rho \ln(c_s) \tag{1}$$

where ρ is the total density, ρ_s is the density of species s, and c_s is the mass fraction of species s. A special property of the relationship in Eq. (1) is that it can be used along with the total mass conservation equation,

$$\frac{\partial}{\partial t}\rho + \frac{\partial}{\partial x_j}\rho u_j = 0 \tag{2}$$

to transform the species mass conservation equation (neglecting diffusion),

$$\frac{\partial}{\partial t}\rho_s + \frac{\partial}{\partial x_j}\rho_s u_j = w_s \tag{3}$$

into a transformed species equation,

$$\frac{\partial}{\partial t}\pi_s + \frac{\partial}{\partial x_j}\pi_s u_j = w_s\frac{\rho}{\rho_s} \tag{4}$$

where u_j is the jth component of velocity, and w_s is the chemical source term for species s. The transformation from Eq. (2) to Eq. (4) retains conservation form.

In theory, all of the species mass conservation equations can be replaced with a corresponding transformed species equation in the form of Eq. (4). In practice, however, this is not done. Although Eq. (4) is in conservation form, its use does not guarantee conservation of mass or conservation of the individual elements. Enforcement of these constraints is achieved by including element mass conservation equations in the form

$$\frac{\partial}{\partial t}\rho_e^* + \frac{\partial}{\partial x_j}\rho_e^* u_j = 0 \tag{5}$$

where ρ_e^* is the total density of element e contained in all of the species (the * is used to avoid confusion between element and species densities; $\rho_N^* \neq \rho_N$). There are as many of these equations as there are elements in the chemical model. The total density is given by

$$\rho = \sum_{e=1}^{\text{Nelements}} \rho_e^* \tag{6}$$

The chemical reaction mechanism used in this work involves 13 species: N_2, O_2, H_2, NO, OH, NO_2, HNO, HO_2, H_2O, H_2O_2, N, O, and H. Since three elements are present in the mechanism (N, O, and H), three equations of the form of Eq. (5) are required. The densities ρ_N^*, ρ_O^*, and ρ_H^* are defined using expressions that are the sum of the contributions from each of the species containing the element of interest. For example, the expression for ρ_N^* depends on the densities of N_2, NO, NO_2, HNO, and N and is written

$$\frac{\rho_N^*}{M_N} = 2\frac{\rho_{N_2}}{M_{N_2}} + \frac{\rho_{NO}}{M_{NO}} + \frac{\rho_{NO_2}}{M_{NO_2}} + \frac{\rho_{HNO}}{M_{HNO}} + \frac{\rho_N}{M_N} \tag{7}$$

where M_s is the molecular mass of species s. The choice of which three species conservation equations to replace with element mass conservation equations is not unique. The selection of N_2, O_2, and H_2 seems appropriate because these species do not exhibit exponential mass fraction growth. The remaining 10 species conservation equations (for species NO, OH, NO_2, HNO, HO_2, H_2O, H_2O_2, N, O, and H) are written in the form of Eq. (4). The densities of N_2, O_2, and H_2 are computed from relations of the type of Eq. (7).

Numerical Formulation

This section presents the Euler equations with the logarithmic form of the species conservation equations. The 13 species mass conservation equations of the conventional formulation have been replaced by equations of similar form except that 3 are elemental mass conservation equations [see Eq. (5)] and 10 are in the logarithmic variable π_s [see Eq. (4)]. The momentum and energy equations in the logarithmic formulation are the same as they were in the conventional formulation. In vector notation the governing equations are written

$$\frac{\partial U}{\partial t} + \frac{\partial F}{\partial x} + \frac{\partial G}{\partial y} = W \tag{8}$$

where U is the state vector, F and G are the convective (inviscid) flux vectors in the x and y coordinate directions, respectively, and W is the vector of source terms. These vectors are given next:

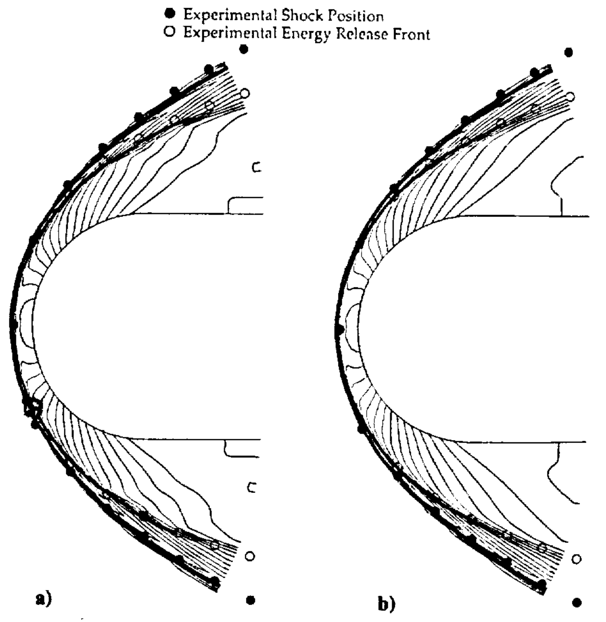

Fig. 3 Density contours from a numerical simulation of the Mach 6.46 experiment in Fig. 1: a) flux-vector splitting, b) upwind TVD.

$$U = \begin{pmatrix} \rho_N^* \\ \rho_O^* \\ \rho_H^* \\ \pi_{NO} \\ \vdots \\ \pi_H \\ \rho u \\ \rho v \\ E_v \\ E \end{pmatrix}, \quad F = \begin{pmatrix} \rho_N^* u \\ \rho_O^* u \\ \rho_H^* u \\ \pi_{NO} u \\ \vdots \\ \pi_H u \\ \rho u^2 + p \\ \rho uv \\ uE_v \\ u(E+p) \end{pmatrix}$$

$$G = \begin{pmatrix} \rho_N^* v \\ \rho_O^* v \\ \rho_H^* v \\ \pi_{NO} v \\ \vdots \\ \pi_H v \\ \rho uv \\ \rho v^2 + p \\ vE_v \\ v(E+p) \end{pmatrix}, \quad W = \begin{pmatrix} 0 \\ 0 \\ 0 \\ w_{NO}/c_{NO} \\ \vdots \\ w_H/c_H \\ 0 \\ 0 \\ w_v \\ 0 \end{pmatrix} \tag{9}$$

where E_v is vibrational energy per unit volume, w_v is the source term representing vibrational relaxation, E is the total energy per unit volume, and p is pressure. A separate vibrational energy equation is not required for the present computations but has been retained from previous work. For the cases presented here, thermal equilibrium is simulated by using a small time constant for vibrational relaxation.

In Eq. (8), pressure is a homogeneous function of degree one in the conserved variables U and the flux Jacobians ($\partial F/\partial U$ and $\partial G/\partial U$) have the same eigenvalues as that of the formulation with the conventional form of the species mass conservation equations. Therefore, existing numerical techniques can be applied in a straightforward manner. In this work, two commonly used shock-capturing numerical techniques are employed. One is a modified Steger-Warming flux-vector splitting technique based on work by MacCormack[13] and Candler[14] (this method shall be referred to as the flux-vector splitting scheme) and the other is the Harten-Yee upwind total variation diminishing (TVD) (non-MUSCL) scheme[15] (referred to as the upwind TVD scheme). Both techniques are spatially second order and solved in a point-implicit manner. That is, the convective terms are treated explicitly whereas the source terms are treated implicitly in time (because of the small time scales of the combustion chemistry and vibrational relaxation). Therefore, a block inversion is required at each point at each time step. Details about the flux-vector splitting scheme using the logarithmic formulation can be found in Wilson.[12]

Several practical details of the logarithmic formulation are addressed next. Because zero mass fractions are not allowed in the transformed equations, the mass fractions of the radical species must be set to small arbitrary values in the freestream (10^{-10} for this work). One-dimensional calculations show that the solutions are relatively insensitive to the freestream radical mass fractions, as long as they remain sufficiently small. An advantage of using logarithms is that mass fractions remain positive. Limiters are required to prevent the mass fractions of species not represented by a logarithm from becoming negative (N_2, O_2, and H_2). In practice, the logarithmic formulation is no less robust than the conventional formulation for the flows presented here. The cost per time step is increased by 10-20% over the conventional formulation due to the cost of computing logarithms and exponentials and also due to the increased complexity of the Jacobian of the chemical source terms.

The logarithmic formulation has limitations at interfaces (contact discontinuities) separating gases of different chemical composition. The inherent numerical diffusion for each species across such an interface is modified by the logarithmic transformation in such a way that the interface is distorted. The use of the transformation is advantageous in this work because the effect of this distortion is small. In simulations of other flows (e.g., the interface in a shock tube), such distortions may not be tolerable, and the use of the logarithmic transformation may not be warranted.

Numerical Simulations

This section presents numerical simulations of ballistic-range shadowgraphs from experiments by Lehr.[4,5] The particular experiments of interest used spherical-nosed projectiles with cylindrical afterbodies of 15-mm diameter. The cases include a range of Mach numbers so that both steady and unsteady flows are represented. All of the cases to be considered have freestream with a temperature of 292 K, a pressure of 320 mm Hg, and a premixed stoichiometric hydrogen-air mixture. At these conditions, the detonation wave speed was reported by Lehr to be Mach 5.11.

Before the unsteady cases are considered, a simulation of the steady Mach 6.46 case in Fig. 1 is shown to demonstrate the advantage of the logarithmic formulation and to give an understanding of why it is practical to use this formulation for the unsteady cases. Figure 3 contains density contours for computations of the Mach 6.46 case using flux-vector splitting and the upwind TVD methods, respectively. Both computations use the 52×52 grid shown in Fig. 4. The experimental bow shock and energy-release front positions are overplotted on the density contours and show that both numerical methods provide good agreement with the experiment. A numerical simulation using the conventional form of the species conservation equations can be found in Wilson and MacCormack.[8] Good agreement with experiment was found in that work as well, but it required an adapted 321×64 mesh (321 points around the body and 64 points normal to the body). The grid for the calculation using the logarithmic formulation is more than eight times smaller because the induction zone is adequately resolved with fewer grid points.

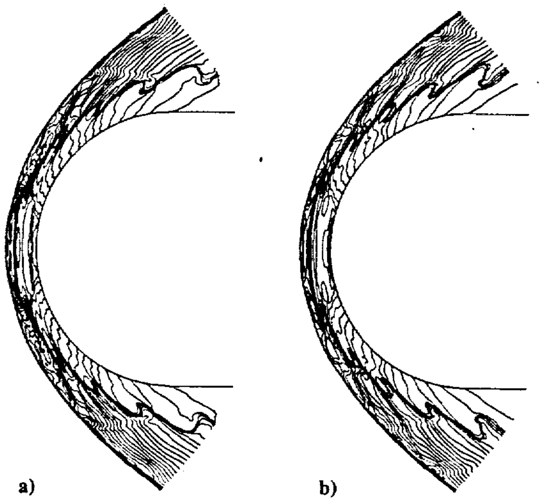

Fig. 5 Density contours from a numerical simulation of the Mach 4.79 experiment in Fig. 2: a) flux-vector splitting, b) upwind TVD.

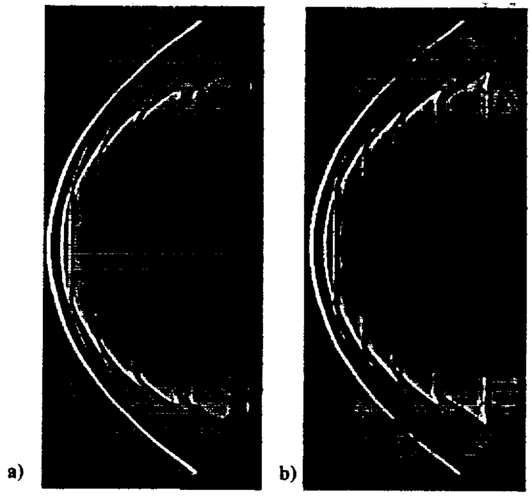

Fig. 6 Computed shadowgraphs from a numerical simulation of the Mach 4.79 experiment in Fig. 2: a) flux-vector splitting, b) upwind TVD (shadowgraphs computed by Yates[16]).

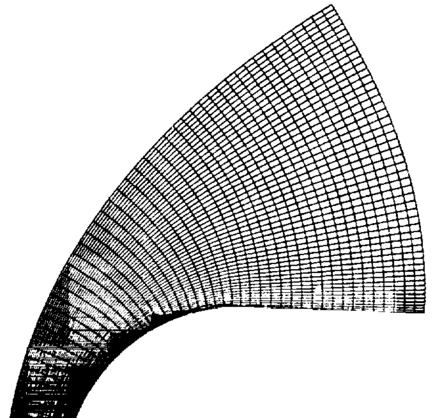

Fig. 4 52×52 grid used for the calculations presented in Fig. 3.

Simulations of Lehr's unsteady Mach 4.79 case shown in Fig. 2 are now presented. Density contour plots for both the flux-vector splitting and upwind TVD methods are presented in Figs. 5a and 5b, respectively. The figures represent one point in time and one point in the period of the instability (the two solutions are not at exactly corresponding points within a period) and show that both computational methods predict unsteady behavior. As in the steady computation of Fig. 3, the density contours exhibit an outer bow shock followed by an induction zone and an energy-release front. The most obvious difference between the unsteady calculation and the steady one is the pulsing structure of the energy-release front. These pulses are seen in the experimental shadowgraph with the off-axis view in Fig. 2b. The computations were started from a flowfield that was initially set to freestream conditions everywhere and advanced in time without chemistry until a bow shock was established, at which time the combustion chemistry was turned on. No other special procedures were used. The

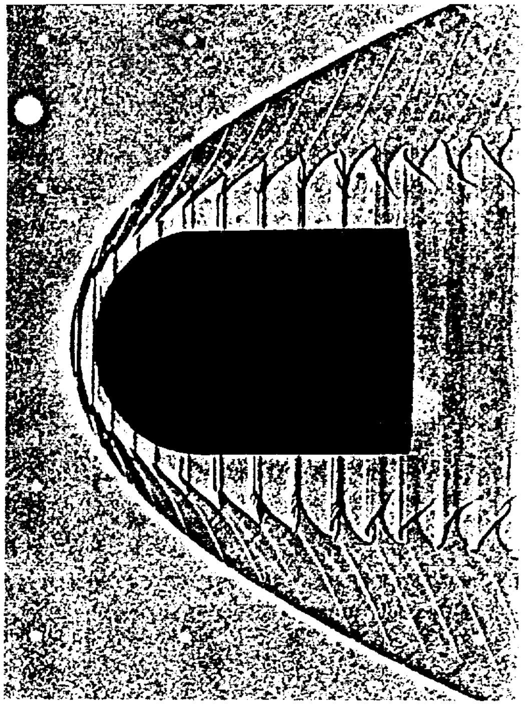

Fig. 7 Enlargement of the Mach 4.79 ballistic-range shadowgraph in Fig. 2a (courtesy of H. F. Lehr).

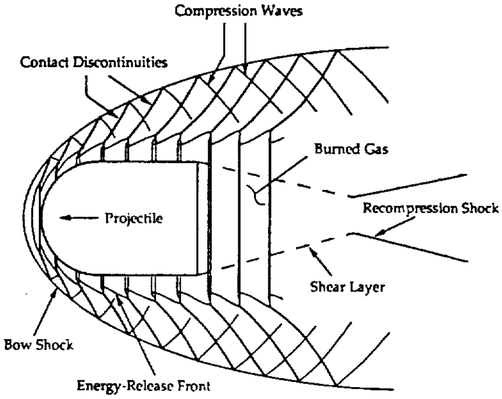

Fig. 8 Schematic diagram of the periodic flowfield structures seen in shadowgraphs of ballistic-range experiments.

computations used a nearly equally spaced 375×161 grid. Computations on a 375×81 grid yielded similar overall flow features and an oscillation frequency near that predicted by the 375×161 grid.[12] (Note that the grid required to resolve the complex unsteady flow structures negates some of the advantage that the logarithmic transformation provides. The usefulness of the transformation is the relative grid independence of the induction zone length and the instability frequency. This allows practical grid refinement studies to be done and adds confidence in the accuracy of the predicted frequencies.) The code uses approximately 2.8×10^{-4} CPU s per time step per grid point on a Cray Y-MP. Depending on the grid, the simulations required between 10,000 and 20,000 iterations and between 16 and 70 h of CPU time.

Figures 6a and 6b contain shadowgraphs computed from the flux-vector splitting and upwind TVD flowfields, respectively.[16] A comparison of these computed shadowgraphs with the enlargement of Fig. 2a presented in Fig. 7 clearly shows many similarities. Note that the pulses in the energy-release front create the vertical line pattern when the axisymmetric flowfield is projected onto a plane. There is a larger streamwise separation between the vertical lines in the computed shadowgraphs compared with the experiment, and thus the computations predict a lower frequency than the experiment. Both numerical methods predict an instability frequency of approximately 530 kHz compared with the measured value of 720 kHz. The primary difference between the flux-vector splitting and upwind TVD solutions is the resolution of the flow structures near the shoulder region of the projectile. The flux-vector splitting smears these features to a larger degree.

Further support of the computations is provided by examining the experimental and computed shadowgraphs in more detail. A schematic diagram of the flowfield that labels the different structures is found in Fig. 8. An analysis of these structures by McVey and Toong[6] identified the waves extending from each pulse of the energy-release front to the bow shock as contact discontinuities (McVey and Toong refer to them as entropy waves). Their identity was established by observing that they are convected with the local fluid speed. Compression or expansion waves would move faster than the local flow with a relative speed that depends on the speed of sound in the mixture. The waves that look like reflections of the contact discontinuities off the bow shock do move at a speed greater than the local flow and were identified as compression waves. The dark-light shadings across the waves support their asserted identities. All of these features can be observed in both the experimental and simulated shadowgraphs.

Investigation of other flowfield quantities adds information that cannot be deduced from the shadowgraphs. Pressure contours reveal that each pulse of the energy-release front creates a compression wave that travels both upstream toward the bow shock and downstream toward the projectile body. Figure 9 shows the pressure contours at one point in time. The wave patterns between the bow shock and the projectile appear quite complicated but can be understood by noting that there are primarily two families. One family is made up of compression waves originating directly from the energy-release front and the other family is made up of compression waves from the first family that have reflected off the projectile body.

Instability Mechanism

The mechanism that causes and sustains the combustion instabilities observed in the ballistic-range has not been observed experimentally. Therefore, plausible explanations for the unsteadiness have been developed by extrapolating data from outside the nose region (mostly from the shadowgraphs) and by transferring knowledge from other flow situations. It was not until the work of Toong and his associates that plausible detailed mechanisms for the regular[6] and large-disturbance[7] regimes were proposed.

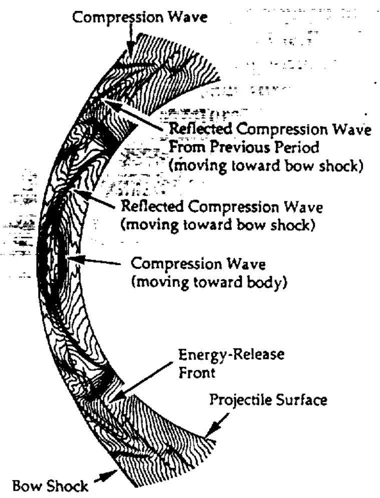

Fig. 9 Pressure contours for the Mach 4.79 case at one point in an oscillation period.

The work of McVey and Toong[6] is discussed further here because it is supported by the present numerical simulations. McVey and Toong used what they called a wave-interaction model to explain the oscillations observed in the regular regime. All of the important processes in this model occur between the energy-release front and the bow shock in the subsonic region ahead of the projectile nose. As an aid to understanding the model, several of the primary components of the model are isolated and described first.

A major component in the McVey and Toong model is the interaction between the bow shock and a compression wave. Figure 10 depicts a one-dimensional flow at several different times (time proceeds from bottom to top). Initially there is a stationary normal shock and a compression wave downstream of the shock moving toward the shock. At a later time the compression wave overtakes the shock, strengthening it and causing the shock to move forward. The strengthened shock causes a change in the fluid properties behind it. Most important for the instability is a higher fluid temperature. This higher temperature fluid is separated from the fluid that has crossed the shock at the original strength by a contact discontinuity that convects downstream. Additionally, a rarefaction wave is created that travels downstream.

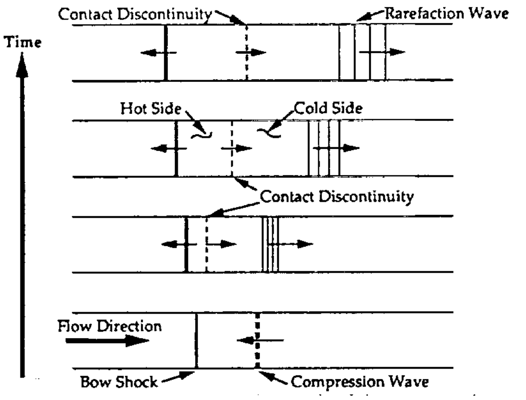

Fig. 10 Schematic diagram of a one-dimensional bow shock/compression wave interaction.

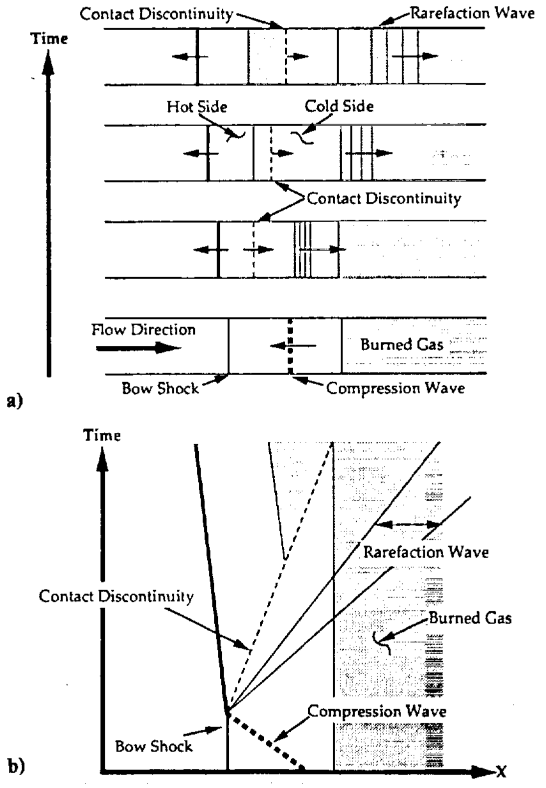

Fig. 11 Schematic diagram of a bow shock/compression wave interaction with shock-induced combustion: a) series of one-dimensional diagrams, b) *x-t* diagram.

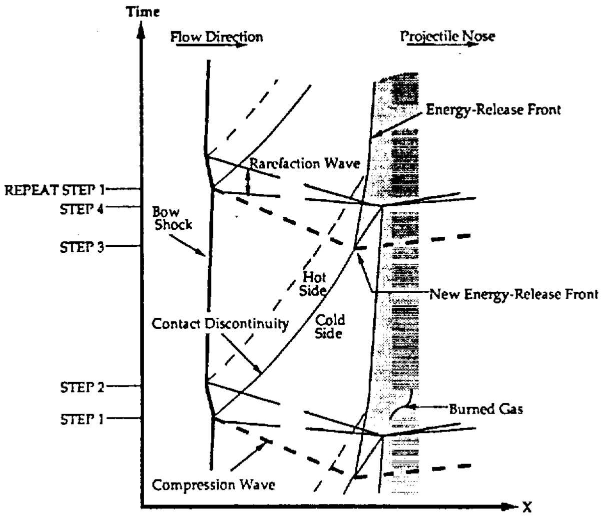

Fig. 12 McVey and Toong[6] wave interaction model.

Interesting flow features are created when the interaction of Fig. 10 is combined with the flow of a combustible mixture. This is the situation presented in Fig. 11a. As in Fig. 10, there is initially a stationary normal shock wave with a compression moving toward it from the downstream side. Now there is also burned fluid downstream of the shock at some induction length. As before, the compression wave overtakes the bow shock, strengthening it and creating a contact discontinuity and a rarefaction wave. Because the fluid on the upstream side of the contact discontinuity is hotter, it has a shorter induction time and burns more quickly. The result is that for a time there are two regions of burning, one at an induction length corresponding to the original postshock conditions, and the other at the shorter induction length corresponding to the strengthened shock. Figure 11b is an *x-t* diagram corresponding to the interaction in Fig. 11a. The general features of this diagram are recognizable in the McVey and Toong mechanism presented next.

The McVey and Toong mechanism is schematically depicted in the *x-t* diagram in Fig. 12. The diagram shows time evolution of the features along the stagnation streamline and is explained in the following four steps.

1) A compression wave on the downstream side of the bow shock overtakes the bow shock, causing the bow shock to move forward, thus creating a reflected rarefaction (which is weak and is ignored in the model) and a contact discontinuity. The gas on the upstream side of the contact discontinuity is hotter than on the downstream side because it has passed through the strengthened bow shock.

2) The rarefaction wave propagating upstream from the energy-release front overtakes the bow shock, weakening it and restoring it to its original strength. The origin of the rarefaction wave is discussed in step 4.

3) The contact discontinuity created in step 1 convects downstream. At a point between the bow shock and the energy-release front, a new energy-release front is produced by the hotter gas on the upstream side of the contact discontinuity. The creation of a new zone of combustion, in turn, creates compression waves that propagate both upstream toward the bow shock (this is the wave that overtakes the bow shock in step 1) and downstream toward the projectile. It can be shown that the upstream and downstream compression waves are necessary to match the fluid velocity jumps across the new

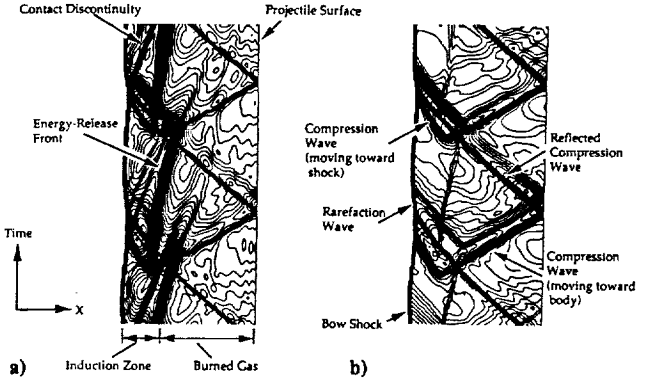

Fig. 13 Computed x-t diagrams of density and pressure along the stagnation streamline for the Mach 4.79 case using flux-vector splitting: a) density contours, b) pressure contours.

energy-release front and satisfy conservation of momentum (see Alpert and Toong[7]).

4) The contact discontinuity (with burning on the upstream side) eventually reaches the position of the original energy-release front. This extinguishes the original energy-release front and creates rarefaction waves that propagate in the upstream and downstream directions. The energy-release front then begins to recede toward the location of the original front as colder gas (through the bow shock of original strength) reaches the front.

From Fig. 12 it is seen that the period of an oscillation is the time required for the contact discontinuity to convect from the shock to the reaction front and then for an acoustic wave to travel back to the bow shock. If the postshock conditions are known, an analytical expression for the period of observed experimental oscillations can be found. Given a period of oscillation provided from an experiment, McVey and Toong were able to use the expression to predict the induction time for the gas mixture. Their predicted induction times agreed with previously published data. Figure 13 contains computed x-t diagrams of density and pressure along the stagnation streamline for the Mach 4.79 case (the flux-vector splitting algorithm was used to produce all of the computed x-t diagrams in this paper). A comparison of these diagrams with the McVey and Toong mechanism in Fig. 12 reveals many similarities. The density contours show a changing position of energy-release front in time that is identical to the pattern predicted by the wave interaction model (note the jagged edge of the energy-release front that appears in both Figs. 12 and 13a). In the region between the bow shock and the energy-release front, density contours also show that a contact discontinuity is created at the bow shock when a compression wave originating from the energy-release front overtakes it. The hotter gas on the upstream side of the contact discontinuity reduces the ignition delay time and causes a new energy-release front to be created. The new energy-release front is the source of the compression waves traveling in both the upstream and downstream directions. These compression waves are clearly seen in the pressure contours of Fig. 13b. The identity of the contact discontinuities labeled in Fig. 13a is verified by their absence in the pressure contours of Fig. 13b because a contact discontinuity has no pressure jump across it.

A phenomenon seen in the computations that was apparently not anticipated by McVey and Toong is the existence and/or importance of the compression waves reflecting off the projectile nose. Figure 13b shows that a compression wave created at the energy-release front travels toward the projectile nose, reflects, and eventually overtakes the bow shock. In this particular calculation, the compression wave reflects off the nose and moves toward the bow shock, overtaking it at nearly the same time that the most recently created compression wave arrives at the bow shock. The coordination between the compression wave and the reflected compression wave is not always exact, and therefore the two waves sometimes hit the bow shock at slightly different times. This tends to deform some of the structures. The importance of the reflection of the compression waves off the projectile has been recognized in the recent work of Matsuo and Fujiwara.[10]

Figure 14 contains computed x-t diagrams of density and pressure from a case at Mach 5.04. As in the Mach 4.79 case, the interactions between the bow shock and energy-release front correspond to the model proposed by McVey and Toong. This case is interesting because the interaction of the wave reflected off the projectile is significantly different than that seen in the Mach 4.79 case. During the time that a compression wave travels from the energy release front to the projectile body and back, two new compression waves are created (i.e., two periods have passed). The computed frequency is 820 kHz whereas the measured frequency is 1.04 MHz. A thorough discussion of this case is given in Wilson[12] along with an additional simulation of an experiment at Mach 4.18 with a much lower oscillation frequency.

Frequency Sensitivity to the Hydrogen-Air Reaction Mechanism

The nearly constant values of the instability frequency predicted by the numerical simulations using different grid sizes (375 × 321, 375 × 161, and 375 × 81) and two different numerical schemes suggest that the underprediction of the frequency in the computations is not caused by numerical error but by the chemical kinetic model. Wilson and MacCormack[8] established that the blunt body exothermic flowfields are quite sensitive to the following chain-branching reaction:

$$H + O_2 \rightarrow OH + O$$

In that work, flowfields were computed with two different rate expressions for this reaction. One was the original expression from the Jachimowski[11] reaction model, and the other was from Warnatz.[17] The rate expression recommended by Warnatz was adopted because it gave better agreement with experiments for the steady cases (this is the rate expression that has been used for all cases presented in this paper). To investigate the influence of the chemical kinetic mechanism on the frequency of the oscillations, the Mach 4.79 simulation is repeated using the Jachimowski rate expression. This rate expression gives shorter ignition times at high temperatures ($T > 1400$ K) than the rate constant recommended by Warnatz. This change should lead to an increase in the oscillation frequency because the induction zone is smaller and therefore the travel time between the energy-release front and the bow shock is reduced. Consistent with this expectation, the computed frequency of the oscillations increased from approximately 530 to 820 kHz. Since the experimentally determined frequency is 720 kHz, it is concluded that the uncertainties in the

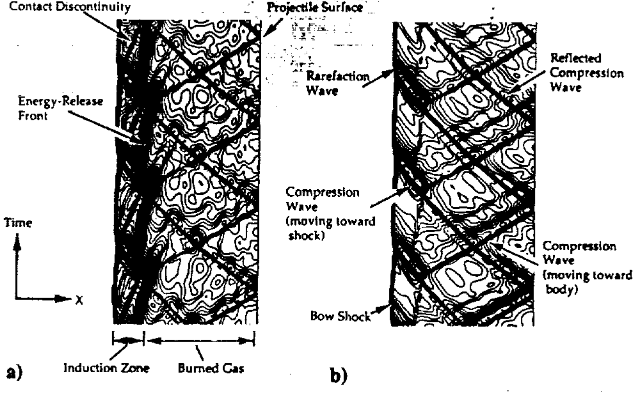

Fig. 14 Computed x-t diagrams of density and pressure along the stagnation streamline for the Mach 5.04 case using flux-vector splitting: a) density contours, b) pressure contours.

rate constants for the reaction mechanism could explain the differences between the experiments and the computations. The sensitivity of the oscillation frequency to the chemical reactions make the simulations a useful validation tool for kinetic models. The unsteady cases appear to provide a better measure of a kinetic model than the steady cases because the oscillation frequency can be determined with greater precision than the positions of the bow shock and energy-release front.

Finally, note that the arrival times of new compression waves and reflected pressure waves at the bow shock sometimes differ significantly (this occurred in the Mach 4.79 case with the Jachimowski rate expression[12]). The separate interactions between the bow shock and each wave lead to separate contact discontinuities and cause the *x-t* diagrams to appear less organized. Further investigations are required to assess the precise contribution to the combustion instability of the compression waves reflected off the projectile nose. In the present calculations they appear to have a secondary effect, but it is possible that they are more important to the instabilities seen in the large-disturbance regime investigated by Alpert and Toong.[7]

Conclusion

The successful simulations of both steady and unsteady exothermic ballistic-range experiments have added to the understanding of shock-induced combustion and have led to improvements in the numerical techniques for these types of flows; namely, proper grid resolution is a primary challenge of simulations with combustion phenomena, and these grid requirements are reduced by the use of the logarithmic transformation of the species conservation equations. The accuracy of the simulations is supported by grid refinement studies and the use of two different numerical methods, a flux-vector splitting scheme and an upwind TVD scheme. Further validation is provided by comparison to past analytical and numerical predictions of the instabilities. Finally, the simulations have reaffirmed the value of ballistic-range experiments as a source of data for high-speed flows with combustion and have demonstrated their usefulness for validating numerical methods and chemical kinetic mechanisms. It is shown that differences in the experimental and computed instability frequencies are probably due to uncertainties in the chemical reaction rates and therefore the experiments provide a means of validating proposed chemical kinetic models.

Acknowledgments

Funds for the support of this study have been allocated by the NASA Langley Research Center and by the NASA Ames Research Center under the joint research interchange number NCA2-455 and are greatly appreciated. This material is also based on work supported by a National Science Foundation Graduate Fellowship and by NASA under Hypersonic Training and Research Grant NAGW 965. The authors would also like to acknowledge the computer resources provided by the Aerothermodynamics Branch of NASA Ames, the Theoretical Flow Physics Branch of NASA Langley, and the National Aerodynamic Simulation (NAS) Program. We are most grateful to H. F. Lehr of Institute Saint Louis for providing original photographs of his ballistic-range experiments and to Leslie A. Yates for computing shadowgraph images from our flowfield solutions. We also acknowledge the support and encouragement of our advisor at Stanford University, Robert W. MacCormack.

References

[1] Ruegg, F. W., and Dorsey, W. W., "A Missile Technique for the Study of Detonation Waves," *Journal of Research of the National Bureau of Standards,* Vol. 66C, No. 1, 1962, pp. 51-58.

[2] Behrens, H., Struth, W., and Wecken, F., "Studies of Hypervelocity Firings into Mixtures of Hydrogen with Air or with Oxygen," *Tenth Symposium (International) on Combustion,* Combustion Institute, Pittsburgh, PA, 1965, pp. 245-252.

[3] Chernyi, G. G., "Onset of Oscillation in the Presence of Detonation Wave Weakening," *Journal of Applied Mathematics and Mechanics,* Vol. 33, No. 3, 1969, pp. 451-461.

[4] Lehr, H. F., Institute Saint Louis (ISL), Final Rept. 20/71, Saint-Louis, France, 1971.

[5] Lehr, H. F., "Experiments on Shock-Induced Combustion," *Astronautica Acta,* Vol. 17, Nos. 4 & 5, 1972, pp. 589-596.

[6] McVey, B. J., and Toong, T. Y., "Mechanism of Instabilities of Exothermic Hypersonic Blunt-Body Flows," *Combustion Science and Technology,* Vol. 3, No. 2, 1971, pp. 63-76.

[7] Alpert, R. L., and Toong, T. Y., "Periodicity in Exothermic Hypersonic Flows About Blunt Projectiles," *Astronautics Acta,* Vol. 17, Nos. 4 & 5, 1972, pp. 539-560.

[8] Wilson, G. J., and MacCormack, R. W., "Modeling Supersonic Combustion Using a Fully-Implicit Numerical Method," *AIAA Journal,* Vol. 30, No. 4, 1992, pp. 1008-1015; see also AIAA Paper 90-2307, July 1990.

[9] Sussman, M. A., and Wilson, G. J., "Computation of Chemically Reacting Flow Using a Logarithmic Form of the Species Conservation Equations," *Proceedings of the 4th International Symposium on Computational Fluid Dynamics* (Davis, CA), Vol. 2, Sept. 1991, pp. 1113-1118.

[10] Matsuo, A., and Fujiwara, T., "Numerical Simulation of Shock-Induced Combustion Around an Axisymmetric Blunt Body," AIAA Paper 91-1414, June 1991.

[11] Jachimowski, C. J., "An Analytical Study of the Hydrogen-Air Reaction Mechanism with Application to Scramjet Combustion," NASA TP-2791, Feb. 1988.

[12] Wilson, G. J., "Computation of Steady and Unsteady Shock-Induced Combustion over Hypervelocity Blunt Bodies," Ph.D. Thesis, Stanford Univ., Stanford, CA, Dec. 1991.

[13] MacCormack, R. W., "Current Status of Numerical Solutions of the Navier-Stokes Equations," AIAA Paper 85-0032, Jan. 1985.

[14] Candler, G. V., "The Computation of Weakly Ionized Hypersonic Flows in Thermo-Chemical Nonequilibrium," Ph.D. Thesis, Stanford Univ., Stanford, CA, June 1988.

[15] Yee, H. C., "A Class of High-Resolution Explicit and Implicit Shock-Capturing Methods," NASA TM 101088, Feb. 1989.

[16] Yates, L. A., "Images Constructed from Computed Flowfields," AIAA Paper 92-4030, July 1992.

[17] Warnatz, J., "Rate Coefficients in the C/H/O System," *Combustion Chemistry,* edited by W. C. Gardiner Jr., Springer-Verlag, New York, 1984, Chap. 5.

Hypersonic Aerodynamic Decelerators Design Using CFD
Part II - Turbulent Computations

Susan Tokarcik and Ethiraj Venkatapthy *
Eloret Institute
Palo Alto, Ca 94303

Abstract

Aerodynamic and heating predictions for a variety of hypersonic decelerators have been performed with a number of Computational Fluid Dynamic (CFD) solvers in order to determine the design parameters. Sample results from the computed solutions are presented for a number of design. In addition to thermo-chemical non-equilibrium effects, turbulent effects are significant in determining the efficiency of the decelarator design. Efficient approximation of treating the thermo-chemical, non-equilibrium gas as an idealized gas has been proven to have significant advantage in the decelerator design and the use of well established algebraic turbulence models are explored in this study. The accuracy of the computations are evaluated by comparing the flow-field solutions and aerodynamic coefficients with experimental measurements.

Introduction

The use of supersonic and hypersonic drag-devices or decelerators have been experimentally investigated for many years with applications ranging from high-performance re-entry vehicle recovery to booster-payload collision avoidance systems. Supersonic and hypersonic drag-device configurations that have been examined in the past include attached and tethered ballute,[1-5] which is a combination balloon and parachute, and rigid flare,[7-10] among others. Recent advances made in modelling hypersonic non-equilibrium flows and flow solvers have significantly improved the design of complex drag devices. [11-13] The drag device designed investigated and designed by the present authors using the CFD solvers include ballutes and flares[12] for solid rocket motor (SRM) casing earth-capture mission and petal-flares for Lunar (and Mars) return vehicles (LRV)[13] . These designs are shown in Figure 1 - 3. In the case of ballute and flare design for the SRM, the CFD solvers were used to determined the size and shape parameters that will produce sufficient drag and

---

* Research Scientist, Eloret Institute. Mailing Address: NASA Ames Research Center, MS 230-2, Moffett Field, Ca 94035. AIAA Member.

survive reentry speeds of 9 Km/sec during reentry. The drag coefficient required were prescribed based on the ballistic coefficient for a no-skip reentry trajectory. Computations were performed for the LRV decelerator to determine the drag and heating for a variety configurations and shapes.

At re-entry speeds around 8 km/sec and at freestream conditions corresponding to an altitude of 80 km, the flow around the fore-body and the decelerator section remains in thermo-chemical non-equilibrium. The flowfield around the decelerator section can be highly complex and often a separated flow region is established. In addition to the separated zone, the inviscid-viscous interaction may produce either a strong or an oblique shock wave and the corner shock interacts with the fore-body shock. The hypersonic forebody is not expected to be turbulent, but the flow field near corner regions of the decelarator, due to flow separation, can be dominated by turbulence. The computed flowfield around the three different decelerators are shown in Figures 4-6. The non-equilibrium issues are addressed in Part I , one of two papers proposed to be presented together. The effectiveness of the decelerator depends on the strength of the corner shock and the size of the separated domain. Turbulent mixing can significantly affect the corner flow domain and hence the efficiency of the decelarator. In addition, if local heating is important to the design, validated CFD solvers are needed to be used in the design process. The viscous-inviscid interaction is non-linear and complex and the effect of the non-equilibrium, turbulent state of the gas on the inviscid-viscous interaction is difficult to quantify. In addition to the flow in the decelarator section, the flow in the base region of the decelerator may influence the upstream flow. In the case of the ballute and axisymmetric flares, the base flow is not significant. But in the case of the LRV decelerator, the base flow interaction with the upstream flow is significant and the complete flow field including the base region need to be solved during the design cycle and the turbulent mixing and modelling becomes significant. In the case of the LRV decelarator, part of the flow is expanded through the gap into the base region and base recirculation is set up. Complex vortex patterns are set up due to the three-dimensionality of the flow and the three-dimensional computational predictions are of great significance to the design.

A number of CFD solvers used by the present authors[12,13] and others[11,15,16,17] in computing the hypervelocity decelerators can be classified into two categories, namely thermo-chemical, non-equilibrium solvers[15,16] and effective real-gas solver.[11,12,17] In the thermo-chemical, non-equilibrium solvers, the Navier-Stokes equations including the thermo-chemistry model equations, represented by the species and energy conservation equations, are solved. In the effective real-gas solver, the gas model is approximated by an idealized gas with an effective specific heat ratio approximating the global non-equilibrium state of the gas and the Navier-Stokes equations alone are solved. The effective-real-gas solver is computationally more efficient but less accurate compared to the full thermo-chemical non-equilibrium solver. The three-dimensional non-equilibrium solvers are prohibitively expensive requiring 40-60 CPU hours on CRAY-2 for one three-dimensional solution[15], but the effective-real-gas solvers[12,17] require very reasonable amount of computer time (1 - 2 CPU hr.). The non-equilibrium issues will be addressed in another paper and in this paper, the turbulent model issues, for the idealized-real-gas solver, are explored.

Numerical Method

Effective-γ Ideal-Gas Solver

The use of CFD in the design often requires a number of solution to be computed. These solutions are used to evaluate the impact of various design parameters on the aerodynamic and heating and to choose the best of the design variables. In order to calculate solutions in a timely and cost effective manner, an ideal-gas solver with an effective specific heat ratio, γ_{eff}, has been used in the design process.[12,13] The underlying assumption is that the global effect of a real- gas flowfield can be simulated sufficiently accurate , by using an effective value of γ. This technique has been used successfully to predict drag and moment coefficients produced by blunt bodies in real-gas flows[17] using the effective-γ ideal-gas solver developed by the first author. This solver uses an implicit, finite-difference, flux-difference splitting method due to Roe and is suitable for both axisymmetric and fully three-dimensional flow problems. The idealized solver is very robust and requires only 10 to 15 minutes of CPU time on Cray-2 for an axisymmetric calculation and between 1 and 2 CPU hours for full 3-D solution.

To model turbulence, algebraic models[19] were used for wall layer region and a modified mixing length model was utilized in the base region. The algebraic models are well suited for simple 2-dimensional and axisymmetric flows, but require carefull fine tuning for complex 3-dimensional flows. Work is currently in progress to include a compressible 2-equation model.[20] Full detail regarding the the turbulence modelling effort will be given in the final paper.

Sample Results and Discussions

A number of design studies have been performed with the effective-γ ideal-gas solvers[12,13] by the present authors. Some of the computed solutions were shown in Figs. 4-6. The fore-body region in these cases is dominated by the non-equilibrium effects and the flow remains laminar. The computational studies performed with the effective-γ ideal-gas solver[17] were validated by comparing the computed results with ballistic range measurements of drag, lift and moment coefficient for a three-dimensional Aero- Orbital Transfer Vehicle geometry. These comparisons prove that the effective-γ approach was reasonably accurate in predicting aerodynamic forces at moderate hypersonic speeds for blunt fore-body flows.

The aerodynamic decelerators, in addition to the blunt forebody, have the added complexity of the corner flows, where turbulent mixing will affect the flow field. To validate the present solver, computed solutions to 2-dimensional corner flow problems are compared with experimental results. A laminar 2-d corner flow comparison is shown in Fig. 7. In this experiment, the flow upstream of the corner remained laminar and through the separation bubble, the flow transitioned from laminar to turbulent. The heat transfer comparison shown in Fig. 7 agrees well in the laminar region and as expected, the difference between the computations and the experiments are in the turbulent region. Computed results using a a number of turbulent models and comparisons will be presented in the final paper.

In addiiton to validating the solver for the corner region, the solution accuracy is need to be assesed for flows with complex 3-d effects. The computed LRV decelarator flowfiled solution are shown in Fig. 8. The figure on the top left corner shows the simulated surface oil-flow patterns along with the surface pressure. The vortical, recirculating flow near the compression-corner region can be seen to be highly complex. The invscid-viscous interaction effects can be visualized from the figure on the top right corner. In this figure, the particle traces along the symmetry plane and the shape of the outer shock surface are shown. The compression corner region produce corner shocks and this shock interact with the outer shock. The corner shock, in addition to raising the surface pressure, causes local heating and the local heating levels are of paramount significance to the design. Only a limited amount of experimental results are available for similar flows. Computations are underway to simulate and compare with these results. The experimental drag coefficient[14] is shown in Figure 9. The effect of the gap ratio on the drag coefficient is seen to be non-linear and 3-d and turbulent effects are beleived to be the cause. Validation efforts and final comparisonswill be reported in the final paper. In addition, design efforts carried out for the LRV decelarator will be discussed.

Summary

The use of CFD in the design of hypervelocity decelerators have proven to be very attractive. In the final paper, turbulent computations for a number of decelerator design will be reported and the preliminary results indicate that the effective-γ approach provides a reasonably accurate computational procedure for the design of complex, hypervelocity decelerators.

References

[1] Nerem, R. M., "Pressure and Heat Transfer on High-Speed Aerodynamic Decelerators of the Ballute Type," Proceedings of the AIAA Aerodynamic Decelerator Systems Conference, Houston, Texas, Sept. 1966, pp. 135-143.

[2] Alexander, W., "Summary of the Development Status of Attached Inflatable Decelerators," AIAA Paper 68-929, Sept. 1968.

[3] Alexander, W., "A Discussion of Governing Decelerator Performance and Design Parameters in the Supersonic Flight Regime," AIAA Paper 68-938, Sept. 1968.

[4] Bohon, H. and Miserentino, R., "Attached Inflatable Decelerator Performance Evaluation and Mission-Application Study," AIAA Paper 70-1163, Sept. 1970.

[5] Aebischer, A. and Suters, E. Jr., "Development Status of Ballute System For Stabilization and Retardation of Aircraft Stores," AIAA Paper 70-1200, Sept. 1970.

[6] Blanco, T., Berman, H., and Steck, H., "Recovery of High Performance Re-entry Vehicles," Proceedings of the AIAA Aerodynamic Decelerator Systems Conference, Houston, Texas, Sept. 1966, pp. 73-77.

[7] Ryan, J., "Aerodynamic Deceleration From as High as Mach 4.0 for the ALARR Project," Proceedings of the AIAA Aerodynamic Decelerator Systems Conference, Houston, Texas, Sept. 1966, pp. 172-180.

[8] Minerva, P., and Turner, R., "Recovery System Requirements for High Performance Re-entry Vehicle," Proceedings of the AIAA Aerodynamic Decelerator Systems Conference, Houston, Texas, Sept. 1966, pp. 188-195.

[9] Wyborny, W. and Kabelitz, H., "Comparison of Hypersonic Aerodynamic Deceleration Systems Based on Gun Tunnel Investigations," AIAA Paper 70-1174, Sept. 1970.

[10] Sims, L. and Bursey, C. Jr., "Comparative Performances of Two Hypersonic Deceleration Devices," AIAA Paper 70-1207, Sept. 1970.

[11] Wang, J.A. and Shih, K.C., "Numerical Studies on Inflatable Ballute as an Aerodynamic Decelerator for a Solid Rocket Motor Hypersonic Reentry," AIAA Paper 91-0841, April 1991.

[12] Tokarcik, S.A., Venkatapathy, E., Candler G., and Palmer, G., "Computational Flow Predictions for Hypersonic Drag Devices," AIAA Paper 91-3303, Sept. 1991. (also to be published by AIAA Journal of Spacecraft and Rockets).

[13] Tokarcik, S.A., Venkatapathy, E., and Tauber, M., "Computational Study of a Lunar Return Aero-Brake Vehicle," AIAA Paper 93-0037, to be presented at the 31st Aerospace Sciences Meeting, Jan 1993.

[14] Wyborny, W. and Kabelitz, H-P, Comparison of Hypersonic Aerodynamic Decelaration Systems, AIAA Paper No. 70- 1174.

[15] Palmer, G., "The Development of an Explicit Thermo-Chemical Nonequilibrium Algorithm and Its Application to Compute Three Dimensional AFE Flowfields," AIAA Paper 89-1701, June 1989.

[16] Candler, G., "The Computation of Weakly Ionized Hypersonic Flows in Thermo-Chemical Nonequilibrium," Ph.D. Dissertation, Dept. of Aeronautics and Astronautics, Stanford University,

Stanford, CA, June, 1988.

[17] Yates, L.A. and Venkatapathy, E., "Trim Angle Measurements in Free-Flight Facilities," AIAA Paper 91-1632, June 1991.

[18] Park, C., "Assessment of Two Temperature Kinetic Model for Ionizing Air," AIAA Paper 87-1574, Honolulu, HA, July 1987.

[19] Coakley, T.J. Turbulence Modeling Methods for the Compressible Navier-Stokes Equations, AIAA Paper 83-1958.

[20] Viegas, J.R. and Rubesin, M.W., Turbulence Modeling of Compressible Free Shear Flows, Sixth National Aero-Space Plane Symposium, Paper No.71, 1989.

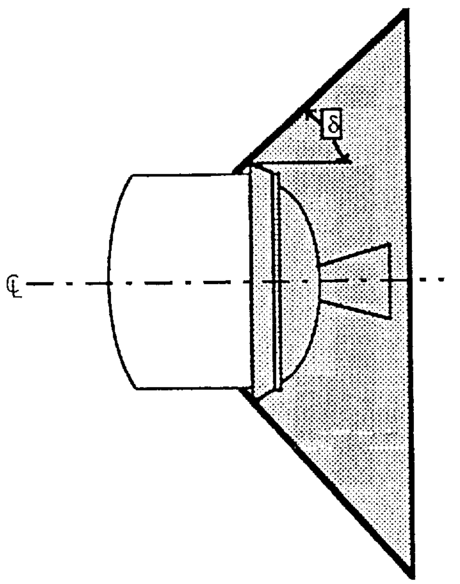

Figure 1. SRM with Flare Decelerator

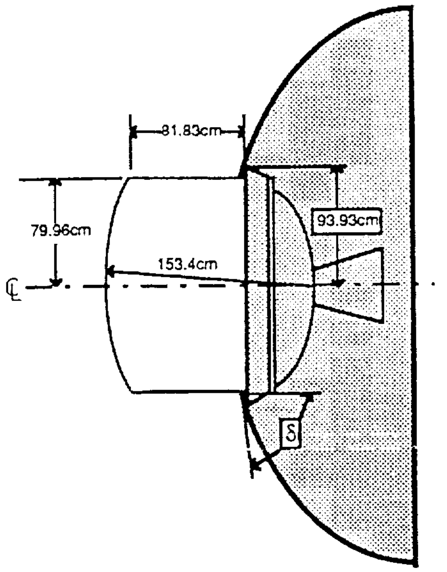

Figure 2. SRM with Basllute Decelerator

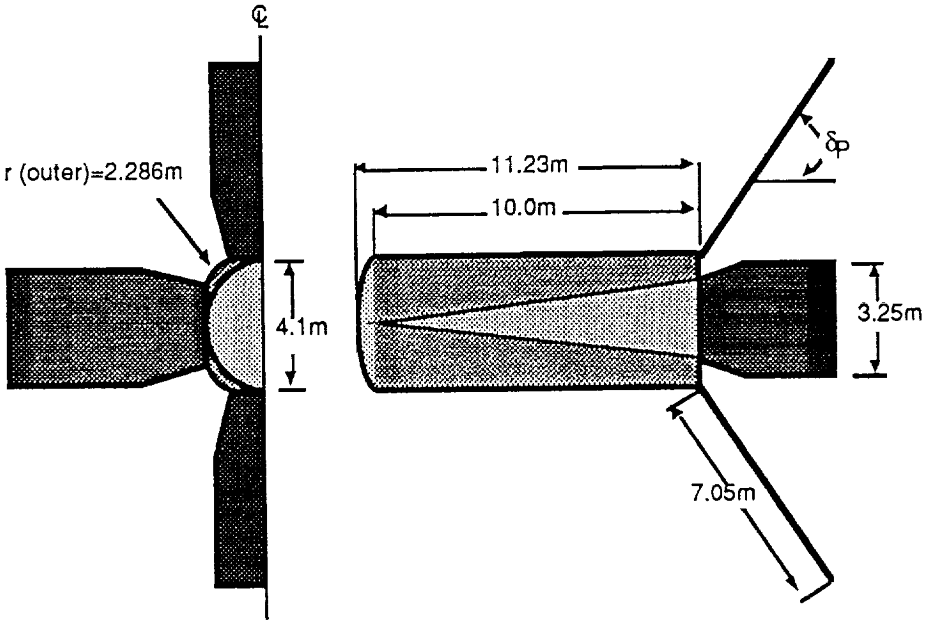

Figure 3. LRV with Petal Decelerator

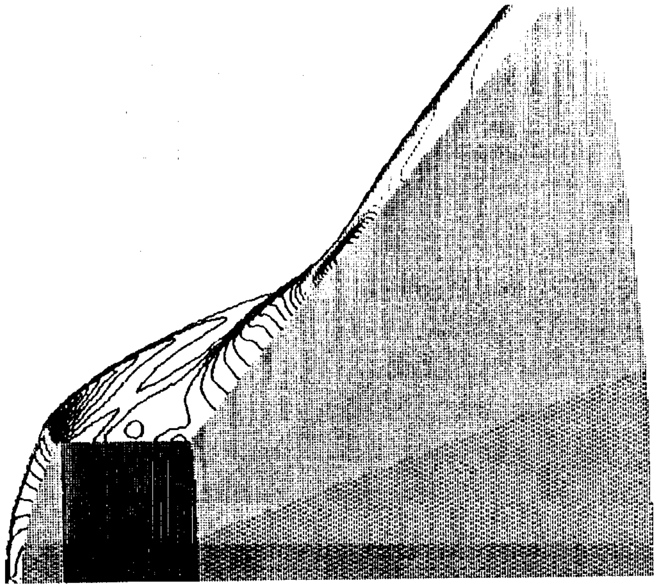

Figure 4. Pressure Contours - Flare Decelerator

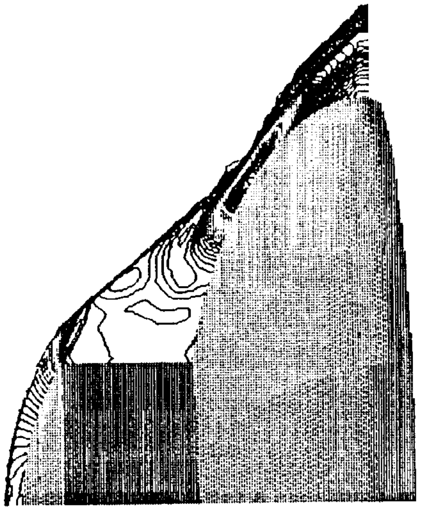

Figure 5. Pressure Contours - Ballute Decelerator

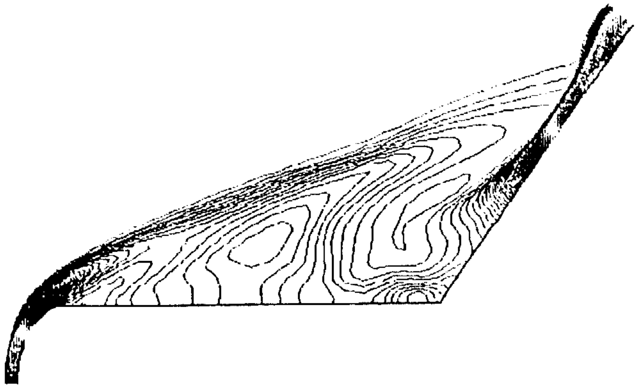

Figure 6. Pressure Contours - Petal Decelerator (symmetry plane)

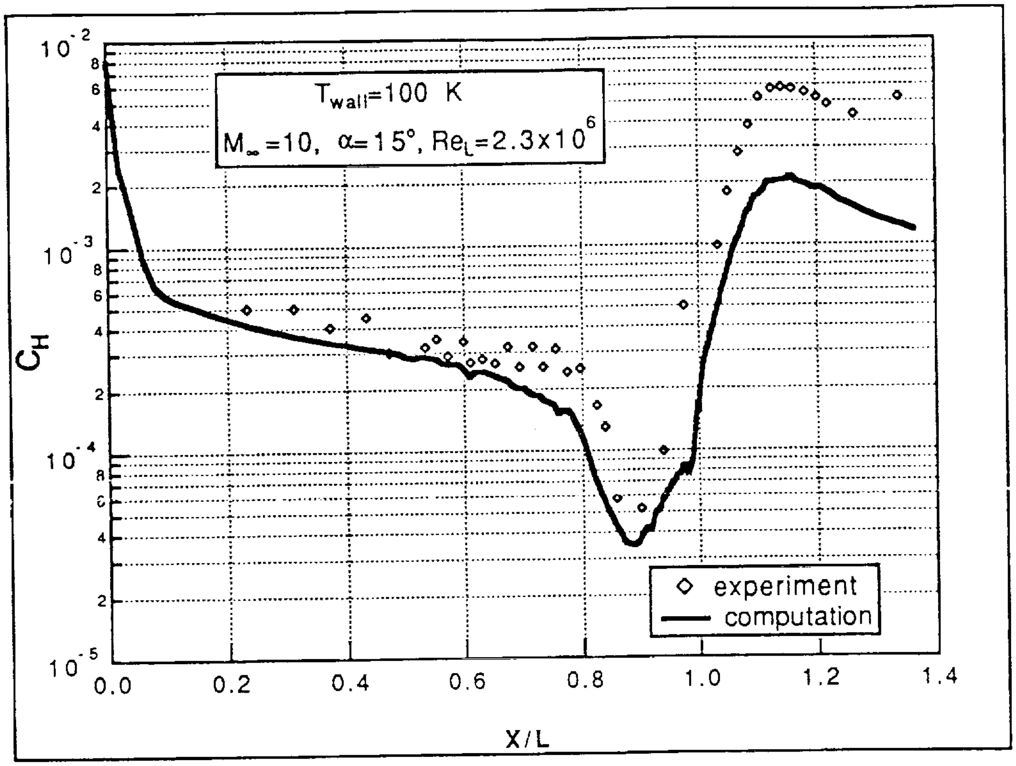

Figure 7. Stanton Number Comparison for 2-D Corner Flow Problem

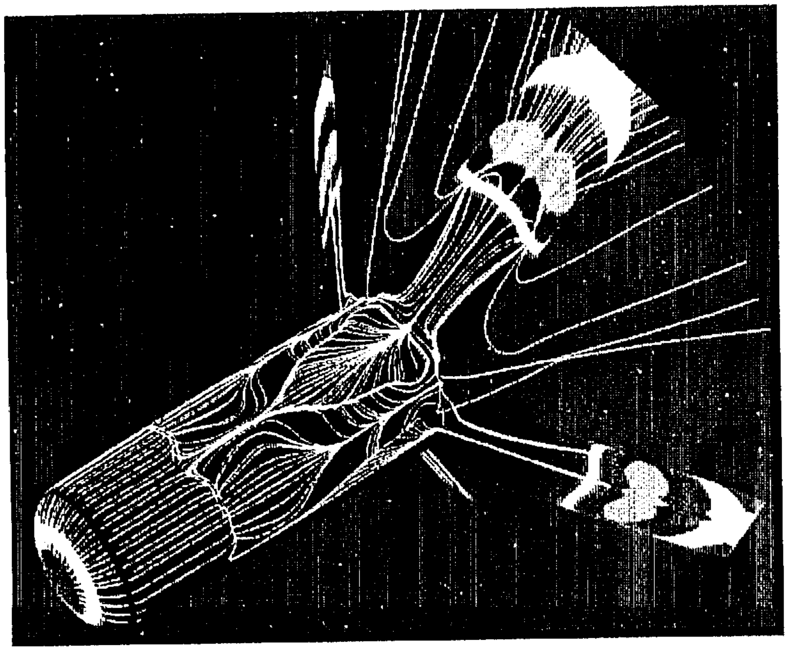

Surface Oil Flow

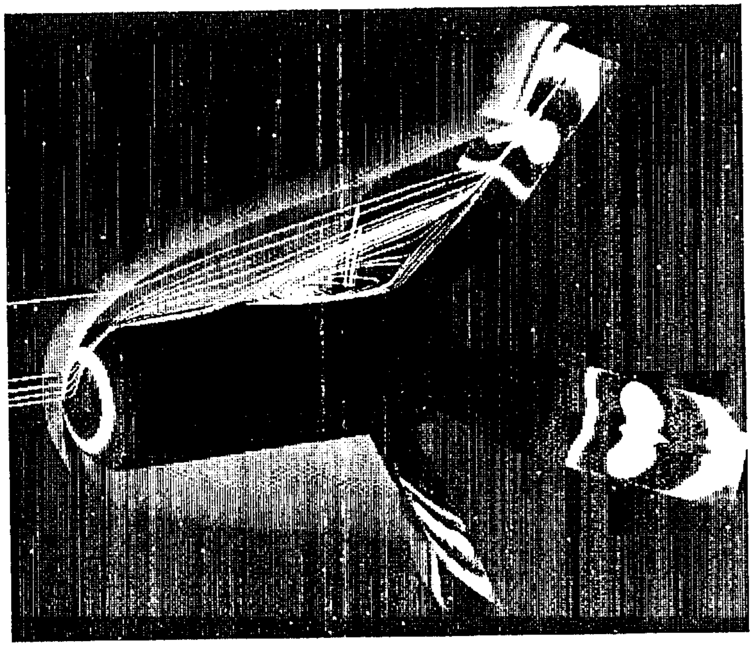

Particle Traces and
Outer Shock Surface

Figure 8. 3-D Solutions Around the LRV Decelerator

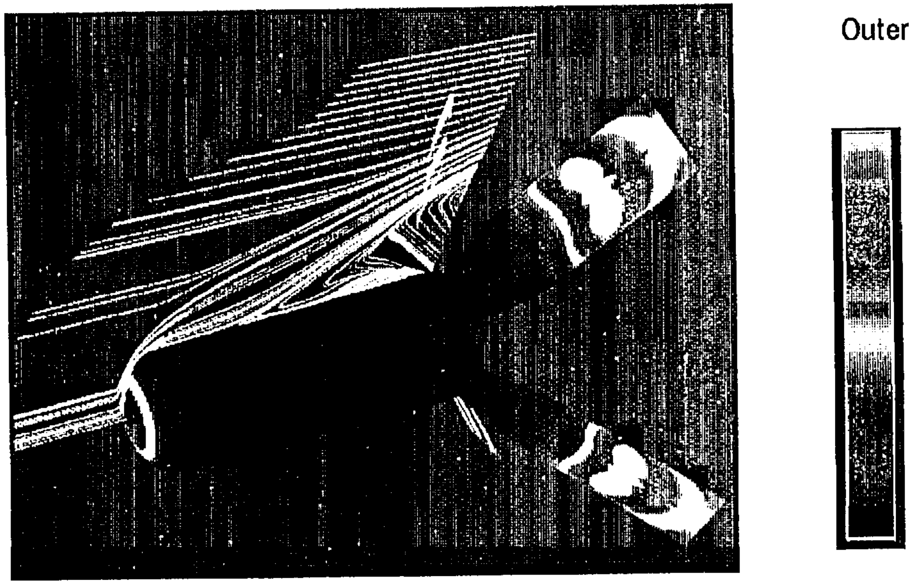

Particle Traces

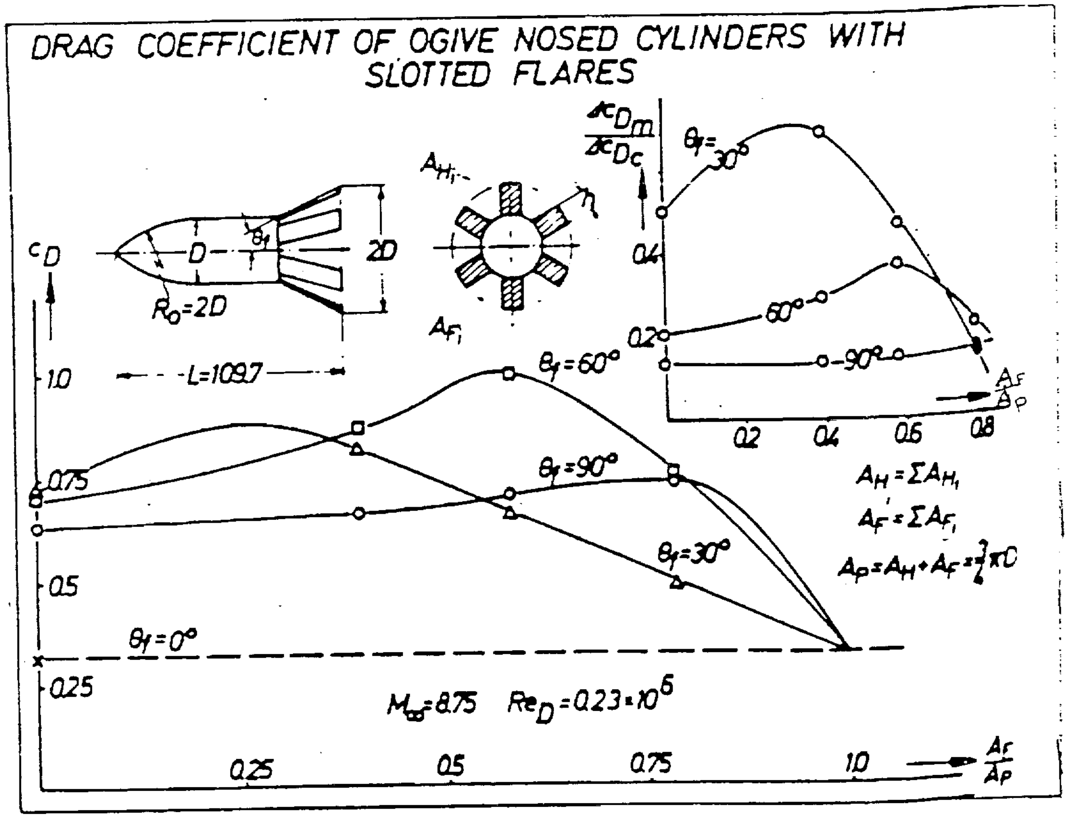

Figure 9. The Effect of Gap Ratio on the Drag Coefficient (Ref.)

Abstract for a Proposed Paper to be Presented at the
AIAA 28st Thermophysics Conference

COMPARISON OF THEORY WITH ATOMIC OXYGEN 1304Å RADIATION DATA FROM THE BOW SHOCK ULTRAVIOLET 2 ROCKET FLIGHT

Deborah A. Levin
Institute for Defense Analyses, Alexandria, VA 22311-1772
Graham V. Candler and Robert J. Collins
University of Minnesota, Minneapolis, MN 55455
Carl L. Howlett and Patrick Espy
Utah State University, Logan, UT 84322-4140
Ellis Whiting and Chul Park
NASA/Ames Research Center, Moffett Field, CA 94035

Abstract

Comparison is made between the results obtained from a state-of-the-art flow and radiative model and bow shock vacuum ultraviolet (VUV) data obtained the recent Bow Shock 2 Flight Experiment. An extensive data set was obtained from onboard rocket measurements at a reentry speed of 5km/sec between the altitudes of approximately 65-85km. The data, a description of the NO photoionization cell used, and interpretation of the data will be presented. The primary purpose of the analyses is to access the utility of the data in the context of a radiation model appropriate to the flight conditions of Bow Shock 2. Theoretical predictions based on flow modelling discussed earlier and a new radiation model are compared with data.

Introduction

The first bow shock flight experiment (April 1990) measured the ultraviolet radiation from shock-heated gas in the nose region of a 0.1016m nose radius rocket traveling at 3.5km/sec at altitudes from 40 to 70km. Papers providing details on the instrumentation[1] and analyzes of results[2] for the ultraviolet sensors have been presented. The second bow shock flight experiment (February 1991) provided similar types of ultraviolet data but for reentry at 5 km/sec between the altitudes of about 100 to 65km.[3,4] In this paper we examine vacuum-ultraviolet data (VUV) obtained from the resonance atomic transition at 1304Å. Such data is available only from the second flight. This data has received lower priority than that of the ultraviolet instruments; however, as will be shown here it is crucial to understanding the shocklayer modelling in its entirety. The reduction of this data was complicated by rocket precession during reentry caused by incomplete second stage

separation. Use of onboard navigational data has permitted us to correlate sensor - stagnation streamline angle as a function of time.

For early time portions of the reentry the atomic oxygen concentration in the shocklayer may be sufficiently low such that the resonance radiation is optically thin. In this case the radiation obtained is directly proportional to the amount of atomic oxygen in the flow. The degree to which theory can match the density dependence of the data indicates the fidelity of the flow thermochemical modelling. For example, atomic oxygen colliding with N_2 is the precursor process to the formation of NO for the flight conditions of the bow shock flight experiments. In Ref. 4 we have discussed the ~~less than perfect~~ inadequate agreement between theory and experiment for the 2300Å NO radiation, particularly at altitudes above 70km. Th~~e~~ S ~~disagreement between theory and experiment~~ may be due to ~~the inadequacies~~ to incorrect ~~in prediction~~ ~~the~~ NO concentration, its temperature, or to choice of the appropriate governing temperature in the radiation model. Of these possibilities the first is considered the most likely source of difficulty. Since the kinetic processes of NO and O are closely coupled it is unlikely that a correct flow solution will be obtained unless both the 2300 and 1304 radiation data sets can be modelled.

At later time portions during reentry (lower altitudes) the atomic oxygen concentration may increase so that self absorption becomes significant. For these conditions the modelling of the shocklayer spatial O concentration and temperature dependence, especially in the boundary layer, becomes important. Unlike the 2300Å radiation which depends primarily on the spatial portion of the shocklayer corresponding to the peak radiation in the flow, these conditions would further test the ability to model the boundary layer.

The radiation model that has been used here ~~incorporates~~ ~~two~~ key assumptions of the are summarized as follows, Excitation of atomic oxygen to the ^3S resonance state is achieved by collisions with neutral species rather than electrons. There are sufficient numbers of collisions such that a steady state assumption for the upper state population is assumed and self absorption of 1304Å atomic oxygen resonance radiation is treated by classical radiative transport theory. The NEQAIR 2 model with certain modifications (which will be enumerated) was the analytic tool used to compute resonance radiation.[5]

Experimental Set-up

Atomic oxygen 1304Å radiation measurements were planned for the first flight experiment with an NO-filled, CaF_2 window ionization chamber located in the stagnation region of the rocket. Due to quartz window spectral cut-off, the sensor diode was sealed

directly to the inside of the payload dome and viewed the ionized gas through a small hole of 0.5mm diameter. The VUV gas diode was compared against an NBS calibrated VUV diode to yield an absolute calibration for the 1304Å radiation measurement. The total dynamic range of this device was limited by uncertainties in the amplifier baseline drift that occurred due to the proximity of the electronics with the telemetry transponder and unanticipated shielding requirements. Thus 1304Å radiation data obtained from the first Bow Shock flight is considered unreliable.

VUV measurements were taken during the second Bow Shock flight with an NO photoionization cell in a configuration similar to the first flight. Major design changes to the preamplifiers from the first flight permitted data to be obtained from 85 to 65km altitudes. Figure 1 shows the cell and its geometry relative to the rocket payload axis. Figure 2 shows the spectral response of the CaF_2 window which can be seen to be much broader than the O transitions. Since there is essentially no atomic nitrogen present in the shocklayer under these flight conditions the radiation obtained from this measurement is assumed to be solely that due to atomic oxygen.

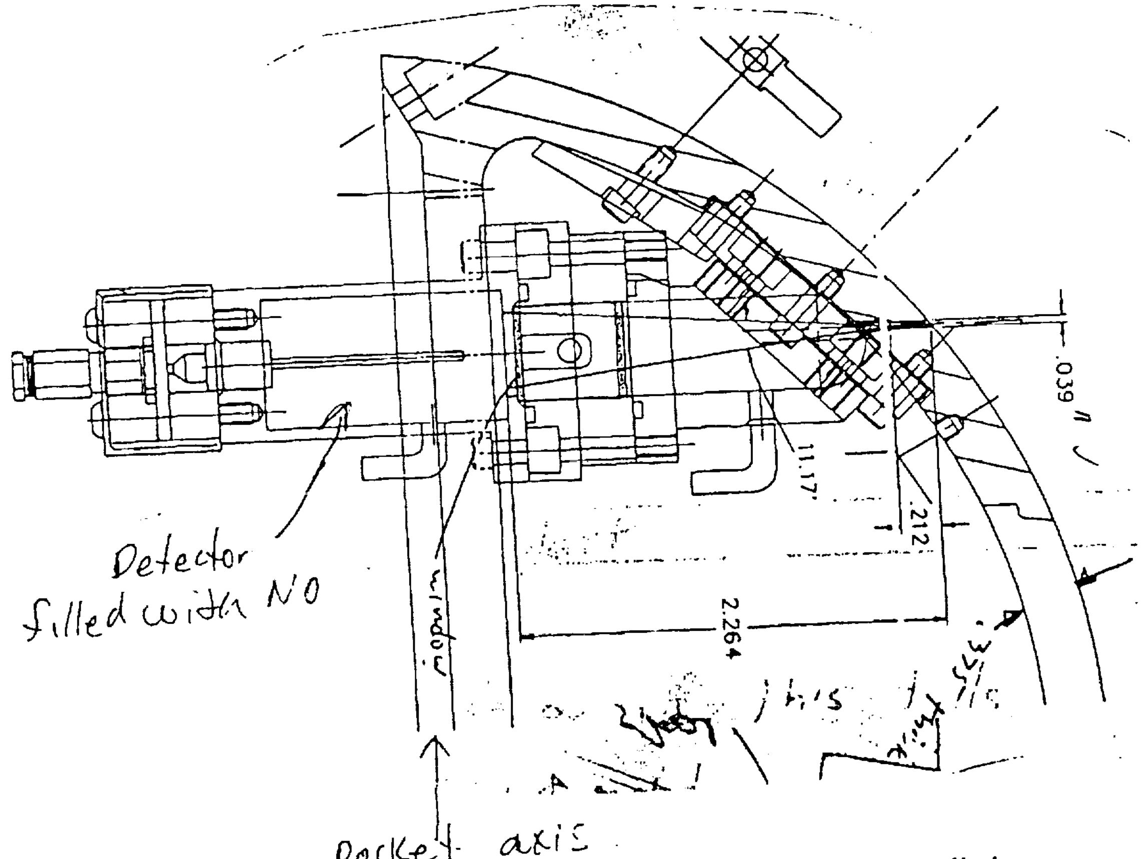

Fig. 1. NO photoionization cell used to measure atomic oxygen radiation.

geometry

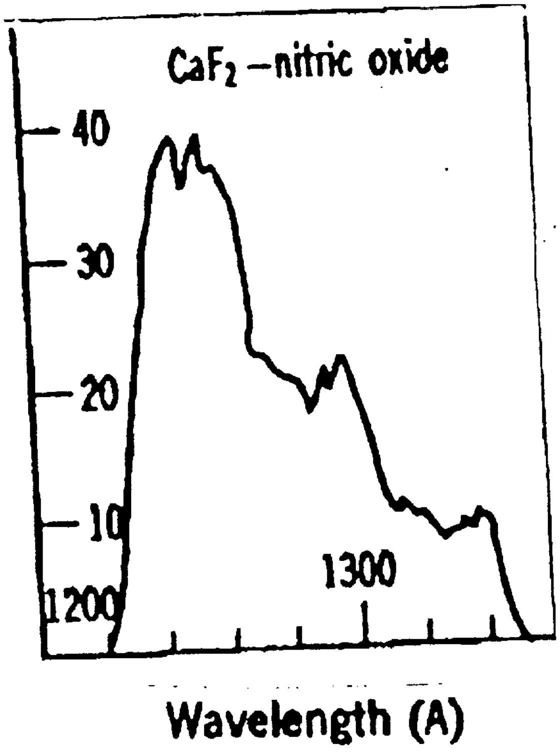

Fig. 2. Spectral response of the CaF$_2$ cell window ← Insert reference to VUV measurements

Data

Figure 3 shows a summary of the atomic oxygen 1304Å radiance data that was obtained during the reentry portion of the second flight along with the corresponding altitude of the rocket. The atomic oxygen sensor was located 37° from the rocket longitudinal axis. The highly oscillatory nature of the signal is due to rocket precession which changes the location of the stagnation point as a function of time during the flight and is more noticeable in the data collected from off-axis sensors. To permit quantitative comparison of data with models, the angle between the sensor and the effective stagnation streamline (γ) must be known. Using the onboard navigational data supplied by Sandia National Laboratories and transformations of the sensor location into the onboard navigational coordinate reference frame[6] ,γ can be computed as a function of time. Figure 4 shows an example of radiance correlated with γ during a time region selected at ~75km. The radiance peaks at small γ (i.e. closer to the stagnation point) and is reduced at the largest values (i.e. towards the wake). The time correlation appears to be good and can provide detailed information on the angular variation in the flow.

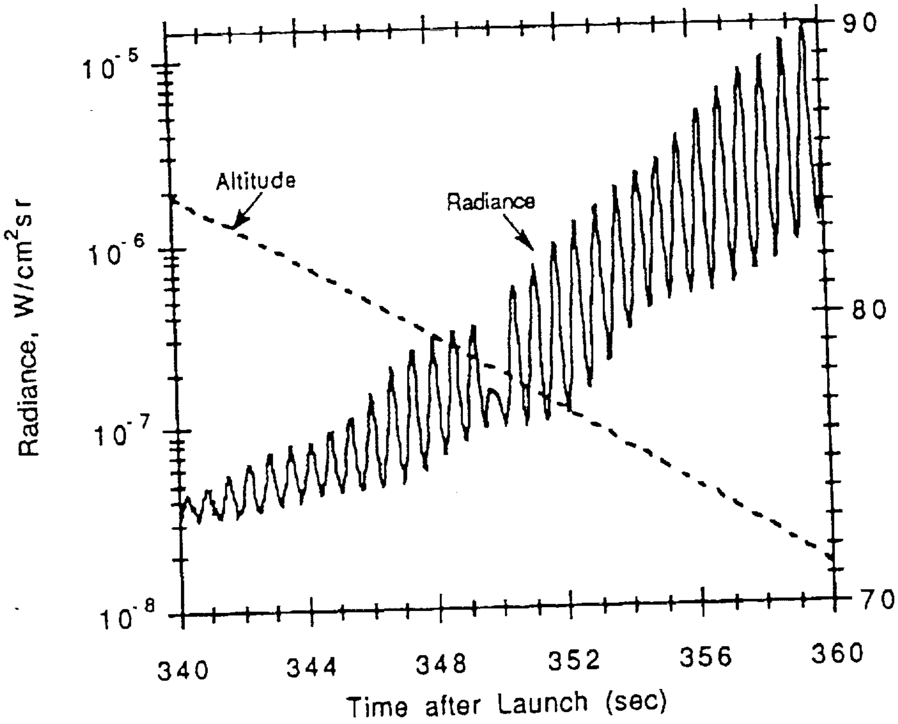

Fig. 3 Atomic Oxygen Radiance and Vehicle Altitude as a Function of Time after Launch - Reentry Portion of Flight

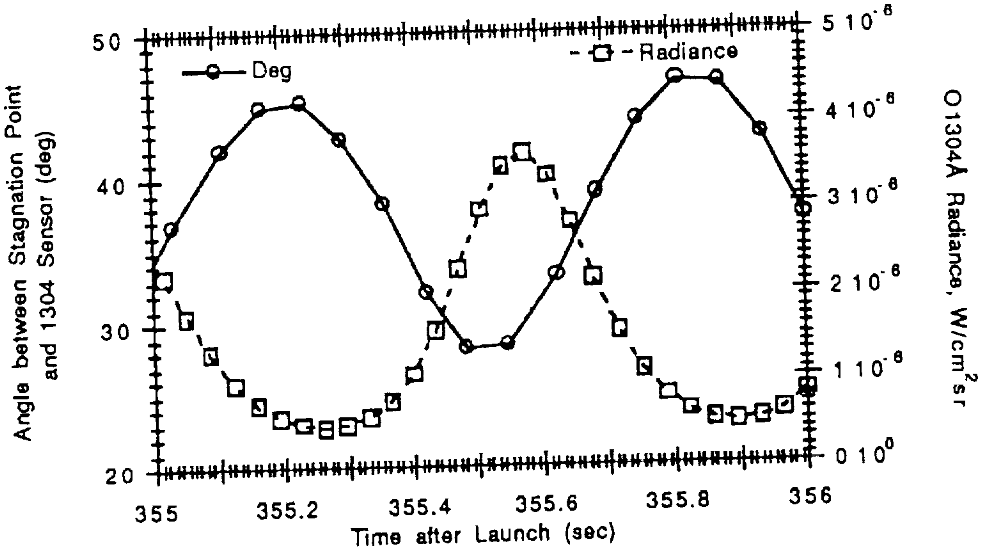

Fig. 4 Comparison of Stagnation Streamline - Sensor angle and VUV Radiance as a Function of Time after Launch

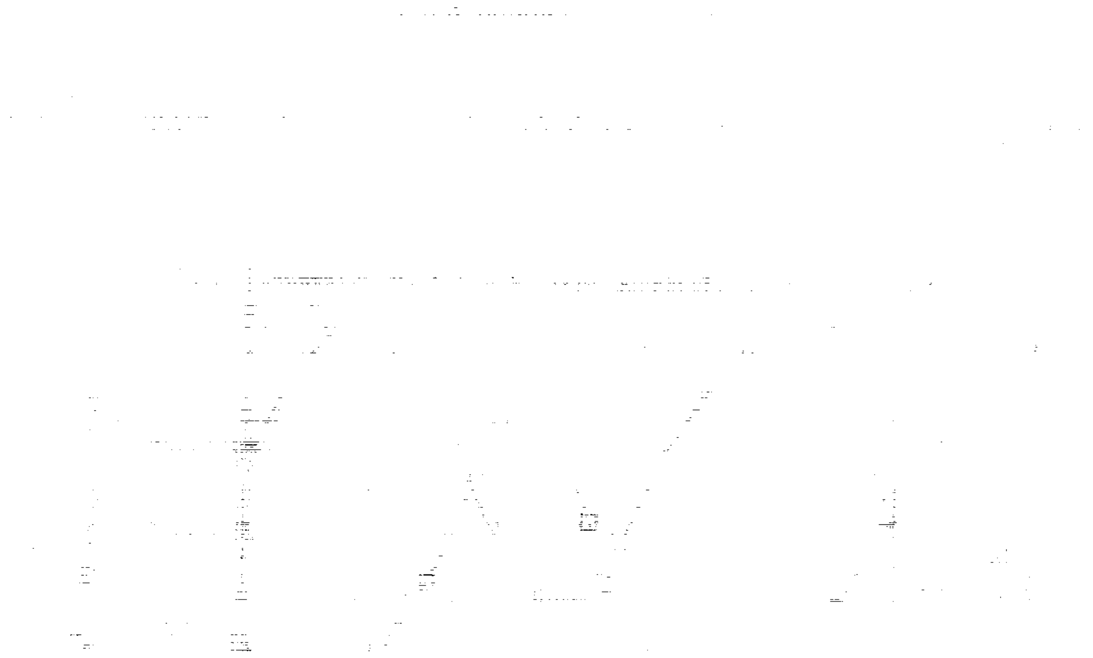

Radiation Model

Modelling of 1304Å resonance radiation has been considered by Whiting and Park[5] to evaluate heating rates for a blunt body reentry at 10km/sec (Aeroassist Flight Experiment). The major excitation processes under AFE conditions are produced by electron collisions with O. For the Bow Shock 2 Flight experiment the atomic radiation observed is due to neutral - O collisions. If it is assumed that there are enough collisions such that the electronic states are in a Boltzmann distribution at the heavy particle translation temperature orders of magnitude more radiation is predicted than was observed. Therefore a rate equation approach must be considered. A new model is proposed that accounts for neutral excitations with O; but, assumes that the upper state ^3S population can be obtained from the steady state solution of the appropriate rate equations.

Table 1 shows the atomic oxygen energy levels for the first five electronic states.[7] Rates for neutral collisional excitations among the first three states have been measured and are high for the temperatures obtained in the shocklayer. Therefore these levels are assumed to be in a Boltzmann distribution at the heavy particle translation temperature. The strongly allowed dipole resonance $^3P \rightarrow {}^3S$ transition can be modelled as the three level system shown in Fig. 5. Collisions of the O(^1D) state with neutrals will produce a transition to the ^3S state, although this rate has probably not been explicitly measured. An estimate of that rate will be used based on data given in Ref. 8.

Table 1. Atomic Oxygen Spectral Properties

State Number	Term Symbol	Degeneracy	Energy Level (cm^{-1})
1	^3P	9	78.
2	^1D	5	15,868.
3	^1S	1	33,792.
4	^5S	5	73,768.
5	^3S	3	76,795.

In the optically thin limit the rate equations for this three level system are

$$\frac{d[O(^1D)]}{dt} = k_f[O(^3S)][M] - k_r[O(^1D)][M] - k_{2f}[O(^1D)][M] + k_{2r}[O(^3P)][M] \qquad (1)$$

$$\frac{d[O(^3S)]}{dt} = -k_f[O(^3S)][M] + k_r[O(^1D)][M] - A[O(^3S)] \qquad (2)$$

Under steady state assumptions the derivatives in Eqs. (1) and (2) are set to zero and an expression for the upper state ^3S concentration is obtained,

$$[O(^3S)]_{qss} = \frac{[O(^3P)]Q_5/Q_1 n_t k_f}{n_t k_f + A\left\{1+\frac{Q_5}{Q_2}\right\}} \cong \frac{[O(^3P)]Q_5/Q_1 n_t k_f}{A} \qquad (3)$$

where n_t is the total free stream density of species M, A represents the Einstein coefficient of $3.8\times10^8 sec^{-1}$ for the resonance transition, Q_i represent the partition functions of the states given in Table 1, and k_f is the quenching rate from the ^3S to ^1D state. It is interesting to note that since the Einstein A coefficient is about a factor of 100 greater than that for NO 2300Å radiation, 1304Å radiation is collision limited whereas for NO collisional quenching dominates.

Since the production of atomic oxygen is second order in n_t, Eq. (3) predicts that the atomic oxygen radiation should be proportional to n_t^3. To test this hypothesis the density dependence of the data can be examined. Figure 6 shows data taken at altitudes between 80-70km sorted to include measurements that occurred at an angle of 36±0.2° from the stagnation streamline. The oscillations can be further reduced with tighter sorting; however, the third law dependence in n_t can be seen to give the best fit.

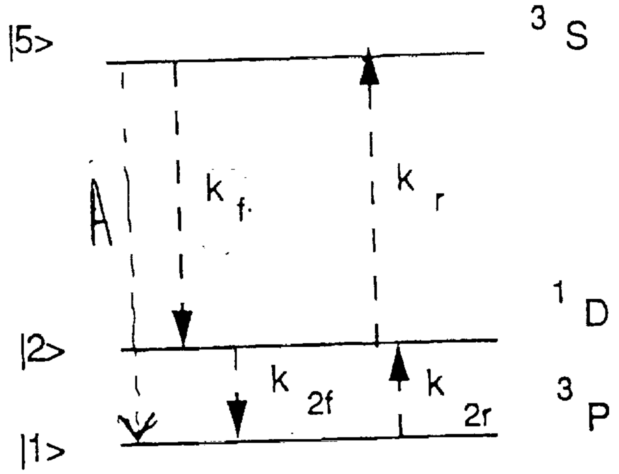

Fig. 5 Three Level Atomic Oxygen System

Calculations

The computational technique that has been used to simulate the stagnation region flowfield is that given in Refs. 2 and 4 which discusses enhancements to the original flow modelling of Candler and MacCormack.[9] Briefly, the shock heated air is modelled by eight chemical species (N_2, O_2, NO, NO^+, N_2^+, N, O, and e^-) that are allowed to react with each other at finite rates. Three independent temperatures in the flow are modelled: heavy particle translational, molecular rotational, and a combined molecular vibrational and

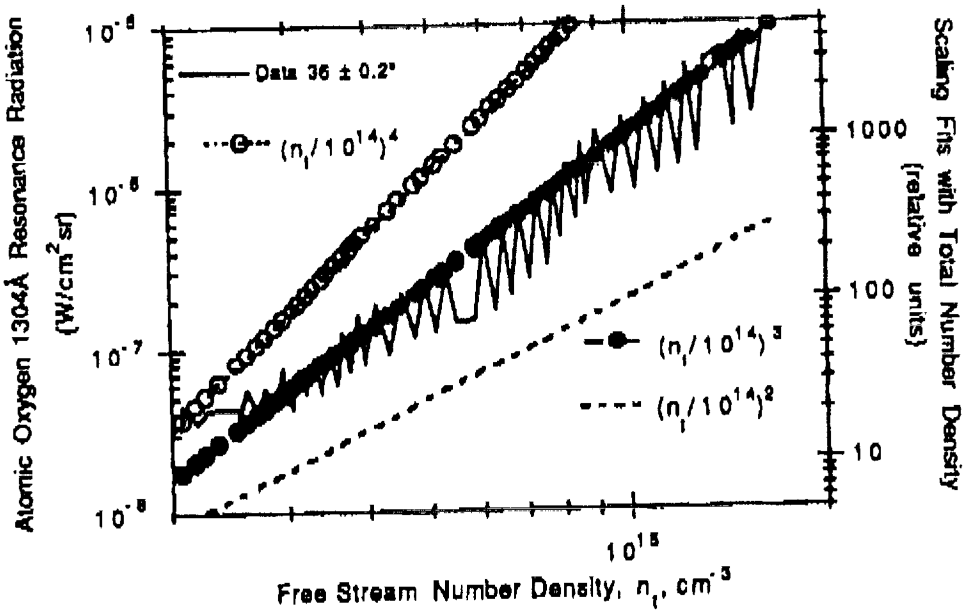

Fig.6 Comparison of Atomic Oxygen Data and Density dependence.

electron translational temperatures. The atomic oxygen concentration and heavy particle temperature obtained at each point in the flow have been used to compute the 1304Å radiation. Two flow models have been considered, a thermochemical "baseline" version and a modified solution based on alternative reaction rates suggested by Wray.[4] These solutions differ substantially in the concentration of ground state O predicted between 70-80km. At 80km there are factors of 100 difference in atomic O concentration between the two solutions.

Equation (3) has been incorporated into the NEQAIR 2 model. The calculations have modelled the dependence of the upper state population on optical thickness through the use of the escape coefficient. This aspect of the calculation may be refined further in the final version of this paper. The full radiative transport capability of the NEQAIR model has been used to evaluate 1304Å radiation at altitudes of 85, 80, 75, 71, and 65km with both flow solutions. A value of k_f of 8×10^{-11}cm^3/sec at 300K obtained from Ref.8 was used. Although the actual value of the quenching coefficient still needs to be obtained, it is fairly constant over the altitude range considered here. Hence if one flow model is superior to the other, the *shape* of its predicted radiance should be in better agreement with the data.

Figure 7 shows the results of the calculations for the full radiative transport radiance at the body (*i.e.*, the location of the 1304 sensor). For convenience the corresponding

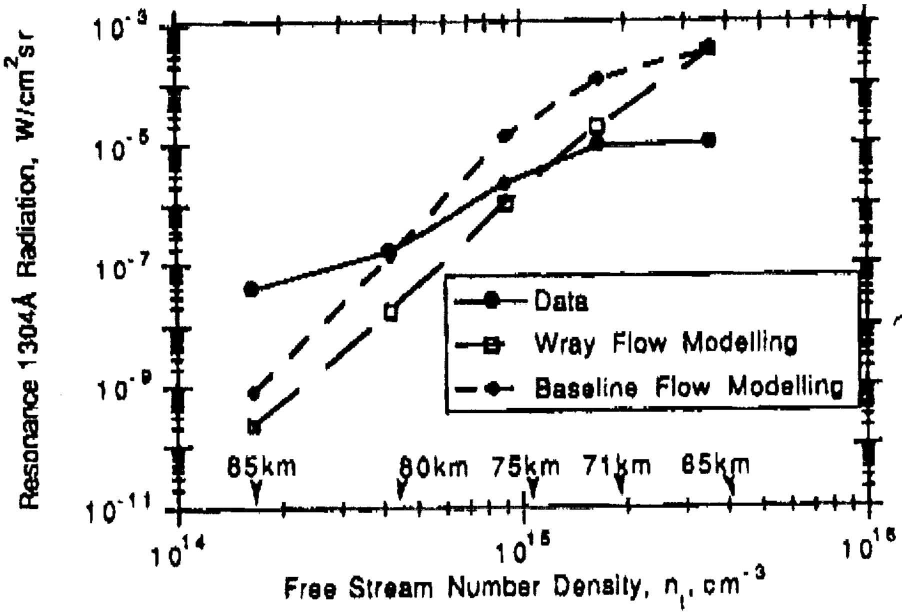

to make symbols bigger

Fig. 7 Comparison of New NEQAIR 2 Calculations with Data - Full Radiative Transport

altitudes are also indicated. The data points at 85 and 65km should have large error bars associated with them. At the highest altitude, the data is becoming shot noise limited making it difficult to correlate exactly sensor viewing location as a function of time in the precession period. At 65km there remains uncertainties regarding the performance of the photoionization cell, which still need~~s~~ to be clarified. These error bars will be specified in the final version of this paper. Both flow models predict the shocklayer to be optically thin for altitudes ≤ 75km. At 71km the baseline model predicts self absorption in the shocklayer to be more important than the Wray flow modelling. Both flow models predict the self absorption in the shocklayer to be substantial by 65km. If the comparison between theory and data is restricted to altitudes between 70 to 80km where all models predict the flow to be optically thin and the data density dependence and radiation modelling are consistent (*i.e.*, Fig. 6) neither calculation predicts the correct radiation density dependence, theory is seen to fall off faster than experiment. Therefore, the thermochemical modelling of atomic oxygen concentration should be further examined.

The disagreement with theory and data for the 65km altitude of orders of magnitude may be due to problems in modelling the atomic oxygen concentration and temperature in the boundary layer. Since the NO 230nm radiation was optically thin, the radiation computed at the body in that case would be less sensitive to errors in the boundary layer

modelling. Grid refinement techniques to emphasize boundary layer modelling will be discussed in the final version of this paper.

Conclusion and Additional Work

A radiation model has been successfully proposed to describe neutral excitations of atomic oxygen that produce 1304Å resonance radiation. The magnitude of the specific quenching rate or the ability to calculate it will be discussed further in the final version of this paper. Self absorption has been included in the calculations shown here; but, the approximate escape coefficient formalism will be replaced with an improved iterative treatment of the radiation field in the final version of this paper.

The difference in density dependence discrepancy that was obtained for the 2nd flight comparison between the 0° viewing 230nm photometers and calculations are seen here for the atomic oxygen calculations as well. This data is important since a rigorous test of any flow solution should include comparison with the 1304 as well as 2300Å radiation. Since atomic oxygen is a precursor to formation of NO the correct calculation of its concentration is crucial in modelling 230nm radiation.

References

[1]Erdman, P., E. Zipf, P. Espy, C. Howlett, R. Loda, R. Collins, D. Levin and G. Candler, "Flight Measurements of Low Velocity Bow Shock Ultraviolet Radiation," *AIAA Paper No. 91-1410*, 1991 (accepted for publication in Journal of Thermophysics and Heat Transfer).

[2]Levin, D., G. Candler, R. Collins, P. Erdman, E. Zipf, P. Espy, and C. Howlett, "Comparison of Theory with Experiment for the Bow Shock Ultraviolet Rocket Flight," *AIAA Paper No. 91-1411*, 1991 (accepted for publication in Journal of Thermophysics and Heat Transfer).

[3]Erdman, P., Zipf, E., Howlett, C., Levin, D., Candler, G., and Collins, R., "Measurements of Ultraviolet Radiation from a 5km/sec Bow Shock," *AIAA Paper No. 92-2870*, 1992.

[4]Levin, D., Candler, G., Collins, R., Erdman, P., Zipf, E., and Howlett, C., "Examination of Ultraviolet Radiation Theory for Bow Shock Rocket Experiments," *AIAA Paper No. 92-2871*, 1992.

[5]Whiting, E. E., "Radiative Heating at the Stagnation Point of the AFE Vehicle," NASA Technical Memorandum No. 102829, 1990.

[6] Private communication from Mr. Larry Rollstin, Sandia National Laboratories, Albuquerque, NM.

[7] Park, C., *Nonequilibrium Hypersonic Aerothermodynamics*, Wiley & Sons, New York, 1990, ISBN 0-471-51093-9.

[8] Bortner, M. H., Bauer T., and Blank, C. A., "DNA Reaction Rate Handbook", Report number DNA 1948H, March 1972.

[9] Candler, G., V. and MacCormack, R. W., "The Computation of Hypersonic Ionized Flows in Chemical and Thermal Nonequilibrium," *J. Thermophysics and Heat Transfer*, Vol. 5, No. 3, pp.266-273, July 1991.

Extended Abstract of a Proposed Paper for the AIAA 28th Thermophysics Conference
July 6-9, 1993, Orlando, Florida

Measurement and Analysis of *NO* Radiation in an Arc-Jet Flow

Nigel K.J.M. Gopaul[1]
Dikran S. Babikian[2]
and
Chul Park[3]

Abstract

Radiation from Nitric Oxide (NO) band systems in the free-stream of NASA Ames $20MW$ arc-jet wind tunnel was measured and computed. The emission measurement was conducted with a 0.3 meter McPherson spectrograph using photographic films in the wavelength region from 185 nm to 300 nm. The NO band systems consist of the following bands; NO_β, NO_δ, NO_ϵ, and NO_γ. The analysis of data indicated that only the ground vibrational level ($v' = 0$) of NO_γ and NO_δ band systems are present.

Excitation temperatures in the free stream of arc-jet flow were deduced by comparing the measured spectra with the calculated spectra using the nonequilibrium radiation code NEQAIR. The deduced rotational, vibrational, and electronic temperatures are: $T_r = 660 \pm 50°K$, $T_v \leq 850 \pm 50°K$, and $T_e = 7560 \pm 340°K$, respectively. The results indicated that the free stream flow was in thermal nonequilibrium.

The Three-Temperature Nonequilibrium Nozzle Flow computer code (NOZ3T) was used to predict the arc-jet nozzle flow. The code assumes the early portion of the nozzle flow to be in equilibrium. The rest was solved assuming three-temperature nonequilibrium flow. Comparing the computed temperatures of T_r, T_v, and T_e to those extracted from the experimental spectra the following two important parameters were determined; the cross section for transfer of vibrational energy to electronic energy, and the ratio of true vibrational relaxation rates to Milikan and White vibrational relaxation rates.

Experiment

Figure 1 shows the schematic of the experimental set-up. The operating conditions of the $20MW$ arc heater were the following: chamber pressure $2.4atm$, flow rate $0.0864kg/sec$, current $2000A$ and voltage $2600V$. Spectral data were taken in the free-stream flow 14 inches downstream of the nozzle exit[1].

A McPherson spectrograph model 218 with a camera attachment was used to collect the data. The spectrograph has a speed of $f/5.3$ and 0.3 meter focal length. The set-up used is known as Criss-Crossed Czerny-Turner optical system[2]. It is an unconventional

---

[1] Graduate Research Assistant, Stanford University, Stanford, California. Member AIAA.

[2] Research Scientist, Eloret Institute, Palo Alto, California. Member AIAA.

[3] Research Scientist, NASA-Ames Research Center, Moffett Field, California. Associate Fellow AIAA.

mounting arrangement where the light beam from the two mirrors and the plane grating are crossed in order to obtain the $f/5.3$ optics. A Joyce Loebel microdensitometer model MK III CS was used to measure the optical densities recorded on the film. The microdensitometer traces were transferred to a computer to be analyzed and compared with the theoretical predictions. Detailed description of the experimental set-up, instrumentation, and data collection and calibration procedures will be given in the full paper.

Data Analysis

The uncalibrated densitometer trace of the second order spectra is shown in Fig. 2. The wavelength calibration was performed using commercial mercury (Hg) and argon (Ar) spectral lamps. The mercury lamp was used in the $400nm$ to $650nm$ spectral range and the argon lamp was used in the $650nm$ to $850nm$ spectral range. From the densitometer traces of the mercury and argon spectra and from the known locations of their spectral lines, the relation between the lamps spectra and the actual free-stream spectra was developed.

The relative intensity calibration was done in two parts. First the film was calibrated for the relative intensity at specific wavelengths. Second the film was calibrated for the spectral sensitivity changes due to the film sensitivity, the spectrograph grating, and the entire optical set-up. This calibration was done using a natural density step-wedge filter. The resulting intensity trace, corrected for the film response is shown in Fig. 3.

The excitation temperatures (rotational, T_r, vibrational, T_v, and electronic, T_e) were determined by comparing the calibrated experimental and the calculated spectra. The calculated spectrum was obtained using the Nonequilibrium Air Radiation code (NEQAIR) [3,4]. The upper limit of vibrational temperature was determined by finding the vibrational temperature in the calculations that extinguishes the radiation from the $v' = 1$ level. The electronic temperature was deduced from the relative intensities of NO_γ and NO_δ. The temperature determination methodology is iterative in nature and will be discussed in the full paper.

Theory

The computer code NOZ3T[5,6] was used to predict the free-stream flowfield through the convergent-divergent nozzle of the arc-jet wind tunnel. The entrance and the begining section of the nozzle were assumed to be at equilibrium. The rest of the nozzle was solved assuming three-temperature nonequilibrium flow. The equilibrium thermodynamic conditions required at the entrance of the nozzle are: pressure, velocity, estimated temperature , and enthalpy. These parameters were computed using Arc Heater Flowfield computer code (ARCFLO) [7,8].

With the operating conditions of the arc-jet wind tunnel given in the preceding section, the ARCFLO predicted the following center line values at the exit of the arc-column: $T = 12189^\circ K$, $V = 226m/sec$, and $h = 60MJ/kg$. The corresponding mass averaged values were: $T = 8918^\circ K$, $V = 185m/sec$, and $h = 22MJ/kg$.

The results of calculation were compared with the rotational, vibrational, and electronic temperatures obtained from the experiment. Two important parameters; the cross-section for vibrational-electronic energy exchange between various species, and the ratio of true

vibrational relaxation rates to Millikan-White vibrational relaxation rates[9], were adjusted to reach to an agreement between the two sets of temperatures.

Results

The spectral bands detected by the spectrograph were identified as the NO_γ and NO_δ band systems in second order. The NO_γ band system is denoted by $A^2\Sigma^+ \rightarrow X^2\Pi$, where $A^2\Sigma^+$ is the upper electronic state and $X^2\Pi$ is the ground state of the Nitric Oxide (NO) molecule. The NO_δ band system is denoted by $C^2\Pi \rightarrow X^2\Pi$ where $C^2\Pi$ is the upper electronic state and $X^2\Pi$ is the electronic state of the NO molecule.

The NO_β band system, which is denoted by ($B^2\Pi \rightarrow X^2\Pi$) and lies in the same spectral region as the NO_γ, was not present in the data. The absence of this band system indicates that the $B^2\Pi$ electronic state was not populated to a significant amount, although it is located at nearly the same energy level as the $A^2\Sigma^+$ state (see Fig. 4). The $B^2\Pi$ state does have a slightly larger internuclear distance than the $A^2\Sigma^+$ state, however this will not affect their population ratio under equilibrium conditions. This phenomenon suggests that the upper electronic states of the NO molecule was populated in a nonequilibrium manner due to a possible selective population mechanism.

The NO_ϵ band system denoted as ($D^2\Sigma^+ \rightarrow X^2\Pi$) lies very close to the NO_δ band system in the energy potential curves. However the strong bands of the NO_ϵ lie in the Vacuum Ultra Violet (VUV) region and only few of the weaker bands are in the spectral region of our experiment. These weak vibrational bands of NO_ϵ system (vibrational-rotational levels (0,5), (0,6), and (0,7)) lie under the much stronger vibrational bands of NO_γ systems (vibrational-rotational levels (0,0),(0,1), and (0,2)) (see Fig. 5). To verify the existence of NO_ϵ in the free stream flow, further emission measurements are needed in the VUV spectral region where NO_γ band system does not exist.

The deduced excitation temperatures are $T_r = 660 \pm 50°K$, $T_v \leq 850 \pm 50°K$, and $T_e = 7560 \pm 340°K$, and the population ratio of the $C^2\Pi$ state to the $A^2\Sigma$ state of the Nitric Oxide (NO) molecule is 0.42 ± 0.04. The study showes that the cross-section for vibrational-electronic energy exchange is in the order of $10^{-18} cm$, where as the dividing factor to Millikan-White relaxation factor is at least in the order of 10^8. The enthalpy deduced from this work is $38 MJ/kg$. Figure 6 is a plot of the computed excitation temperatures using NOZ3T.

References (partial list for the abstract)

[1] Gopaul N.K.J.M., "Spectral Measurement of Nonequilibrium Nitric Oxide in the Free-Stream of an Arc-Jet Flow," Degree of Engineer Thesis, Stanford University, Stanfored, 1992.

[2] Mcpherson Instruments, "Instruction Manual for Model 218, 0.3 Meter Combination Scanning Monochromator and Spectrograph," Acton, MA. USA.

[3] Park, C., "Nonequilibrium Air Radiation (NEQAIR) Program: User's Manual," NASA Technical Memorandum 86707, 1985.

[4] Moreau, S., Laux, C., Chapman, D.R., MacCormack, R.W., "A More Accurate Nonequilibrium Air Radiation Code: NEQAIR Second Generation," AIAA Paper 92-2968, 1992.

[5] Park, C. and Babikian, D.S., "Users Manual for NOZ3T The Three-Temperature Nonequilibrium Nozzle Flow Code," 1992.

[6] Seung-Ho, L. and Park, C., "Validation of Three-Temperature Nozzle Flow Code NOZ3T," Proposed Paper for the AIAA 28th Thermophysics Conference, Orlando, Florida, 1993.

[7] Watson, V.R. and Pegot, E.B., "Numerical Calculations for the Characteristics of Gas Flowing Axially Through a Constricted Arc," NASA TN D-4042, 1967.

[8] Nicolet, W.E., Shepard, C.E., Clark, K.C., Balakrishnan, A., Kesselring, J.P., Suchsland, K.E., and Reese, J.J., "Methods for the Analysis of High-Pressure, high Enthalpy Arc Heaters," AIAA paper 75-704, AIAA 10th Thermophysics Conference, Denver, Colorado, 1975.

[9] Millikan, R.C., and White, D.R., "Systematic of Vibrational Relaxation," Journal of Chemical Physics, Vol. 139, 1963, pp. 3209-3213.

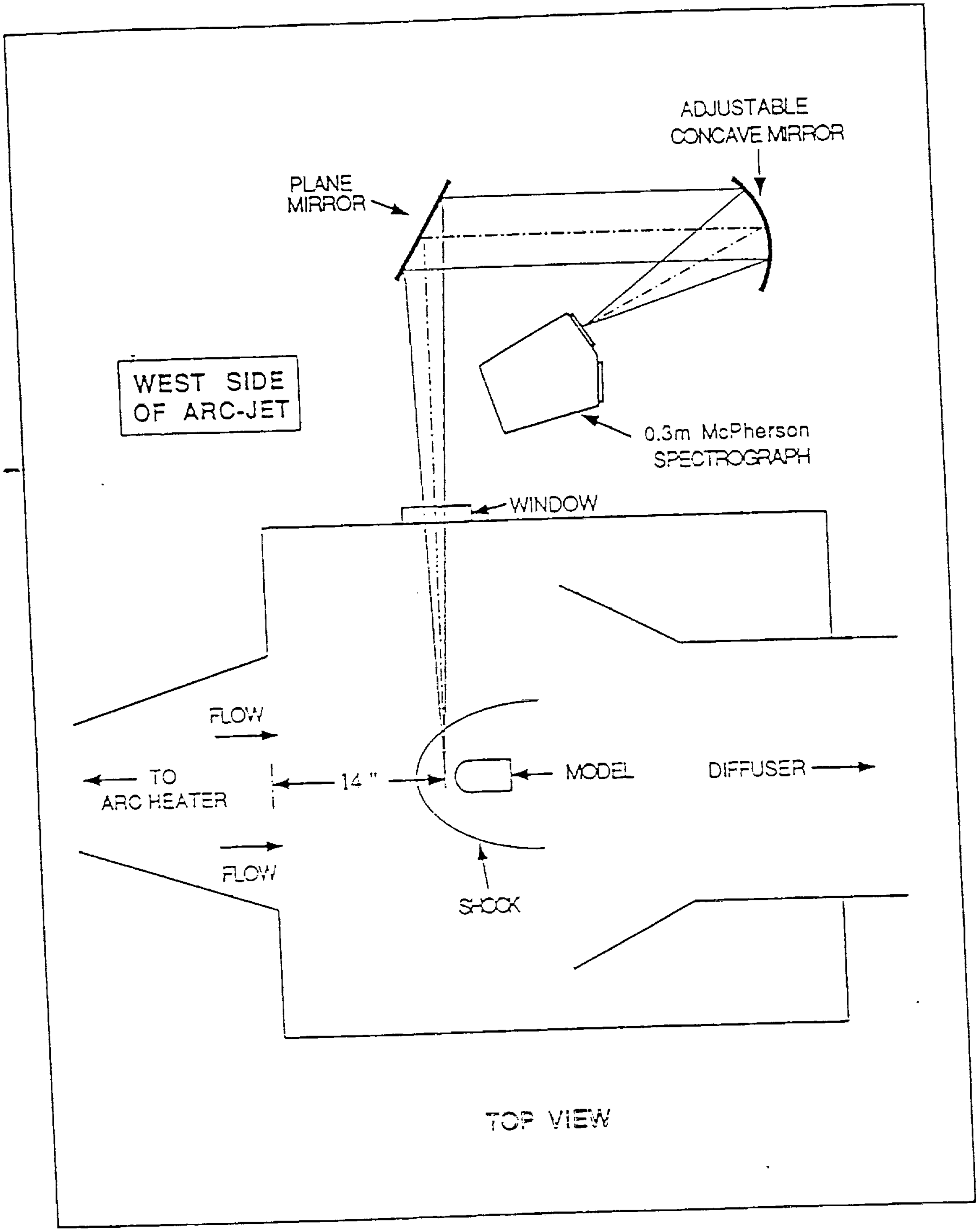

Figure 1. Experimental Optical Set-Up at the 20 MW Arc-Jet Facility.

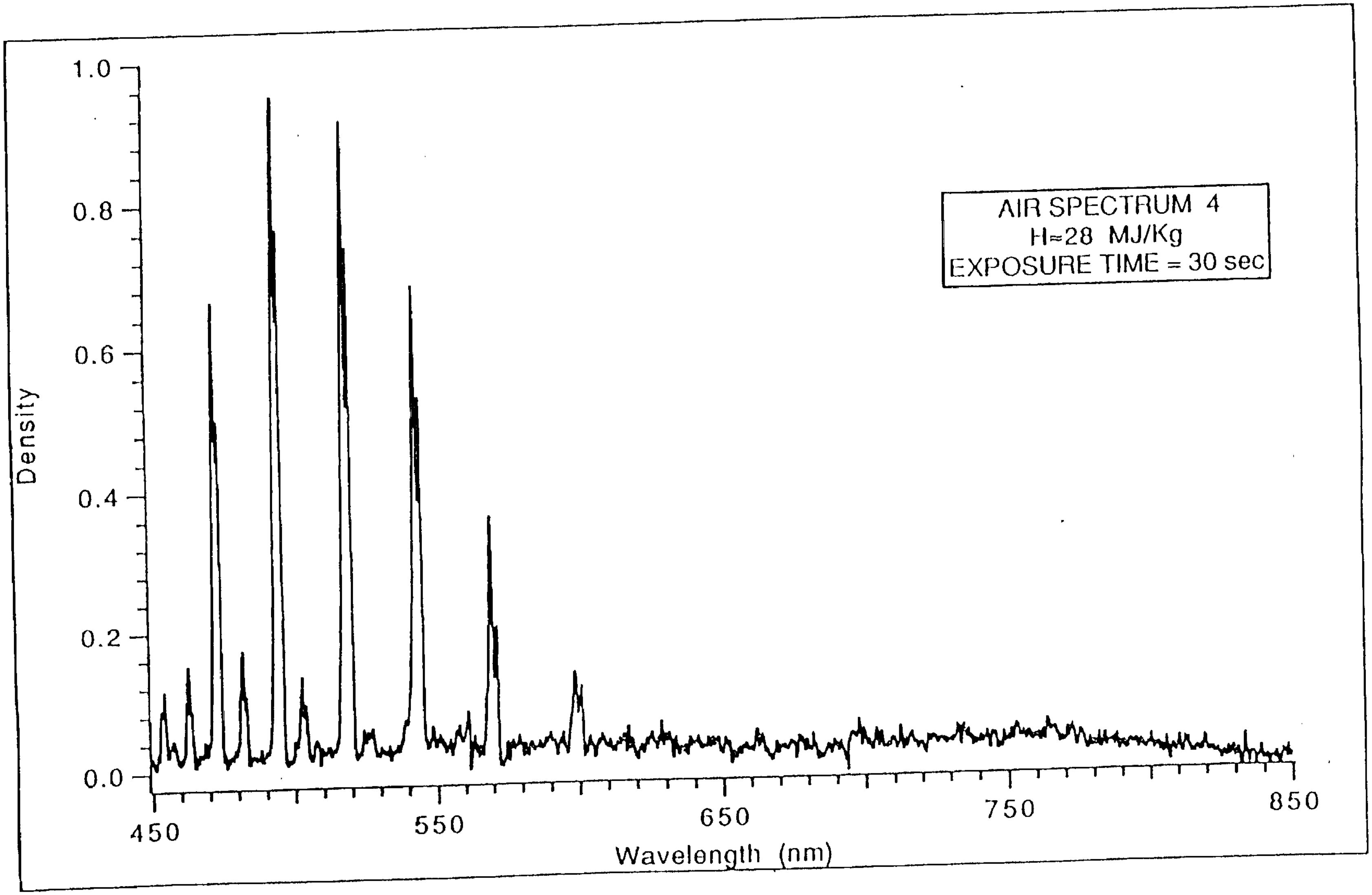

Figure 2 . Air Spectrum Covering 450 nm to 850 nm of the Free-Stream Arc-Jet Flow for Run 4.

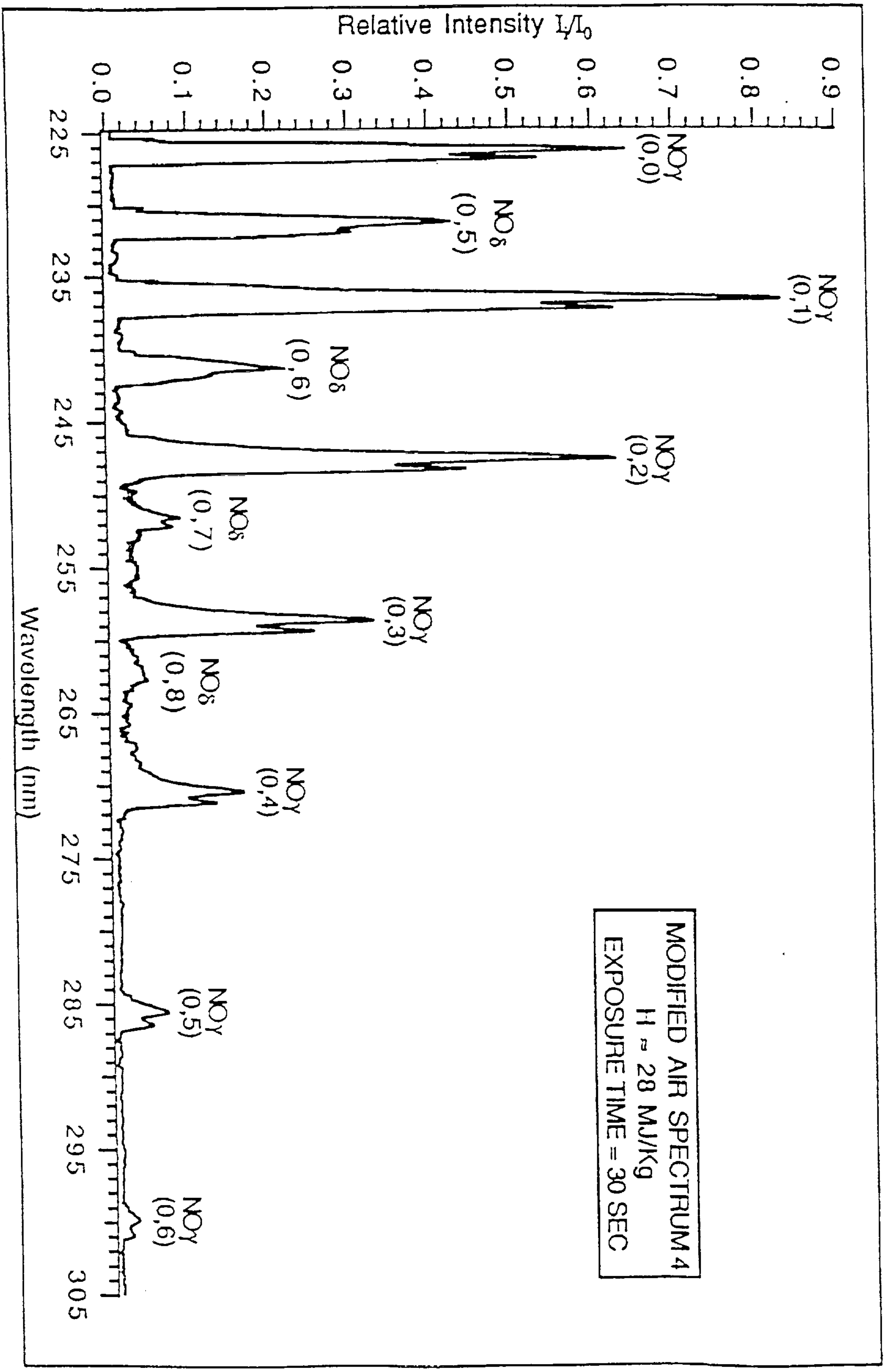

Figure 3. Modified Air Spectrum of the Free-Stream Arc-Jet Flow for Run 4.

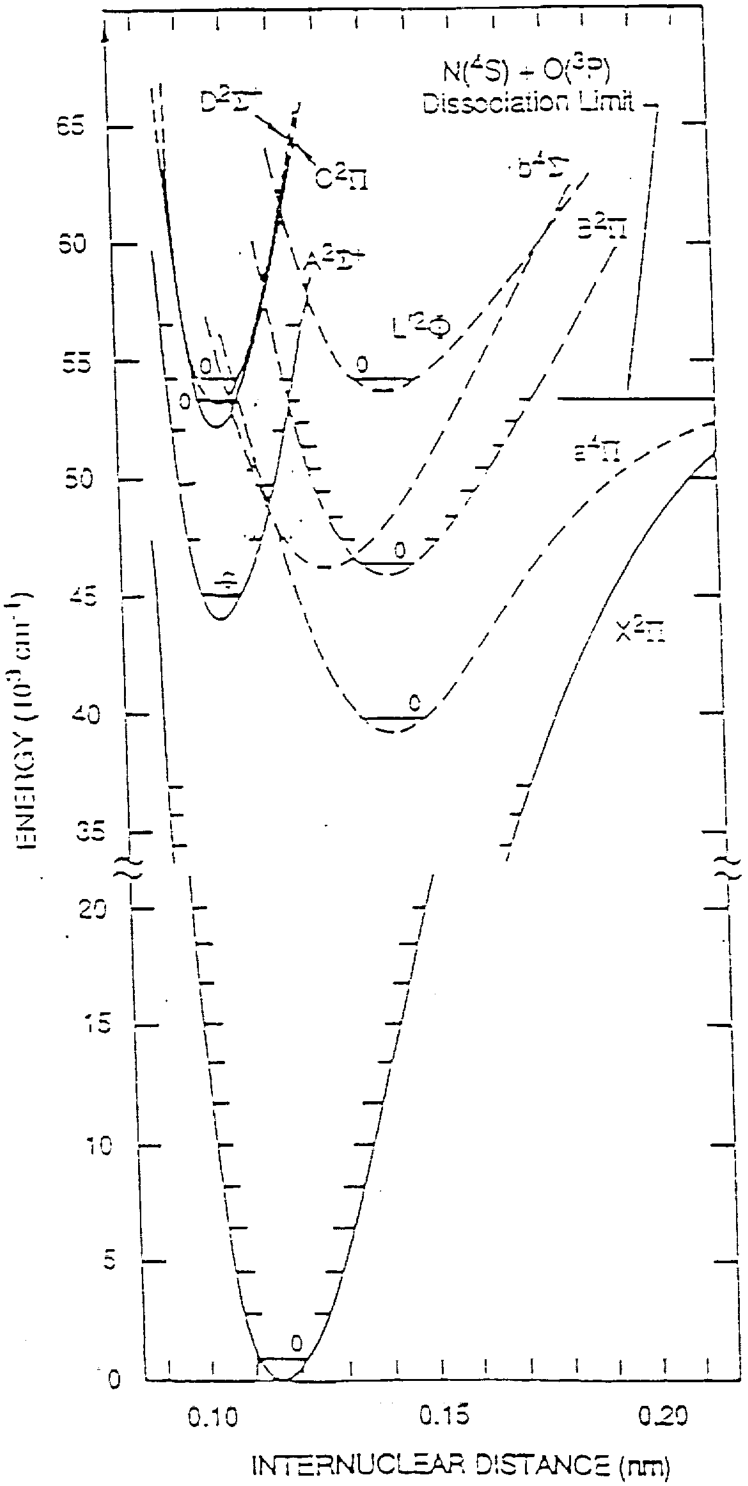

Figure 4. Nitric Oxide Potentials Curves Shown on an Energy Diagram.

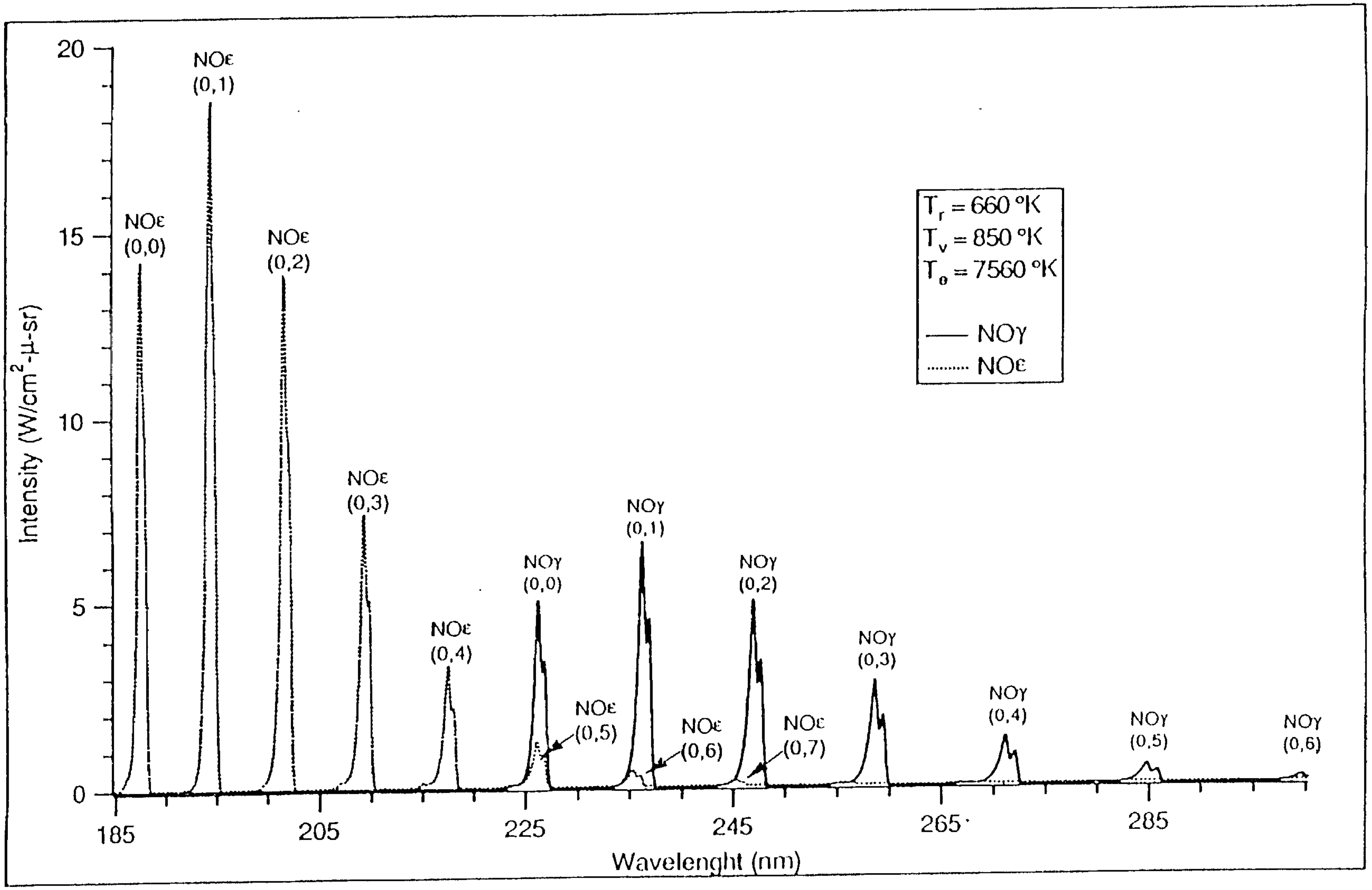

Figure 5. Synthesized Spectrum of NOγ and NOε Band Systems from 185 nm to 300 nm.

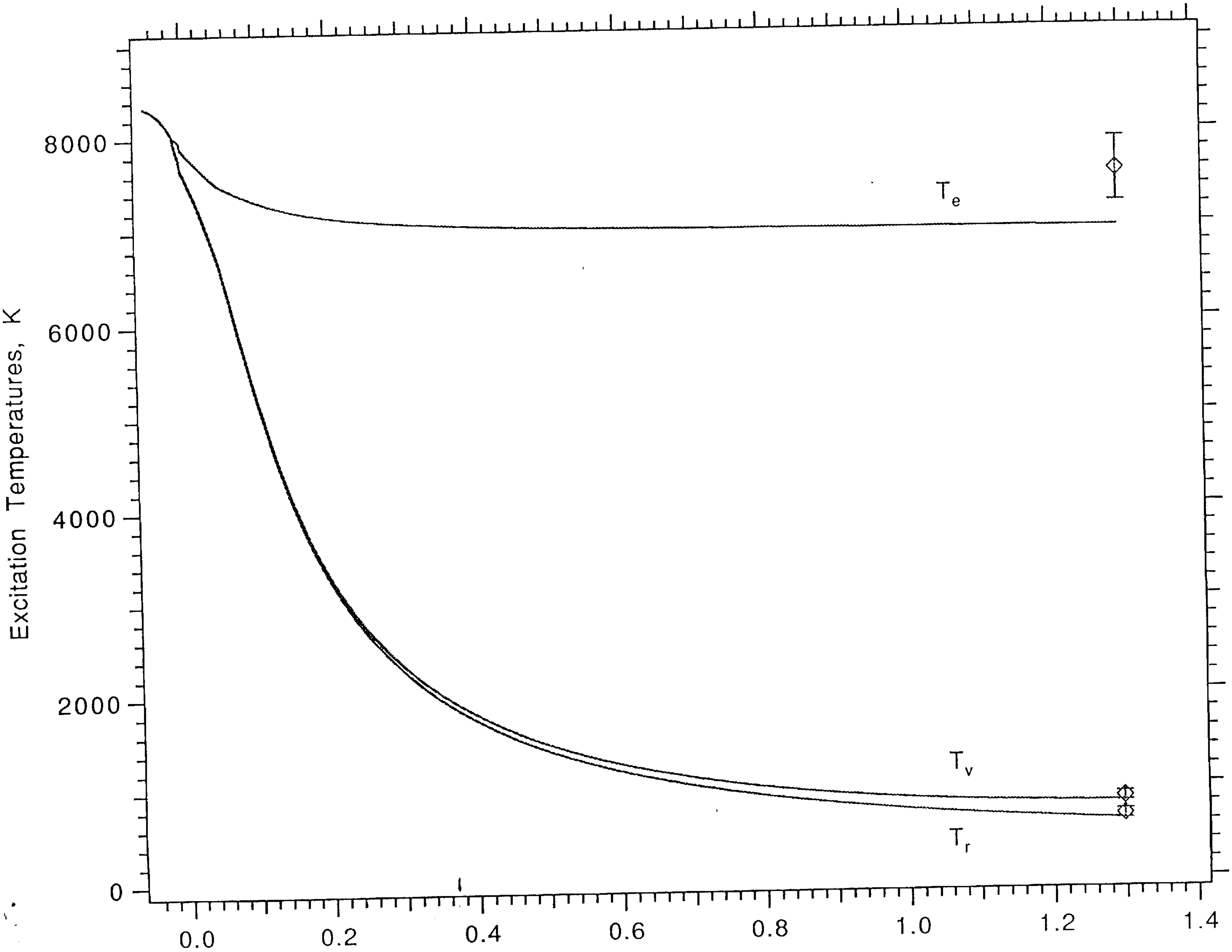

Figure 6. Axial Distance From Nozzle Entrance, m